Neutrino Astrophysics With The Askaryan Radio Array

DISSERTATION

Presented in Partial Fulfillment of the Requirements for the Degree Doctor of Philosophy in the Graduate School of The Ohio State University

By

Jorge Torres, M.Sc.

Graduate Program in Physics

The Ohio State University

2021

Dissertation Committee:

Professor Amy Connolly, Advisor

Professor John Beacom

Professor James Beatty

Professor Rolando Valdés-Aguilar

Abstract

Neutrinos of the highest energies ($> 10^{17}$ eV), named ultra-high energy (UHE) neutrinos, provide a window to study the distant, most energetic universe. Other particle messengers, such as cosmic rays and high-energy ($> 10^{15}$ eV) gamma rays are deflected by magnetic fields or attenuated upon interaction with other particles as they travel, so they never reach the Earth. On the other hand, due to their small cross sections, an neutral charge, UHE neutrinos can eventually reach the Earth and be detected. However, having such a small cross section and very low flux requires immense detectors. One of these detectors is the Askaryan Radio Array (ARA) experiment, which is also the focus of this thesis, particularly on analysis. We first present a diffuse analysis for four years of data of ARA stations 2 and 3, which utilized more than 4 times the livetime of the previous ARA analysis, resulting in the best UHE flux limit set by ARA to date, and the best limit among in-ice radio experiments above 10^8 GeV. We next report on assessing the signal polarization reconstruction capabilities of ARA with both simulation and data, and we show the impact that this can have in constraining the neutrino direction, which will be of the utmost importance for the rapidly developing field of multi-messenger astronomy. This work will inform the design and construction of the next-generation of in-ice Askaryan experiments such as RNO-G and IceCube-Gen2. Finally, we present the optimization of a source search of four years of data of ARA station 2 (A2), configuration 1. This lays the groundwork for extending this analysis to all the configurations and, ultimately, ARA station 3 (A3). This study pioneers ARA's efforts to study neutrinos from a point-source, and preliminary shows that the final efficiency is significantly larger than that obtained for our previous diffuse analysis.

As ARA collects more data and improves its analysis efficiency, it is projected to have a leading limits on the diffuse flux of UHE neutrinos by the end of 2022. Also, the prospects of having an increased analysis for point-source analyses is good news for multi-messenger astronomy, as we optimistically envision joint searches with other observatories such as IceCube, HAWC, MAGIC, LAT, etc.

To my family.

Acknowledgments

First and foremost, I am indebted to my advisor Amy Connolly for her incredible advice and support during my PhD. Amy, thanks a lot for helping me to become an independent researcher and for helping me to stay on track. I am also thankful to my graduate committee John Beacom, Jim Beatty and Rolando Valdés-Aguilar for their advice during my career. I had the opportunity to collaborate with a plethora of incredible scientists and researchers, and I would not be at this stage without the advice and support of many of you. I am particularly grateful for my collaboration with my colleague and friend Brian Clark. Thanks a lot for your mentorship and support whenever I needed it, you are an admirable human being. I was lucky enough to collaborate with several people in the ARA experiment: thanks to the "Daves" (Besson and Seckel), Stephanie Wissel and Simona Toscano for guidance and mentorship. Thank you Seckel for sometimes having zoom calls with me on the weekend to help me understand lots of things regarding reconstruction. Thanks Besson (Galactique Acid) for always answering my questions regarding ice effects, and for all your music. Thanks Stephanie for encouraging me to start the ARA sources working group, and for your support. Thanks Simona for convincing me that there is no reason to have imposter syndrome, and for encouraging me to step out of my comfort zone and apply for postdocs.

I am also grateful for the early career researchers in the ARA collaboration: thanks Cosmin for always being helpful whenever I had a question or problem, thanks Carl for helping me get started doing ARA analysis when I joined the Connolly group, thanks Uzair for being a nice collaborator and for all the beers we had in Germany and Palo Alto, thanks Ming-Yuan for being an awesome collaborator during the last stage of the A23 diffuse analysis, thanks Ben for writing such an amazing simulation code (`PyREx`) and for answering all my coding questions, thanks to Myoung-Chul for sharing knowledge, thanks Yue for co-leading the operations team and sharing all you knew about the stations. Thanks to other collaborators who I might be forgetting.

Outside of ARA, I am grateful for all the magnificent postdocs at the Center for Cosmology and Astroparticle Physics (CCAPP) during my PhD studies. Special thanks to Jordan Hanson for being my first mentor when I joined the Connolly group, I really enjoyed work-

ing on the “BuckArray” project. Also, thanks a lot Steven Prohira for teaching me lots of things while we were deployed at SLAC for the T-567 experiments, and for the subsequent collaboration. Thanks to Patrick and Mauricio for your expertise and for answering all my questions.

Thanks to my physics friends: Andrew, Keith, Derek, Matt, Chris, Danny, Joey, Andrés and other folks who I might be forgetting. We had wonderful times during grad school, and it is kind of a bummer that we do not get eat lunch together for the last time before we have to graduate. Thanks to all the amazing professors from whom I learned a lot during my grad classes. Thanks to all the administrative and technical staff that literally keep the physics department running.

To my friends outside of physics: thanks Brennan for being a very good friend and an adequate roommate for six years, thanks to Tessa for being such an amazing friend and for sharing the same sense of humor as me, thanks Waylon for all the adventures we shared and for your knowledge of the best restaurants in Columbus. Thanks Jacqueline, Celia, Fernando and the rest of joyful Latinos/Spaniards friends that always had a party to go to every single weekend when I was feeling exhausted from doing physics. Thanks to all my salsa dancer friends: Alice, Akshay, Rachel, Christina, Brian, Denethi, and others, for the uncounted number of fun times. Similarly, thanks to the trivia folks with whom I shared lots of Thursday nights being useless in pop culture questions :).

Thanks to the people that supported me economically when I had to move to the US during my first year, when all my savings were depleted due to graduate school applications and GRE/TOEFL fees. I will make sure that the favor I received will be passed on to another person that needs it when the time comes. Special thanks to Ed Cassidy for all his support since I was a high school student.

Finally, I am leaving the last set of acknowledgments to the people that matter most to me: gracias a mis padres y hermano por siempre estar ahí, por recordarme que no estoy solo en esta travesía y que tengo gente a unos cuantos miles the kilómetros que me aprecian y se preocupan por mí. Thanks to Shelley Mackaman for letting Kiki and myself live in her house, and for treating us really well, while this dissertation was being completed. Thanks to Billie, Judy, Josephine and Janet for all their support. Even though you are Kiki’s family, it feels as if you were my family too. Kiki, you have been a great source inspiration and encouragement for completing this dissertation. You were always there whenever I felt anxious about not finishing my dissertation on time, when all the unfortunate events of 2021 happened while I was interviewing for jobs, and when I had stressful times dealing with the US Immigration system. For that I will always be thankful to you. Looking forward to spending a lifetime together!

Vita

December 1993	Born—Comala, Colima, Mexico
August 2015	B.S., Universidad de Colima Colima, Mexico
June 2017	M.Sc., The Ohio State University Columus, OH USA

Publications

P. Allison *et. al.* for the ARA Collaboration, **co-author**. *Constraints on the Diffuse Flux of Ultra-High Energy Neutrinos from Four Years of Askaryan Radio Array Data in Two Stations*. Phys. Rev. D 102, 043021 (2020).

S. Prohira *et. al.* (incl. **J. A. Torres**) *Observation of Radar Echoes From High-Energy Particle Cascades*. Phys Rev Lett. 2020 Mar 6;124(9):091101 (2020).

S. Prohira *et. al.* (incl. **J. A. Torres**) *Suggestion of Coherent Radio Reflections from an Electron-Beam Induced Particle Cascade*. Phys. Rev. D 100, 072003 (2019)

Fields of Study

Major Field: Physics

Studies in:

Ultra-High Energy Neutrino Astrophysics	Prof. Amy Connolly
Neutrino pyhsics	Prof. Alfredo Aranda, Dr. Jonathan Paley

Table of Contents

List of Figures

List of Tables

Chapter 1
Introduction

Ultra-high energy (UHE) neutrinos ($> 10^{17}\,\mathrm{eV}$) open a window to studying the distant, energetic universe in the multi-messenger era. Due to their small cross section and their neutral charge they can travel cosmic baselines undisturbed (besides oscillation effects), unlike other charged messengers. This is of great importance, as they can be detected at neutrino telescopes on Earth and will give information about their source.

1.1 The case for UHE neutrinos

1.1.1 Neutrino astronomy

Due to the small cross sections, neutrinos escape dense and energetic astrophysical sources that are opaque to other cosmic messengers such as photons. Above $10^{15}\,\mathrm{eV}$ [34], the extragalactic Universe becomes opaque to photons as they interact with the cosmic microwave background (CMB) and extragalactic background light (ELB) through the process

$$\gamma + \gamma_{\mathrm{CMB/ELB}} \rightarrow e^+ + e^- \tag{1.1}$$

The electron-positron pair eventually disappears into other particles through other energy loss mechanisms. Charged particles are deflected by extragalactic magnetic fields or interact with other particles, thus not pointing back to their sources.

For this reason neutrinos are the only cosmic messenger particles that can eventually arrive at the Earth, be measured, and provide information about the most energetic particle accelerators in the Universe. In these accelerators, UHECRs are produced with energies greater than $10^{20}\,\mathrm{eV}$, which corresponds to roughly the kinetic energy of a baseball traveling at $\sim$100 mph.

UHE energy neutrinos are tied to UHE cosmic rays (UHECR) as the latter can interact with matter or radiation fields, either in the sources or during propagation, leading to the production of UHE neutrinos that will point back to their source. As a consequence, the observation of UHE neutrinos and measurement of the UHE neutrino flux will allow us to

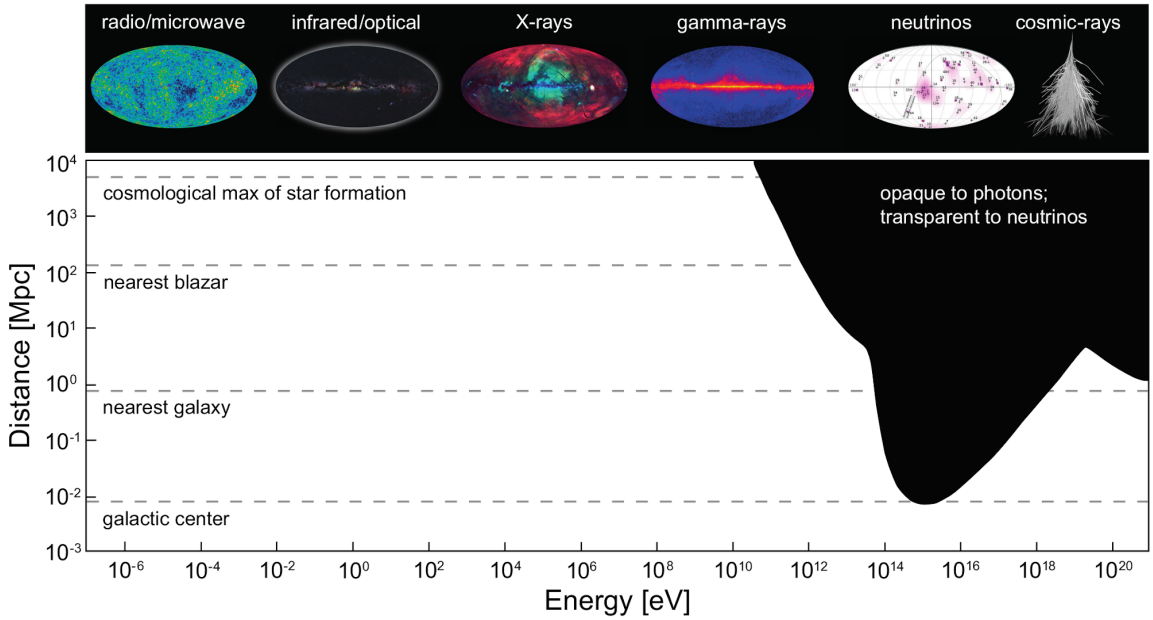

Figure 1.1: Distance at which the Universe becomes opaque to electromagnetic radiation as a function of energy in eV. The black region corresponds to the area where photons have very short mean free paths before being attenuated by pair production. Figure by the IceCube collaboration [1].

answer questions related to the origin and production mechanism of UHECRs, such as how these cosmic rays get accelerated to UHE.

1.1.2 Probes of fundamental physics

Due to its high energy and long baselines, measuring the UHE neutrino flux, or the lack thereof, can be used to perform probes of fundamental physics. These probes often require the observation of neutrinos over certain baselines (for oscillation studies, for example), or at energies where their properties have not been measured, for example the neutrino-nucleon cross section. Measurements of the neutrino-nucleon cross section at the highest energies has been done indirectly by observing the absorption of neutrinos in the Earth for different energies and arrival angles [4, 35]. Deviations from the Standard Model prediction could indicate exotic physics such as extra dimensions [36] or leptoquarks [37].

Neutrinos travel cosmic baselines, and small effects could accumulate and become observable. During propagation over very large distances, neutrino decay could leave a footprint on the energy spectrum and flavor composition [38]. Theories of Lorentz-invariance violation, where neutrinos are predicted to lose energy as they propagate in space [39], can be constrained by measuring the UHE neutrino flux [40]. Cosmic neutrinos can probe dark matter theories in which dark matter may decay or self-annihilate into neutrinos leaving

imprints on the neutrino energy spectrum [41]. Other theories in which UHE neutrinos interact with cosmic backgrounds through beyond-standard model physics can be tested by looking for anisotropies in the UHE neutrino sky.

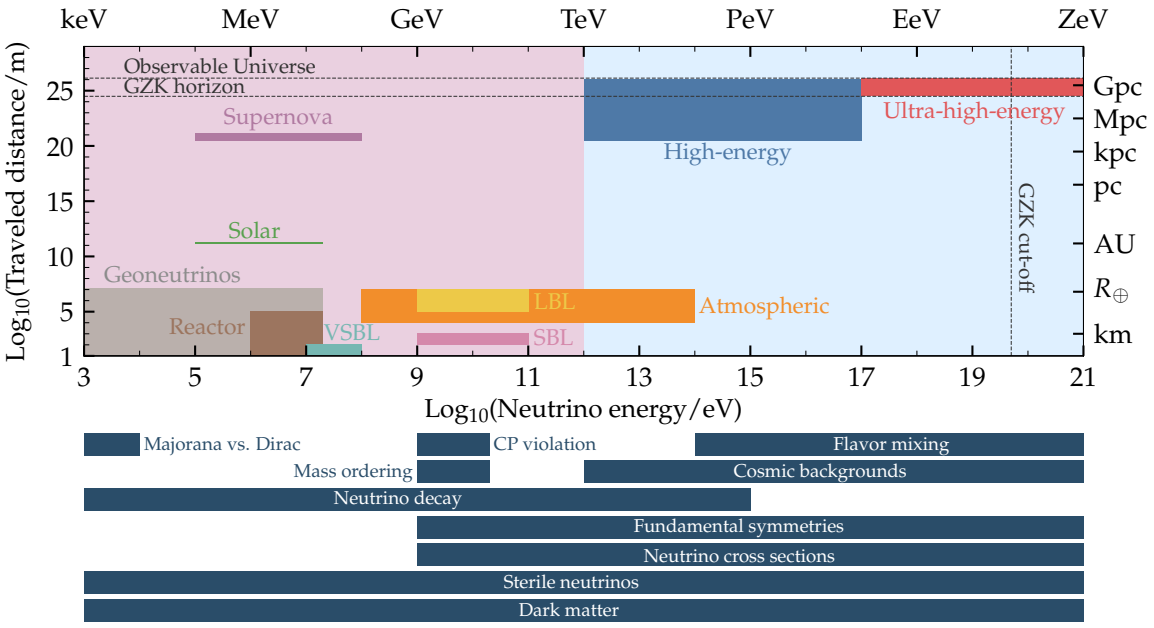

Figure 1.2: Different probes of fundamental physics with neutrinos. As can be seen, many tests of fundamental physics can be performed by observing UHE neutrinos. Figure from [2].

These exciting physics aims becomes challenging from the same fact that enables them: low cross section. Furthermore, at these UHE the flux is extremely small, needing huge experiments to detect them. The radio-technique allows the detection of these particles by measuring the radio waves produced when they interact with the ice.

1.2 The physics behind UHE neutrinos

In this section I will describe the physics behind the production and detection of UHE energy neutrinos via the radio-technique, as well as what properties can be inferred from the measured radiation. I will talk about the experimental landscape of the IceCube observatory and of radio-experiments such as Askaryan Radio Array (ARA), Antarctic Impulsive Transient Antenna (ANITA), and Antarctic Ross Ice-Shelf Antenna Neutrino Array (ARIANNA). Finally, I will briefly mention where the field is going, and the planned experiments in the future.

We can divide UHE neutrinos into two groups due to their production mechanism:

astrophysical and cosmogenic. We call astrophysical neutrinos to those neutrinos that are produced in an astrophysical source. Cosmogenic neutrinos are those that are produced via the so-called Greisen–Zatsepin–Kuzmin (GZK) mechanism, which will be introduced later in this section.

1.2.1 Astrophysical neutrinos

Since these particles are originated inside of astrophysical objects, their observation allows the study of the most energetic phenomena happening in our observable Universe. Their low cross sections allows them to escape dense environments that are opaque to photons.

The first measurement of (lower energy) astrophysical neutrinos dates back to 1987, when the explosion of the supernova SN1987A in the Large Magellanic Cloud, a galaxy of the Milky Way, emitted a burst of MeV neutrinos that was observed by three different neutrino observatories: Kamiokande II [42], the Irvine-Michigan-Brookhaven detector (IMB [43]), and the Baksan Neutrino Observatory [44]. At higher energies, PeV astrophysical neutrinos were first observed by the IceCube Observatory in 2013 [45], offering important clues about their origin. However, crucial mysteries regarding the production mechanism remain unsolved.

The observation of neutrinos from astrophysical point sources would be a smoking gun proof that their production is due to hadronic mechanisms. There are models that suggest that protons (p) or heavy nuclei can be accelerated to very high energies inside an astrophysical object due to the release of gravitational energy as a consequence of accretion of matter or binary mergers. These particles (p) will in turn interact with the matter (p and γ) inside the object producing neutral and charged secondary pions ($p + \gamma \rightarrow p + \pi^0$ and $p + \gamma \rightarrow n + \pi^+$). Neutral pions will decay as $\pi^0 \rightarrow \gamma + \gamma$ creating a high flux of high-energy gamma rays, whereas the charged pions will create high-energy neutrinos (and their respective antiparticles) via the following decay channel (and its charged conjugated):

$$\begin{aligned} \pi^+ &\rightarrow \mu^+ + \nu_\mu \\ \mu^+ &\rightarrow e^+ + \bar{\nu}_\mu + \nu_e \end{aligned} \tag{1.2}$$

These neutrinos will escape the astrophysical object, unless it is a very-dense environment, and will potentially reach the Earth were they can be measured.

Currently, there is lack of established neutrino point sources. The first evidence for neutrinos emitted from a source was the coincident observation of neutrinos and γ-rays from the blazar TXS 0506+056 [46, 47], but more events from the same source are needed to claim an statistical observation.

1.2.2 Cosmogenic neutrinos

Unlike astrophysical neutrinos, cosmogenic neutrinos are not created inside astrophysical sources, but they are products of the interaction of UHE cosmic rays (UHECR) with Cosmic Microwave Background (CMB) radiation or with extragalactic background light (EBL) via the Greisen–Zatsepin–Kuzmin (GZK) mechanism. The GZK mechanism involves photo-production of pions via the following process:

$$p + \gamma \to \Delta^+ \to p + \pi^0, \tag{1.3}$$

and

$$p + \gamma \to \Delta^+ \to n + \pi^+. \tag{1.4}$$

The resulting products will consequently decay. Neutral pions will decay into neutrinos and photons. Neutrons will decay into neutrinos, among other particles. However, the energy of these neutrinos will have lower energies than UHE. Charged pions will produce charged leptons that will in turn decay into neutrinos via a similar process as in Equation 1.2 . These neutrinos retain $\mathcal{O}(5\%)$ [48] of the primary proton's original energy.

We can calculate the energy that UHECRs should have in order to undergo the GZK mechanism. CMB photons have a temperature of about 3 kelvin, which corresponds to an energy of $E_\gamma = k_B T_\gamma = 2.63 \times 10^{-10}$ MeV, where $k_B = 1.38 \times 10^{-23}$ J/K is the Boltzmann constant. Let $\boldsymbol{p}_\gamma$ and $\boldsymbol{p}_{\mathrm{CR}}$ be the four-momenta of the photon and the UHECR, respectively:

$$\boldsymbol{p}_\gamma = (E_\gamma, \vec{p}_\gamma) \tag{1.5}$$

$$\boldsymbol{p}_{\mathrm{CR}} = (E_{\mathrm{CR}}, \vec{p}_{\mathrm{CR}}) \tag{1.6}$$

Note that we are using natural units, so $c = 1$. For the resulting particles, let $\boldsymbol{p}_n$ (the result for the proton will be similar, as they have equivalent mass) and $\boldsymbol{p}_\pi$ be the four-momenta of the resulting neutron and pion in the rest frame, respectively:

$$\boldsymbol{p}_n = (E_n, \vec{0}) \tag{1.7}$$

$$\boldsymbol{p}_\pi = (E_\pi, \vec{0}) \tag{1.8}$$

Because of conservation of energy, we can equate the invariant mass of both sides of Equation 1.3:

$$(\boldsymbol{p}_\gamma + \boldsymbol{p}_{\mathrm{CR}})^2 = (\boldsymbol{p}_n + \boldsymbol{p}_\pi)^2 \tag{1.9}$$

Let us use the $(-1, 1, 1, 1)$ metric. We can workout the left-hand side of Equation 1.9 first.

Since $(\boldsymbol{p}_\gamma)^2 = -M_\gamma^2 = 0$ and $(\boldsymbol{p}_{\rm CR})^2 = -M_{\rm CR}^2$, it reduces to

$$(\boldsymbol{p}_\gamma + \boldsymbol{p}_{\rm CR})^2 = \boldsymbol{p}_\gamma^2 + \boldsymbol{p}_{\rm CR}^2 + 2\boldsymbol{p}_\gamma \cdot \boldsymbol{p}_{\rm CR} \tag{1.10}$$

$$= -M_{\rm CR}^2 + 2\boldsymbol{p}_\gamma \cdot \boldsymbol{p}_{\rm CR}. \tag{1.11}$$

Conservation of momentum requires that $\vec{p_\gamma}$ and $\vec{p}_{\rm CR}$ have opposite directions, thus their dot product becomes

$$\boldsymbol{p}_\gamma \cdot \boldsymbol{p}_{\rm CR} = -E_\gamma E_{\rm CR} + (E_\gamma)(-|\vec{p}_{\rm CR}|), \tag{1.12}$$

where we have used the fact that photons are massless ($|\vec{p_\gamma}| = E_\gamma$) and Equation 1.11 becomes

$$(\boldsymbol{p}_\gamma + \boldsymbol{p}_{\rm CR})^2 = -(M_{\rm CR}^2 + 2E_\gamma E_{\rm CR} + 2E_\gamma|\vec{p}_{\rm CR}|) \tag{1.13}$$

Now, using the fact that $\boldsymbol{p}^2 = -M^2$, the right-hand side of Equation 1.9 becomes

$$(\boldsymbol{p}_n + \boldsymbol{p}_\pi)^2 = -(M_n + M_\pi)^2. \tag{1.14}$$

We can combine these last two equations to get an expression relating the masses of the products and the energies and momenta of the initial particles.

$$M_{\rm CR}^2 + 2E_\gamma E_{\rm CR} + 2E_\gamma|\vec{p}_{\rm CR}| = (M_n + M_\pi)^2 \tag{1.15}$$

Note that we know each variable, except $E_{\rm CR}$ and $|\vec{p}_{\rm CR}|$. However, since $E_{\rm CR} \gg M_{\rm CR}$, we can approximate $|\vec{p}_{\rm CR}| \approx E_{\rm CR}$. Plugging into Equation 1.15 and solving for $E_{\rm CR}$ yields

$$E_{\rm CR} = \frac{(M_n + M_\pi)^2 - M_{\rm CR}^2}{4E_\gamma}. \tag{1.16}$$

Assuming that the cosmic ray is a proton, we can estimate $E_{\rm CR}$ by using the following values for the masses: $M_n = 939.6$ MeV, $M_p = 938.3$ MeV, $M_{\pi^+} = 139.6$ MeV. This gives that the needed energy for a UHECR to undergo the GZK mechanism is

$$E_{\rm CR}^{\rm thres} \sim 10^{20}\,{\rm eV}.$$

As a consequence, we expect the UHECR flux on Earth to steeply fall at energies greater than 10^{20} eV. We call this the GZK cutoff, and can be seen in Figure 1.3. This cutoff correpsonds to about 50 Mpc [49] propagation length, after which is very likely that UHECRs produce other particles via the GZK mechanism. Since it is unlikely to observe UHECRs after they have traveled distances greater than 50 Mpc, studying UHE neutrinos, which we can observe on Earth, will allow us to unravel the sources, composition and production mechanism of the precursor UHECRs, which are critical questions in particle astrophysics.

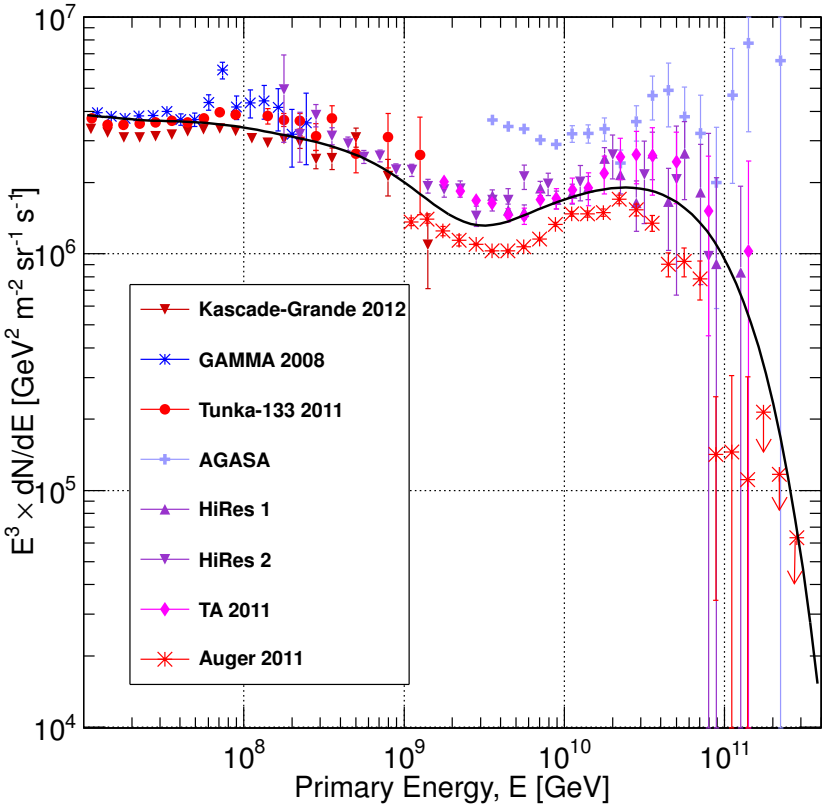

Figure 1.3: All particle cosmic ray spectrum from air shower experiments as a function of energy. The GZK flux cutoff can be interpreted as the dip at about $10^{10.5}$ GeV. Figure from [3].

1.3 The physics of UHE detection

After UHE neutrinos are created, either inside sources or by the GZK mechanism, they will travel cosmological distances ($\mathcal{O}$(Gpc)) undisturbed. This is not true for charged particles, which get deflected by extragalactic magnetic fields or get attenuated upon interaction, or for photons with $E_\gamma > 10^{12}$ eV, which can get attenuated into an electron/positron pair before they can reach the Earth. This is schematically depicted by Figure 1.4.

1.3.1 Landing on Earth

A small number of neutrinos will arrrive at Earth, and a small fraction of them will interact. We expect UHE neutrinos to arrive at Earth with an incident flux of about 10 events km^{-2}y^{-1}sr^{-1}. The probability that they will interact is proportional to the neutrino-nucleon cross section ($\sigma_{\nu N}$) at a given energy, and the density of the interaction medium. For the

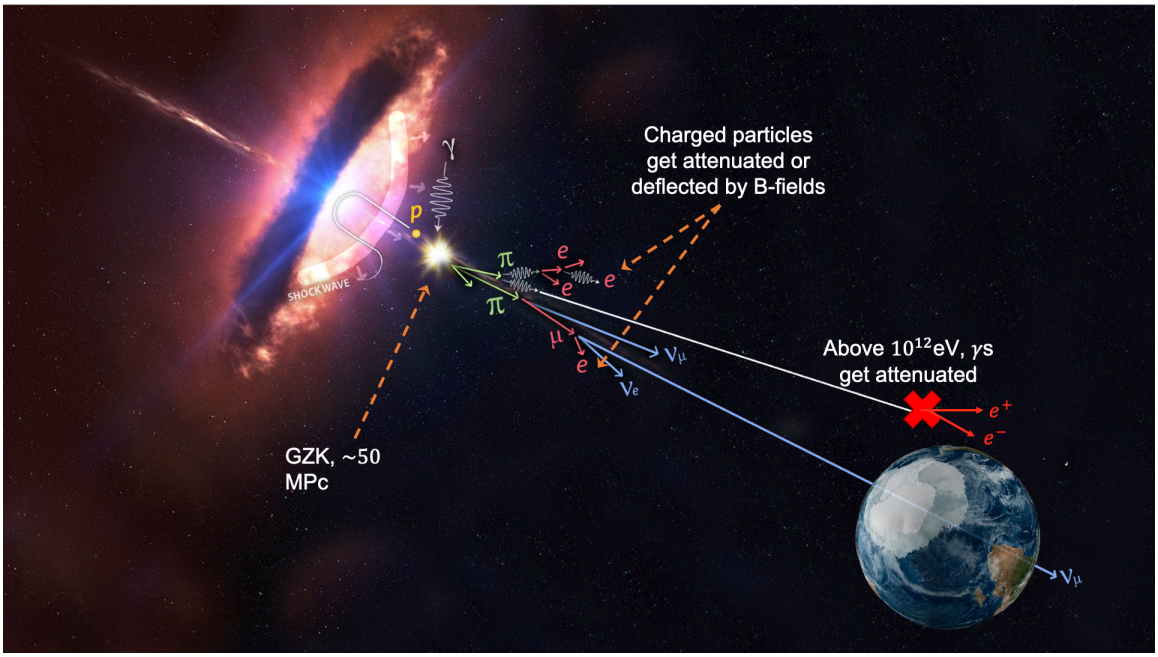

Figure 1.4: Cosmic rays interact within a ∼50 Mpc radius via the GZK mechanism, producing neutrinos, which are the only messengers that can potentially arrive and be observed at Earth at UHE. Figure adapted from the IceCube Collaboration.

entirety of this document, we will assume that the medium is the Antarctic ice ($\rho = 0.9$ g/cm^3).

Even at the highest energies, $\sigma_{\nu N}$ remains small. Figure 1.5 shows the measured and projected neutrino-nucleon cross section for the highest energies.

At 10^{18} eV, the neutrino nucleon cross section is of the order of 10^{-32} cm^2. From the previous quantities, one can estimate that the rate of neutrinos (per volume, per time, per sterradian) interacting with the ice would be

$$\mathcal{N} = N_{\text{target}} \sigma_{\nu N} \Phi_\nu \tag{1.17}$$

$$\sim 10^{-3}\ \text{km}^{-3}\ \text{y}^{-1}\ \text{sr}^{-1}, \tag{1.18}$$

where N_{target} is the number density of target nucleons in the ice, $\sigma_{\nu N}$ is the neutrino-nucleon cross section and Φ_ν is the UHE neutrino flux.

This small number means that we require immense ($\mathcal{O}(\text{km}^3)$) detectors in order to observe a statistically significant amount of UHE neutrinos. This was already understood back in the 1970s [50]!

Neutrinos can interact via deep inelastic charged current (CC) or neutral current (NC) interactions. For CC interactions, a neutrino (ν_ℓ) scatters off the quarks of a nucleon (N) exchanging a charged $W^\pm$ boson, and producing a charged lepton ℓ ($\ell = e, \mu, \tau$) and

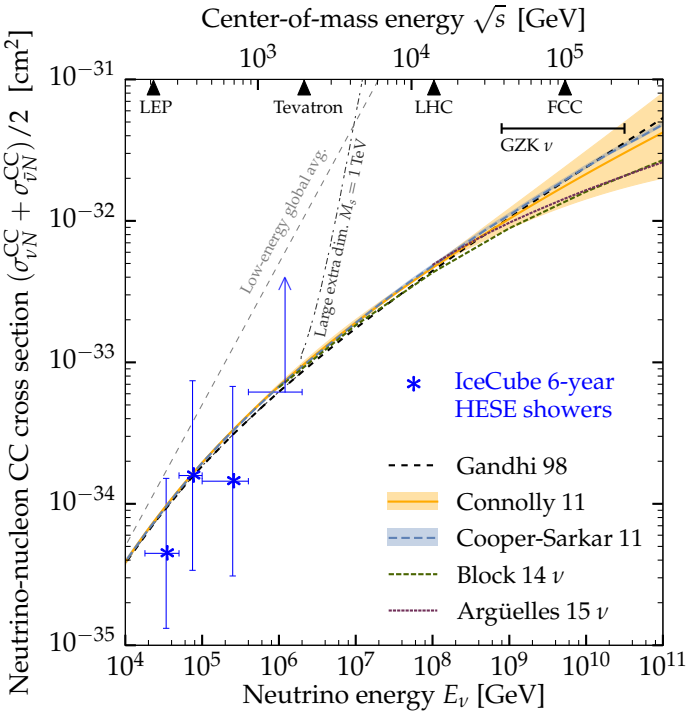

Figure 1.5: $\sigma_{\nu N}$ as a function of energy [GeV] from [4]. As it can be seen from the top x-axis, fundamental physics can be probed with UHE neutrinos at energies not yet attainable by human-made accelerators.

fragmenting the nucleus into high-energy units, creating a hadronic shower X in the medium. For NC interaction, the neutrino (ν_ℓ) interacts with the quarks in a nucleon via a Z boson exchange producing a secondary neutrino of the same flavor as the primary, and, similarly as in the CC interaction, a hadronic shower N^*. The Feynman diagrams for these two different processes are shown in Figure 1.6. About 80% of the energy of the primary neutrino is transferred to the daughter lepton. Both the secondary particles and the produced hadronic showers will be useful for the detection of neutrinos.

1.3.2 Detection of neutrino signatures

When charged particles move faster than the speed of light in a dielectric medium of refractive index n, i.e. $\beta \equiv \frac{v}{c} > \frac{1}{n}$, they emit Cherenkov radiation [51] in a ring pattern of aperture angle θ_C given by $\cos\theta_C = \frac{1}{\beta n}$. The intensity of this light is proportional to $\frac{1}{\lambda^2}$, so short wavelengths dominate, namely blue light. If in a transparent medium, this light can be observed by photo-detectors placed close to it. This is how neutrino detectors such as IceCube [52] and KM3NeT [53] detect neutrino events. They employ photomultipliers (PMTs) that detect faint Cherenkov radiation emitted by relativistic daughter leptons and

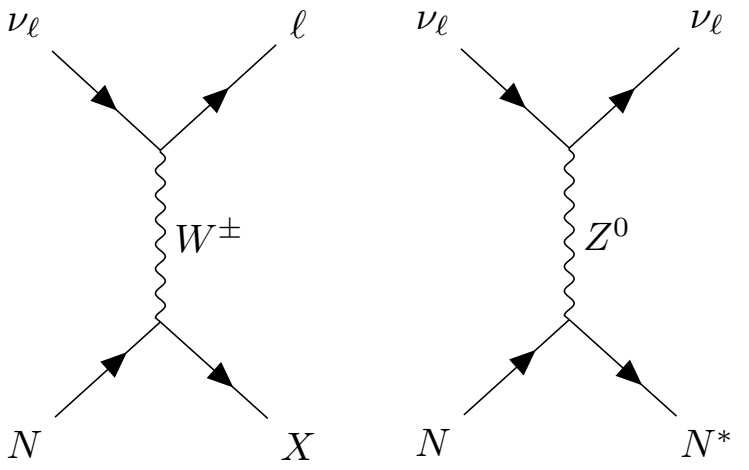

(a) Charged current interaction (b) Neutral current interaction

Figure 1.6: Feynman diagrams for CC and NC interactions of neutrinos. Figure made with `TikZ-Feynman` [5]

convert it to a digital signal that can be analyzed and classified. From this, properties such as the neutrino energy, direction and flavor can be inferred . There are two classes of patterns, "tracks" and "cascades": "tracks" correspond to elongated, contained patterns due to Cherenkov light emitted by long-lived muons (from ν_μ) passing through the detector. "Cascades" correspond to scattered patterns from Cherenkov light emitted by electrons or taus, which get quickly attenuated or are short-lived, respectively.

The use of Cherenkov light for the detection of neutrinos has been around since the 1980s, with pioneering experiments such as the KamiokaNDE experiment [54]. However, a new technique for the detection of neutrinos, UHE neutrinos specifically, was proposed by the Russian physicist Gurgen Askaryan back in 1962 [55]: the detection of radio-waves (Askaryan radiation) emitted by relativistic particle showers in dense media.

1.3.3 Askaryan radiation

Consider an UHE electron neutrino ν_e entering the ice and undergoing a charged current interaction, $\nu_e + N \to e + N'$. Most of the energy that the ν_e originally had is transferred to the resulting electron. While passing through matter, the energy of the electron is degraded by interactions with the ice. Among the interactions that the high-energy electron can undergo, the most important is bremsstrahlung in the fields surrounding the nuclei in the ice, since it has the largest cross section. After bremsstrahlung, which creates a secondary photon, the energy is (roughly) uniformly distributed between the electron and this secondary photon [56]. The secondary photon will create an electron-positron pair

in interactions with other nuclei, as its cross section dominates at high energies, which will in turn interact to form more secondary particles. This iterative process produces an electromagnetic cascade shower that continues until the secondary particles reach energies at which the bremsstrahlung and ionization rates are equal. This energy is called the critical energy E_c.

Once this energy is reached, the remaining particles can likely undergo other processes besides bremsstrahlung and pair production, since their cross sections become equally important [57]. Among these processes, the main interaction channel for photons is Compton scattering ($\gamma + e^-_{\text{atom}} \to \gamma + e^-$), which degrades their momenta until they reach energies at which the photoelectric effect cross section is dominant, terminating the photons in the cascade shower. Electrons and positrons interact via Bhabha scattering ($e^+ + e^-_{\text{atom}} \to e^+ + e^-$), via positron annihilation ($e^+ + e^-_{\text{atom}} \to \gamma\gamma$), and via Møller scattering ($e^- + e^-_{\text{atom}} \to e^- + e^-$). Through these interactions, energy is deposited in the ice. The radius of a cylinder containing on average 90% of the shower's energy deposition is called the Molière radius R_{M}, and $R_{\text{M}} \sim 10$ cm in ice. Note that the interactions aforementioned contribute to a negative charge excess in the shower, either by annihilating positrons or adding electrons from the medium to the electromagnetic cascade. Monte Carlo simulations by Zas, Halzen and Stanev (ZHS) [58] and GEANT simulations [59, 60] predict the negative charge excess to be $\sim 20\%$ for shower energies > 1 PeV.

This 20% charge excess is not static in time. As the shower evolves, and the number of particles changes, the net charge grows reaching a maximum and then declines again. This can be understood as a time-varying "longitudinal current" [61], which produces electromagnetic radiation, polarized radially outward and perpendicular to the surface of the Chrenkov cone. Askaryan radiation has been observed at accelerator facilities in sand, salt, and ice [62–64].

For wavelengths larger than the Molière radius in a dense medium, corresponding to frequencies < 1 GHz, the amplitudes of the fields coherently add, producing a broadband (200 MHz-1.2 GHz) coherent radio impulse. The energy of this coherent emission scales with the square of the charge excess in the shower, which is in turn proportional to the square of the energy of the incident particle E_ν. From this, the amplitude of the field scales as E_ν. This emission is maximal at a cone (Cherenkov cone) of half-angle θ_C satisfying $\cos\theta_C = 1/n$, where n is the refraction index of the medium and has a duration of less than a nanosecond [65]. For ice, $n = 1.78$, and thus $\theta_C \approx 57°$.

Askaryan radiation has been parametrized by Alvarez-Muñiz *et. al.* [66]. We can express this parametrization in terms of proportions:

$$R|\vec{E}(f, R, \theta_C)| \propto \frac{E_\nu}{1\ \text{TeV}} \frac{f}{f_0} \frac{1}{1 + (f/f_0)^{1.44}} \exp\left(-\frac{1}{2}\left[\frac{\theta - \theta_C}{\sigma_\theta}\right]^2\right), \tag{1.19}$$

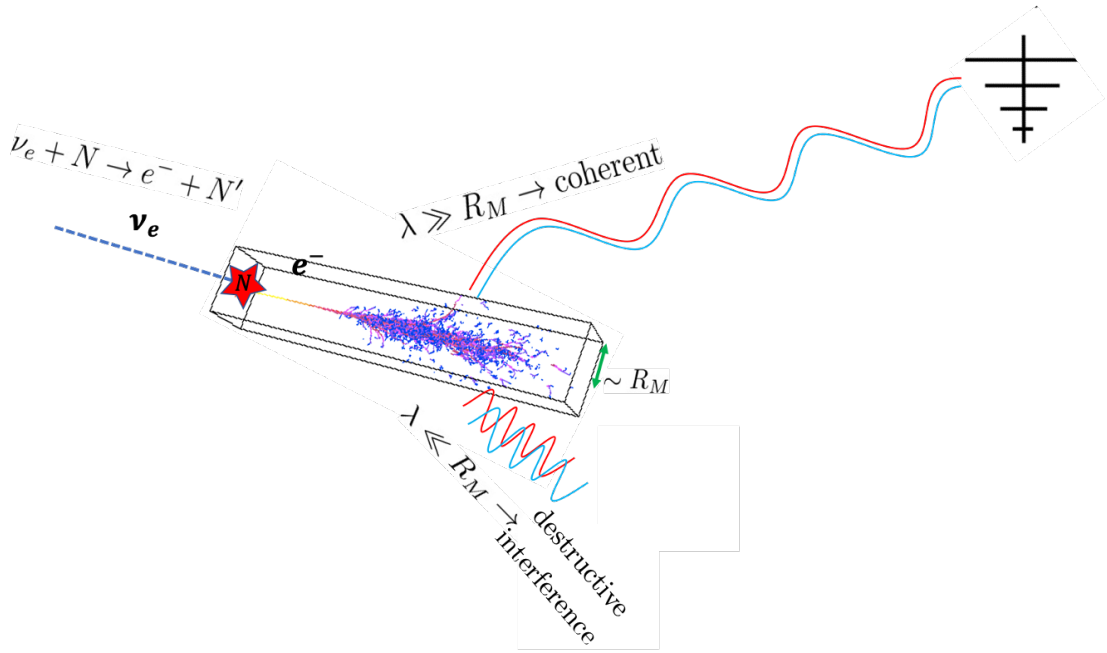

Figure 1.7: Schematic depiction of the production of Askaryan radiation

where E_ν is the primary neutrino energy, f is the frequency of the emitted radiation, f_0 = 1.15 GHz is a normalization factor, θ is the observation angle, and it represents the angle between the observer and the shower propagation direction. The Gaussian term corresponds to a dampening in amplitude as the observer moves away from the Cherenkov angle, with the half-width of the gaussian approximately given by $\sigma_\theta = 2.2°(1\ \text{GHz}/f)$. This parametrization of the Askaryan radiation has allowed simulations of Askaryan detectors to run rather quickly, since there is no need to fully simulate the particle shower. Posterior work by the same authors detailed parametrizations in both time and frequency domain, including a more detailed treatment of the signal and additional optical effects [6].

Askaryan radiation can be detected by placing antennas near the neutrino vertex. An advantage of detecting radio waves over optical light is that radio waves can travel longer than optical light before being attenuated. Studies performed in the Antarctic ice have shown that radio waves [21, 67–69] have as much as 10 times larger attenuation lengths than optical light in ice [70]. At radio frequencies, electromagnetic radiation can travel several hundreds of meters to about 1 km, allowing radio detectors to observe more volume than optical detectors with less instrumentation.

The measurement of Askaryan radiation and simultaneous modeling have allowed the design of experiments aimed towards the detection of UHE neutrinos via Askaryan radiation.

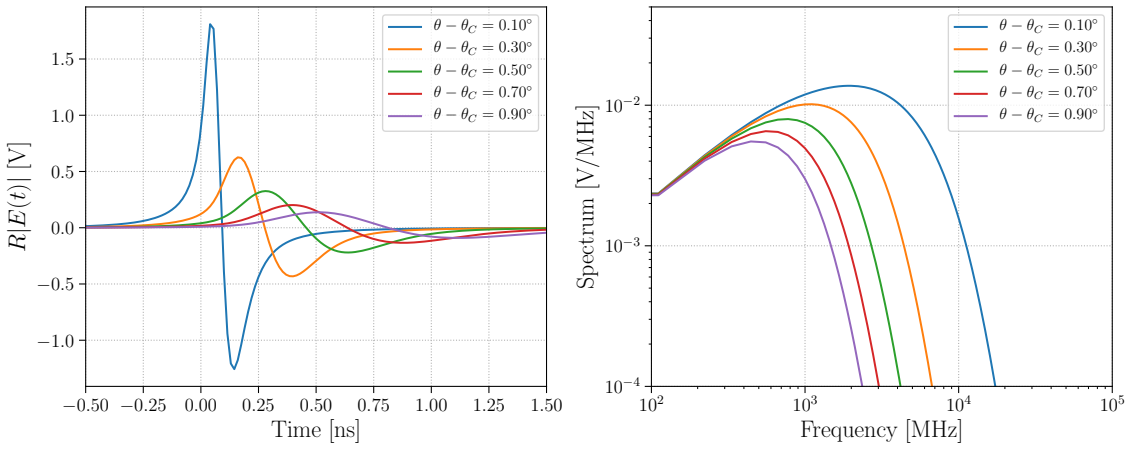

Figure 1.8: Magnitude of the electric field and spectrum of Askaryan radiation produced by a hadronic shower induced by the interaction of a neutrino of energy $E_\nu = 10^{18}\,\text{eV}$ in the ice. Both quantities are shown for different viewing angles (in degrees), to highlight the gaussian dependence. Obtained using the parametrization from [6]

I will refer to these method as the radio-technique henceforth. Starting in the early 2000s, three Askaryan experiments have been deployed. In the next section I will talk about these experiments, and also IceCube for completeness.

1.4 Detection of UHE neutrinos using ice as a medium: current experiments

In this section I will describe the current experimental landscape in the field. I will start with IceCube, which targets neutrinos at lower energies using optical light, and finally move onto experiments targeting neutrinos of the highest energies, which employ the radio-technique.

As was explained in the last section, optical experiments have the disadvantage of optical light having shorter attenuation lengths, i.e. light can only travel for a few tens of meters before becoming too faint to be detected. This translates into a loss of sensitivity at the highest energies, where the UHE neutrino flux becomes very small and more instrumentation, or detectors with larger observation volume, are needed to cover greater areas. On the other hand, since the amplitude of the Askaryan radiation is proportional to the energy of the neutrino, there is a threshold below which this signal becomes buried under the noise floor. This translates into an energy gap between $10^{16} - 10^{17}\,\text{eV}$ where neither the optical experiments nor the Askaryan experiments are sensitive enough. However, the sensitivity of experiments using the radio-technique increases as the energy increases. This can be seen in Figure 1.9. IceCube has 81 stations and has the limit shown is from nine years of data [8], but its sensitivity becomes comparable to that of radio experiments, consisting on only a

few stations, that have been operating for a few years. Projections indicate that ARA will have the same, if not greater, sensitivity as IceCube by 2023 and with only 5 stations.

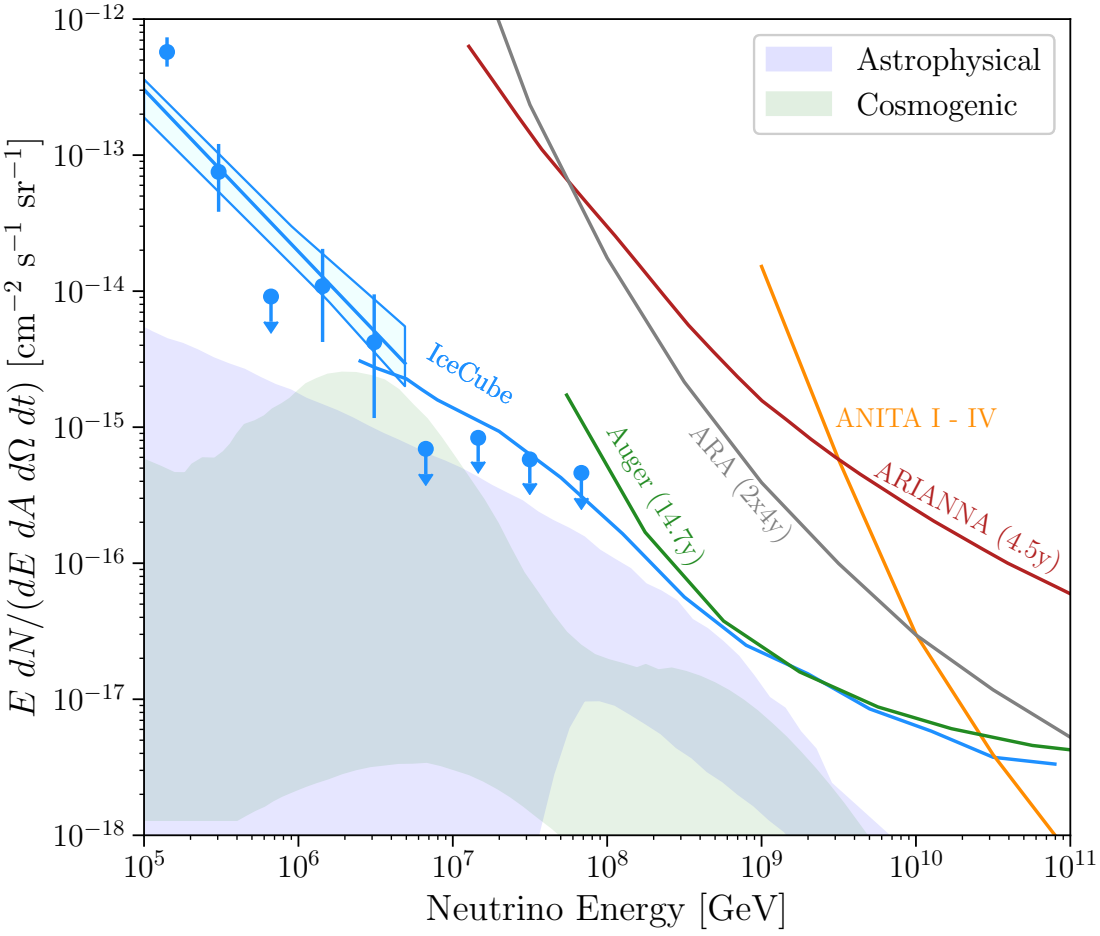

Figure 1.9: Current UHE neutrino experimental landscape. The data corresponds to the measured limit on the cosmic neutrino flux from nine years of data [7]. The solid lines correspond to limits set by IceCube [8], Auger [9], ANITA [10], ARA [11], ARIANNA [12]. The shaded bands correspond to theoretical models for astrophysical [13–15] and cosmogenic [16, 17] neutrinos.

As of now, no UHE ($E_\nu > 10^{17}$ eV) neutrino has been discovered. However, a few experiments have been deployed to look for them. I will talk about these experiments in the next subsections: IceCube, ANITA, ARA, and ARIANNA .

1.4.1 IceCube Neutrino Observatory

Also called by its short name, IceCube is a gigaton detector located at the South Pole. Its primary target is the detection of high-energy neutrinos $E_\nu > 10^{11}$ through the observation of Cherenkov radiation produced by the interaction of neutrinos in the ice. IceCube has an in-ice array and an on-ice array component, also known as IceTop. The in-ice array consists of 5160 digital optical modules (DOMs), each connected to a photomultiplier tube (PMT) and a digitizer. The quantity of recorded light with the PMTs as well as the pattern on the array is useful information to reconstruct the energy, direction and flavor of the primary neutrino. The DOMs are deployed on 86 strings with depths between 1450 m to 2450 m, each string holding 60 DOMs. There are 8 of these strings densely packed at the center of the in-ice array, which are used for lower threshold studies (∼10 GeV) such as neutrino oscillations.

The on-ice array, also known as IceTop, also consists of 81 stations, one on top of each string. IceTop serves as a veto and calibration detector for IceCube, but its main scientific goal is the measurement and reconstruction of cosmic rays coming from the Southern Sky.

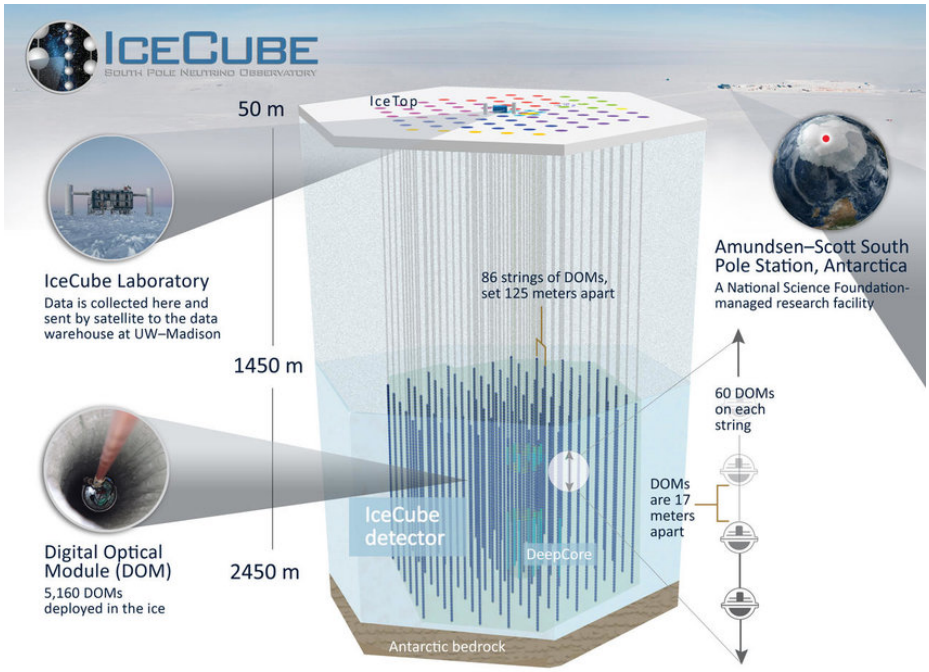

Figure 1.10: An schematic depiction of the IceCube Neutrino Observatory at the South Pole.

1.4.2 The Antarctic Impulsive Transient Antenna (ANITA)

ANITA [71] is a balloon-borne experiment designed to look for broadband, impulsive Askaryan radiation. The balloon flies for about one month at an altitude of ∼40 km over the Antarctic surface. It consist of 48 horn antennas, which are highly-beamed and dual-polarized antennas. ANITA can observe Askaryan emission from neutrino interactions as well as geomagnetic emission from extensive air showers (EAS) induced by particles interacting with the atmosphere.

So far ANITA has had four campaigns, and has placed the best limit among Askaryan-experiments on the UHE neutrino flux at energies of 10^{10} GeV and above. The successor of ANITA will be a similar balloon-borne experiment called PUEO [72]. PUEO is projected to have one of the best sensitivities to UHE neutrinos at energies greater than 1 EeV, building from the knowledge acquired from its predecessor, but with an improved system. New features include additional antennasm, and an interferometric phased array trigger that will allow to lower the trigger threshold, ability to filter anthropogenic noise in real-time, and improved pointing resolution.

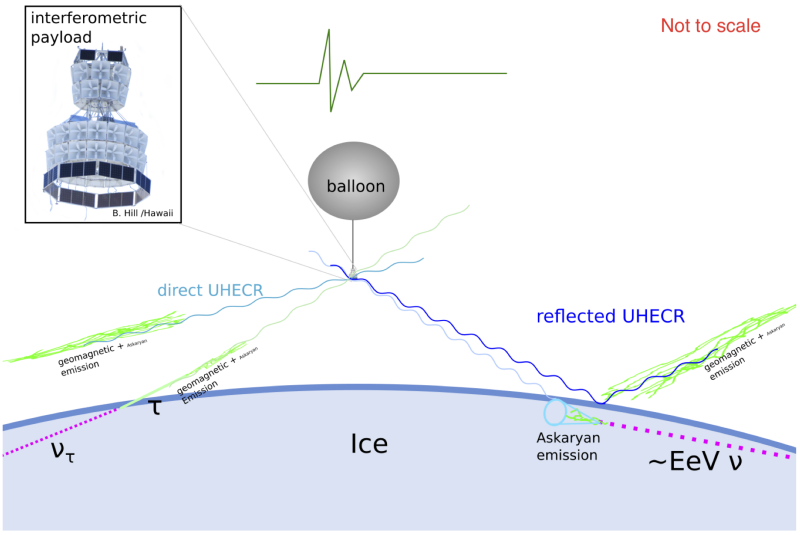

Figure 1.11: Schematic description of the ANITA experiment

1.4.3 The Antarctic Ross Ice-Shelf ANtenna Neutrino Array (ARIANNA)

ARIANNA is an Askaryan experiment located at Moore's Bay on the Ross Ice Shelf, with two additional stations at the South Pole. Each ARIANNA station consists of four log-periodic dipole antennas (LPDA) antennas buried face-down slightly below the ice surface in two pairs with perpendicular orientation. The fact that the antennas are deployed close to snow level has the advantage of not having technical difficulties that drilling a hole at hundreds of meters below the ice represents. However, the trade-off is that their observation volume is lower, as they observe less detection medium (due to a more limited range of angles) compared to in-ice experiments. Similarly, the location of the experiment (Moore's Bay) provides a radio quiet environment, although it presents station-powering challenges due to ARIANNA's remote location that limit the operational livetime of ARIANNA to about 151 days per stations throughout the year. The ARIANNA collaboration released his latest analysis results of 4.5 years of data, imposing a 90% confidence upper limit on the diffuse flux of UHE neutrinos, which can be seen in 1.9.

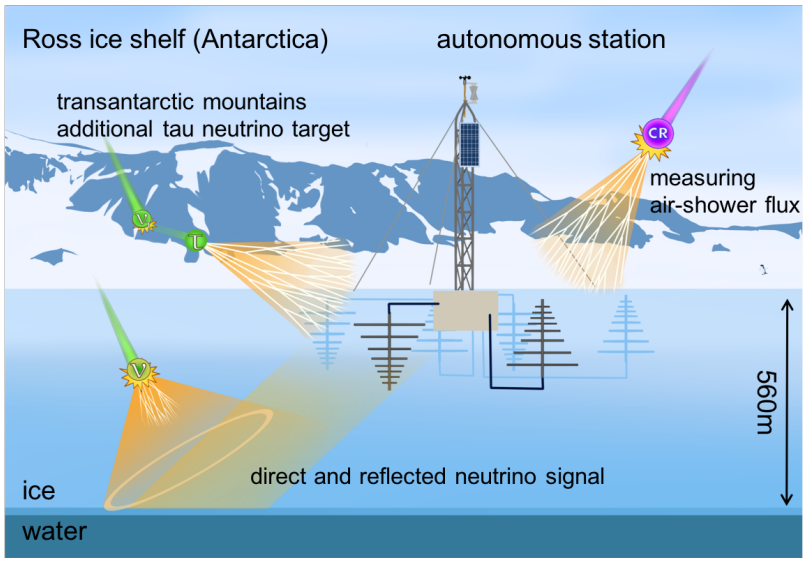

Figure 1.12: Schematic description of the ARIANNA experiment.

1.4.4 The Askaryan Radio Array (ARA)

This thesis will be devoted to this experiment, so a more complete description will be introduced in the next chapter. We will briefly summarize the experiment here and compare

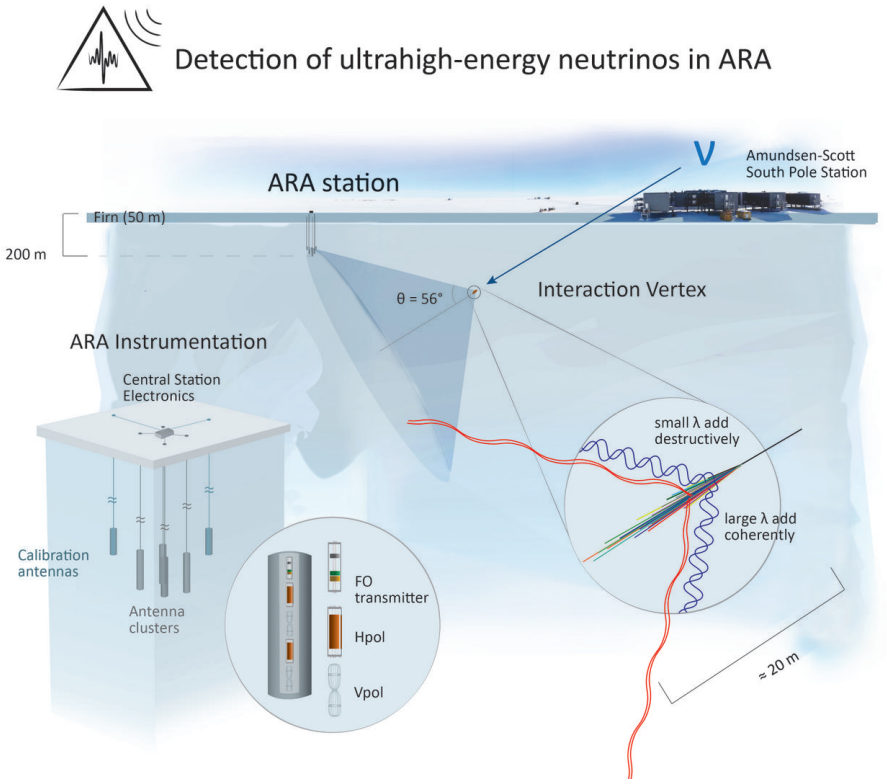

Figure 1.13: Schematic description of the ARA experiment.

it to the other previously described experiments.

The ARA experiment is located at the South Pole, a few kilometers away from the IceCube experiment. Up to date, ARA has deployed five stations at about 200 m under the ice surface. Each station consists of 16 antennas, 8 horizontally polarized (Hpol) and 8 vertically polarized (Vpol) arranged in four clusters. Figure 1.13 shows a graphic depiction of the experiment.

Being at 200 m under the ice allows ARA to observe a greater detection volume than ARIANNA, but it comes with the logistical disadvantage of ice drilling and deploying, as the antennas need to be narrow enough to fit in the borehole ($\sim$ 50 cm wide). On the other hand, being close to IceCube lets ARA benefit from IceCube's power grid, allowing detector uptimes close to 100%.

1.5 My contributions to ARA

In this section I will briefly summarize my contributions to the ARA experiment. I mainly focused my PhD on analysis of ARA's data, simulation of the ARA detector and the development of a reconstruction framework.

1.5.1 Analysis

I was part of the team that lead the analysis of 4 years of data for stations 2 and 3 of the ARA experiment. This work resulted in setting the best limit on the diffuse UHE neutrino flux above 10^8 GeV among in-ice radio experiments [11]. I have also led the analysis of SpiceCore data to give an estimate of ARA's polarization reconstruction capabilities. This is described in Chapter 3.

Finally, I built from work started from other colleagues for the Solar paper [33] to develop a point-source search framework with the addition of a directional cut. This allowed us to lay the groundwork for ARA's first steady point-source search with a significant increase on the analysis efficiency compared to that of the diffuse analysis. This is described in Chapter 4.

1.5.2 Simulation

During my PhD studies, I developed new features for ARA's simulation software `AraSim`. Along with other colleagues, I was in charge of adding different geometry layouts to `AraSim` to assess the sensitivity of the next generation of Askaryan-experiments such as RNO-G. I also enhanced `AraSim` capabilities for directional reconstruction of UHE neutrinos by correcting simulation parameters such as neutrino direction and gain application at the antenna that were not optimized for precision studies.

I developed a framework to reconstruct the neutrino polarization by deconvolving the antenna response of the detector. This framework allowed me to give an estimation of ARA's polarization reconstruction capabilities, which consequently were used to assess the neutrino directional reconstruction resolution of ARA.

For the diffuse paper, I led the study on systematic uncertainties by adapting the simulation for different simulation modes and models. These results were included in the final limit that was published in [11].

Chapter 2

Diffuse neutrino search with ARA

ARA recently released its strongest limit on the UHE neutrino flux, achieving the best sensitivity among in-ice experiments above 10^8 GeV. This limit was set by analyzing four years of data from ARA stations 2 and 3. I was part of the team that led this work, along with Ohio State graduate student (now a postdoctoral researcher at Michigan State University) Brian Clark, and University of Wisconsin-Madison graduate student Ming-Yuan Lu. For this work, my contributions were the tuning of major cuts such as the thermal cut, power out-of-band cut and others, and the study of systematic uncertainties that were included in the final UHE neutrino diffuse flux limit. This work resulted in a publication, from which parts of this chapter were taken:

> P. Allison *et. al.* for the ARA Collaboration. *Constraints on the Diffuse Flux of Ultra-High Energy Neutrinos from Four Years of Askaryan Radio Array Data in Two Stations*. Phys. Rev. D 102, 043021 (2020).

In this chapter I will talk about the diffuse paper in general, with emphasis on my work. Sections that were almost entirely taken from our publication are marked with an asterisk (*).

2.1 The Askaryan Radio Array experiment*

2.1.1 The instrument

The Askaryan Radio Array is a UHE radio neutrino detector consisting of five stations located a few kilometers grid-west of the geographic South Pole in Antarctica, as drawn in Figure 2.1 [21]. A single station consists of 16 antennas, eight for detecting horizontally-polarized (HPol) radiation and eight for detecting vertically-polarized (VPol) radiation, along with signal conditioning and Data Acquisition (DAQ) electronics. The antennas are deployed at the bottom of holes at up to 200 m depth on four "measurement strings",

forming an rectangular solid 20 m tall and 15 m deep and wide. At each corner of the rectangle an HPol quad-slotted cylinder antenna sits a few meters above a VPol wire-frame bicone antenna. Each antenna is approximately sensitive to radiation in the 150-850 MHz band [21]. Two "calibration strings" are deployed about 40 m radially away from the center of the station. Each calibration string contains a VPol and an HPol antenna, and is capable of emitting broadband RF pulses, which provide an *in-situ* calibration of station geometry and timin. A calibration pulse is emitted at a rate of 1 Hz and serves as a measurement of livetime.

The construction of ARA began in 2011, when a prototype station (Testbed) was deployed [21, 73] at 30 m depth to evaluate the RF environment and electronics performance. The first design station (A1) was deployed in 2012, but only up to 100 m depth due to limited drill performance. In 2013, two deep stations (A2, A3) that are the focus of this work were deployed at up to 200 m depth [74]. Two more 200 m depth stations (A4, A5) were deployed in 2018.

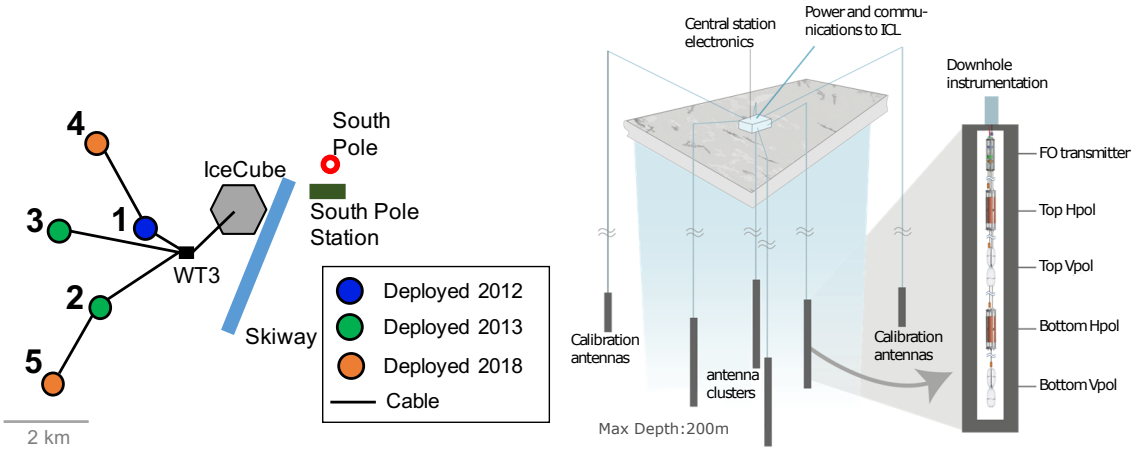

Figure 2.1: (Left) A top-down view of the ARA5 instrument as deployed at the South Pole, with stations color-coded by the year they were deployed. The green stations, A2 and A3, are the focus of the analysis described in this paper. (Right) A schematic of the electronics and instrumentation in an ARA station; "FO" is a fiber-optic transmitter.

2.1.2 The ARA Electronics

A schematic drawing of the ARA instrumentation and electronics is shown in the right of Figure 2.1. After an incoming signal excites an antenna, it enters an antenna-mounted front-end signal-conditioning module; there, the signal undergoes a strong (> 50 dB) notch

filter at 450 MHz to remove South Pole Station communications, is band-passed between 150-850 MHz, and boosted by approximately 40 dB through two stages in low Low-Noise Amplifiers (LNAs). The signal is then transmitted to the surface via RF-over-Fiber (RFoF) to reduce attenuation (compared to copper cabling) over the 200 m journey to the top of the borehole. At the surface, the optical signal is converted back to an electronic signal, amplified again by 40 dB, before finally being bandpass filtered once more to remove any out-of-band noise contributed by the amplifiers. The signal is then split into two paths, one for triggering and one for digitization.

The trigger path is routed through a tunnel-diode that serves as a passive, few-nanosecond power integrator. When the rising edge of the tunnel diode output exceeds roughly five times the ambient thermal noise level, the lowest-level of the multi-level trigger logic, the single channel trigger, fires. If three same-polarization antennas register a single channel trigger within 170 ns (the light propagation time in the ice across the station's diagonal), all 16 antennas in the station are read out. This scheme is optimized to trigger on Askaryan pulses, which should generate significant power in very short time windows and traverse the array at the speed of radio propagation in ice ($\sim$0.16 m/ns).

The signal is recorded through the digitization path, and stored in the circular buffer of an IceRay Sampler 2 (IRS2) chip, which is a high-speed 3.2 Gs/s digitizer ASIC [75]. To minimize power consumption, the buffers are implemented in analog as Switched Capacitor Arrays (SCA) [76, 77]. After a global trigger is issued, sampling is halted and analog-to-digital conversion commences. Each readout records 400-600 ns of waveform, roughly centered on the trigger. The bundle of 16 waveforms and the associated housekeeping data (UTC timestamp, etc.) defines an *event*. An example VPol calibration pulser event is shown in Figure 2.2, where "TVPol" notes a vertically-polarized antenna deployed at the top of a string, "BHPol" notes a horizontally-polarized antenna deployed at the bottom of a string, and so forth.

Triggering is performed by four Triggering DAughter boards (TDAs), while digitization is handled by four Digitizing DAughter boards (DDAs), with four RF channels per board. The logic and readout to storage for the eight daughter boards is managed by the ARA Triggering and Readout Interface (ATRI). The ATRI communicates via USB with a Linux Single Board Computer (SBC) for run control and data archiving. A more detailed discussion of the ARA electronics can be found in previous work [21, 74].

The precise triggering threshold for a given antenna is adjusted to maintain a single channel trigger rate for that antenna. The targeted single channel rates are chosen so that the global trigger rate, after taking into account combinatorics and trigger coincidence windows, is maintained at 5 Hz. The dominant source of these "RF triggers" is fluctuations in the blackbody thermal noise background of the ice, but also includes any potential neutrino signals, as well as anthropogenic (human-made) signals such as aircraft, motor

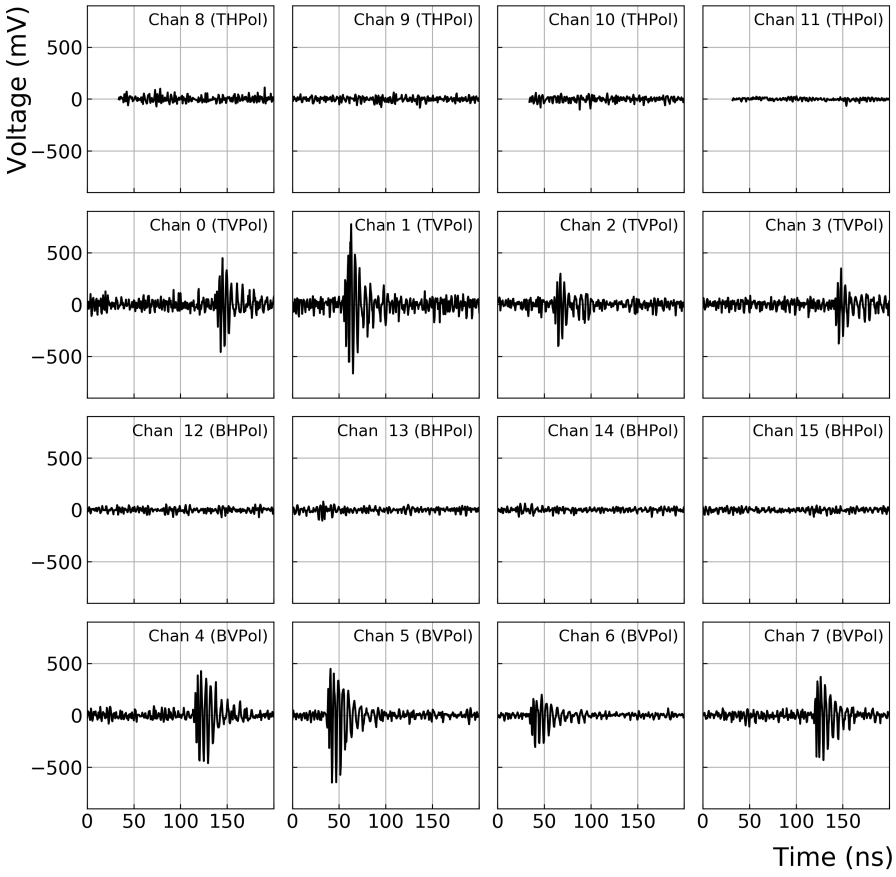

Figure 2.2: An event display showing the sixteen waveforms recorded in A2 for a VPol calibration pulser. As expected, only the Vpol channels are illuminated.

vehicles, etc. In addition, each station collects a sample of background "software" internally-generated triggers as well as the calibration pulses, both at 1 Hz, for a total 7 Hz global trigger rate. Every triggered event invokes approximately 1 ms of deadtime in the electronics readout system, which has negligible $< 1\%$ impact on the livetime.

2.1.3 Detector livetime

This analysis comprises data recorded by ARA Stations 2 and 3 (A2 and A3) between initial deployment in February 2013 and the end of December 2016. Over the course of these four years, each station accumulated roughly 1100 days of livetime, as shown in Figure 2.3, recording over 1.2 billion events total between the two stations. The two detectors were operated in several different "configurations", representing different combinations of operating parameters such as trigger window size, etc. For all configurations in A2, the bottom

HPol channel of string 4 was non-operational, and it is excluded from participating in the trigger for configurations 3-5. Additionally, for configurations 3-5 of A3, the fourth string of the detector participates in forming triggers normally, but due to technical problems in the digitization chain it does not produce useful signal for analysis.

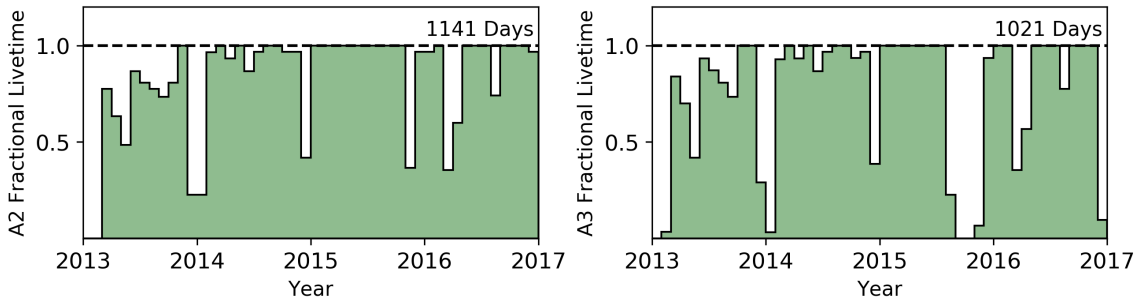

Figure 2.3: Operational fractional livetimes for A2 (left) and A3 (right) from deployment in February 2013 through the end of the analysis period in 2016; each bin is one month wide. From the 4 years of deployment, 1141 days (78% of total deployed time) from A2, and 1021 days (74% of the total deployed time) from A3, are good for analysis.

In Table 2.1, we provide a table of the different station configurations, outlining the key parameters that differentiate them, along with the quantity of livetime for which they were active and the total number of events recorded (in millions). Note that A3 configuration 5 varies from A3 configuration 1 by the loss of quality digitizer data in string 4. The *Trigger Window* is the amount of time during which 3/8 same-polarization antennas must have coincident single-channel triggers to trigger the readout of the instrument. The *Readout Window* is the length of time for which the digitizers are read out. The *Active Delays* column represents whether a set of trigger delays were applied to account for different cable lengths from different channels or not.

2.2 Simulation*

We generate simulated data sets with the Monte Carlo package `AraSim`, which has been previously described extensively in Allison *et al.* [73, 74], and Eugene Hong's thesis [78]. This code models the generation of neutrino events from a diffuse flux and their interactions with Earth and Antarctica. After simulating interactions in-ice, `AraSim` renders a time-domain parameterization of the Askaryan radiation and propagates that radiation through the ice, taking into account signal attenuation and ray bending based on a depth-dependent index of refraction model.

Station	Config.	Readout Window (ns)	Trigger Window (ns)	Active Delays	Livetime (days)	Num Events (millions)
2	1	400	110	yes	179	108.9
	2	400	110	no	142	97.3
	3	400	110	yes	94	54.5
	4	520	170	yes	439	216.8
	5	520	170	no	287	129.7
3	1	400	110	yes	79	43.7
	2	400	110	no	147	114.2
	3	520	170	yes	345	207.0
	4	520	170	no	260	171.8
	5	400	110	yes	191	118.8

Table 2.1: Configuration definitions for A2 and A3, highlighting their various trigger parameters and livetimes.

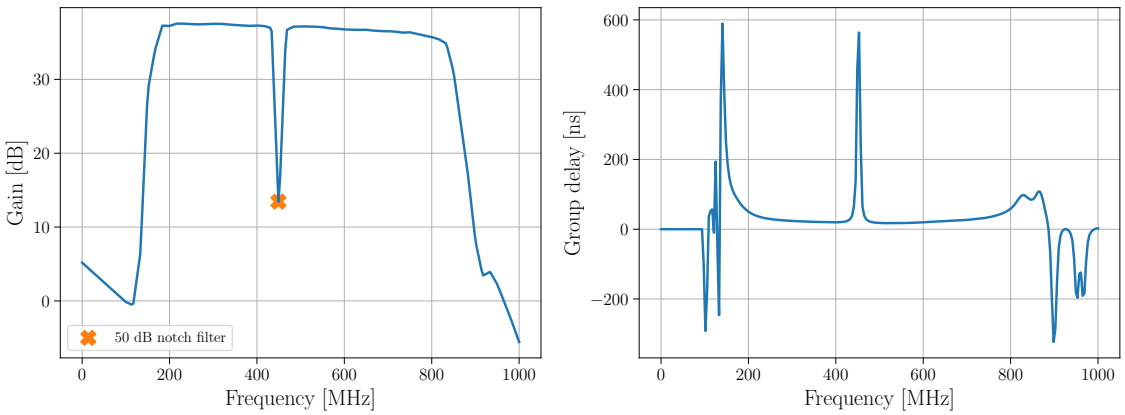

Figure 2.4: Left:simulated frequency domain filter response in AraSim. The y-axis corresponds to the filter gain in dB as a function of frequency. The 50 dB notch filter removes South Pole Station communications from the recorded signal. Right: group delay in nanoseconds as a function of frequency. As shown, the filter provides most of the dispersion in the signal chain.

When the radiation arrives at a simulated station, it is convolved with a frequency-dependent model of the detector, including the antennas, signal chain, and the trigger logic. The model of the instrument, which agrees with the real instrument, includes the dispersive effect of the signal chain that induces a frequency-dependent group delay, which can be seen in Figure 2.4. If the event satisfies a simulated trigger, it is stored in the same

format as real data so that our analysis codes can be executed on either data or simulated events interchangeably.

The models of the A2 and A3 stations are data-driven, and include calibrations derived from the 2012-2013 dataset as described in [74]. In particular, the antenna locations, the noise temperature of the ice, and the gain of every channel are all implemented in the model based on *in situ* measurements. The simulation also models the configuration-specific variations in the electronics behavior (readout length, trigger window size, trigger delay values, etc.).

In Figure 2.5, we show the aperture ($[A\Omega]_{\text{eff}}$) of A2, averaged over configurations. The effective area is derived via Monte Carlo techniques with `AraSim`. For comparison, we also plot the effective area of the IceCube experiment [18]. As can be seen in the bottom panel, we find that A2 and A3 have comparable effective areas to within a few percent. We additionally find that triggering and readout parameters specific to each livetime configuration do not result in differences in the trigger level effective area in excess of a few percent. The two detectors, A2 and A3, are simulated independently; previous studies have shown that only a small fraction of events trigger both A2 and A3 simultaneously, amounting to about 5% of events at 1 EeV [74].

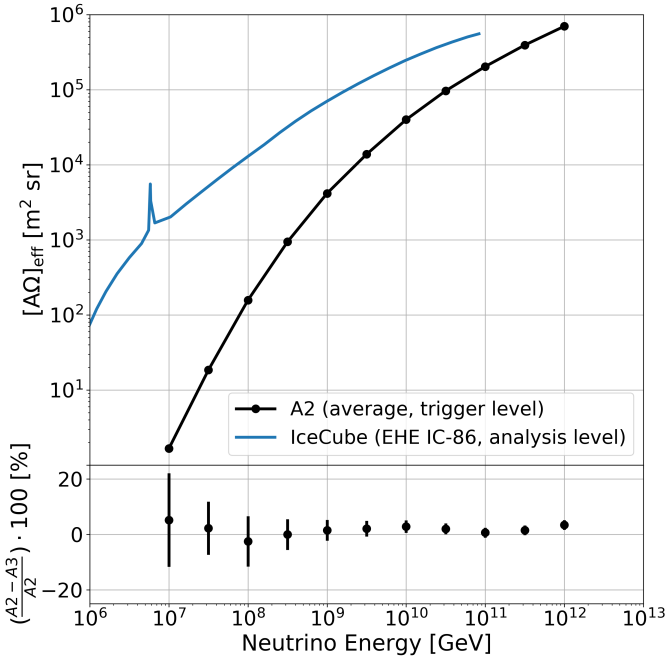

Figure 2.5: (Top) The simulated trigger-level effective area-steradian ($[A\Omega]_{\text{eff}}$) for A2, averaged across configurations. For comparison, we also show the analysis-level sensitivity of IceCube [18]. (Bottom) The percent difference between the A2 and A3 effective areas.

2.3 Data analysis

Most of the data analysis for this work was carried out by Brian Clark and Ming-Yuan Lu. I was involved in the tuning of major cuts and in the partial unblinding of ARA station 3 (A3). In this section I will talk about my work for this paper. A more detailed discussion on the data analysis and final unblinding can be found in Brian's and Ming-Yuan's theses [28, 79].

2.3.1 Wavefront-RMS cut

More than 99.9999% of ARA's recorded data correspond to triggered events due to thermal noise fluctuations. This corresponds to about $\mathcal{O}(10^8)$ events that need to be cut with a computationally fast algorithm, while ensuring that the efficiency of the search remains optimal. For this, the Wavefront-RMS cut was designed. This technique was designed by Carl Pfendner, and then tuned and optimized by Brian Clark for A2.

The principle behind this method is, *grosso modo*, as follows: consider an incident plane wave on the detector. We can calculate the time delay between the peaks that this incoming wave would produce on each channel, and for an event to have these timings calculated we require that the peak yields an SNR of 2.0 of greater. Because we also know the length of the baseline of the antenna pair, we can calculate an incidence angle assuming that the wave travels at the speed of light in ice $\frac{c}{n_{\text{ice}}}$, where $n_{\text{ice}} = 1.78$. This incidence angle can be calculated for each antenna pair, and a quantity that measures how different these angles are can be defined. This number is denoted as ξ and it corresponds to the log base 10 of the difference of the cosines for the different angles. We expect it to be small for Askaryan pulses, where the time delays, and subsequently the incidence angle, are well defined. On the other hand, this will not be true for thermal noise events, where the time delays will be random. Events are cut on the smallest wavefront-RMS value of any antenna pair combination. This cut was tuned for A2, obtaining cut values for ξ of $\xi < -1.3$ in Vpol and $\xi < -1.4$ in Hpol.

Choosing ξ for A3

Unlike A2, A3 only had three functional strings for some of the station configurations. The analysis had to be adapted so only the three working strings were included. To assess the usability of the wavefront-RMS filter, we applied the filter to a set of neutrino events that we simulated with `AraSim` with a configuration that mimicked that of A3. From this we found that the usability of the filter does not change considerably for three strings, as can be seen in Figure 2.6.

To choose a cut value we scanned different choices of ξ and calculated the rate of passing events for both data and simulation. To be consistent with A2, we decided to keep the thermal noise passing rate close to 10% and to keep at least 95% of the simulated

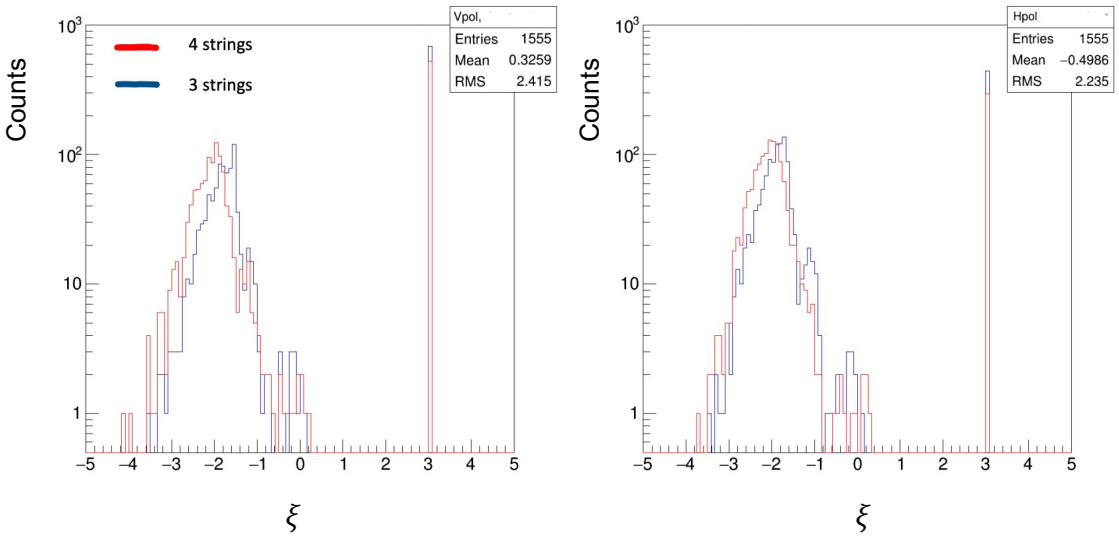

Figure 2.6: Left: distribution of calculated ξ value for Vpol antennas in A3 from a simulated set of triggered neutrinos. The red distribution corresponds to a simulated detector with four functional strings, and the blue distribution corresponds to the same simulation but only using three strings corresponding to the three functional strings for some configurations of A3. The pile-up at $\xi = 3$ correspond to events that did not meet the SNR> 2 condition and were not analyzed by the filter. Right: same plot as in the left but for Hpol channels.

neutrino events. Because each configuration was different and some configurations had only 3 active strings, we had to tune this cut for each configuration separately. Figure 2.7 shows an example of this parameter scan for configuration 1 data of A3. As expected, increasing the cut value for ξ decreases the number of rejected events. A similar plot but for simulated data can be seen on the right panel of Figure 2.7. Note the discrepancy between the passing rate for Vpol channels versus Hpol channels, which accounts for factors of 2-4. We did not observe these differences for A2, so we looked at at the distributions of ξ for both polarizations.

When we looked at the data, we noticed that much more Hpol events are kept by the cut at every choice of cut than for Vpol. We discovered that the reason for this is that the SNR distribution for Hpols has a higher mean and longer tail than that for Vpol channels, which can be seen in Figure 2.8. This results in more events passing the threshold requirement in Hpol than in Vpol. A proposed solution was to raise the Hpol threshold from 2.0 to 2.1, while leaving the Vpol threshold at 2.0. This results in the two distributions being much more comparable for data while having minimal impact on simulation. Figure 2.9 shows this for data, configuration 1 of A3. We then select thresholds for each configuration based on the passing rate criteria for both thermal noise and neutrinos. These are organized in Table 2.2.

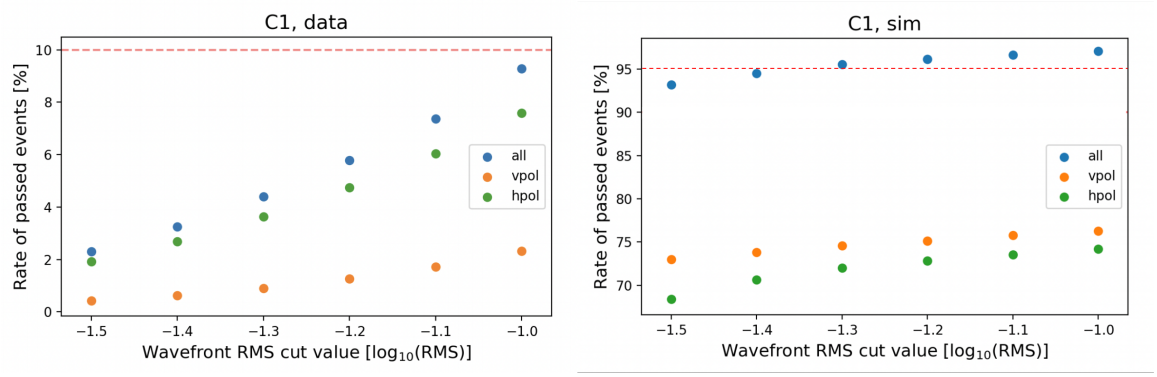

Figure 2.7: Left: rate of passed thermal noise events as a function of ξ for data from configuration 1 of A3. The dashed, red line represents the desired passing rate value for this filter, which was chosen so about 95% of neutrinos pass this cut. Right: rate of passed simulated neutrino events for different choices of ξ. The red line corresponds to the desired rate.

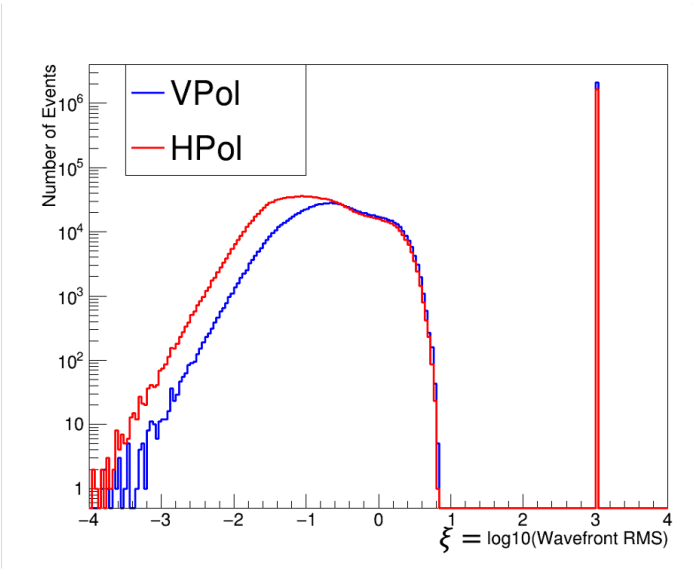

Figure 2.8: Distribution of the ξ value for both Hpol and Vpol channels. As it can be seen, the Hpol has a mean shifted to the left, and a longer tail. This resulted in a higher passing rate of thermal events.

2.3.2 Phase variance cut

Once most of thermal events ($\sim 90\%$) have been rejected, we proceed to apply more computational expensive cuts. The phase variance cut targets continuous waveform (CW) events.

When a CW signal arrives at the detector, we expect the relative phase (φ) of this signal

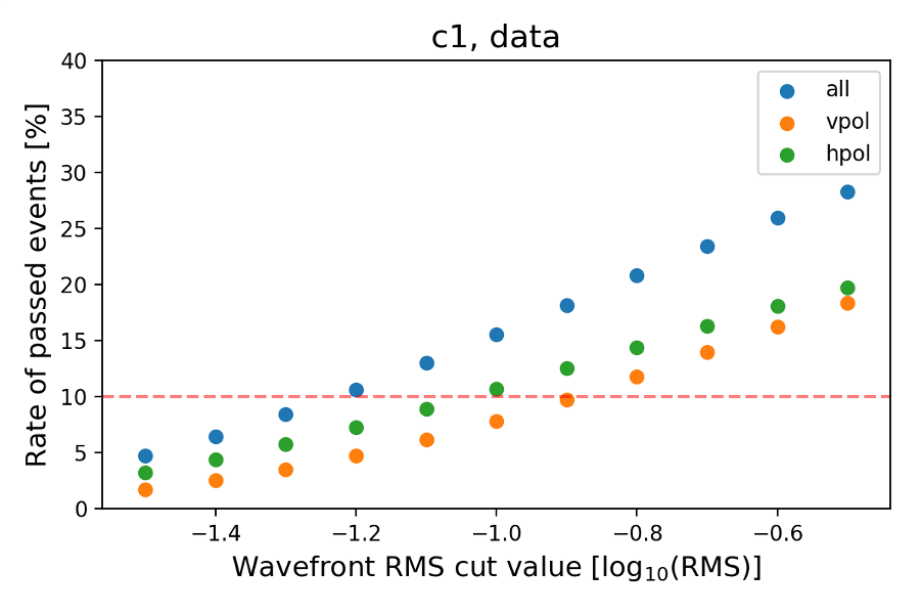

Figure 2.9: Grid scan for the wavefront RMS cut value for A3 config. 1. We chose the value that let a global passing rate of about 10%.

A3 Wavefront-RMS cut				
Configuration	Vpol threshold	Vpol thermal noise passing rate (%)	Hpol threshold	Hpol thermal noise passing rate (%)
1	-1.2	4.8	-1.3	5.9
2	-1.3	5.3	-1.4	5.8
3	-1.0	4.6	-1.1	5.9
4	-1.0	4.5	-1.1	6.2
5	-0.7	4.7	-0.8	6.4

Table 2.2: Selected cut values and passing rates

in the frequency (Fourier) domain to be the roughly the same between neighboring events for a pair of channels. This means that there will be a constant offset in the CW frequency bin between the phases of two different channels across neighboring events, i.e. $\varphi_2 - \varphi_1 =$ constant. For noise we expect this difference to be random.

This is the idea behind the phase variance filter used for the diffuse analysis, inspired by work from the LOFAR collaboration [80] and originally designed by Carl Pfendner. For

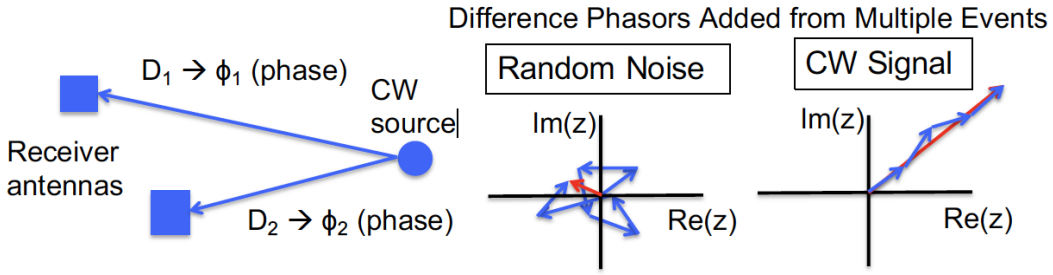

Figure 2.10: Schematic representation of the phase variance technique. For random noise the phasor representing the phase difference between two different antennas for multiple events randomly varies, whereas for a CW event it adds up and can be used to identify CW signals. Figure by Carl Pfendner.

this, the quantity V is defined as

$$V = 1 - \frac{1}{N}\left|\sum_{k=1}^{N} e^{(i(\varphi_1 - \varphi_2))}\right|, \tag{2.1}$$

where N is the number of neighbouring events. For noise, the second term on the right of the equality will tend to zero for a large N due to it behaving as a random walk. If CW is present, $e^{(i(\varphi_1-\varphi_2))} \rightarrow$ constant and then $V \rightarrow 0$. For this analysis, $N = 15$.

Figure 2.11 shows the phase variance value (V) as a function of frequency for two different periods of time. The first period corresponds to 403 MHz weather balloon events. These events correspond to radiosondes attached to NOAA weather balloons that are launched twice a day at the South Pole. The figure on the right corresponds to a period of time where no CW was observed. As it can be seen on both figures, there are some tagged frequencies (125 MHz, 300 MHz, 500 MHz) for which the phase variance value has minima. These are believed to correspond to contamination generated by the DAQ hardware, and are thus not taken into consideration when analyzing the data for CW contamination.

Issues with the phase variance technique on A3

When analyzing A3 data with the phase variance technique, we discovered that there was unexpected behavior around 200-400 MHz, where the phase variance technique appeared to tag CW contamination. Further inspection led us to conclude that this behaviour was caused by calibration pulser events. Events in periods of time when this behaviour was present where studied, and we found no evidence of critical problems with these calibration pulser events other than they were being identified by the phase variance technique as CW events. More information on this can be found in Section C.2

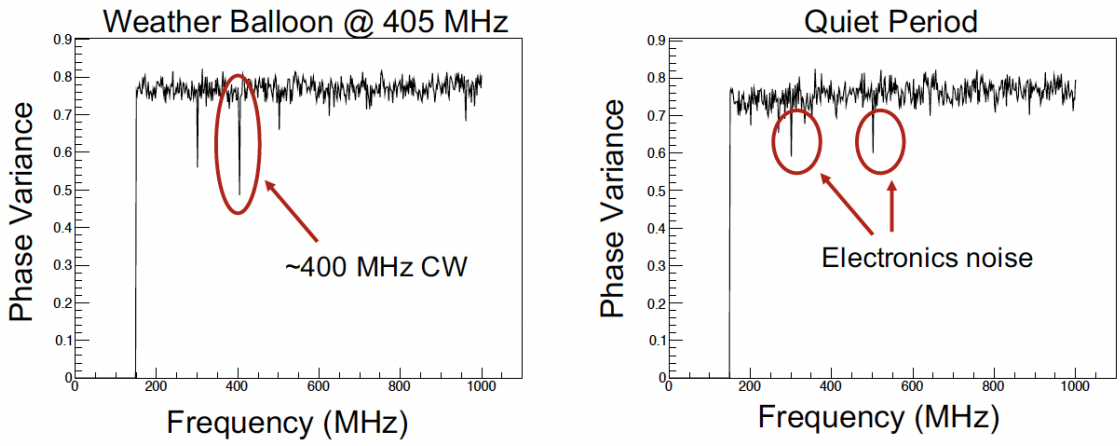

Figure 2.11: Left: phase variance for a period of time where weather balloon signals were present. The 400 MHz minimum in the phase variance factor corresponds to a weather balloon event. Right: a similar plot but for a quiet period. The minima there, which are also seen on the plot on the right, correspond to contamination from the DAQ. Figure by Brian Clark.

The threshold that was used for A2 for tagging a frequency, and therefore an event, as CW was $V = 1.5$, but this was not optimal for A3 as it would tag events with the unexpected behavior as CW even though they were not. To solve this issue, a study was performed by varying this threshold until these kind of events stopped being tagged as CW while at the same time ensuring that true CW events, such as balloon events, were still identified as CW by this technique. The result of the study was to increase the threshold to 2.

2.3.3 Stragglers identification and removal

I collaborated along with my colleague Brian Clark to unblind A3. Once all of the cuts were tuned, and thermal events rejected and CW events filtered, the next step consisted of setting the RCut as described in Subsection 4.2.4 and consequently studying the passing events, all of this for the 10% data. Before performing the optimization and setting the RCut, we needed to study and remove stragglers so those would not affect the aforementioned process. To do that, we plotted each event passing all the previous cuts on the bivariate plane (peak correlation value vs. SNR) and observed deviations from the main cluster of events. This can be seen on Figure 2.13.

From the study of these for each configuration we noticed that several events were in the same category. These events corresponded to digitization glitches that were not caught by the initial quality cuts, but that were first identified by our colleague Ming-Yuan Lu and who created cuts to reject them. We followed the method used by our collaborator

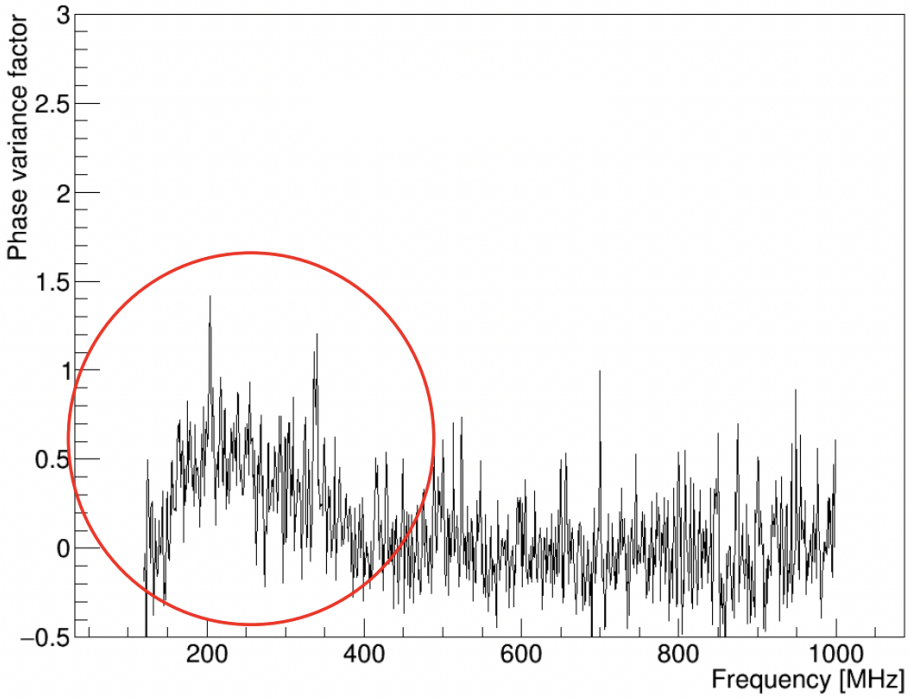

Figure 2.12: An example of the phase variance factor calculated for a series for 15 calibration pulser events for A3 where odd behaviour was observed. Even though this was not a CW event, it got tagged as such as it surpassed the threshold of 1.5 that we used for A2. After a quick study, we decided to increase the threshold to 2.0, which solved this issue.

Ming-Yuan Lu, in which events whose peak power was outside the experiment's bandwidth $150-850$ MHz were rejected. This implementation is named `hasOutofBandIssue` and lives in `tools_Cuts.h`.

Other types of stragglers were events that reconstructed to the South Pole station, and 400 MHz balloon events that were not tagged by the peaks-over-baselines method as the baselines had themselves 400 MHz contamination.

Optimization

The optimization was done for the 10% as described in Section 4.3. We chose a single slope but 5 intercepts, one for each configuration, that maximize the ratio S/S_{up} where S corresponds to the simulated signal events that pass all the cuts and S_{up} is the 90% confident level (CL) upper limit on the number of signal events. Once the slopes and intercepts have been found for each configuration, we can give an estimate of the number of expected backgrounds for each configuration. Results of the optimization for configuration 1 of A3 are shown in Figure 2.14. The upper panels correspond to Vpol channels and the lower panels to Hpol channels. From left to right, the first plot corresponds to the bi-variate cut

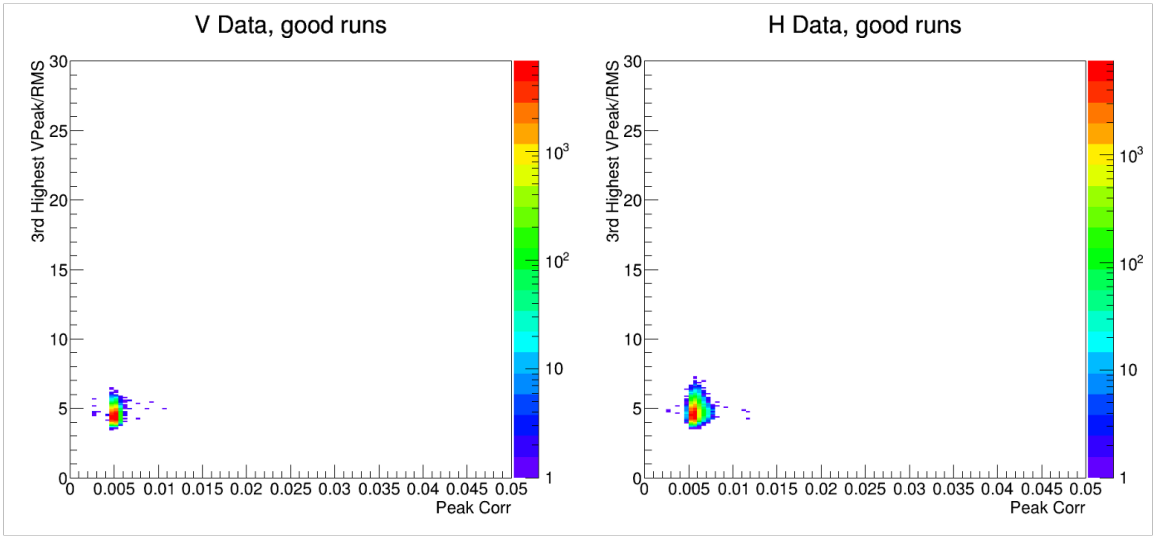

Figure 2.13: The 2D space (peak corr. value vs. SNR) for A3 configuration 1. We used these plots to determine the presence of stragglers and consequently to study them. We identified stragglers as events that did not fall within the cluster of events. Those were individually studied and then rejected by identifying their origin.

with the x-axis being the correlation value, the y-axis being the 3rdPeak/RMS cut, the color axis corresponding to the number of events, and the red line representing the RCut that was optimized for this particular configuration. The second plot represents the differential distribution of events rejected by the final cut as a function of the y-intercept. The third plot corresponds to a zoomed version of the second plot around the region where an exponential model fit was performed. The final plot is similar to the first plot but for simulated events, with the color axis corresponding to the number of events. The fourth corresponds to the efficiency of the different cuts as a function of SNR, where SNR is computed as the third highest V_{peak}/RMS, where V_{peak} is the highest absolute voltage peak in a waveform, and the RMS is the root-mean-square of the voltage values in that waveform. The efficiency is calculated as the ratio of the number of weighted neutrino events that pass the cuts over the total number of triggered events. The final plot is similar to the previous plot but as a function of energy instead of the SNR.

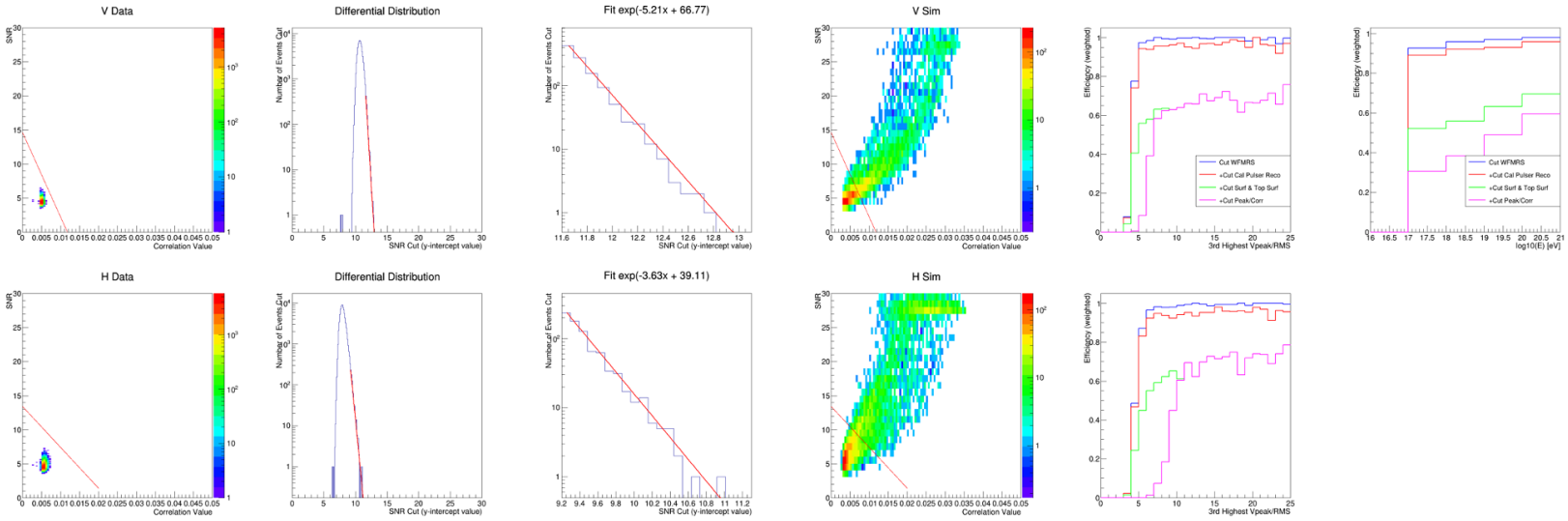

Figure 2.14: Optimization results for A3. Each plot is described in the text.

In Figure 2.15, we present the analysis efficiency of our analysis for both A2 and A3; we plot the average signal efficiency, taking into account the variations due to different run configurations and their respective livetimes. On the left, we show the efficiency as a function of SNR. The analysis becomes efficient near an SNR of 6, and does not fully saturate to a value between 75-90% until it is above an SNR of 8. The saturated efficiency for A3 is $\sim 10\%$ lower than for A2 because A3 required a larger angular cut region to reject surface events. On the right, we show the efficiency as a function of energy. At 10^{16} eV, the analysis has a relatively low efficiency of about 5%. The efficiency rises to $\sim$35% by 10^{18} eV and peaks near 10^{20} eV at between 50-60%, depending on the specific station.

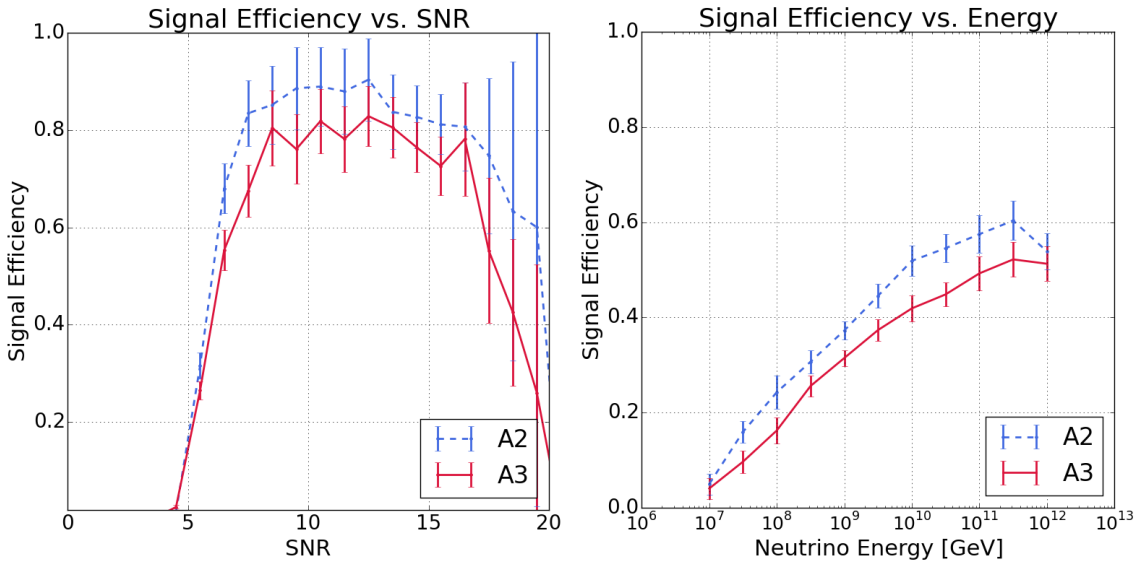

Figure 2.15: Monte-Carlo estimated analysis efficiency as a function of signal-to-noise ratio (left) and neutrino energy (right) for Analysis A. For context, the trigger efficiency of an ARA station has been measured to reach 50% at an SNR of 3.7 [19]. In the left figure, we assume an unbroken power-law spectrum with a spectral index of -2.13 to weight the energies contributing to the efficiency. The efficiency decrease around SNR=14 is due to waveform saturation effects as simulated in `AraSim`.

2.3.4 Results*

After post-unblinding examination, we observed 0 events on a background expectation of $(5 \pm 2) \times 10^{-2}$ events per station. The unblinding of the stations was led by my colleague Brian Clark.

At unblinding, we observed two events in the candidate neutrino signal region in A2.

While both reconstruct inside the ice using an interferometric technique that utilizes all VPol channels of the array, both only have visibly identifiable signals in the bottom row of VPol antennas. When the reconstruction is repeated utilizing only antennas where the signal strength exceeds the event filter threshold, both events confidently reconstruct to above the surface. We consider both of these events to be backgrounds of surface origin.

At unblinding, we observed four events in the candidate neutrino signal region in A3. Three cluster in time to within a few minutes, and are located in a run which contains a burst of surface noise, but was sub-threshold in one of the cuts designed to remove this events. The fourth event is reconstructed inside the ice when all VPol channels participate in the interferometry. Again, if only channels with signal strength above the event filter threshold are considered, the event reconstructs to above the surface. It is therefore determined to be consistent with a background of surface origin.

Since all events observed in our analysis can, with currently available tools, be identified to be of surface origin, or cluster in time with bursts of surface activity, we do not consider it to have measured any events. The post-unblinding cut necessary to remove the misreconstructed surface events results in a negligible efficiency loss ($\leq 0.25\%$). Before computing the final limit, we estimate the effect of systematic uncertainties so they can be included in our results. This is described in the following section.

2.4 Systematic uncertainties study

In this section, we describe the systematic uncertainties considered in the analysis. The impact of these systematics on $[A\Omega]_{\text{eff}}$ are shown in Figure 2.22, and a table summarizing the magnitude of their effects at 10^{18} eV is provided in Table 2.3. We consider systematic uncertainties broadly in two classes. The first class is associated with theoretical uncertainties on the neutrino-nucleon cross section and Askaryan emission, and are shown in Figure 2.22 as solid bands, reported at the trigger level. The second class is associated with uncertainties in our understanding of the detection medium and our instrument. The latter are taken into account in setting the final limit as described in App. 2.5, and are shown as dashed/dotted lines in Figure 2.22 at the analysis level.

2.4.1 Theoretical uncertainties*

Neutrino-nucleon cross section ($\sigma_{\nu-\mathrm{N}}$)

For the neutrino-nucleon cross section ($\sigma_{\nu-\mathrm{N}}$), `AraSim` uses the model derived by Connolly, Thorne, and Waters (CTW) [20]. The upper and lower bounds for $\sigma_{\nu-N}$ are substituted for the central value in the simulation to estimate the effect of the uncertainty on the simulated $[A\Omega]_{\text{eff}}$ at the trigger level. In the CTW model, the uncertainties on $\sigma_{\nu-\mathrm{N}}$ are large and grow as a function of energy, exceeding 100% above 10^{21} eV. At 10^{18} eV the uncertainties

on the trigger-level effective area due to the cross-section are estimated at -15%/+18%. In Figure 2.22, for comparison we also show the uncertainties if we use an alternative cross-section developed by Cooper-Sarkar *et. al.* (CS) [81] which has smaller uncertainties at high energies by about a factor of four. We additionally studied $d[A\Omega]_{\rm eff}/d[\sigma_{\nu-{\rm N}}]$, and find it to be approximately linear; for example, at 1 EeV, a 10% increase in $\sigma_{\nu-{\rm N}}$ corresponded to a 10% increase in $[A\Omega]_{\rm eff}$.

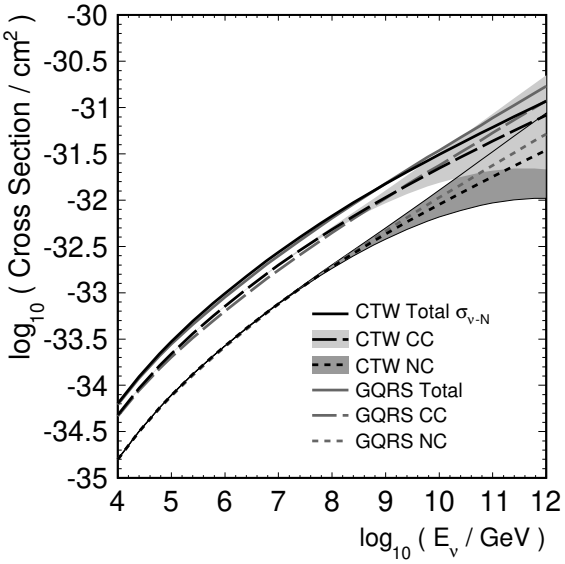

Figure 2.16: $\sigma_{\nu-{\rm N}}$ model as a function of energy from [20]. The error bands of this model correspond to the associated uncertainties due to parton distribution functions. These have the greatest impact on the systematic uncertainties on the effective area above 10^9 GeV.

Askaryan emission

For the Askaryan emission, `AraSim` implements a modified version of the model derived by Alvarez-Muñiz *et. al.* [6]. A full description of modifications is provided elsewhere [73], but the primary differences arise due to the inclusion of of the LPM effect by Alvarez-Muñiz but not by `AraSim`, and in `AraSim`'s use of functional parameterizations for the shower profile instead of directly simulated shower profiles. The relative difference between waveform amplitudes produced by `AraSim`, and those derived from a full shower Monte-Carlo are at most ∼12% [78]. We conservatively estimate the effect of this systematic uncertainty by reducing or increasing the simulated field amplitude by ±12% and assessing the change in $[A\Omega]_{\rm eff}$ at the trigger level. The relative difference between the default parameterization and

the scaled parameterization has a maximum value of about 25% near 10^{16} eV, and starts falling as energy increases. This is because at high energies the instrument acceptance becomes dominated by geometric effects (ray tracing, etc.) and not signal amplitude. At 10^{18} eV the estimated uncertainties due to the Askaryan emission model are -11%/+13%.

2.4.2 Measurement uncertainties*

In the second category of uncertainties, we consider those arising from our detector response and from measurements of quantities such as the index of refraction in ice and the attenuation length of radio waves in ice. These systematics are included in our calculation of the final limit. We consider uncertainties associated with (1) the attenuation length (L_{att}) of South Pole Ice and (2) the depth-dependent index of refraction ($n(z)$) of South Pole ice, (3) the calibration of the ARA signal chain, and (4) the triggering efficiency of the detector.

Ice attenuation length (L_{att})

The model for the attenuation length (L_{att}) of South Pole ice was derived from data taken with the ARA Testbed prototype [21]. Confidence bands providing an upper and lower limit on L_{att} are given in the model. To set upper/lower limits on our sensitivity, in `AraSim`, the upper and lower bounds for L_{att} are substituted for the central value. At 10^{18} eV the uncertainty on the analysis level effective area due to uncertainties in attenuation length are -8%/+50%.

Ice refractive index

The model for the depth-dependent index of refraction $n(z)$ was obtained by fitting data obtained by the RICE experiment [82]. The data was fitted with an exponential as a function of depth z of the form $n_d - (n_d - n_s)e^{-zn_c}$, finding the following parameter values and their respective uncertainties: $n_d = 1.788 \pm 0.016$,, $n_s = 1.359 \pm 0.022$ and $n_c = 0.0132 \pm 0.0017\text{m}^{-1}$. We recalculate the sensitivity, setting all parameters to their upper and lower limits simultaneously. The lower (upper) limit generally corresponds to a slower (faster) transition from surface to deep ice, and correspondingly have a smaller (larger) geometric acceptance for neutrinos. Additionally, since we do not change the ice-model assumption used to reconstruct the incoming direction of the RF emission, this systematic uncertainty also captures errors which may be present if the true ice model for radio wave propagation does not match that used for reconstruction. At 10^{18} eV the uncertainties on the analysis level effective area due to the index of refraction model are 5%.

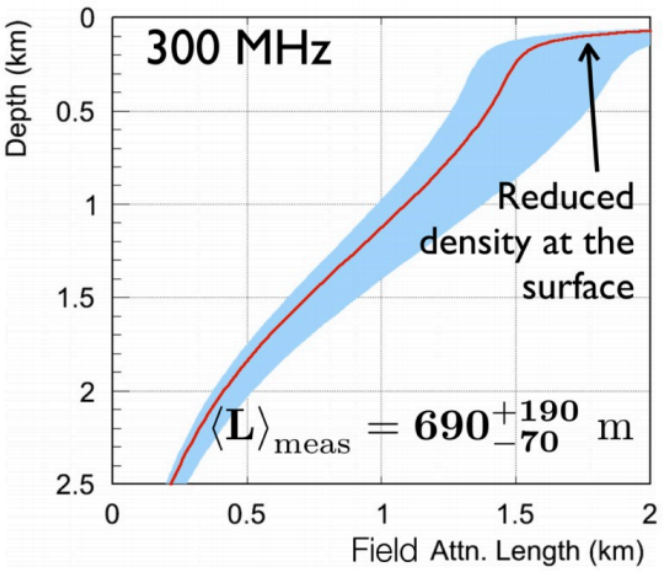

Figure 2.17: Electric field attenuation length in ice as a function of depth from deep pulser data observed by ARA Testbed [21]. The attenuation length as a function of depth was extrapolated from a measurement done at a single depth, with the red solid line being the mean of this extrapolation and the shaded blue bands representing the error range.

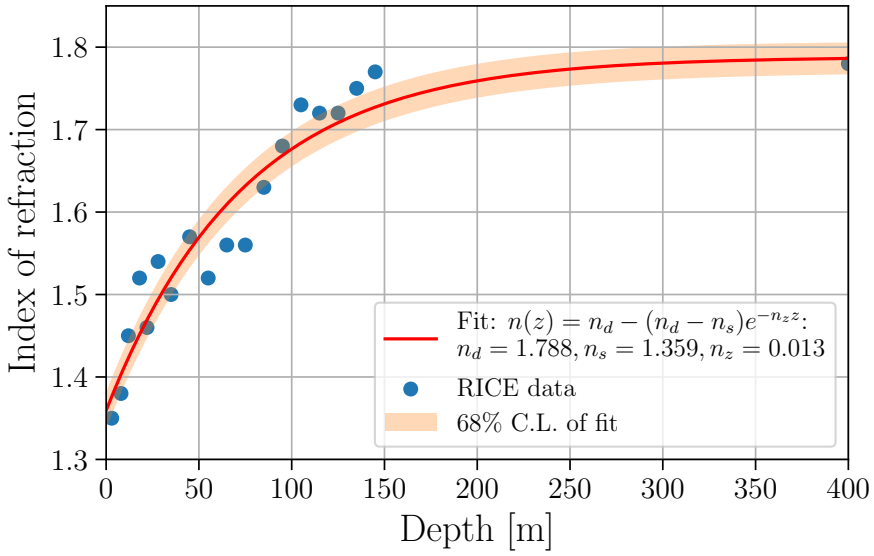

Figure 2.18: Fit of a function of the form $n_d - (n_d - n_s)e^{-n_c z}$ to RICE's data and its associated 1σ uncertainty (shaded band).

Signal chain

This study was performed by my colleague Ming-Yuan Lu. We consider four sources of uncertainties that exist in the signal chain. They are the transmission coefficient t representing the impedance mismatch between the ice and the antenna, as well as between the antenna and the coaxial cable, the ambient noise power received N_{ant}, the signal chain noise power N_{sc}, and the antenna directivity D. We follow the treatment used in the previous ARA result [74] where we consider the system signal-to-noise ratio representing the ratio of input signal power to total system noise power in a given channel:

$$SNR_{\text{sys}} = \frac{tDP_{\text{sig}}}{tN_{\text{ant}} + N_{\text{sc}}} \tag{2.2}$$

with P_{sig} being the received signal power. The four sources of uncertainty translate to an uncertainty in SNR_{sys} by standard error propagation, which is then implemented as an uncertainty in the antenna gain G in code ($\Delta G = \Delta SNR_{\text{sys}}/P_{\text{sig}}$). In line with previous ARA work, here we only consider the case where the effective gain of the instrument is reduced, providing a conservative estimate of our sensitivity. This is done because we lack sufficient calibration data at this time to constrain the upper bound on the gain. The VPol antenna gain has an overall estimated uncertainty of -10%, while the HPol antenna gain is estimated at -32%. The modified gain values are substituted in the simulation to assess the impact of this uncertainty, and the uncertainty at 10^{18} eV is found to be -3%.

Trigger efficiency

For the systematic uncertainty associated with the trigger efficiency of the detector as a function of the root-power-ratio (RPR), $\epsilon(RPR)$, which is defined as $RPR = E_{\text{j,max}}/\sigma_{E_{\text{j,noise}}}$, where $E_{\text{j,max}}$ is the maximum of the square-root of a rolling 25 ns integrated power average of the waveform, specifically:

$$E_j = \sqrt{\frac{1}{n}\sum_{i=j}^{j+n} V_i^2} \tag{2.3}$$

where n is the number of samples in the 25 ns window and $\sigma_{E_{\text{j,noise}}}$ is the RMS value of E_{j} in the half of the waveform that does not contain the maximum. This RPR variable has been used in a previous ARA analysis [74], and was chosen to more-closely emulate the power-integrated envelope that is used in the ARA trigger. We compare the simulated trigger efficiency $\epsilon_{\text{sim}}(RPR)$ to the measured trigger efficiency in calibration pulser data $\epsilon_{\text{dat}}(RPR)$: $\Delta\epsilon = \epsilon_{\text{dat}}(RPR) - \epsilon_{\text{sim}}(RPR)$. We measure $\epsilon_{\text{dat}}(RPR)$ by varying a tunable attenuator on the local calibration pulsers and counting the number of calibration pulsers recorded. Using `AraSim` we find that the uncertainties on the trigger efficiency decreases the simulated $[A\Omega]_{\text{eff}}$ from between 2-5% depending on energy, and at 10^{18} eV the size of

the effect is -3%. This particular study of trigger efficiency was performed by my colleague Brian Clark.

We observed in previous calibration exercises that the stations trigger inefficiently on calibration pulsers whose direct ray-tracing solution intercepts the array at an angle steeper than $-25°$ from from horizontal; this can be seen in Ref. [83], where there is a deficiency of triggers in A2 and A3 after the pulser is lowered below 1300 m depth, despite the pulser being lowered to a total depth of 1700 m. Therefore, for the calculation of $[A\Omega]_{\text{eff}}$ used in the limit, we conservatively exclude neutrino simulated events with the same ray-tracing conditions. This is schematically described in Figure 2.19.

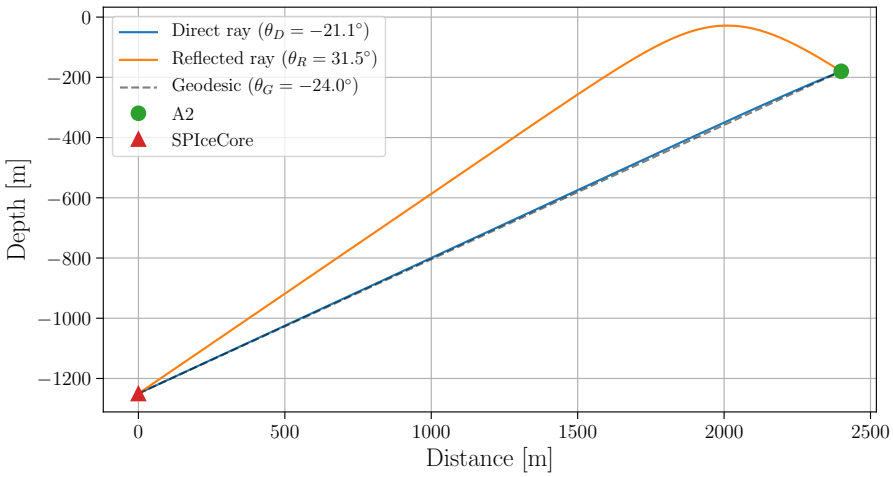

Figure 2.19: Diagram showing the depth at which the SpiceCore pulses started to not be observed by ARA station 2. The diagram shows both the refracted/reflected (yellow solid line) and direct (blue solid line) rays with their respective receiving angles (as viewed by A2). A geodesic (gray dashed line) connecting the SpiceCore transmitter and A2 is also shown, as well as the angle that it makes with the horizontal.

I performed a simulation study on how this would affect our limit calculation using the same simulation dataset that was produced for the other systematic uncertainties studies. Simulated triggered events whose receiving angle was steeper than $(-25°)$ were rejected from the effective area calculation.

Figure 2.20 shows the distribution of events as a function of the receiving angle for different neutrino energies, marking with red those events that were excluded. The results show a $\sim 10-30\%$ reduction in sensitivity, depending on energy, which can be see in Figure 2.21. Excluding these steeply upgoing events is a conservative approach, as more exhaustive future studies might reveal that the cause of the trigger inefficiency to the calibration pulses

does not have the same effect on neutrino events.

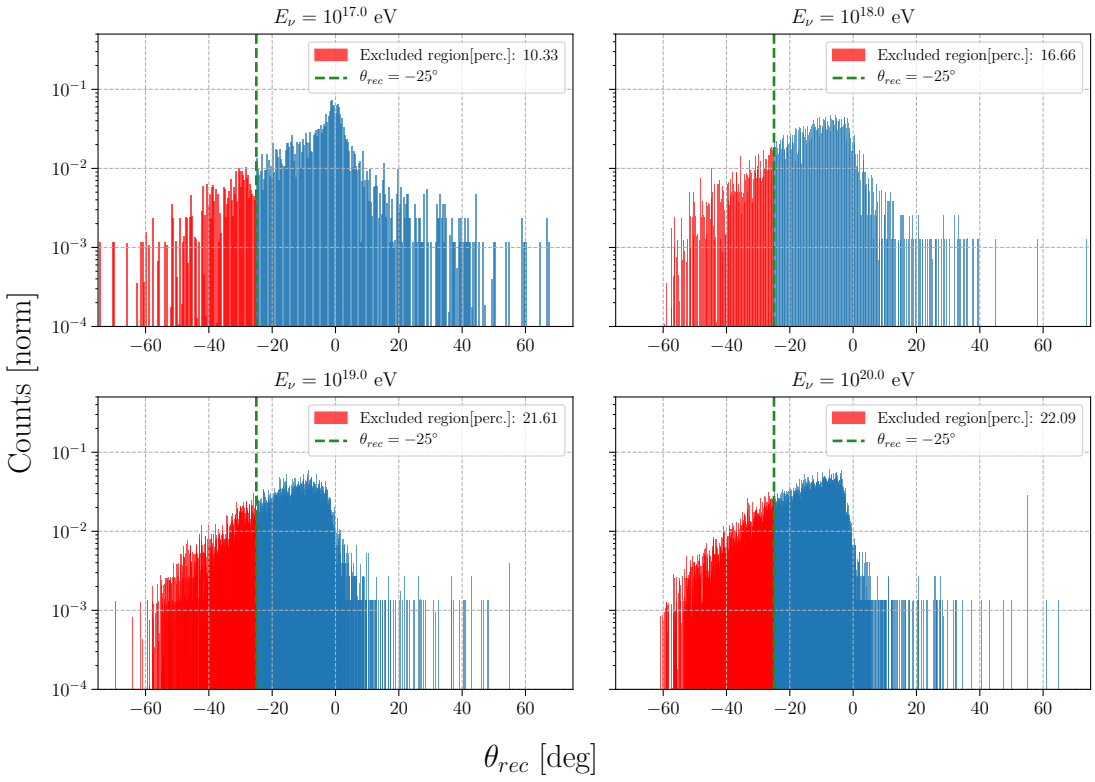

Figure 2.20: Distribution of triggered events as a function of the receiving angle (θ_{rec}) at the antenna for different energies. The red area corresponds to triggers that have a receiving angle deeper than $-24°$ (green dashed line), and the percentage of events that are within this area is noted in the legend.

2.5 Limit Calculation*

We set a 90% confidence level upper limit on the flux $E_{\mathrm{i}}F(E)_{\mathrm{i}}$ in the i-th energy bin of width $\mathrm{dlog}_{10}E$ according to Equation 2.4:

$$E_iF(E)_i = \frac{n_i}{\Lambda_i \ell n(10) \mathrm{dlog}_{10}E} \tag{2.4}$$

where n_{i} is the Feldman-Cousins upper limit for zero measured events on a background of zero, accounting for the systematic uncertainties (added in quadrature) described in the

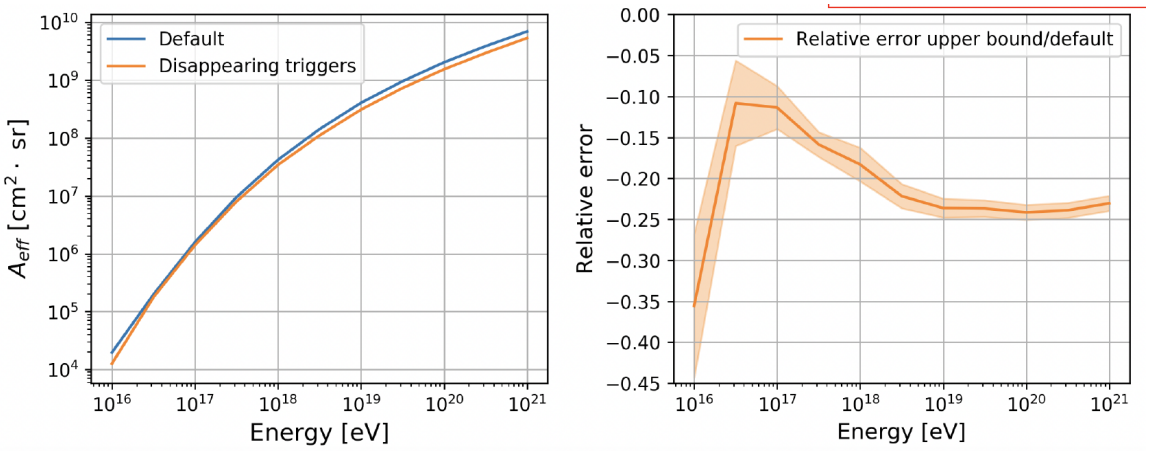

Figure 2.21: Effect of disappearing triggers on the effective area. As seen from Figure 2.21, the greatest fraction of disappearing triggers happens at the highest energies, which translates into a decrease of the effective area at those same energies. That can be seen in this plot.

Systematic Uncertainty	+ (%)	- (%)
Cross-Section (CTW)	18	15
Askaryan Emission	13	11
Attenuation Length	50	8
Index of Refraction	5	5
Signal Chain		3
Triggering Efficiency		3
Total	50	11

Table 2.3: A summary of the systematic uncertainties in the neutrino sensitivity at a neutrino energy of 10^{18} eV.

previous section. This is done according to the prescription in Conrad *et. al.* [84] with the improvements suggested by Hill *et. al.* [85]. Note that in the absence of uncertainties, $n_{\rm i} = 2.44$, as commonly observed in the literature [86]. Use of zero instead of the actual background estimate for the analysis setting the limit is conservative by $\sim 2\%$, and does not substantially change the result.

We take $\mathrm{dlog}_{10}E = 1$, corresponding to decade wide bins in energy. Λ_i is the exposure of the instrument summed over stations and configurations, taking into account analysis efficiencies as presented in Figure 2.15. Λ_i for a given energy bin is defined explicitly as:

$$\Lambda_i = \sum_{j_{\rm stations}=1}^{2} \sum_{k_{\rm configs}=1}^{5} \epsilon_{i,j,k} \ [A\Omega]_{{\rm eff},i,j,k} \ T_{j,k} \tag{2.5}$$

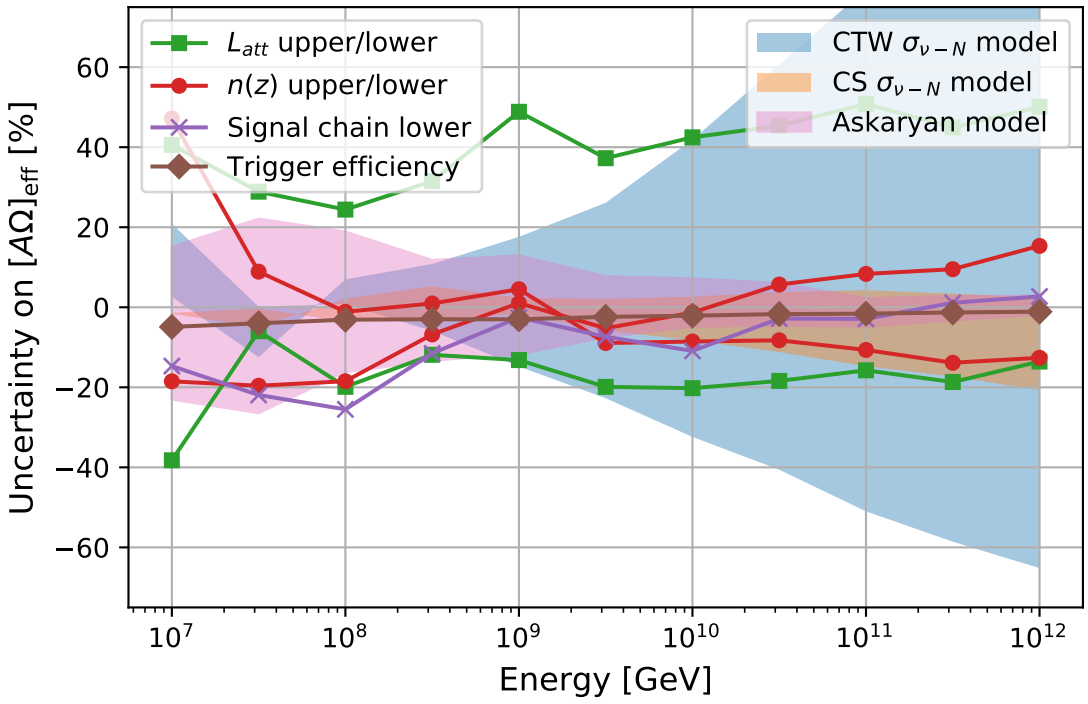

Figure 2.22: Uncertainties between the central values used in the simulation and upper/lower bounds for each model parameters. Theoretical systematics (shaded regions), such as the Askaryan model and the neutrino-nucleon cross section, are not accounted for when calculating the neutrino limit. Uncertainties associated with the detector and medium (dashed and solid lines) are accounted for in the calculation.

where for a specific energy (i), station (j), and configuration (k), $\epsilon_{\text{i,j,k}}$ is the efficiency and $[A\Omega]_{\text{eff,i,j,k}}$ is the effective area as shown in Figure 2.5. $T_{\text{j,k}}$ is the livetime of the instrument for a specific station and configuration as reported in Table 2.1.

The effective areas $[A\Omega]_{\text{eff}}$ of the instruments are computed from the effective volumes $[V\Omega]_{\text{eff}}$ through the thin-target approximation:

$$[A\Omega]_{\text{eff}} = \frac{[V\Omega]_{\text{eff}}}{\mathcal{L}_{\text{int}}} \tag{2.6}$$

where $\mathcal{L}_{\text{int}} = m_N/(\rho\ \sigma_{\nu-N})$ is the interaction length of a neutrino in the earth,

where $m_N = 1.67 \times 10^{-24}$g is the mass of a nucleon, $\rho = 0.92$ g/cm^3 is the average density of ice, and $\sigma_{\nu-N}$ is the neutrino/anti-neutrino-nucleon cross-section in the units of cm^2 as computed in Connolly *et. al.* [20]. The effective volumes are calculated by Monte Carlo methods. Using `AraSim` at specific energy, we simulate a number of neutrinos N_{thrown} in an interaction volume V_{thrown} with an isotropic distribution of arrival directions, and with

an equal number of events between the three neutrino flavors and between neutrinos/anti-neutrinos. The sum of the weights of triggered events, $\sum w_{\text{trig}}$, determines the effective volume:

$$[V\Omega]_{\text{eff}} = \frac{\sum w_{\text{trig}}}{N_{\text{thrown}}} \times V_{\text{thrown}} \times 4\pi \tag{2.7}$$

where the weighting accounts for the neutrino survival probability up to the interaction vertex.

In the absence of detection, in Fig. 2.23 we compute the 90% confidence level (CL) upper limit on the diffuse flux of neutrinos. Inclusion of the systematic uncertainties in the limit has an $\mathcal{O}(5\%)$ effect.

As a benchmark, the number of events expected to be observed in the analysis ranges from 0.25 for an unbroken extrapolation of the astrophysical neutrino flux as measured by IceCube with a spectral index of -2.13 [7], to 0.027 in the case of a cosmogenic neutrino flux where protons make up only 10% of cosmic ray primaries [16].

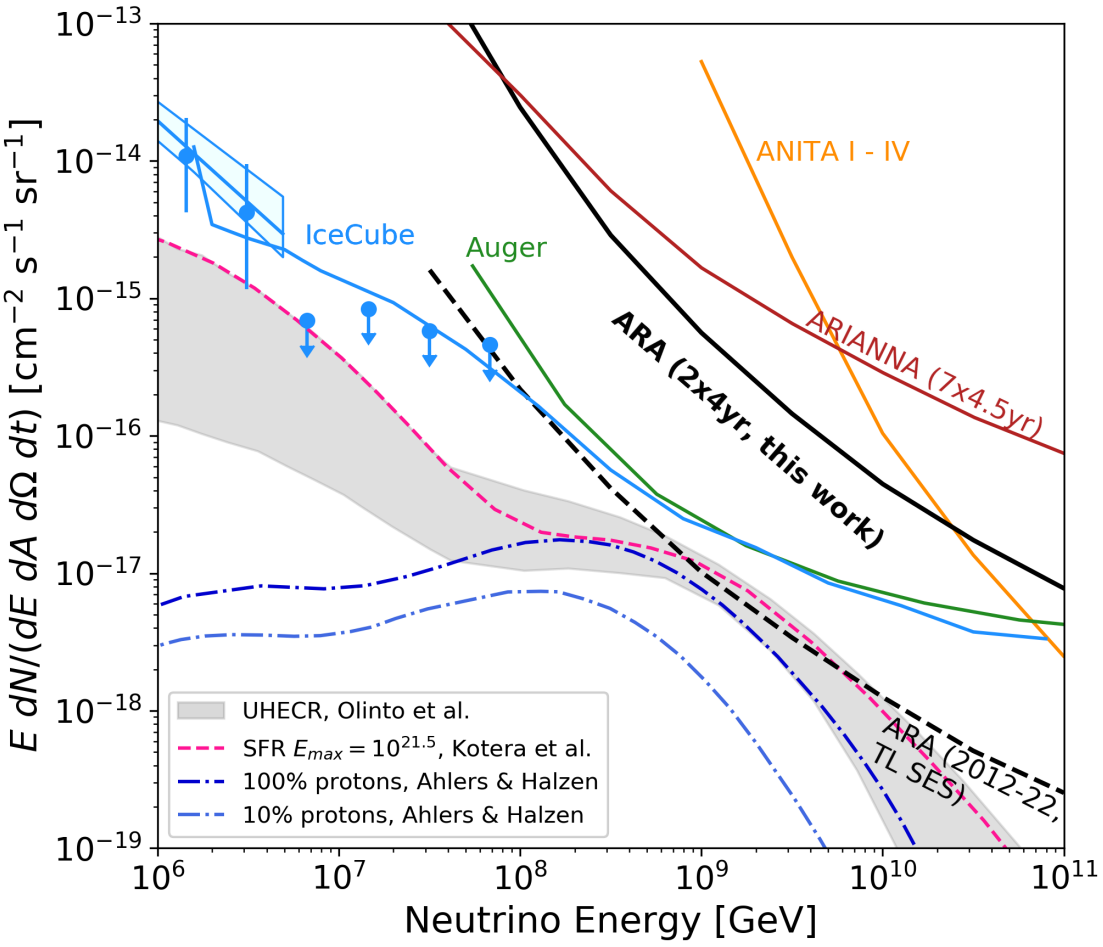

Figure 2.23: The 90% confidence-level upper limit on the all-flavor diffuse flux of neutrinos set by this analysis (thick black line). The limit accounts for uncertainties in the background estimate and systematic uncertainties on the neutrino sensitivity. We also plot the projected trigger-level single-event sensitivity (TL SES) for the five-station ARA5 array by 2022 as a black-dashed curve. Also shown are the latest limits and flux measurements from IceCube [7, 8], Auger [9], ANITA [10], and ARIANNA [12]. Shown for comparison are several benchmark cosmogenic neutrino flux models [16, 22, 23].

Chapter 3

Directional reconstruction framework for ARA

The Askaryan radiation emitted by neutrinos interacting in the ice, which can be measured by ARA antennas, contains information that can let us estimate both the energy and the direction of the primary neutrino. This is of utmost importance for both multi-messenger astronomy and fundamental physics as it will allow us to constrain the origin of the neutrino in the sky and study quantities such as its cross section for that particular energy, among others.

ARA sees about 60% of the Southern Sky at all times due to being in the South Pole, and several astrophysical objects that are expected to emit neutrinos lay in its field-of-view (FOV). Because neutrinos with energies above 40 TeV [87] are expected to be absorbed while they go through the Earth, most of the Northern sky (down into the ice, in ARA's perspective) is not visible to ARA. The 40% of the Southern sky that ARA cannot see is due to mainly two factors. The first is the detector sensitivity to mostly down-going signals. The second is that neutrinos have to go through a length of ice larger than the attenuation length of radio waves ($\sim$ 1 km) before interacting, and the produced Askaryan radiation is thus not observed. Figure 3.1 shows ARA's sky coverage for different simulated neutrino energies. As expected, there is a hard cut-off for neutrinos of the highest energies below the horizon due to absorption effects. Figure 3.2 shows ARA's FOV with a green band, along with radio-loud AGNs from the Rachen and Eichmann catalogue [24] that are within such FOV.

Developing a reconstruction framework will be important so that we can pinpoint the source of a neutrino in the sky, allowing for multi-messenger searches with other observatories. Also, a framework will be useful because targeted searches in a constrained area of the sky will decrease the background level, which consequently leads to a decrease in the search threshold.

In this chapter I will describe my efforts to build a directional reconstruction framework

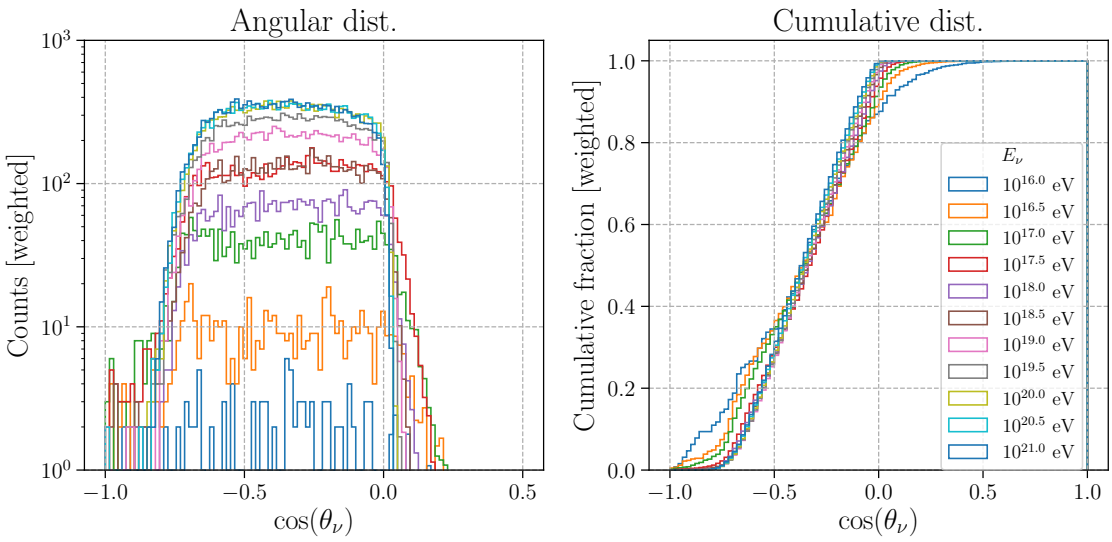

Figure 3.1: ARA's sky coverage as a function of the simulated neutrino zenith-direction for different energies. The plot on the left shows the distribution of triggered events: $\cos(\theta_\nu) = -1$ corresponds to downgoing events, and $\cos(\theta_\nu) = 1$ corresponds to upgoing events. As expected, there are more triggered events for the highest energies, but these events have a smaller sky coverage due to absorption effects in the ice: the highest the energy, the greatest the cross section.

for the ARA experiment, as well as the assessment of ARA's capabilities to constrain the signal polarization at the antenna using data from a pulser run at the South Pole.

3.1 Directional reconstruction

Let $\vec{v}$ be the direction of the primary neutrino. Upon interaction in the ice, a shower will be produced along the same direction $\vec{v}$, and the Askaryan signal will be propagated at some direction $\vec{\ell}$ (also called launch vector). The polarization $\vec{p}$ of the Askaryan radiation will be perpendicular to both the launch vector and in the plane containing the launch vector $\vec{\ell}$ and the neutrino direction vector $\vec{v}$:

$$\hat{p} = \hat{\ell} \times (\hat{v} \times \hat{\ell}), \tag{3.1}$$

assuming unit vectors for simplicity. Equation 3.1 can be solved for $\hat{v}$, yielding

$$\hat{v} = \sin\theta_{\text{view}}\hat{p} - \cos\theta_{\text{view}}\hat{\ell}, \tag{3.2}$$

where θ_{view} is called the viewing angle and is the angle between the neutrino direction $\hat{v}$ and the launch vector $\hat{\ell}$

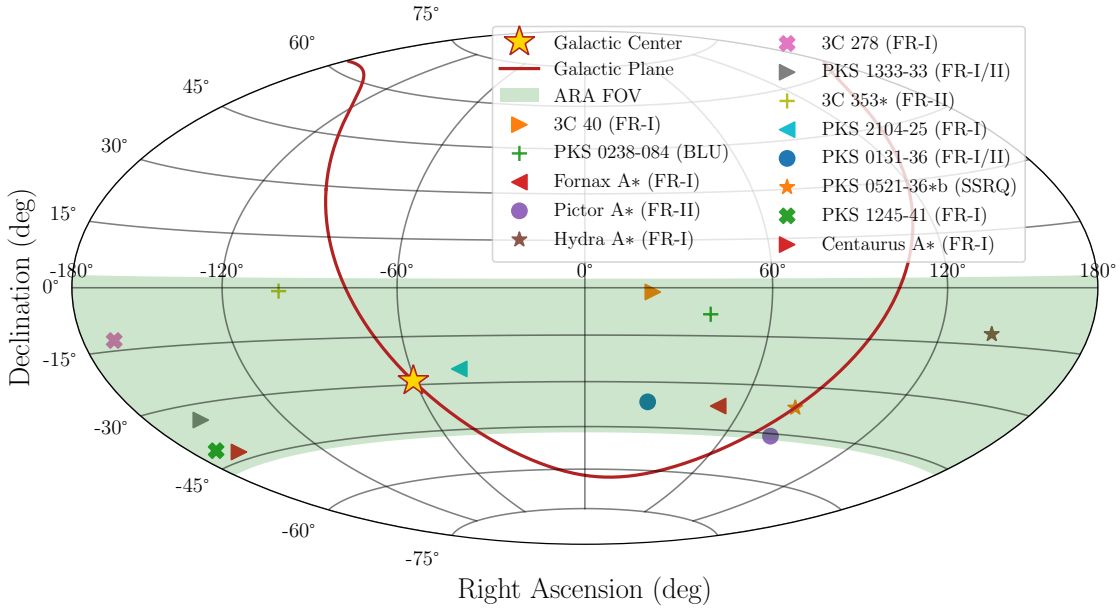

Figure 3.2: Radio galaxies as UHECR sources in ARA's FOV from the Rachen and Eichmann catalogue [24].

Due to the depth-dependent refractive index of the ice, the signal direction will bend and therefore the polarization vector will be rotated to satisfy orthogonality as the signal propagates in the ice. The magnitude of this bending will be determined by the vertex distance to the detector, and it will be a big effect for vertices near the ice firn, where the index of refraction varies more abruptly. This means that one needs to apply this correction to the polarization measured at the detector in order to correctly determine the neutrino direction. What I just described can be seen in Figure 3.3.

3.2 Polarization reconstruction

3.2.1 Signal measurement at the antennas

ARA deployed antennas of two different polarizations (horizontally polarized and vertically polarized) in order to be able to estimate the polarization of an incoming signal. Antennas are deployed in four different strings. In a given string there are four antennas: two top antennas (top Hpol and top Vpol), and two bottom antennas (bottom Hpol and bottom Vpol). The top and bottom antennas are separated by 15 m, the adjacent antennas of different polarizations are separated by 2 m, as shown in Figure 3.4.

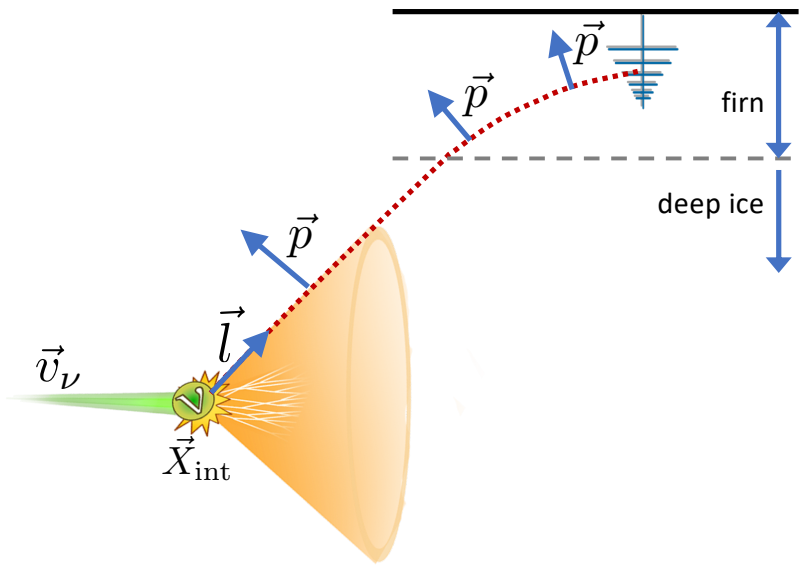

Figure 3.3: Important quantities to consider when reconstructing the neutrino direction. Figure by Christian Glaser.[25]

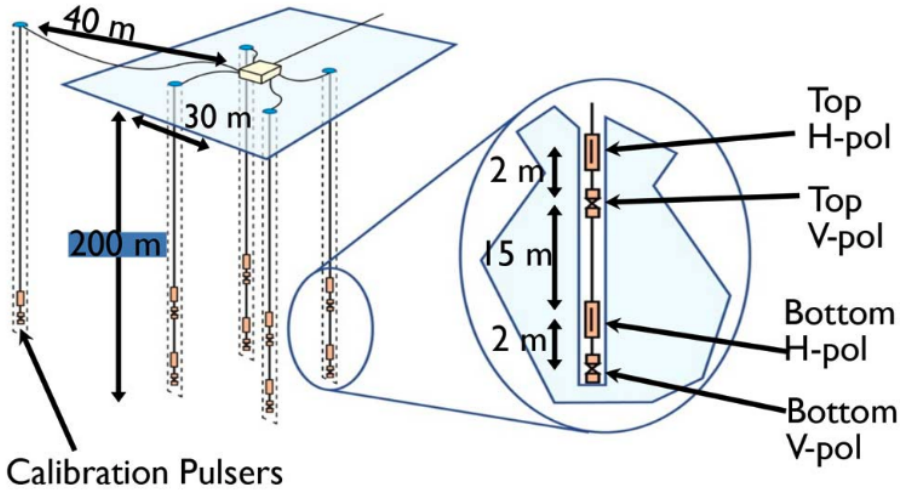

Figure 3.4: Diagram of an ARA station

The polarization vector can be estimated by comparing the amplitudes of the signal traces at adjacent antennas of different polarizations, and using the signal arrival information. The arrival information can be estimated by using the hit times across different antennas.

Let $\boldsymbol{\mathcal{E}}$ be the electric field arriving at the antenna, with components $\boldsymbol{\mathcal{E}} = (\mathcal{E}_\phi, \mathcal{E}_\theta)$. The

sub-indices ϕ and θ correspond to the polarization states that are perpendicular to the propagation vector in spherical coordinates centered at the antenna. The measured voltage output at the antenna $\mathcal{V}$ is given by the convolution of $\boldsymbol{\mathcal{E}}$ with the antenna system response $\boldsymbol{\mathcal{H}} = (\mathcal{H}_\phi, \mathcal{H}_\theta)$:

$$\mathcal{V} = \boldsymbol{\mathcal{E}} \cdot \boldsymbol{\mathcal{H}} \tag{3.3}$$

For our reconstruction work we assume that ARA's Vpol antenna has no azimuth response ($\mathcal{H}_\phi$) and that ARA's Hpol has no zenith response ($\mathcal{H}_\theta$). The antenna response for both antenna polarizations can be seen in Figure 3.5. This is an ideal approximation, as there is evidence that the antennas have cross-polarized responses. From this, the two different antennas will observe a voltage given by Equation 3.3:

$$\mathcal{V}_H = \mathcal{E}_\phi \mathcal{H}_\phi \tag{3.4}$$

$$\mathcal{V}_V = \mathcal{E}_\theta \mathcal{H}_\theta, \tag{3.5}$$

where $\mathcal{V}_H$ and $\mathcal{V}_V$ correspond to the Hpol and Vpol measured voltages, respectively.

3.2.2 Signal deconvolution

Antennas of different polarization are not identical. Because limitations on the size of the borehole, antennas have to be introduced vertically leaving no option to rotate a Vpol antenna by 90 degrees to make it Hpol. For this reason, a different antenna with a different system response had to be constructed for the Hpol channels. The shape of the system response for both antennas is similar, but the overall difference is the magnitude of the gain, as shown in Figure 3.5. To account for this difference when reconstructing the polarization, a deconvolution method is applied, which consists of undoing the antenna phase response and applying the inverse of the antenna gain in the Fourier space. Additionally, a Bessel filter was included to bandpass the signal around a bandwidth where we expect the Askaryan signal to have most of its power (200-600 MHz).

For this work, we decided to only account for the antenna response since we are assuming that there is uniformity in the system response across channels, i.e., the same amplifier/filter response is applied to all channels. While this assumption is not completely realistic for real data, it is realistic for `AraSim` since the simulation is constructed in such a way.

I next show an example of how the system response is applied in simulation and how deconvolution is done. Let us start from an Askaryan signal propagated at the antenna but without having the ARA system response folded in yet, folding in the system response, and then deconvolving that same system response. As it will be seen, through the convolution process there is information that goes missing. This is because the filter bandpasses the signal, effectively destroying information outside of it that is not possible to re-obtain with

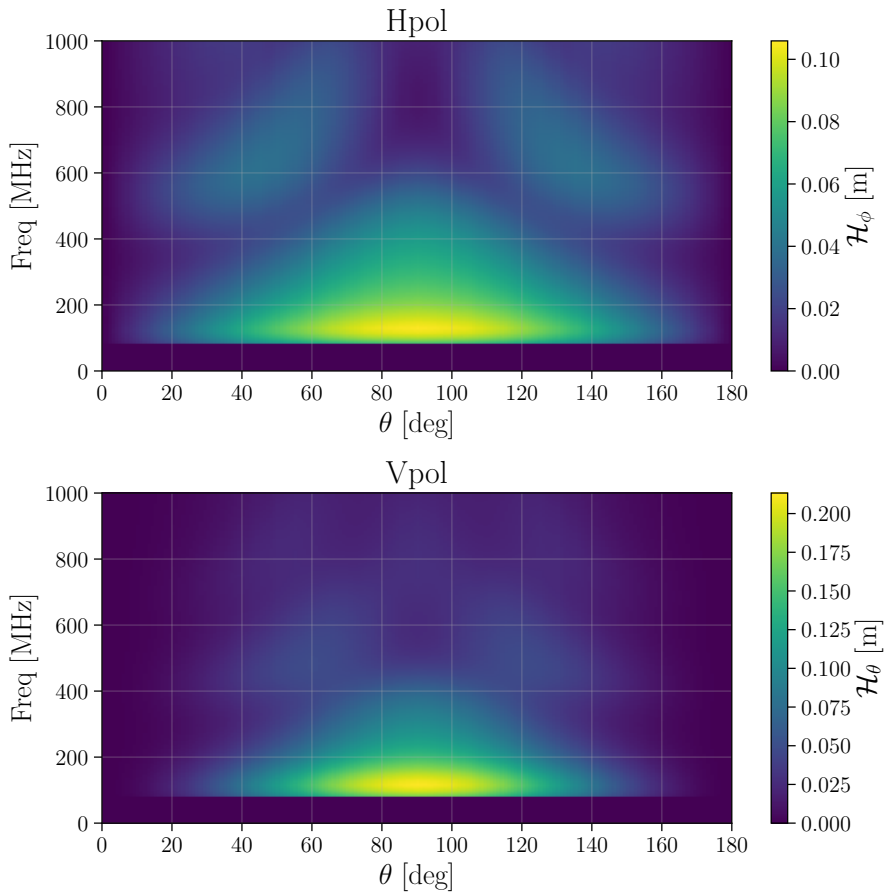

Figure 3.5: Antenna response for the Hpol and Vpol antennas as a function of receiving angle and frequency. The complex antenna response, on the color axis (z-axis) is folded into the arriving signal to account for dispersion and gain. From the plot, it can be seen that the bandwidth of the antenna is between 170-600 MHz.

a simple algorithm as the one that I am using for this work. A big fraction of the code written for this was adapted from `PyREx` [88]. This can also serve as an example of how the system response is applied in `AraSim`.

Signal at the antenna

Consider a hadronic shower with energy 10^{18} eV produced by a neutrino interaction in the ice at 5 km away from the detector, producing an Askaryan pulse with a viewing angle of 55.8°. The magnitude of the electric field as a function of time at the antenna, before the system response and any polarization factors are applied, is described by Figure 3.7.

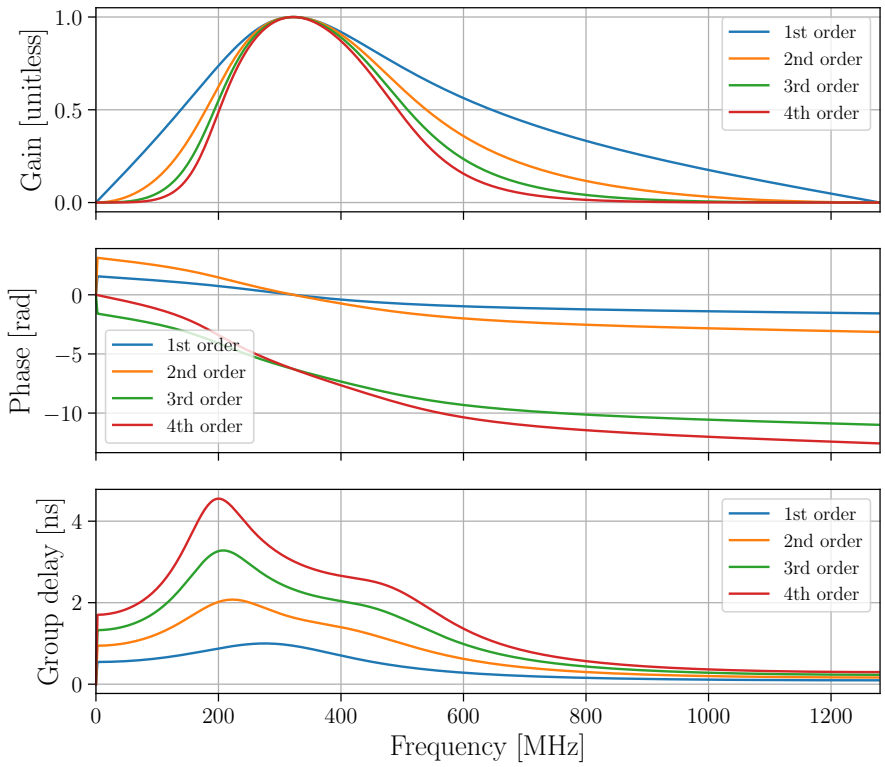

Figure 3.6: Properties of the different Bessel filter orders (as a function of frequency in MHz) that we considered to use as a bandpass around 150-400 MHz, where we expect the Askaryan signal to have most of its power. We chose the 4th order Bessel filter, as the gain bandwidth was further constrained around that region.

Folding the antenna response

Let us also take the incident wave arrives horizontally at a pair of adjacent Vpol and Hpol antennas, and that the polarization of the signal is along the $\hat{\theta}-$direction, to simplify our example. For this example, let us assume that there is no noise added to the signal. For this case, the signal will only be observed at the Vpol antenna, and the magnitude of the observed amplitude after the signal response will be given by Equation 3.3. There will also be some additional dispersion in the signal due to the antenna response, which can be seen in Figure 3.7.

Folding the electronics response

After the signal gets convolved with the antenna response, the signal is bandpassed and amplified by the electronics chain, which is composed by a filter and an amplifier whose combined response as a function of frequency is shown in Figure 2.4. As it can be seen from

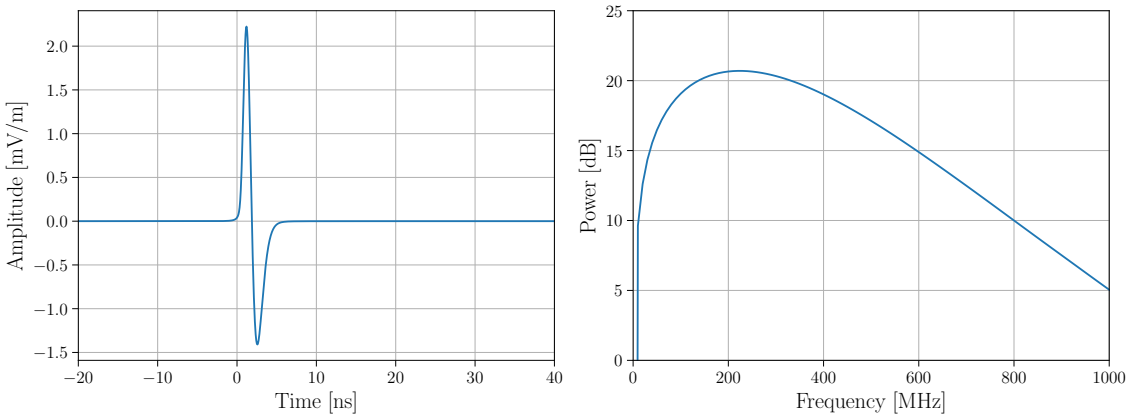

Figure 3.7: Left: the magnitude of the electric field in mV/m as a function of time in nanoseconds for a 10^{18} eV hadronic shower 5 km away from the detector. Right: the power spectrum of the Askaryan pulse on the figure on the left.

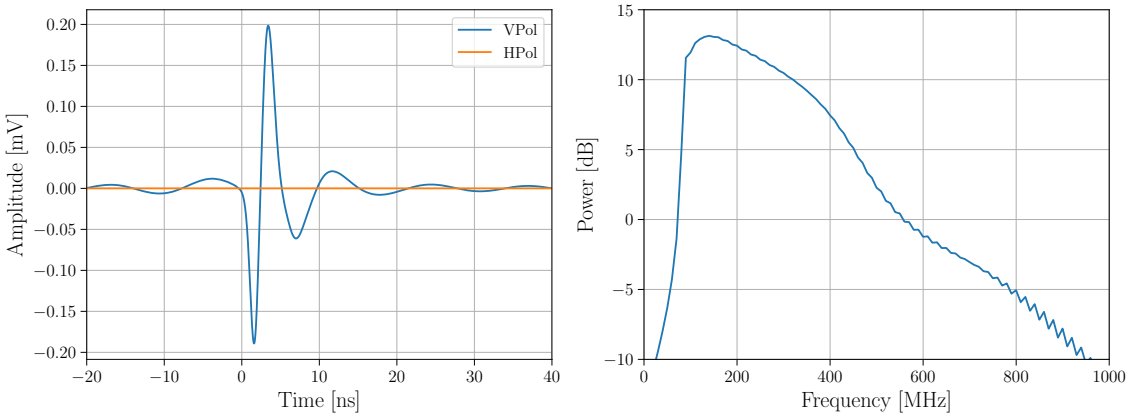

Figure 3.8: Left: the measured amplitude at the detector after the antenna response has been applied. Note that because of our choice of signal direction and polarization only the Vpol antenna observes a signal Right: the power spectrum of the Askaryan pulse on the figure on the left. We have decided to drop the HPol signal plot for clarity.

the same figure, the filter provides a significant dispersion effect, elongating the signal in time as shown in Figure 3.9.

Antenna response deconvolution

Due to the discrepancy in antenna response for the two different polarizations, one needs to correct for that if a comparison between relative amplitudes needs to be made. As

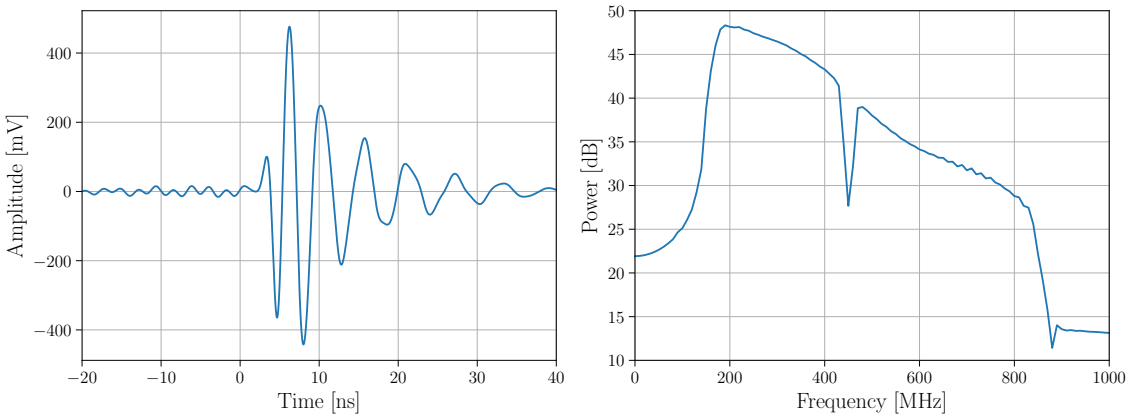

Figure 3.9: Left: Askaryan signal for the Vpol antenna after both the antenna and the filter/amplifier responses have been applied. Due to group delay effects from the filter, the signal disperses in time. Right: The power spectrum of the signal from the plot on the left. The dip at around 450 MHz corresponds to the notch filter to exclude power from South Pole radio communications.

explained before, to carry out the antenna response deconvolution we applied the inverse of the effective height phase response and the inverse of the absolute value of the effective height gain.

Continuing with the same example, we deconvolve the system response from the signal in Figure 3.9. We know that the signal arrived horizontally ($\theta = 90°$), and so we can obtain the Vpol antenna response at that angle. Figure 3.10 shows the antenna response and group delay for the Vpol antenna at $\theta = 90°$. Both the phase response and the gain are removed, resulting in the signal shown in Figure 3.11. If we compare it to Figure 3.7, we can notice that the signals are not identical, and this is due to the fact that the filter response is still convolved into the signal. Deconvolving the antenna response is enough for our work, as the issue we were facing was that the two antenna responses are different.

3.2.3 Vertex reconstruction

Most of this subsection was taken from our published work:

> P. Allison *et. al.* for the ARA Collaboration. *Constraints on the Diffuse Flux of Ultra-High Energy Neutrinos from Four Years of Askaryan Radio Array Data in Two Stations*. Phys. Rev. D 102, 043021 (2020).

ARA uses arrival time differences for all of its antennas to determine the source of the signal using an interferometric reconstruction technique. This technique has been used in other ARA analyses [33, 73, 74, 89] and in the ANITA experiment [90]. The interferometric

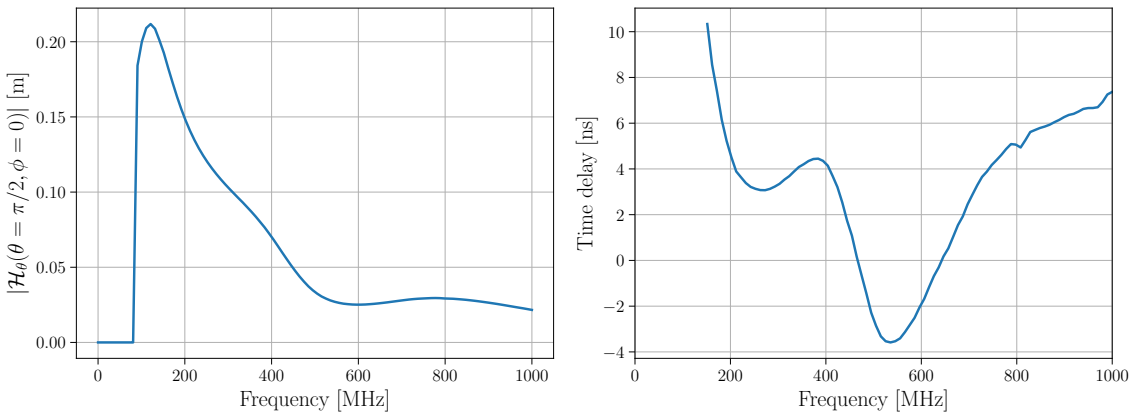

Figure 3.10: Left: The absolute value of the theta component of the antenna effective height ($\mathcal{H}_\theta$) for a horizontally arriving signal. Right: Group delay of the antenna response as a function of frequency.

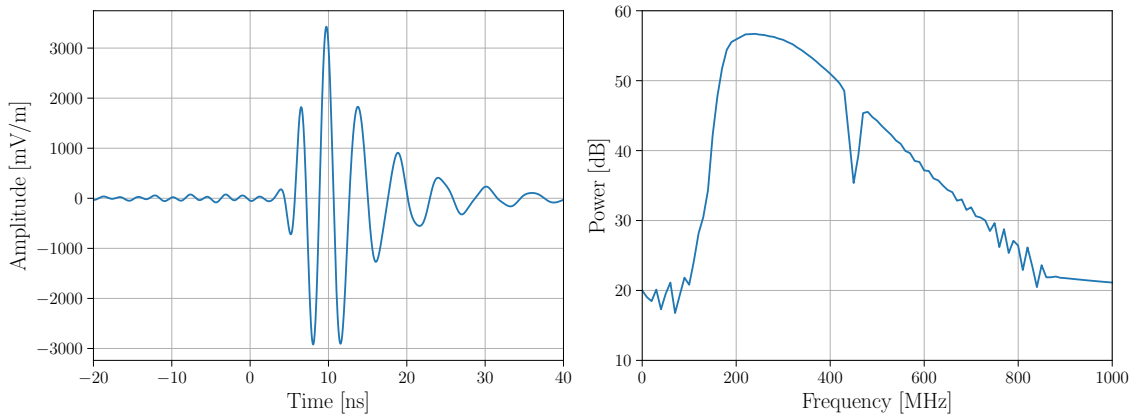

Figure 3.11: Left: Askaryan signal for the Vpol antenna after the antenna response deconvolution method has been applied. Right: The power spectrum of the signal from the plot on the left.

technique relies on the relationship between the location of an emitting source in space and the time delays expected for two measurement antennas with known separation.

For a given pair of antenna waveforms, the cross-correlation $C_{\mathrm{i,j}}$ between the voltage waveform on the i-th antenna (V_{i}) and the voltage waveform on the j-th antenna (V_{j}) as a function of time lag τ can be expressed in Eq. 3.6:

$$C_{i,j}(\tau) = \frac{\sum_t V_i(t) V_j(t+\tau)}{RMS_i \times RMS_j} \tag{3.6}$$

where the RMS are the root-mean-square voltages of the waveforms in the absence of signal. The lag τ defines the the time delay of one antenna waveform relative to the other and depends on the position of the source emitter relative to the array center, characterized by an elevation angle (θ), an azimuthal angle (ϕ), and a distance to the source (R). The array center is defined as the centroid of all sixteen measurement antennas in the station.

The pairwise time lags τ for a given point on the sky θ, ϕ are computed by calculating the path a light ray would take from a hypothesized source located at a distance R to an antenna. The calculation accounts for the changing index of refraction of the Antarctic firn, which causes rays to follow curved, rather than rectilinear trajectories. With $n(z)$ the depth-dependent index-of-refraction, and z the (negative) depth from the ice surface, the ray-tracing method models the changing index of refraction as:

$$n(z) = 1.78 - 1.35e^{0.0132z}. \tag{3.7}$$

This index of refraction model was determined by fitting data collected by the RICE experiment in Antarctica [82]. We consider the index to be unity above the surface.

The total cross-correlation strength for a given point on the sky is given by summing over all like-polarization pairs of antennas as in Eq. 3.8:

$$C_{\text{sky}}(\theta, \phi; R) = \frac{\sum_{i=1}^{n_{ant}-1} \sum_{j=i+1}^{n_{ant}} C_{i,j}[\tau(\theta, \phi; R)]}{n_{\text{ant}}} \tag{3.8}$$

To smooth uncertainties in the ice model and other systematics (such as differences in the phase responses of the various contributing antennas), we calculate the Hilbert envelope of the cross-correlation function before summing over pairs, as is done in previous analyses. The Hilbert envelope of the cross-correlation $H(C_{\text{i,j}})$ is calculated according to Eq. 3.9:

$$H(C_{i,j}) = \sqrt{C_{i,j}^2 + h^2(C_{i,j})} \tag{3.9}$$

where $h(C_{\text{i,j}})$ denotes the Hilbert transform.

The cross-correlation function for an individual pair of antennas, $C_{\text{i,j}}$, is expected to be maximal when the lag is equal to the true difference in the arrival times of a signal at the two different antennas. The sky map is therefore expected to have a peak at the putative source direction.

Studies performed by the ARA collaboration using a calibration pulser have shown that the interferometric reconstruction method has a sub-degree resolution. These studies were performed by reconstructing the location of both calibration pulsers: C5 and C6. The positions of these pulsers are fixed and known, and they trigger the station at a rate of 1 Hz, providing enough statistics for these studies. Only one of them is active at a single time.

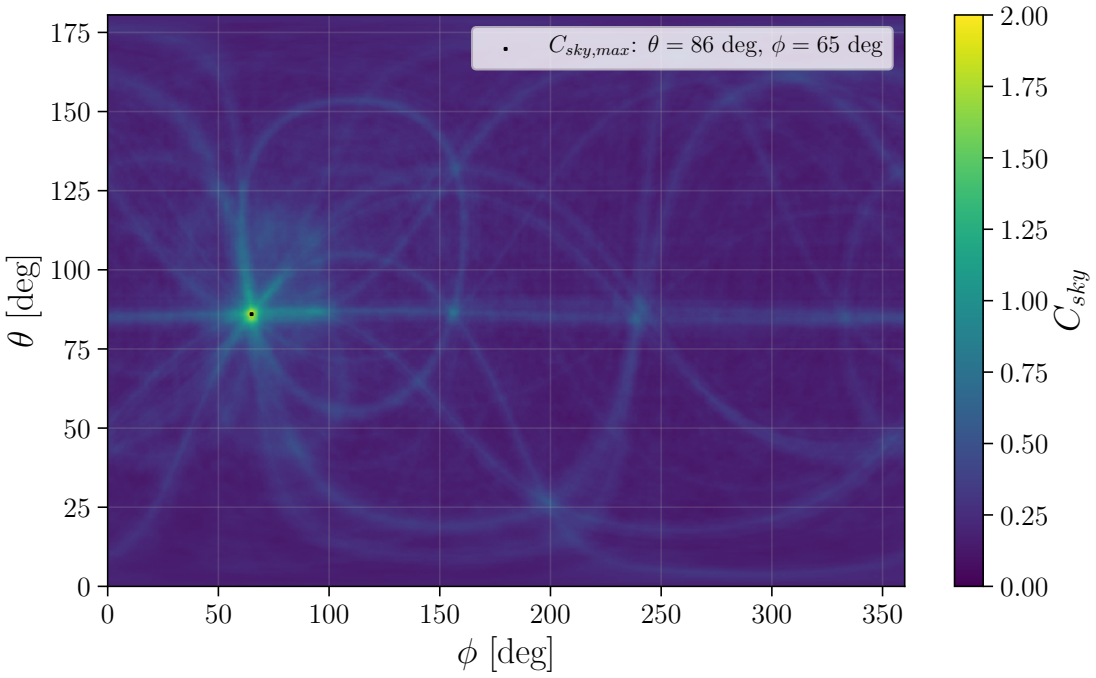

Figure 3.12: An example of an interferometric correlation (sky) map of a calibration pulser signal observed by A2.

Let $\hat{d}$ be the ray propagation unit vector at the antenna given by the following expression in spherical coordinates:

$$\hat{d} = (\sin\theta\cos\theta,\ \sin\theta\sin\theta,\ \cos\theta), \tag{3.10}$$

where ϕ and θ are the angles of the arriving signal at the antenna.

3.2.4 Estimating the polarization vector

After constructing the arriving signal direction at the antenna, the polarization can be estimated as follows: Let $\hat{\phi}$ and $\hat{\theta}$ be unit vectors in spherical coordinates in the direction of ϕ and θ, respectively. Let A_H and A_V be the deconvolved signal amplitudes (in units of mV/m) at the Hpol and Vpol antenna, respectively. The measured amplitudes are related to the electric field in the following way:

$$A_H \propto \boldsymbol{\mathcal{E}} \cdot \hat{\phi} \tag{3.11}$$

$$A_V \propto \boldsymbol{\mathcal{E}} \cdot \hat{\theta}, \tag{3.12}$$

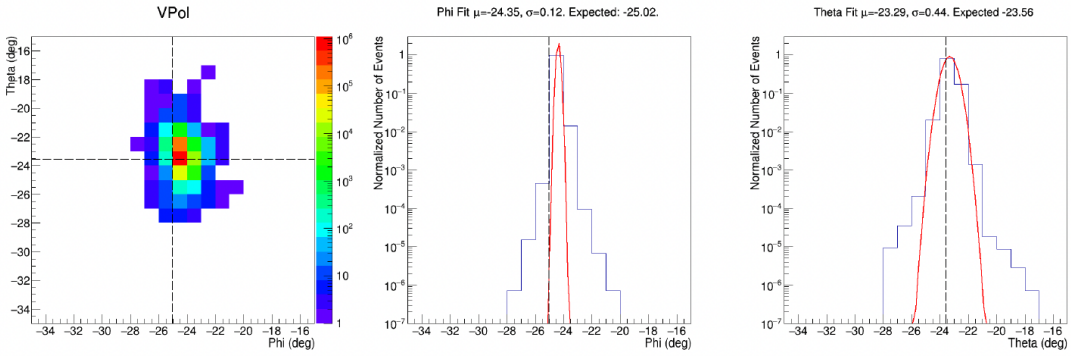

Figure 3.13: Spatial distribution of calibration pulser events that reconstruct in the direction of CP5. The coordinates of CP5 are $(\phi, \theta) = (-25.02°, -23.56°)$, which corresponds to the intersection of the dashed lines on the left panel. The middle and right panel show the ϕ and θ projections of the 2D distribution on the left panel, along with the parameters of a Gaussian fit. As it can be seen, the difference between the expected and measured parameters is $\mathcal{O}(1°)$. Figure by Brian Clark.

where the proportionality sign indicates that part of the system response (such as filters) are still present, as the deconvolution only removes the antenna response.

We can relate the ratio of measured, deconvolved amplitudes in the two types of antennas to the polarization direction in the following way:

$$R \equiv \frac{A_H}{A_V} = \frac{\hat{p} \cdot \hat{\phi}}{\hat{p} \cdot \hat{\theta}}, \tag{3.13}$$

where $\hat{p}$ is the unit polarization vector of the electric field arriving at the antennas. We can use Equation 3.13 along with the condition that the propagation vector is perpendicular to the polarization vector to obtain the components of the polarization unit vector $\hat{p}$ (the detailed calculation is done in Section B.1):

$$p_x = \pm \frac{\cos\theta \cos\phi - R \sin\phi}{\sqrt{1 + R^2}}, \tag{3.14}$$

$$p_y = \pm \frac{\cos\theta \sin\phi + R \cos\phi}{\sqrt{1 + R^2}}, \tag{3.15}$$

$$p_z = \mp \frac{\sin\theta}{\sqrt{1 + R^2}}. \tag{3.16}$$

Note that all the quantities defining $\hat{p}$ are measurable by ARA. We will not talk about the two solutions, as they will become a single solution when we relate them to Ω and Ψ.

Let us relate the components of $\hat{p}$ to the angles Ω and Ψ graphically defined in Fig-

ure 3.14:

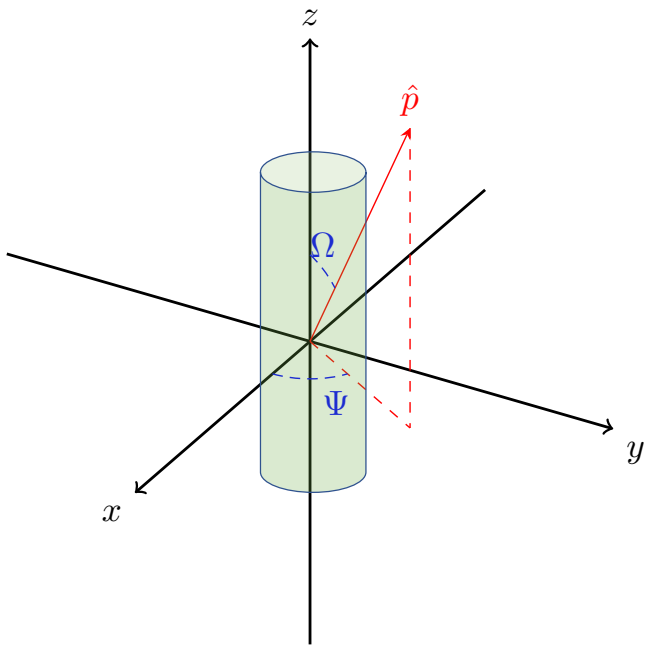

Figure 3.14: Graphical definition of Ω and Ψ. The green cylinder is a graphic representation of a Vpol antenna, whose polarization is along the z-axis. Omega is defined as the angle between the polarization vector and the polarization of the Vpol antenna (in this case the angle between $\hat{p}$ and $\hat{z}$).

$$\Omega = \arccos\left(p_z\right), \tag{3.17}$$

$$\Psi = \arctan\left(\frac{p_y}{p_x}\right). \tag{3.18}$$

The choice of solution does not impact the reconstructed Omega and Psi angles since arccos is an even function, and p_y and p_x have the same preceding sign.

We estimated the capability of A2 to measure the polarization using both simulated events and data. The details for each treatment are described in the next subsections.

3.2.5 Simulation

We assessed the polarization reconstruction capabilities of ARA by simulating neutrino events of different energies ($10^{17} - 10^{20.5}$ eV) interacting in ARA's fiducial volume. Whereas

most events produce both direct and reflected/refracted signals due to the changing index of refraction of ice, we only used direct signals to simplify our work. Similarly, ice effects such as focusing and magnification were turned off. The digitizer crops waveforms if they exceed amplitudes of 1.5 V, to which we refer as saturated events. For this work, we reject those events since their amplitudes would lead to erroneously reconstructed polarizations.

For our work, the ratio of amplitudes described in 3.13 was modified to use the noise-subtracted ratio of powers over a certain window centered at the signal peak, which we will call $\mathcal{P}_H$ and $\mathcal{P}_V$ for the Hpol and Vpol antenna, respectively. This power was defined as

$$\mathcal{P} = \int_{t_{\text{peak}}-20\text{ ns}}^{t_{\text{peak}}+60\text{ ns}} A(t)^2 dt - \int_{0\text{ ns}}^{80\text{ ns}} A_{noise}(t)^2 dt \tag{3.19}$$

For the first term in 3.19, the window was taken from the previous ARA diffuse analysis [11]. The window integration for the second term was chosen to have the same length (80 ns), with the lower limit at the beginning of the waveform where no signal is expected (in simulation).

We reconstructed both zenith (Ω) and azimuth (Ψ) polarization angles by analyzing the measured amplitudes by a single pair of adjacent antennas and comparing them to the true values that our simulation produced.

Reconstruction of simulated events without noise

We first reconstructed the polarization of events without noise. This would serve as a cross-check in our work, since we expect events without noise to reconstruct almost perfectly. The results for both Ω and Ψ are shown in Figure 3.15 and Figure 3.16. As expected, the distribution is centered at zero, and its standard deviation is of a few degrees. The fact that the distribution is not narrower is in part due to information lost during the signal filtering, which is not recovered during the antenna response deconvolution process.

3.2.6 Reconstruction of simulated events with noise

`AraSim` has the capability to simulate events with noise if a ray-tracing solution exists for a specific neutrino event. The noise is produced by calculating the average power that the ice and the electronics would produce due to their black-body radiation in ARA's 150-850 MHz bandwidth (see Section B.3). From this flat spectrum, a random phase between 0 and 2π is applied to each frequency bin and then the result is converted to time domain by taking the Fourier transform. This noise waveform is added to the signal produced by the Askaryan radiation arriving at the antenna just before the system response is applied. We expect the resolutions on the reconstructed polarization angles to degrade when noise is added, as the integrated power for the waveforms will change.

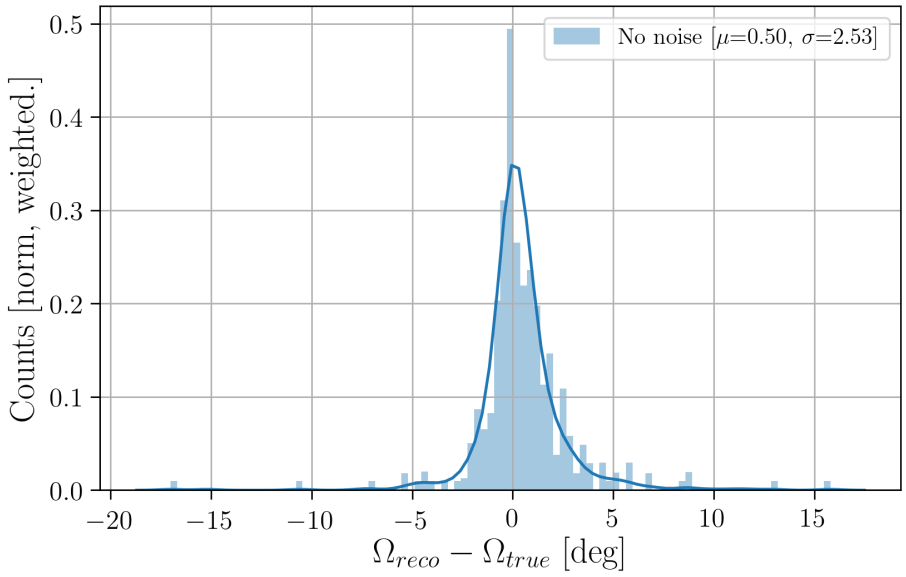

Figure 3.15: Comparison between true and reconstructed values of Ω for a set of simulated events with `AraSim`. The events are attributed weights produced by `AraSim`, and then normalized.

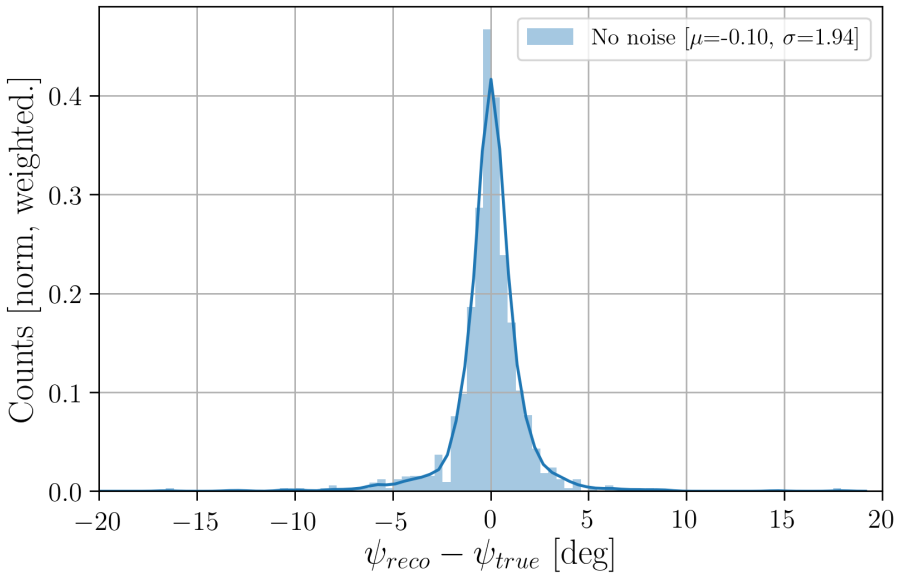

Figure 3.16: Comparison between true and reconstructed values of Ψ for a set of simulated events with `AraSim`. T The events are attributed weights produced by `AraSim`, and then normalized.

A similar set of neutrino events with the same conditions as for the no-noise case, but not exactly the same set, was simulated. The same algorithm was used to reconstruct the

polarization of the events as in the case with no noise. Because noise is present, the polarization resolution will depend on the signal-to-noise ratio, which for a particular channel is calculated as the peak value of the trace over the noise root-mean-square value:

$$\mathrm{SNR} = \frac{V_{\mathrm{peak}}}{\sigma_{\mathrm{noise}}} \tag{3.20}$$

Caveats and limitations

Our work has some caveats: 1. We take the reconstruction of the signal arrival vector at the antenna to be perfect. This is realistic, since from previous studies it has been shown that the error in vertex reconstruction with ARA is of about 1 degree. 2. We assume that we know the polarity of the signal, which has not been assessed with real ARA data.

Since the response for the two antenna types are different, the antenna responses are removed from the signal (deconvolution), and the resulting signal amplitudes are compared. There are a few caveats to this approach: the estimation of the polarization will be affected by systematic errors in the modeling of ARA's system response, and also by additional uncertainties in the determination of the arriving direction of the signal at the antenna (see vertex reconstruction section).

Method and results

We estimate the resolution on reconstructed polarization angles as a function of SNR. This can be seen in Figure 3.17. This figure corresponds to applying all the cuts previously described and rejecting events whose SNR in the Vpol channel $\mathrm{SNR_V} > 5$ and the SNR in the Hpol channel $\mathrm{SNR_H} > 3$. The green-dashed line at SNR$\approx$ 20 corresponds to the SNR that A2 would have seen the SPICEcore signal if it was placed at the site of the ARIANNA station (c.f. Section B.2). This was done to compare our results to ARIANNA results [91]. They quote a resolution of $\Psi = 2.7°$, and from our results we observe a resolution in Ψ of about 5° at the same Vpol SNR. The resolution increases to about 2° at the same Hpol SNR.

The polarization resolution can also be put in terms of the simulated neutrino energy. Figure 3.18 shows the polarization resolution as a function of the simulated neutrino energy. For this plot, we are applying all the cuts previously described, and we are requiring that the SNR for both channels be greater than 3. The improvement in resolution is not as dramatic as for the one as a function of SNR as neutrinos with high energies could have interacted far from the detector yielding small SNRs. Figure 3.19 shows something similar, but with the requirement that the SNR for both channels be greater than 5.

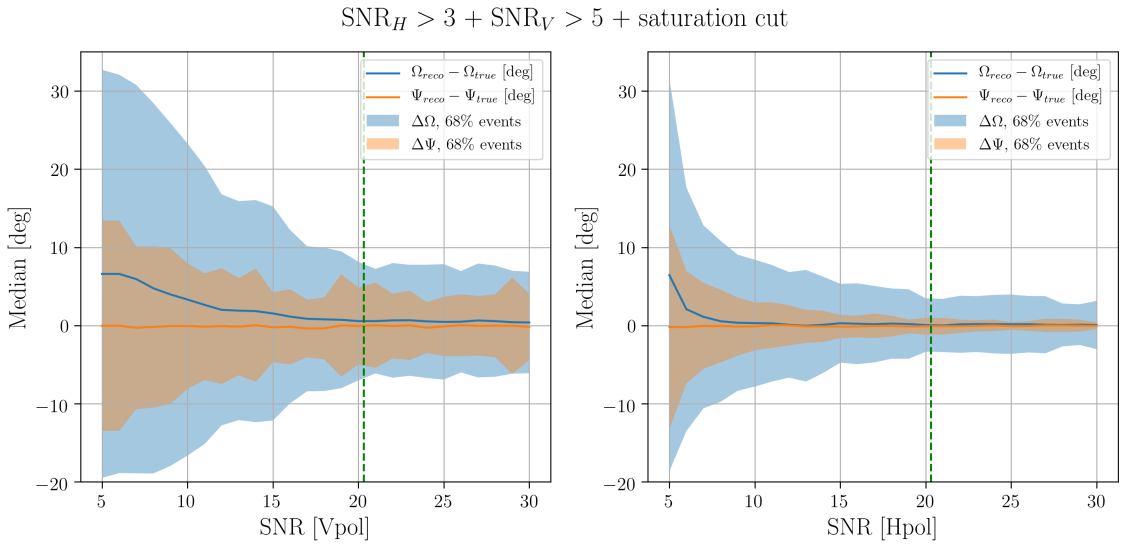

Figure 3.17: Polarization angle resolutions for Ω and Ψ as a function of Vpol SNR and Hpol SNR. The shaded regions represent the region in which the 68% of the data are contained. The panel on the left was obtained by rejecting events whose Vpol SNR was smaller than the one on the $x-$axis (while keeping the Hpol constrain at $SNR_H > 3$) and then obtaining the median and 68% confidence limit from the corresponding distribution. The plot on the right panel is similar, but was obtained by varying the Hpol SNR while keeping the constrain at $SNR_V > 5$.

3.3 SPICEcore pulser data

In Dec 2018, a fat-dipole antenna was lowered into the Antarctic ice reaching a maximum depth of about 1700 m. This experiment was performed by a team of scientists from the University of Kansas, and was called the SPICEcore experiment. The transmitter antenna, also known as the South Pole University of Kansas Pressure Vessel Antenna (SPUNK PVA), was designed to match the 97-mm diameter of the borehole in which it was dropped.

Over a period of 6-8 hours, the SPUNK PVA transmitted was lowered into the borehole reaching maximum depths between 1100-1700 m and then returned to the ice surface. Figure 3.20 shows the drop as a function of time of the day for Dec 24. During that period, pulses were emitted by the transmitter and observed by ARA stations. Because of ray bending in the firn, we expect to observe two pulses: one corresponding to the direct signal and one corresponding to the reflected/refracted signal.

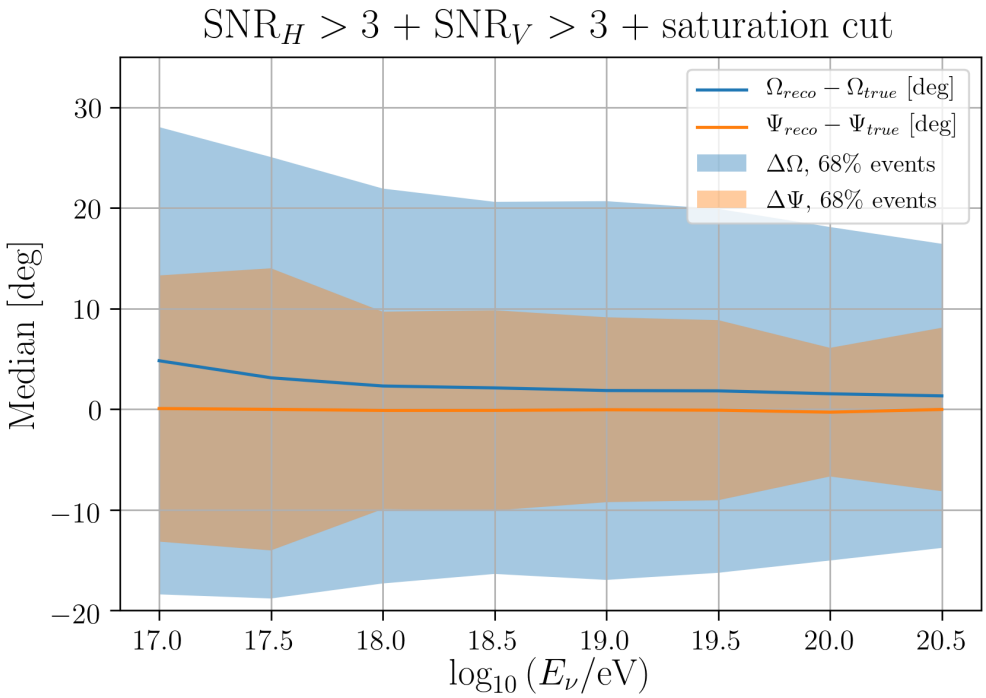

Figure 3.18: Polarization angle resolutions for Ω and Ψ as a function of the neutrino energy. We require that the SNR for both the Vpol channel and the Hpol channel be greater than 3.

3.3.1 Data analysis

The SPICEcore drop happened over a span of several days, producing several runs. I used run 012559 that happened during the night of Dec 24, 2018 to reconstruct the polarization angles.

Removing non-SPICEcore events

The data taken during that period was taken under normal station conditions, meaning that software-triggered and calibration pulser events were recorded. These events can be easily removed with `AraRoot`, as they are flagged as such. The remaining events are a combination of SPICEcore events and noise-triggered events. To successfully isolate SPICEcore pulser events from the remaining data, a simple signal-to-noise-ratio (SNR) cut was designed. Let the SNR be defined as

$$\mathrm{SNR} \equiv \frac{V_{\mathrm{peak,dir}}}{\sigma_{\mathrm{noise}}}, \tag{3.21}$$

where $V_{\mathrm{peak,dir}}$ is defined as the peak amplitude of the direct pulse, and σ_{noise} is the noise root-mean-square (rms) obtained by averaging the rms from soft-triggered events over a

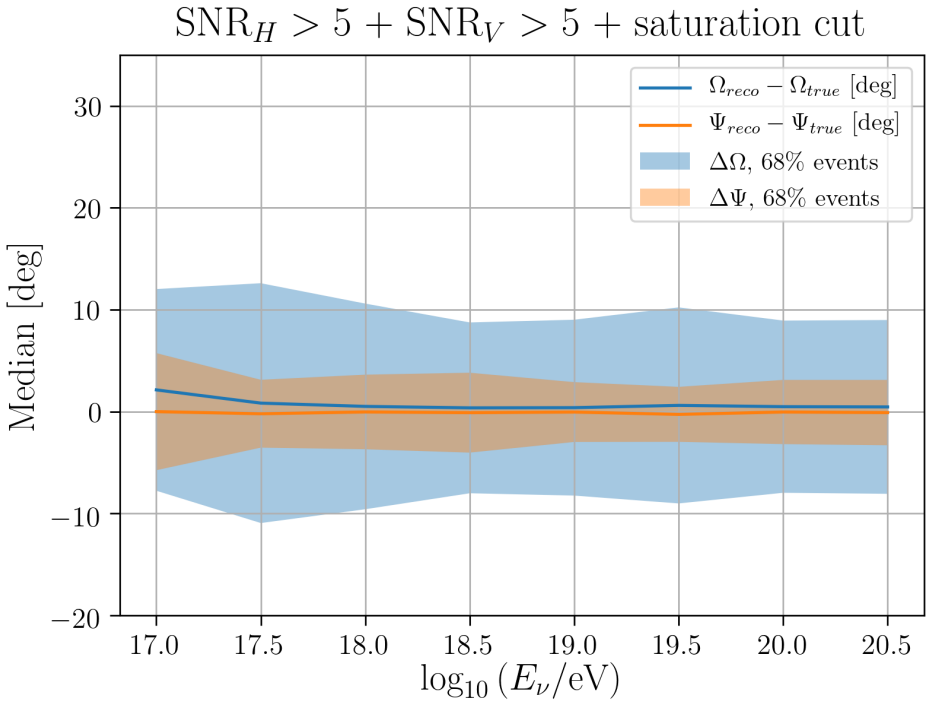

Figure 3.19: Polarization angle resolutions for Ω and Ψ as a function of the neutrino energy. We require that the SNR for both the Vpol channel and the Hpol channel be greater than 5

run. We rejected events whose Vpol channels satisfy $SNR > 8$. This was chosen as we do not expect noise events to achieve that level, or SPICEcore events to be below that threshold.

Peak finding

Because there are two peaks due to direct and reflected/refracted events, an algorithm designed to isolate the direct peak had to be designed. We use the `find_peaks` function from the signal processing (`scipy.signal`) package of `Scipy` [92] to find the peak that happens first in time (as we expect it to be the one corresponding to the direct solution). To do this, we first normalize the waveform by the value of the highest peak (regardless of whether it is direct or reflected/refracted). We then find the Hilbert envelope of the normalized waveform and use the `find_peaks` function to locate peaks with a duration greater than two samples and above a normalized value of 0.5. If there are no peaks that satisfy this, the event is not used for our analysis. This function will return an array containing the bins at which the peaks are located, and we choose the peak with the smallest bin, which should correspond to the direct pulse.

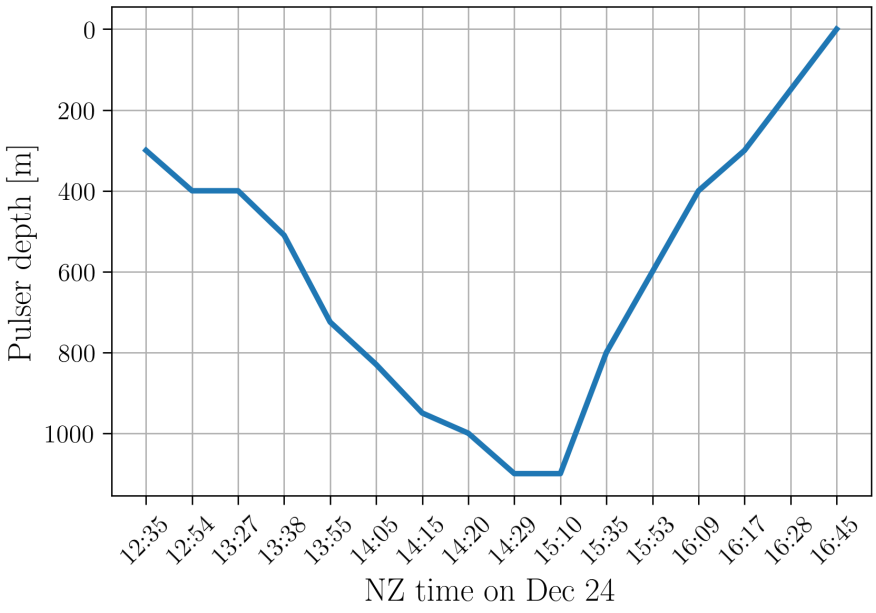

Figure 3.20: New Zealand local time vs. depth in meters for a SPICEcore drop on Dec 24

Saturated events

The ARA digitizer truncates amplitudes greater than 1.5 volts. Since the polarization reconstruction relies on the ratio between the two amplitudes, an event whose amplitude is truncated will not give a reliable measured value. We reject those events whose peak amplitude (of either pulse) is greater than 1.5 volts.

Power integration

As explained in the last section, we use integrated power over an 80 ns window to calculate the polarization angle. For the Vpol channels, the window is centered at the time of the peak of the direct pulse, and the window is 20 ns long to the left of the peak and 60 ns long to the right thereof. The same treatment as what was done for simulation. On the other hand, there is a difference for how we treat the window for the Hpol channels: due to the measured birefringence in ice by Besson *et al.* [83], for a A2-SPICEcore trajectory, we expect an delay of $\Delta T_{h,v} = -14.1 \pm 2.8$ ns between the signal measured at Hpol channels and Vpol channels in A2, with the Hpol signal coming first. To account for this, the integration window was shifted by 14.1 ns to earlier times. This can be seen in Figure 3.23

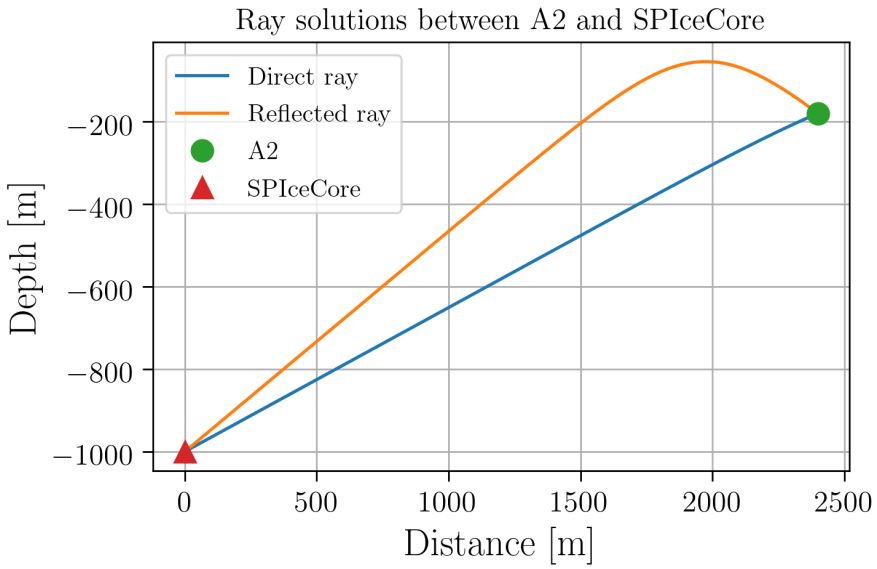

Figure 3.21: Example of the two signals for a SPICEcore pulse coming from the emitter located at a depth of 1000 m and observer by ARA station 2 (A2). A2 was located at a horizontal distance of 2400 m from the pulser. We expect to observe two peaks in the waveform captured by A2, with a time separation given by the extra distance traveled by the refracted/reflected ray.

Special considerations for some channels

As can be seen in Figure 3.22, Channel 1 and Channel 3 have direct peaks that are not completely captured in the trace. Even though the first block of the waveforms is truncated, the main reason is that the trigger latches in such a way that the first pulse is sometimes truncated for channels 1 and 3 due to the trigger readout being too short. We exclude channel 1 and channel 3 for this reason, and consequently channel 9 and channel 11 will not be used since they are adjacent, and thus would be needed to estimate the signal polarization.

Noise subtraction

As we did for simulation, we want to account for thermal noise in our polarization estimation. ARA automatically triggers at a rate of 1 Hz to capture noise. We call these software triggers, and the events have a length of about 200 ns, compared to the 600 ns length of RF triggered events. All of the waveforms used for this work were deconvolved through the process described in Subsection 3.2.2. For the case of noise, because we cannot determine a singular incoming direction as we can for SPICEcore events, we decided to deconvolve

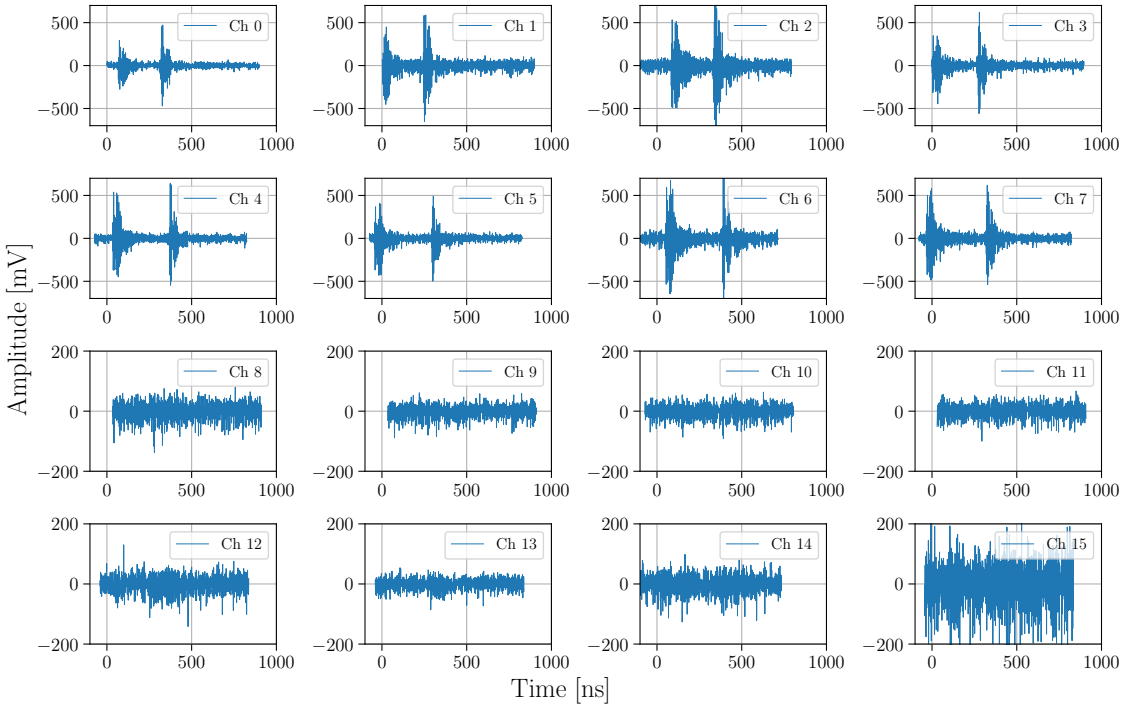

Figure 3.22: Example of a SPICEcore event waveform recorded by A2. As expected, there are two pulses: the first one corresponding to the direct signal and the second one corresponding to the refracted/reflected signal. Because of the polarization of the emitter (mainly vertically polarized), the Hpol channels (ch. 8-14, ch. 15 is broken) do not observe a clear peak.

them by assuming that they arrive at the antenna boresight. This provides a conservative approach to noise subtraction, as we assume it treats noise as being maximally amplified by the antenna gain.

Our first attempt to do noise subtraction was to integrate the power ($\mathcal{P}_{\text{noise}}$) in a software-triggered waveform within an 80 ns window whose start corresponds to the start of the waveform, as we expect the noise to have a random phase. We did that for all the software trigger events in our run and then averaged the result. We subtracted the result of the 80 ns-integrated power from the SPICEcore power integrated in an 80 ns window ($\mathcal{P}_{\text{trace}}$) as was described before. Note that $\mathcal{P}_{\text{trace}}$ corresponds to the sum of the SPICEcore event power and power due to thermal noise over the duration of the event:

$$\mathcal{P}_{\text{trace}} = \mathcal{P}_{\text{pulser}} + \mathcal{P}_{\text{noise}}$$

We found, however, that this method resulted in negative powers for some events in the

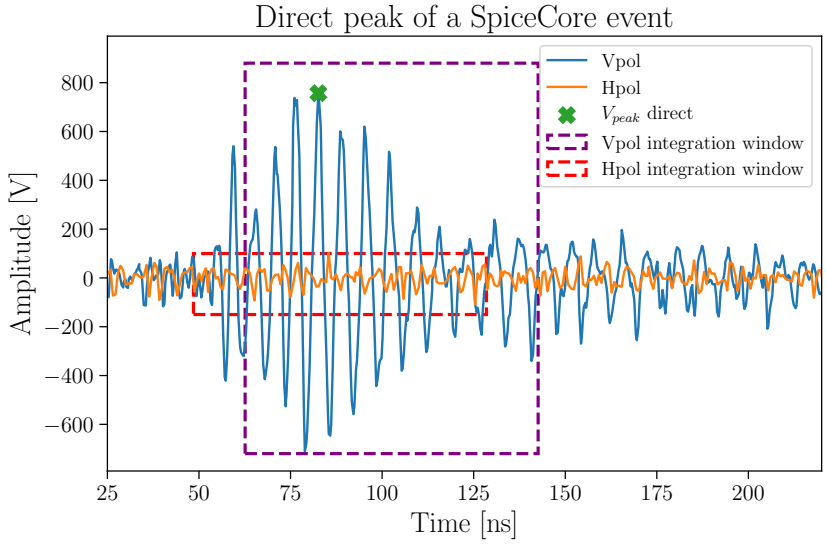

Figure 3.23: Example of how the windows are chosen for a direct pulse of a SPICEcore event in A2. The green cross represents the location of the peak amplitude of the pulse. The window (purple-dashed rectangle) is chosen such that it captures 20 ns to the left of the peak and 60 ns to the right of the peak in the Vpol channel. Similarly, a window (red-dashed rectangle) is chosen for the Hpol channel but shifted by $\Delta T_{h,v}$ from the location of the peak amplitude

Hpol channels. As it can be seen in Figure 3.22 and Figure 3.24, Hpol channels do not show any obvious signal for some events and the mean power of software trigger events can be larger than the power in Hpol channels. Another approach had to be found.

We decided to perform noise subtraction by combining the software trigger waveform and the SPICEcore event waveforms, for each software triggered event in the run. This would give us a distribution for a single SPICEcore event. This was repeated for each SPICEcore event, so we had as many distributions as pulser events. For each distribution, the mean ($\mu_{\text{trace+noise}}$) was found and the noise subtraction was done by calculating

$$\mathcal{P}_{\text{pulser}} = 2\mathcal{P}_{\text{trace}} - \mu_{\text{trace+noise}}$$

The reason for doing this is that adding random, incoherent noise increases the power of the signal, which already has noise. We can assume that since noise is not in phase with the signal $\mathcal{P}_{\text{pulser+noise}}$ can be factored as

$$\mathcal{P}_{\text{trace+noise}} = \mathcal{P}_{\text{pulser}} + 2\mathcal{P}_{\text{noise}}.$$

This method still yields events with negative power at a similar rate as the method before. However, it takes a more correct approach in the sense that it uses the noise

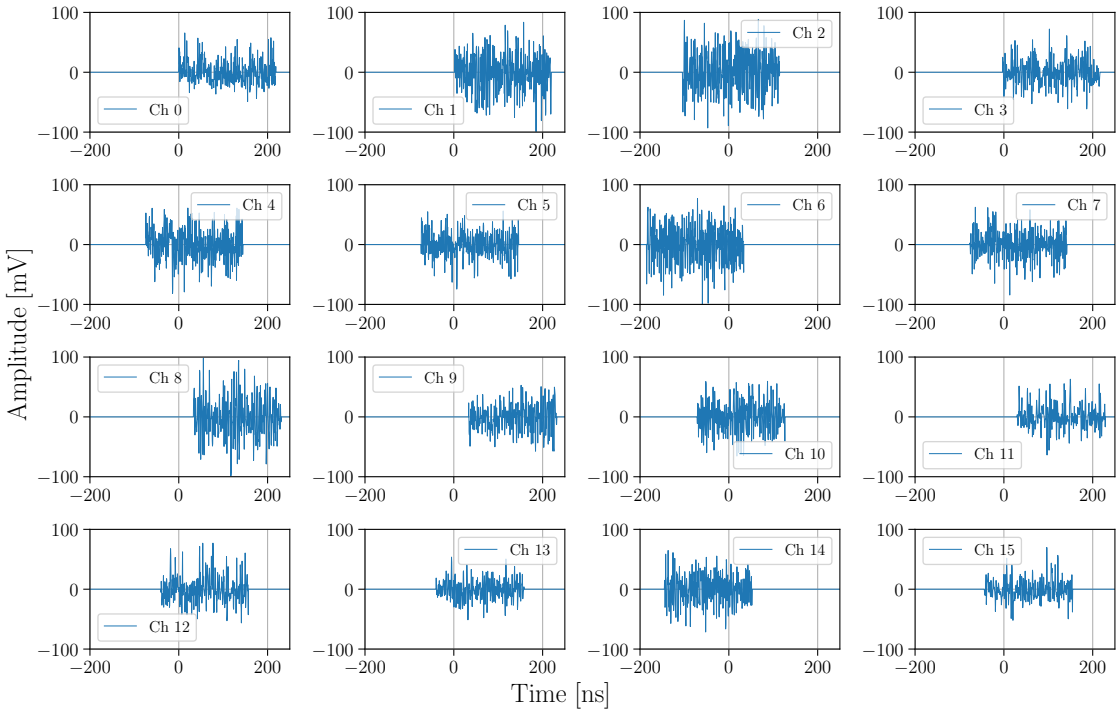

Figure 3.24: Example of a software trigger event recorded by A2. Channel 15 is broken.

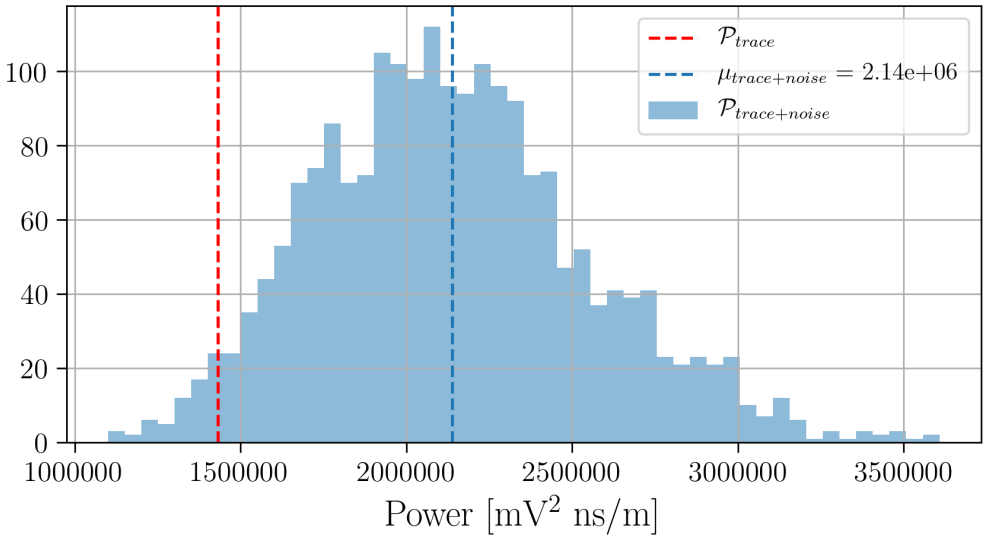

Figure 3.25: Example showing the distribution of noise subtracted peak.

information of each soft-triggered waveform, and not the average. We therefore use this method for our analysis.

Discrepancies across channels

We obtained the noise power distribution for each channel in A2, as can be seen in Figure 3.26, and noticed that there exist discrepancies across channels in measured power. Ideally the electronics response applied to each channel would be the same, but in reality there are some differences in amplifier gain and filters in the signal chain. At first order, this can be corrected for by normalizing all the distributions by their peak, and doing something similar for the power in SPICEcore events. A more targeted approach would be to correct for the noise figure of each channel, but unfortunately those data are not available.

Other considerations

The shadow zone corresponds to those regions in the ice from where we expect no signal due to the non-existence of ray-tracing solutions when one assumes a smooth exponential density profile for the index of refraction of the ice n_{ice}. This zone is represented by a red band in Figure 3.27, whereas the zone where solutions exist is represented by a blue band. This figure shows a receiver at about 180 m under the ice, and it can be seen in the figure that we expect them to not be observable at the receiver from depths above 500 m.

The assumption of an exponential depth dependent for n_{ice} is an simplified case, and signals from such "forbidden" regions have been observed [93]. However, ray-tracing codes are written under that assumption to simplify calculations and speed-up Monte Carlo simulations of Askaryan detectors.

Because our ray-tracing algorithm has that limitation, and because we do not entirely understand the shadow zone, we perform our study for depths greater than 600 m. Another reason to use depths>600 m is that the direct and reflected/refracted pulses start to merge for shallower depths, due to their traveling times becoming comparable, rendering our peak isolating algorithm unreliable. An example of this can be seen in the waveforms on Figure 3.28.

On the other hand, as was described in Subsection 2.4.2, it was noticed that triggers were not observed by the receiver after the pulse was lowered below $\sim$ 1300 m. For this reason we limited our study to depths less than 1100 m.

3.3.2 Results

The polarization reconstruction algorithm was initially implemented for run 012559, which was taken on December 24th of 2018. We chose that run as it was one of the runs where the SPICEcore pulser was clearly seen by A2 (some of the runs were attenuated so that

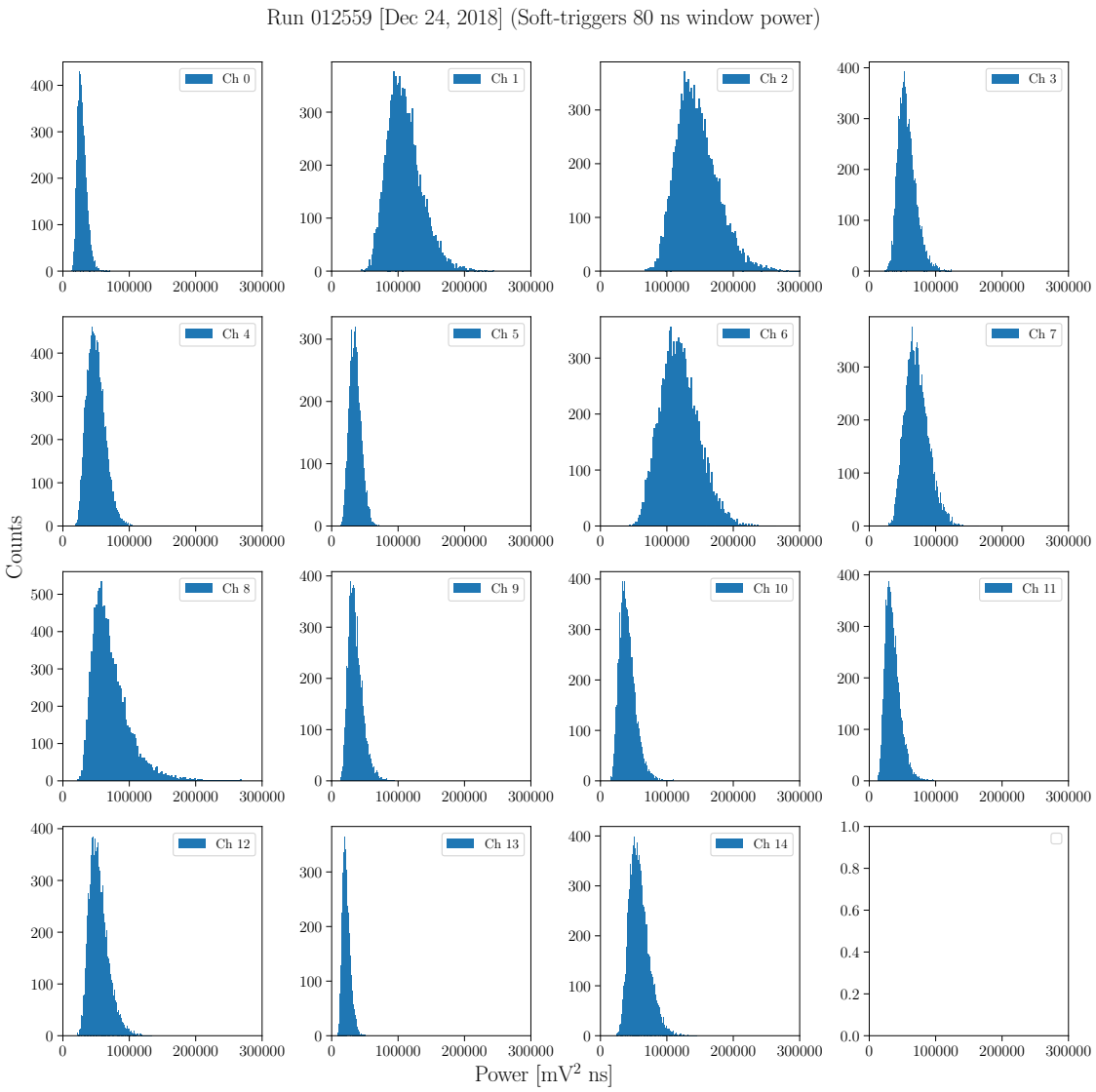

Figure 3.26: Distribution of (deconvolved) integrated power within an 80 ns window for software-triggered events . Ideally, one expects the power distributions to be very similar for noise, with variations of the order of few percent as they undergo through the same signal chain. As it can be seen, that is not the case for all channels.

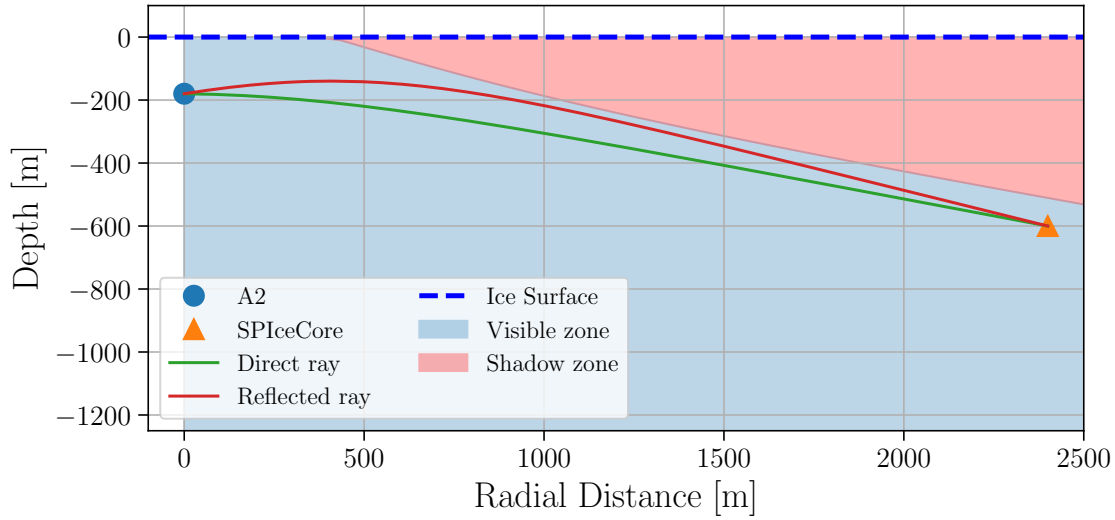

Figure 3.27: Visible (blue band) and shadow (red band) zones for A2 (blue circle). Pulses emitted from the SPICEcore pulser (orange triangle) start to become not observable from pulser depths above ~ 500 m, according to our ray-tracing method.

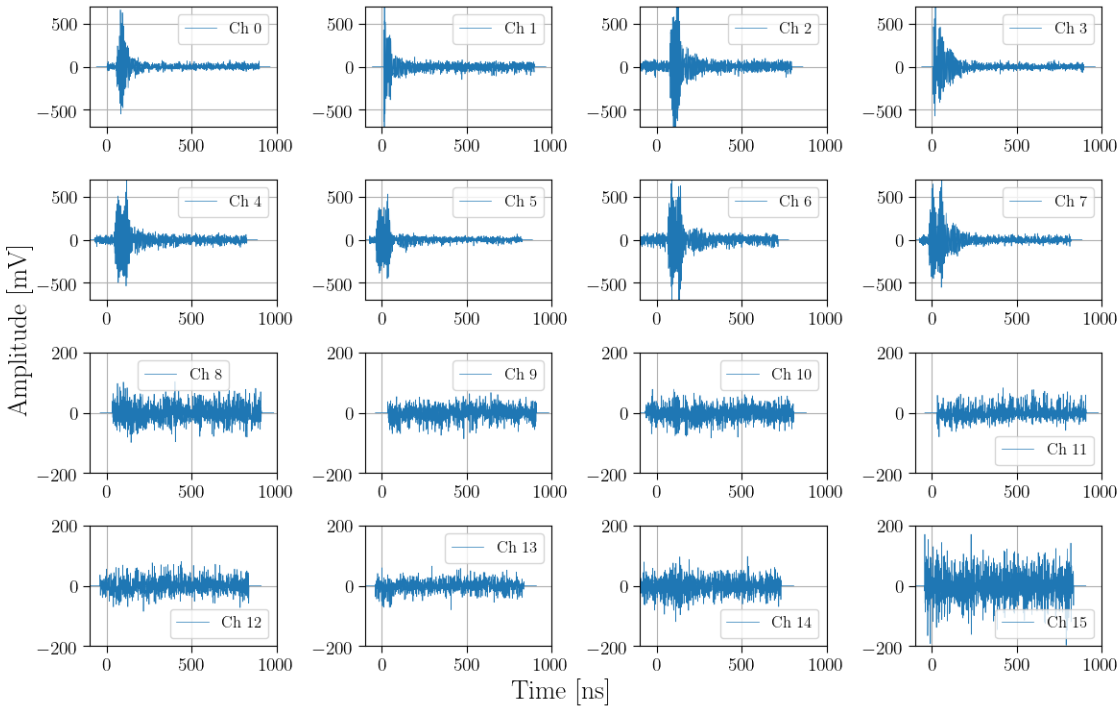

Figure 3.28: Example of an pulser event emitted from a pulser depth of ~ 600 m. As it can be seen in channels 6 and 7, for example, the direct and reflected/refracted signals start to merge and our algorithm is not reliable at isolating peaks anymore.

they could be measured by the nearby ARIANNA station), and there was no strong radio interference as in other runs (we believe some of the data is contaminated from radio signals emitted by a snowmobile).

We were able to observe the pulser clearly for all the Vpol channels, as it can be seen in Figure 3.22. Because of the cross-polarization measured by ARIANNA [91], we expect to observe an Hpol component in ARA. However, the pulse was not evident for any of the Hpol channels for none of the events in that particular run. We investigated this by imposing an SNR cut that would reject all events whose Hpol channels were smaller than certain value. We tried this with the condition SNR$>$ 5 for all Hpol channels, but this just returned events with high noise fluctuations. We continued to decrease the cut, but no events with a clear pulse in the Hpol channels were found by eye. Collaborator Dave Besson mentioned that signal averaging methods could be able to reveal the signal, but these were not implemented for this work.

We also calculated the power in the 80 ns window that we discussed previously as a function of depth. The ARIANNA collaboration measured the transmitter polarization, finding a cross-polarization component of about 10% in power [91], and so we expect signals in the Hpol channels to become more prominent as the pulser is lowered. This can be seen in Figure 3.29 and Figure 3.30. From these figures, it is evident that there is a clear pattern for the Vpol channels: the power decreases as the depth increases. This is expected from both a polarization perspective (the polarization vector becomes less vertical), and due to the amplitude attenuation (the field amplitude decreases as $1/R$). On the other hand, it is not evident that there is a clear trend for the Hpol channels. Moreover, the trend seems to be different across channels.

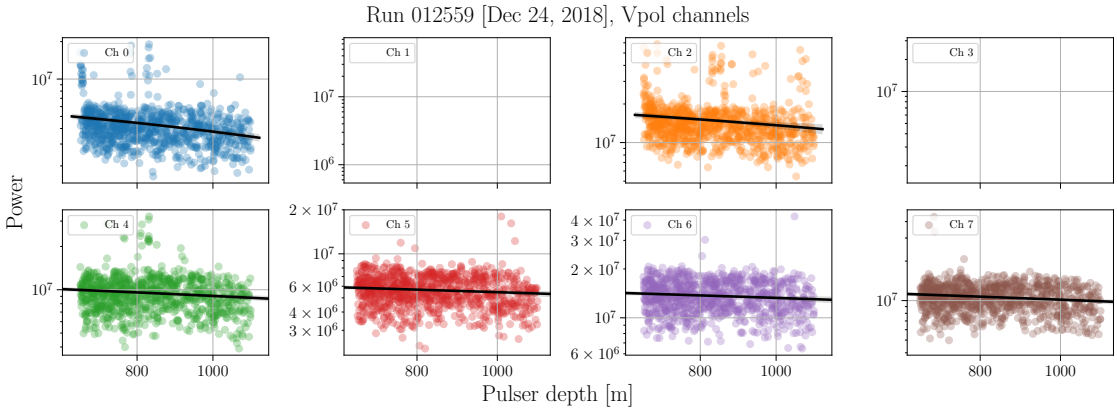

Figure 3.29: Vpol power

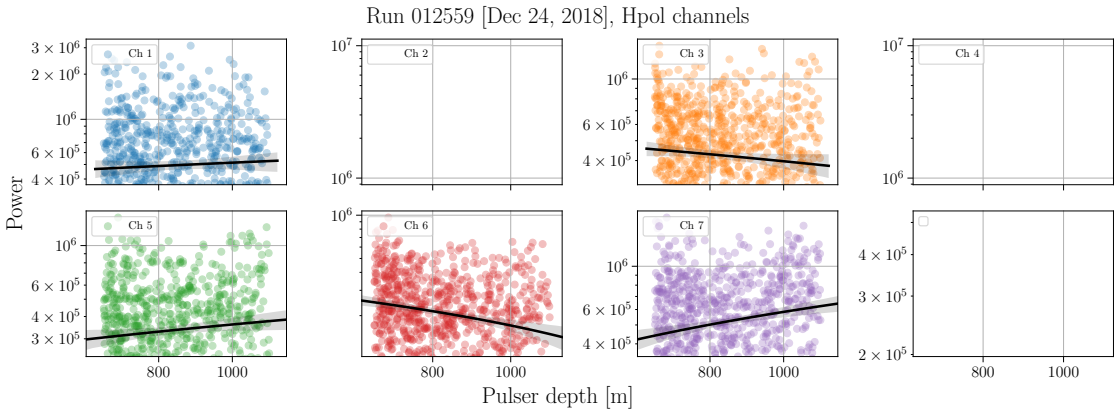

Figure 3.30: Hpol power

We estimate the resolution on Ω by calculating the expected polarization at the antenna with the assumption of a 100% Vpol transmitter and comparing to the measured polarizations. The expected Ω is calculated by setting $R = 0$ in Equation 3.16 and taking the inverse cosine of the resulting quantity. The results are shown in Figure 3.31.

Further studies are needed to understand the behavior we observe for the Hpol channels. A more sophisticated noise subtraction method could extract the signal from the Hpol channels and therefore estimate Ψ. Other explanations involve ice effects such as birefringence, which are currently under study by the ARA collaboration.

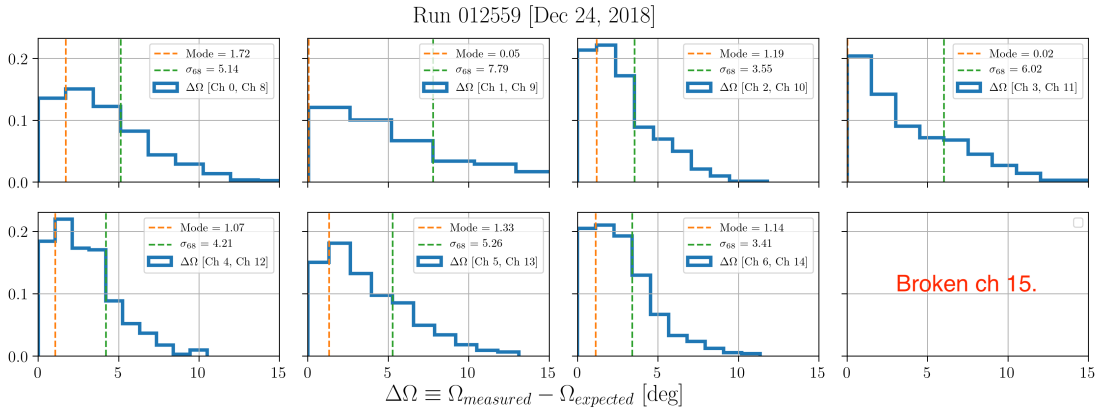

Figure 3.31: Resolution on the polarization angle Ω.

3.4 Implications for neutrino directional reconstruction

From our work with simulations, we are now able to estimate how well the ARA experiment can constrain the source of a neutrino event under certain conditions. We have not yet studied what resolution ARA would have on the viewing angle, but, as explained in Subsection 1.3.3, the amplitude of the signal is expected to fall in a Gaussian manner [6]. This implies that we can constrain the viewing angle to be less than a few degrees away from the Cherenkov angle in the ice $\theta_C = 55.8°$. From the same principle, one can determine the viewing angle by measuring the frequency content of the arriving signal at the antenna. This presents, however, a series of challenges as part of the frequency information is lost when the signal filtering happens, and when the antenna response is folded (currently it is impossible to build an antenna that has uniform response over the entire bandwidth). Also, thermal noise and interference between signals make the signal reconstruction more difficult. Techniques that use information field theory for the reconstruction of the signal frequency content are currently being developed by Welling, *et. al.* [94].

The angular vertex reconstruction (via the interferometry method) resolution has already been studied, yielding sub-degree resolution. This angle is, however, different from the launch angle, which is needed for the neutrino reconstruction. To obtain the launch angle one needs to trace the ray back to its source, which requires knowledge of the distance between the detector and the vertex. We currently do not have a method to calculate the vertex distance, but from simulations we can estimate the difference between the launch angle and the receiving angle. Figure 3.32 shows how the launch angle as a function of the receiving angle for a set of neutrinos simulated at all depths (emitted from a fixed source at $\phi_\nu = 0°, \theta_\nu = 48.22°$), and only using the direct solution. As expected, nearly-horizontally ($\theta_{\text{launch}} \sim 0$) traveling rays are expected to suffer less bending than rays that are more vertical. We also expect rays that originate deep in the ice, where the index of refraction does not change as dramatically as near the firn (c.f. Figure 2.18), to suffer less bending for a deep receiver. We can therefore also take the error on the launch angle to be of few degrees. Of course, this becomes more complicated if we consider reflected/refracted rays, but this is beyond the scope of this work.

If we assume that the polarization resolution is about 6°, based on our previous work, we have two parameters (the viewing angle and the launch angle) that we can vary to study their effect on the resolution on neutrino directional reconstruction. To study how the change in these parameters influence the neutrino directional reconstruction we use `AraSim` to simulate about 15,000 triggered neutrinos of energy $E_\nu = 10^{18}$ eV coming from a fixed source but interacting at different depths in the ice. We use the MC truth variables that are stored in the `Report` class of the `AraSim` output for the polarization vector at the antenna (`Pol_vector`), the viewing angle (`view_ang`), the launch angle at the vertex (`launch_ang`),

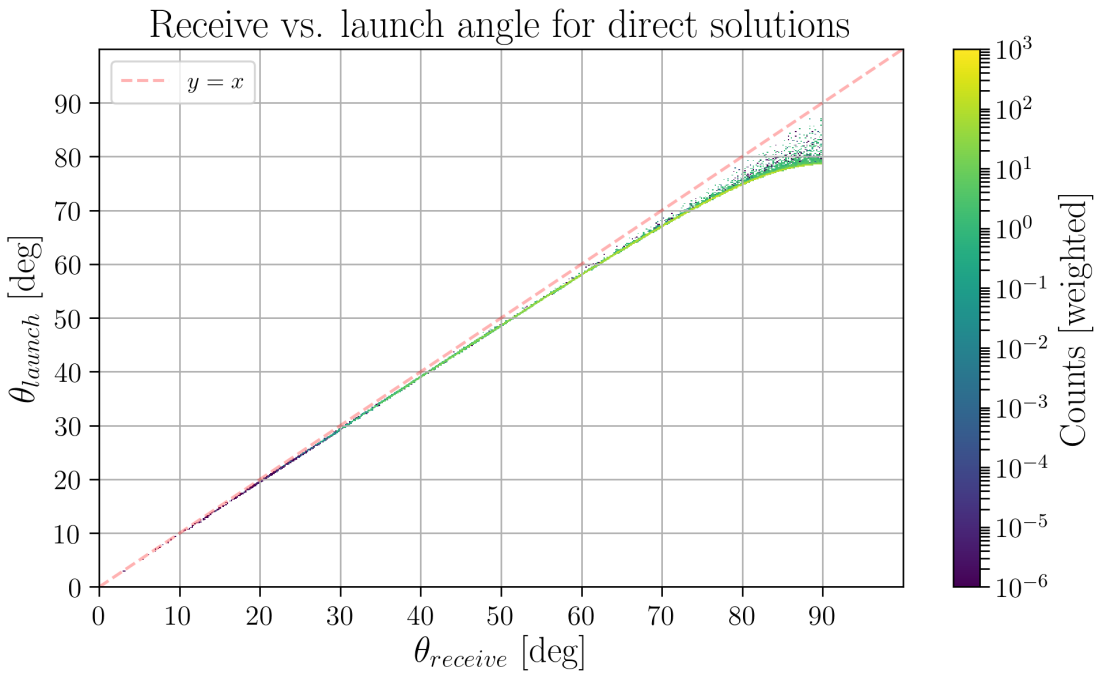

Figure 3.32: Launch angle vs. receiving angle at the antenna for simulated direct solutions for simulated neutrinos from a fixed source and an ARA antenna at a depth of approximately 200 m.

and the receiving angles at the antenna (`theta_rec, phi_rec`) for the direct solution. Note that `Pol_vector` is the polarization vector at the antenna, so this needs to be rotated to account for ray-bending. We do this by finding the matrix that transforms the launch vector to the receiving vector, and consequently rotating `Pol_vector` by the same matrix.

To find the neutrino direction, we use Equation 3.2:

$$\hat{v} = \sin\theta_{\text{view}}\hat{p} - \cos\theta_{\text{view}}\hat{\ell}$$

As a sanity check we use the MC truth variables that we obtained from `AraSim` to obtain the neutrino direction. Because `AraSim` returns the neutrino momentum, we invert the z-component of the neutrino momentum so it points back to the neutrino source, and we then compare it with the true value that we used as the neutrino source. This is a validation of the simulation, and it can be seen in Figure 3.33 that there is good agreement between the true value and the reconstructed value.

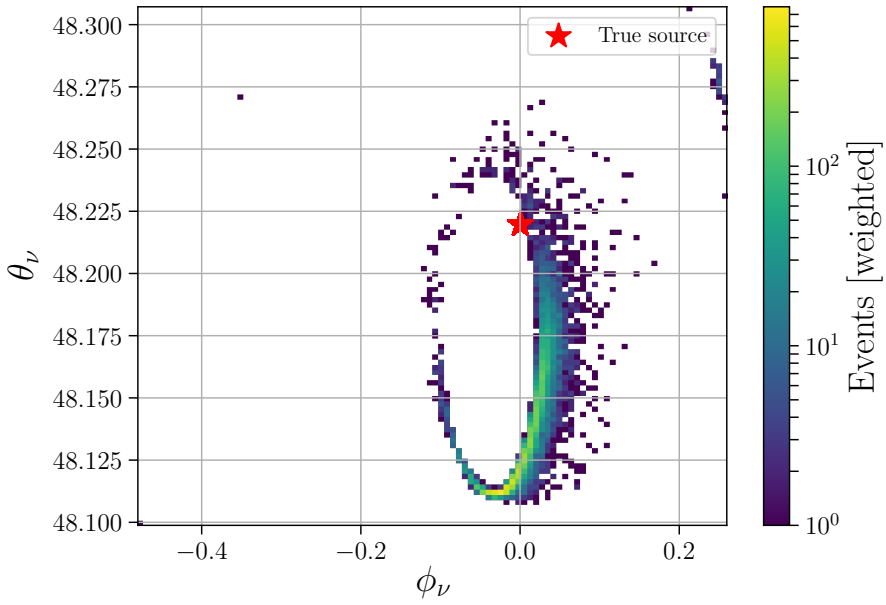

Figure 3.33: Reconstructed coordinates of the neutrino source by using the inverse Monte Carlo approach with no noise added. As expected, they reconstruct to the true source.

We introduce a Gaussian error on the variables used to reconstruct the neutrino direction with a standard deviation equal to the resolution of the variables that we want to study. As an optimistic scenario for the viewing angle resolution, we use $\Delta\theta_{\text{view}} = 1^\circ$ and

$\Delta\theta_{launch} = 1°$, but we use the value of $\Delta\Omega = \Delta\Psi = 6°$ that we obtained from the simulation work. Figure 3.34 shows the probability density function (PDF) of the distribution of reconstructed directions for this optimistic scenario. This figure was obtained through a Gaussian smoothing with a Kernel Density Estimator (KDE) [92], which returns the probability density. The x-axis corresponds to the azimuth angle of the neutrino direction, the y-axis corresponds to the cosine of the zenith arriving angle, and the z-axis (in color) corresponds to the value of the PDF at each particular point. The red star locates the truth neutrino source and the green cross indicates the point at which the PDF has its maximum value. The expected "banana" shape can be seen in the yellow area.

Figure 3.35 corresponds to a corner plot [26] displaying the angular distribution of the arriving events along with their projections along the ϕ_ν and $\cos\theta_\nu$ axes. The dashed lines in the projections enclose 68% of the data and correspond to the confidence intervals on top of the panel for each projection. The intersection of the orange lines correspond to the true value of the neutrino source. Table 3.1 shows the 68% C.L. on the neutrino source estimation ($\Delta\phi_\nu$, $\Delta\cos\theta_\nu$), and plots for each different entry on the table are located in Section B.4.

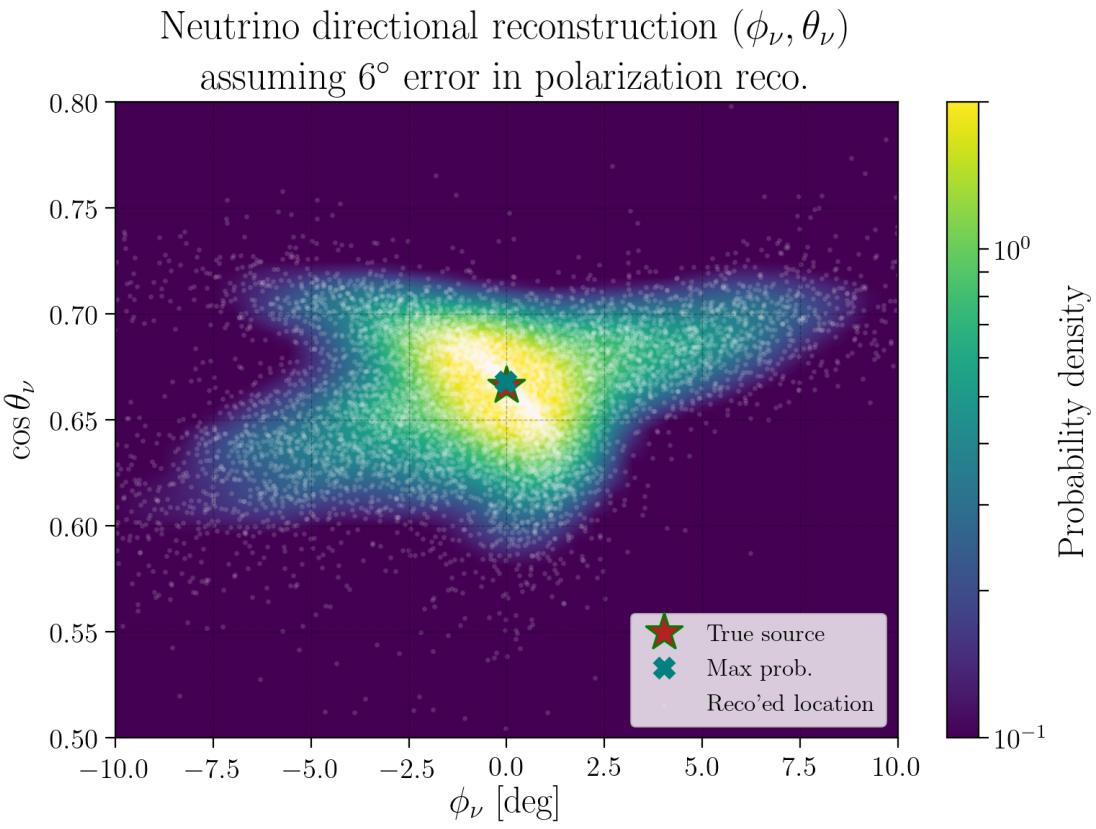

Figure 3.34: KDE of the neutrino directional distribution for $\Delta\theta_{\text{view}} = 1°$, $\Delta\theta_{launch} = 1°$, $\Delta\Psi = \Delta\Omega = 6°$.

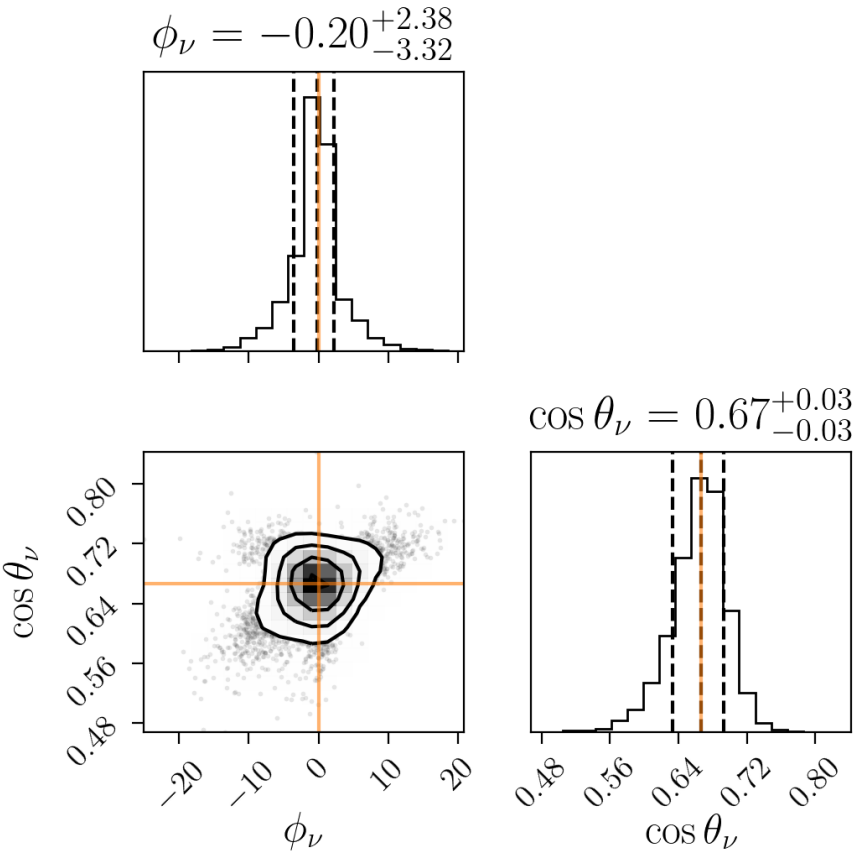

Figure 3.35: Corner plot of the neutrino directional distribution for $\Delta\theta_{\text{view}} = 1°$, $\Delta\theta_{launch} = 1°$, $\Delta\Psi = \Delta\Omega = 6°$. Made with `corner.py` [26]

$\Delta\Psi{=}\Delta\Omega$	$\Delta\theta_{launch}$	$\Delta\theta_{\rm view}$	$\Delta\phi_\nu$	$\Delta\cos\theta_\nu$
1.0	1.0	1.0	$0.007^{+1.036}_{-1.077}$	$0.667^{+0.018}_{-0.018}$
1.0	1.0	5.0	$0.001^{+2.091}_{-2.080}$	$0.666^{+0.059}_{-0.065}$
1.0	1.0	10.0	$0.010^{+3.630}_{-3.747}$	$0.667^{+0.110}_{-0.129}$
1.0	5.0	1.0	$0.087^{+3.951}_{-4.261}$	$0.667^{+0.060}_{-0.066}$
1.0	5.0	5.0	$0.088^{+4.438}_{-4.917}$	$0.667^{+0.082}_{-0.092}$
1.0	5.0	10.0	$0.187^{+5.617}_{-6.343}$	$0.667^{+0.124}_{-0.148}$
1.0	10.0	1.0	$-0.045^{+7.631}_{-8.531}$	$0.669^{+0.111}_{-0.133}$
1.0	10.0	5.0	$0.294^{+7.716}_{-9.305}$	$0.668^{+0.123}_{-0.153}$
1.0	10.0	10.0	$0.334^{+8.509}_{-10.601}$	$0.673^{+0.146}_{-0.192}$
3.0	1.0	1.0	$-0.059^{+1.509}_{-1.708}$	$0.667^{+0.022}_{-0.023}$
3.0	1.0	5.0	$-0.059^{+2.530}_{-2.546}$	$0.666^{+0.061}_{-0.066}$
3.0	1.0	10.0	$-0.059^{+3.957}_{-4.033}$	$0.666^{+0.111}_{-0.131}$
3.0	5.0	1.0	$-0.086^{+4.111}_{-4.540}$	$0.667^{+0.061}_{-0.068}$
3.0	5.0	5.0	$-0.001^{+4.643}_{-5.229}$	$0.668^{+0.083}_{-0.093}$
3.0	5.0	10.0	$0.059^{+5.792}_{-6.497}$	$0.667^{+0.124}_{-0.146}$
3.0	10.0	1.0	$0.080^{+7.649}_{-8.907}$	$0.665^{+0.114}_{-0.132}$
3.0	10.0	5.0	$0.259^{+7.661}_{-9.393}$	$0.666^{+0.123}_{-0.152}$
3.0	10.0	10.0	$0.481^{+8.478}_{-10.669}$	$0.666^{+0.150}_{-0.194}$
6.0	1.0	1.0	$-0.182^{+2.354}_{-3.243}$	$0.666^{+0.029}_{-0.036}$
6.0	1.0	5.0	$-0.299^{+3.437}_{-3.708}$	$0.663^{+0.067}_{-0.070}$
6.0	1.0	10.0	$-0.333^{+4.744}_{-4.829}$	$0.662^{+0.113}_{-0.132}$
6.0	5.0	1.0	$-0.155^{+4.636}_{-5.363}$	$0.665^{+0.065}_{-0.075}$
6.0	5.0	5.0	$-0.166^{+5.043}_{-6.078}$	$0.664^{+0.087}_{-0.097}$
6.0	5.0	10.0	$-0.135^{+6.229}_{-7.215}$	$0.666^{+0.126}_{-0.151}$
6.0	10.0	1.0	$-0.017^{+7.868}_{-9.492}$	$0.665^{+0.115}_{-0.139}$
6.0	10.0	5.0	$0.221^{+7.903}_{-10.387}$	$0.664^{+0.127}_{-0.152}$
6.0	10.0	10.0	$0.280^{+8.718}_{-11.286}$	$0.661^{+0.151}_{-0.192}$
10.0	1.0	1.0	$-0.541^{+3.578}_{-5.885}$	$0.665^{+0.037}_{-0.059}$
10.0	1.0	5.0	$-0.746^{+4.715}_{-6.041}$	$0.659^{+0.074}_{-0.082}$
10.0	1.0	10.0	$-0.856^{+6.281}_{-7.019}$	$0.654^{+0.122}_{-0.136}$
10.0	5.0	1.0	$-0.584^{+5.606}_{-7.799}$	$0.663^{+0.070}_{-0.086}$
10.0	5.0	5.0	$-0.603^{+6.364}_{-7.967}$	$0.655^{+0.093}_{-0.106}$
10.0	5.0	10.0	$-0.691^{+7.456}_{-8.798}$	$0.655^{+0.132}_{-0.157}$
10.0	10.0	1.0	$-0.364^{+8.477}_{-11.739}$	$0.663^{+0.115}_{-0.147}$
10.0	10.0	5.0	$-0.105^{+8.812}_{-11.946}$	$0.658^{+0.127}_{-0.161}$
10.0	10.0	10.0	$-0.133^{+9.978}_{-13.198}$	$0.658^{+0.158}_{-0.198}$

Table 3.1: Estimated central value and errors (68% C.L.) for the neutrino directional reconstruction for different uncertainties in the polarization angle, launch angle and viewing angle.

Chapter 4

Point-source neutrino search with ARA

Unlike a diffuse source, for a point-source search we limit the area on the sky in which our analysis is performed around a celestial object that has the potential to produce UHE neutrinos. A condition for likely astrophysical neutrino sources is that they also be sources of UHECRs. Some specific sources believed to produce UHE neutrino emission are the following:

- Active galactic nuclei (AGNs): these are galaxies whose nucleii are sources of radiation (radio, X-ray photons), or that have luminous relativistic jets originating from their nucleus and that can be detected via radio, X-rays, optical and/or γ-rays. The jets are powered by mass accretion onto a super-massive black hole. A sub-category of AGNs are blazars, which have one jet pointed near the line of sight of the Earth. The electromagnetic emission from blazars can be explained by hadronic models, which can also explain neutrino production [95]. This, along with their high-luminosity, makes them excellent neutrino source candidates. Moreover, the observation of high-energy neutrinos from the direction of the blazar TXS 0506+056 [46] by IceCube provides strong evidence of this. The detection of AGNs as neutrino point-sources would be a smoking gun for hadronic production, as neutrinos can only be produced by hadronic interactions (unlike photons). AGNs are also promising candidate point-sources of UHECRs.

- Gamma-ray bursts (GRBs): These can be short (< 2 s) or long-lasting (> 2 s) phenomena that are associated with core collapse supernovae (long GRBs) and with the merger of compact objects such as neutron stars and/or neutrino stars and a black hole (short GRBs). GRBs are detected by satellites such as Swift [96] and Fermi [97]. GRBs have been suggested as sources of UHECRs and UHE neutrinos by Waxman and Bahcall [98] following the acceleration of protons to energies of $\sim 10^{20}$ eV, but data from IceCube has found no coincident neutrino emission from 1,172 studied

GRBs [99]. These were, however, GRBs that triggered satellites, which leave low luminosity GRBs as potential UHE neutrino and UHECRs sources [100].

- Tidal disruptions events (TDE): produced when a star approaches very close to a super-massive black hole and is tore apart. It has been proposed that TDEs can be accelerators of UHECRs [101], and also that shocks similar to those observed in GRBs can lead to the production of neutrinos [102].

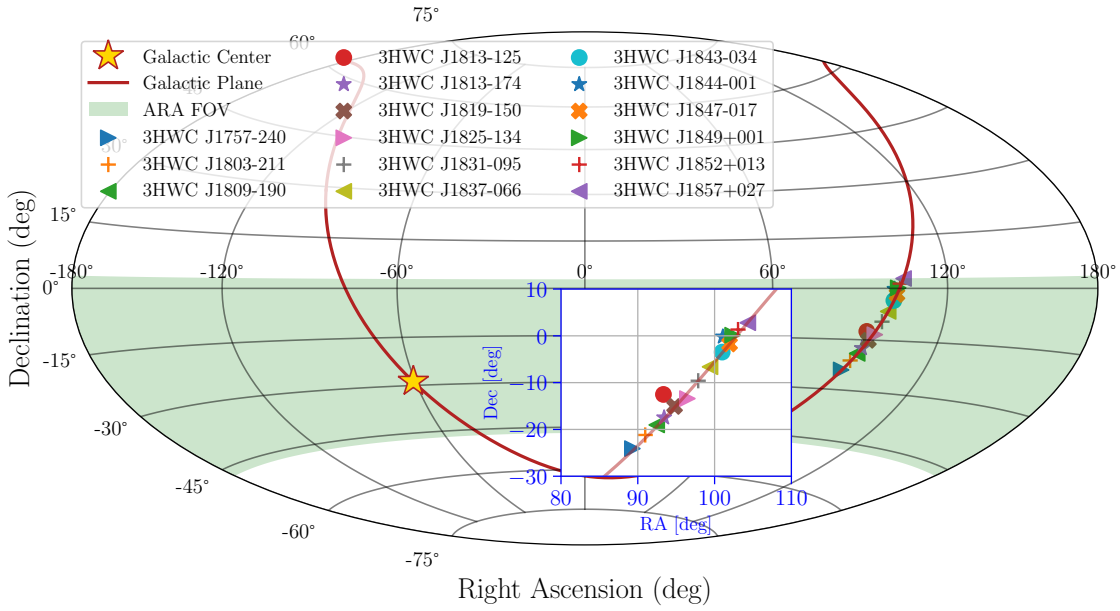

Figure 4.1: Third HAWC catalog of sources with very-high-energy gamma-ray emission [27] in equatorial coordinates. Only sources that fall in ARA's field-of-view were included on this plot.

4.1 Point-source search with ARA

As stated previously, ARA sees about 60% of the Southern Sky. Figure 4.1 shows ARA's FOV in a green band, along with very-high-energy gamma-ray sources form the third HAWC catalog [27]. This limitation narrows down the number of sources we can study in our analysis.

For this study, we chose Centarus A (Cen A) to be the celestial object for which the point-source search would be targeted. This choice was driven by the fact that Cen A is in the field-of-view (FOV) of ARA, and by works by Cuoco *et. al.* [103], and Kachelriess *et. al.* [104]. These suggest that Cen A is a potential candidate for the emission of UHECRs and UHE neutrinos. Additionally, the Pierre Auger Observatory detected two UHECRs close to Cen A [105].

Cen A is located in the Southern sky at an altitude of about 43° from the perspective of an observer at the South Pole. Because ARA is located at the South Pole, Cen A's altitude with respect to ARA remains nearly constant (at least for our purposes), whereas its azimuth angle completes a cycle every 24 hours.

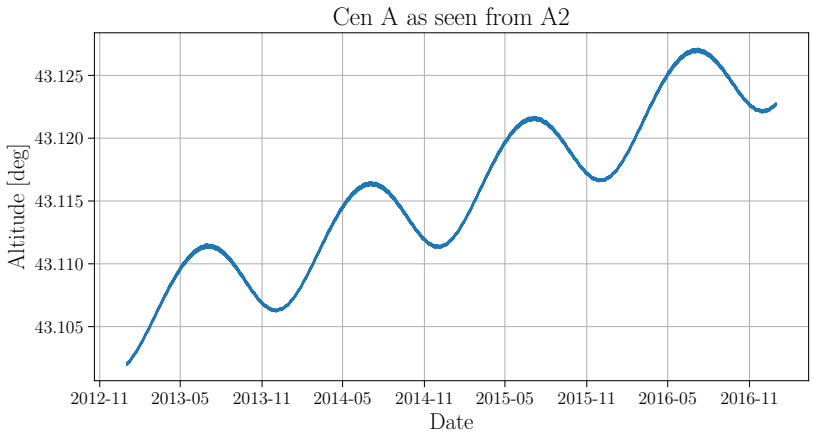

Figure 4.2: Altitude of Cen A as seen from A2 plotted for the dates that will be used for the point-source analysis.

4.1.1 Preliminary estimations

We can estimate the threshold reduction that we can achieve for a source search by using the results that we obtained from the diffuse search. For a diffuse search, neutrinos, as well as RF background noise, may originate from any direction. This requires us to impose the stringest cuts on signal SNR, for example. For a transient point-source search, one can loosen the cuts by restricting the timing, i.e., choosing a time window for which we think that the transient event happened and reject events outside of it. This will allow us to limit the number of RF backgrounds by a factor dictated by the size of the window. For steady sources, which are the main focus of this work, one can instead use a cut on the direction of the incoming signal. This allows us to constrain the search area on the sky,

and consequently also allows us to reduce the number of backgrounds. Intuitively, this is because we also limit the area on the sky from which backgrounds and anthropogenic noise (from the South Pole station, for example) originate.

In previous ARA analyses, a data-driven exponential model for the number of background events has been used, in which an exponential function is fitted to the tail of the distribution of events passing the final cut of the analysis. For the latest ARA analysis, this corresponds to the differential number of events rejected by the bivariate plane cut (SNR vs C_{sky}), also named RCut (which is detailed later in Subsection 4.2.4), as a function of the SNR value (y-intercept), as shown in Figure 4.3. The exponential fit to the differential distribution is a function of the form $f(SNR) = e^{\beta_1 SNR + \beta_2}$, where $\beta_1 < 0$ and corresponds to the slope of a line on a log-linear plot, and β_2 corresponds to its intercept. The fit was chosen to start mid-way between the peak and the end of the tail.

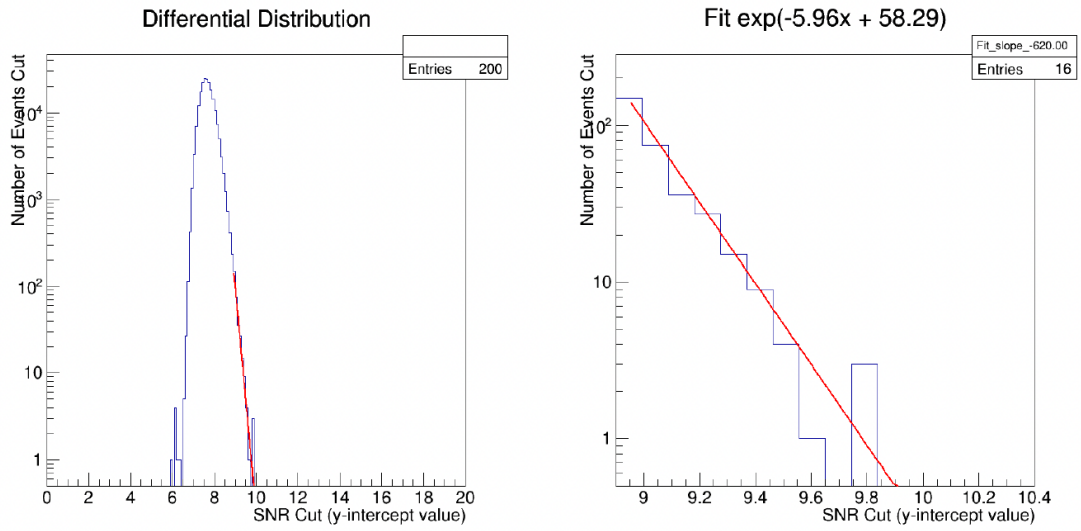

Figure 4.3: Figure by Brian Clark [28]

We can estimate the number of background events N_{bkg} that will pass the selected cuts for a given value of the SNR cut (let us call it y_i) by integrating the exponential model from y_i to infinity:

$$N_{bkg} = \int_{y_i}^{\infty} d(SNR) e^{\beta_1 SNR + \beta_2} = -\frac{1}{\beta_1} e^{\beta_1 y_i + \beta_2} \equiv a e^{\beta_1 y_i}, \tag{4.1}$$

where we have defined $a \equiv -\frac{e^{\beta_2}}{\beta_1}$.

We are interested in knowing how much we can reduce the threshold for analysis cuts

by constraining either the direction or the timing of the events. The analysis threshold is controlled by the SNR cut, so we can reduce the search threshold by decreasing the SNR cut. If we require N_{bkg} to be the same for the point source as for the diffuse search, we can estimate by how much the threshold can be reduced, i.e. where will the new cut on the y-intercept (y_i') will fall. Without loss of generality, for a constrained (either direction or timing) source search we can assume that the number of background events in the constrained region can still be modeled with an exponential function with the same parameters. Furthermore, since we expect our RF backgrounds to be isotropic, we can take the number of background events will be reduced by a factor α, and $\alpha = \frac{a'}{a}$. Again, for the same N_{bkg} we have

$$N_{bkg} = a' e^{\beta_1 y_i'} \tag{4.2}$$

This expression is equivalent to the last expression in Equation 4.1, so we get

$$a e^{\beta_1 y_i} = a' e^{\beta_1 y_i'} \tag{4.3}$$

$$\implies \log\left(e^{\beta_1 y_i}\right) = \log\left(\alpha e^{\beta_1 y_i'}\right) \tag{4.4}$$

Equation 4.4 can be rearranged to give

$$y_i - y_i' = \frac{\log(\alpha)}{\beta_1} \tag{4.5}$$

Note that since we expect $\alpha \leq 1$, $\log(\alpha) \leq 0$ and then both sides of Equation 4.5 are always positive, and equal to zero when $\alpha = 1$.

Threshold reduction with interferometric reconstruction

I performed an investigation on how far we can reduce the analysis threshold by reconstructing the neutrino direction with the interferometric technique. As we explained in Chapter 3, we use the interferometric technique to reconstruct the direction that points to the neutrino interaction vertex, but not the source in the sky. Although just using the interferometric method yields favorable results, we can further reduce the analysis threshold by better constraining the neutrino direction once methods are developed. I quantified the threshold reduction if we only use the interferometric method by estimating the area on the sky that could be constrained if we take the 68% of simulated events to be inside the search window.

I simulated events from Cen A with an energy spectra given by the predicted flux from Cen A in [103]. All events that triggered the detector were reconstructed using the interferometric technique, and no cuts were applied at all. Each event has a peak correlation factor C_{sky} for both direct and reflected/refracted solutions, but we only used the direct

solutions' peak C_{sky} as a proxy for the neutrino direction, and only the reconstructed RF peak locations from the Vpol channels were considered. This can be seen in Figure 4.4.

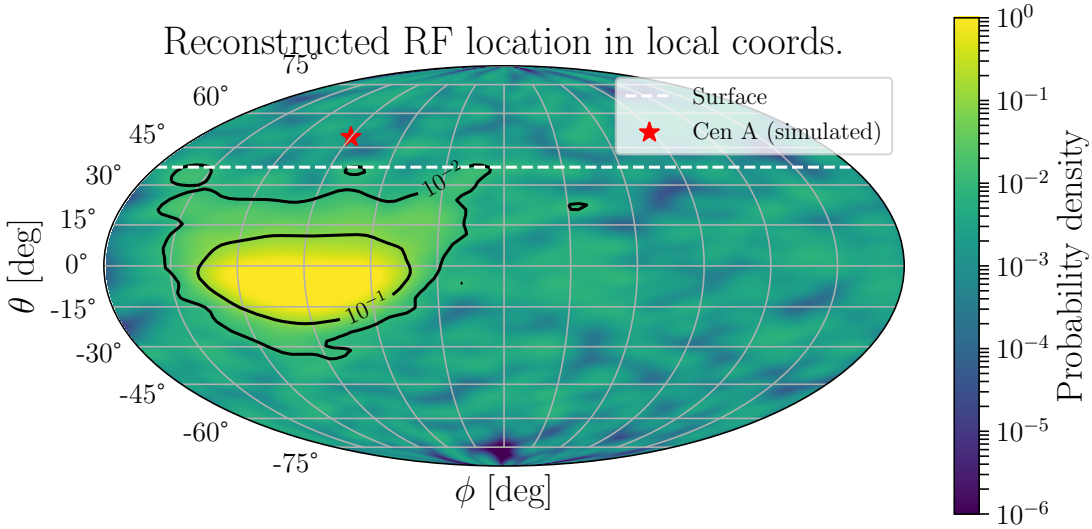

Figure 4.4: Reconstructed direct signal peak C_{sky} with interferometry method for only VPol channels from simulated neutrinos generated at a fixed point in the sky.

Although ARA cannot see neutrinos from all over the sky due to neutrino absorption and detector sensitivity, the antennas can observe backgrounds in a 4π solid angle. We can then estimate α by taking the ratio of the area that encloses 90% of the simulated events in Figure 4.5 and the 4π aperture. The area was calculated by taking the product of $\cos(\theta_{\max}) - \cos(\theta_{\min})$ and $\phi_{\max} - \phi_{\min}$ as defined by the edges of the box. The resulting area is $a' = 29.03°$.

One can calculate α using this information:

$$\alpha = \frac{a'}{a} = \frac{(\cos\theta_{max} - \cos\theta_{min})(\phi_{max} - \phi_{min})}{4\pi} \tag{4.6}$$

$$= 0.027 \tag{4.7}$$

Using Equation 4.5 and the calculated value of β_1 for the A2 diffuse analysis, we can

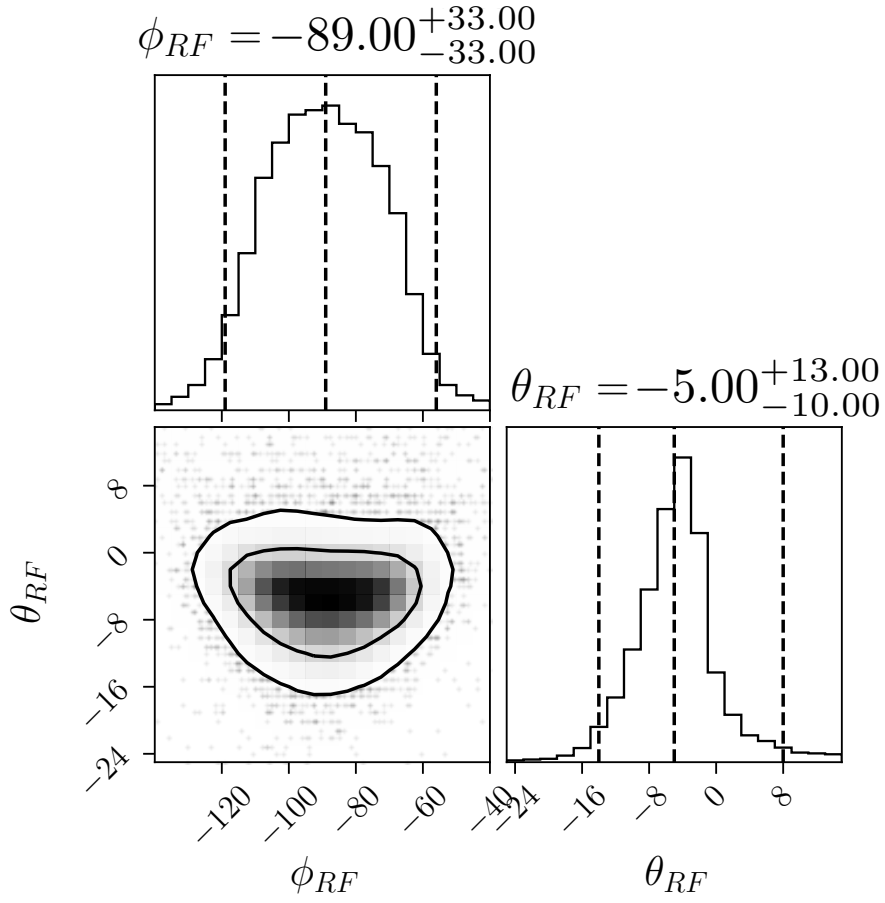

Figure 4.5: Corner plot of the reconstructed RF sources for simulated neutrinos from Cen A. The dashed lines indicate the 90% confidence limits, quantified on top of each distribution.

estimate the threshold reduction:

$$y_i - y_i' = \frac{\log(\alpha)}{\beta_1} \tag{4.8}$$

$$= \frac{\log(0.027)}{-5.96} \tag{4.9}$$

$$= 0.61 \tag{4.10}$$

This reduction in the SNR cut allows more events to pass the final bivariate cut, increasing the analysis efficiency. The analysis efficiency is calculated as the number of neutrino events that pass all of the cuts divided by total number of triggered neutrinos, and it is usually plotted as a function of SNR or neutrino energy. This can be seen in Figure 4.6. For different values of error in the neutrino directional reconstruction, we calculate the analysis efficiency. As it can be seen, there is improvement as we better resolve the neutrino

direction.

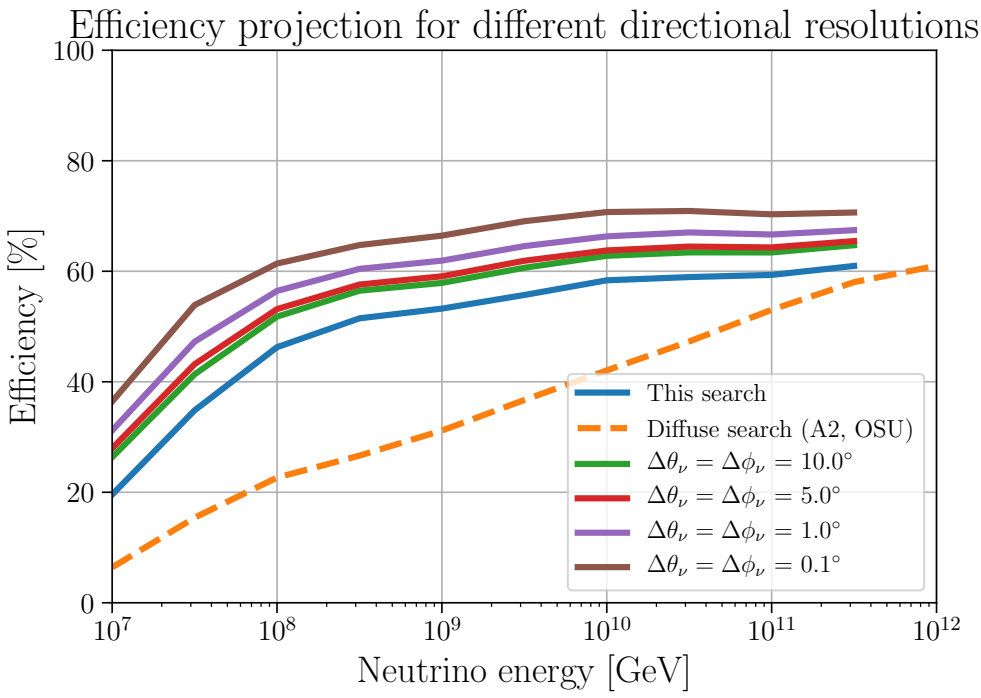

Figure 4.6: Analysis efficiency plotted as a function of energy and SNR. Each different line corresponds to a different neutrino directional resolution.

4.1.2 Model selection and simulation

We decided to use one of the models in Kachelriess *et. al.* paper [104] for our energy spectrum. This because the model proposed by Cuoco *et. al.* [103] predicts that a few neutrinos would have been already detected by IceCube. The chosen model is consistent with no observation of UHE neutrinos from Cen A by current neutrino observatories.

To optimize our cuts to achieve the best sensiticvity, we simulate approximately 17k triggered neutrinos following the flux model for neutrinos emitted near the core of Cen A with a spectrum $dN/dE = E^{-2}$ for the injected protons from the work by Kachelriess *et. al.* paper [104]. It is important to mention that this model contains significant uncertainties that arise from the fact that the neutrino flux is normalized based on the assumption that two protons observed by the Pierre Auger Observatory originate from CenA [105], which is uncertain.

4.2 Data analysis

We will perform a data analysis similar to the one performed in the diffuse search [11]. Since we will be searching for neutrinos with the same characteristics that the diffuse analysis was designed to detect, but in a constrained area of the sky, the same set of cuts (except the same final cut) will be applied but with the addition of one important cut. As was previously explained, this cut constrains the search to a particular area on the sky, which allows us to decrease the threshold. To set the placement of thhe cut, we will do a full optimization. In the next subsection we will briefly explain the different stages of the data analysis and how this optimization is done. Most of the analysis code described in this section was developed by my colleagues Brian Clark and Carl Pfenfder, and a detailed description of it can be found on Brian's thesis [28].

4.2.1 Data processing

Quality cuts

During the first stage of the analysis, DAQ self-triggered events such as calibration pulsers and software pulsers are removed. This is done by the functions in `AraRoot` `AraRoot::AraEvent::isCalpulserEvent` and `AraRoot::AraEvent::isSoftwareTrigger`, respectively. The former tags events by using a timing criterion, and the latter identifies events by checking their triggering information stored in the metadata.

Once all DAQ self-triggered events are rejected, a second class of events will follow suit: corrupted events due to digitizer glitches or system readout errors in the DAQ. Several cuts were designed by Ming-Yuan Lu [79] and Brian Clark [28] to address these kind of events, and those were included in `AraRoot` via the class `AraQualCuts`. Let us briefly describe them here:

- Short waveform cut: events correctly digitized should have blocks of 64 samples each, and should contain more than one block. Events that do not meet this criterion are rejected. Similarly, events that have less than 500 samples are also rejected. This last cut was chosen to also reject untagged software triggers.
- Timing error cut: it rejects events whose timing samples are not in order and consequently their times are not monotonically increasing.
- Block gap cut: normal events have blocks that are digitized in succession. Events that do not meet the condition `final block = first block + num readout blocks` are rejected.
- First five events cut: it was observed for A2 and A3 that the first five events of each run are generally corrupted after November 24, 2015 and the beginning of 2014,

respectively. For this reason, the first 5 events in a run are rejected.

- Offset block cut: events are calibrated to have a mean amplitude of zero. Occasionally, digitizer glitches lead to events whose mean is not zero during some duration in the middle of the waveform. These events are rejected by this cut.
- Bad spare channel cut: the ARA digitizer boards have spare channels that should not contain significant signal. Corrupted events can be identified when these unused channels exhibit a large root-mean-square voltage. These events are rejected.

Events remaining after all these cuts are applied enter the next stage in the analysis chain, where thermal noise events are identified and rejected.

Waveform RMS filter

More than 99.999% of ARA's data is due to thermal noise. The waveform RMS filter is a computationally inexpensive algorithm that rejects most of thermal noise events based on the difference between incidence angles across different baselines of the station. This cut rejects about 90% of the entire dataset, with a neutrino efficiency of about 95%.

CW events identification, filtering and rejection

The next stage includes cuts that are aimed at excluding anthropogenic events, these are events that are human-made by sources such as radio-communications from people at the South Pole, satellites communications, and weather balloon events (the most common occurrence). These kind of events often exhibit a continuous waveform behavior (excess of power in narrow frequency bands) and point to known sources. The following cuts were designed to address this kind of events.

Continuous waveform (CW) contamination appears more obvious in Fourier-space than in the time domain, as CW events have an excess of power in a narrow frequency band. To decide whether an event is contaminated with CW, the power spectrum is calculated for that event by using a Fast Fourier Transform (FFT) compared to the average power spectrum (baseline) of the run that contains the event. A particular frequency spectrum is tagged as CW noise if it meets the following to conditions (taken from the Testbed diffuse analysis [89]): 1. the spectral power exceeds 6 dB over the baseline for three or more channels of the same polarization, 2. if in a single channel less than 50% of the frequency bins in the neighboring 40 MHz have peaks that are 5.5 dB over the baseline. As a second filter, the phase variance technique is applied (c.f. Subsection 2.3.2), which relies in phase differences for CW events being close to constant between neighboring events.

Events that are tagged as being CW-contaminated go through a geometrical filter designed by Brian Daley for the ANITA experiment at Ohio State, where the contaminated

frequencies are filtered from the waveform. Events are reject if the third-largest amount of power removed in a waveform exceeds 6% of the original power. This is done to prevent cases where the filter removes excessive amounts of the original power in the waveform.

Reconstruction

The direction of the source of the incoming signals are calculated at this stage by using the interferometric technique described in Subsection 3.2.3. This stage is the most computationally expensive (about 1 second/event), and it is performed for all of the events in the 10% dataset. The location of the reconstruction peak (θ, ϕ) and the cross-correlation value at the peak are saved for later use. This is done for two hypotheses for the radial distance: 41 m (the distance to the calibration pulser) and 300 m. We reject any events that reconstruct to above the surface (called the surface cut, and it corresponds to about 37°), and events that reconstruct to known locations in the ice, such as the IceCube Lab (ICL). Events that reconstruct within a box centered at the calpulser locations of sides 15° in θ and 10° in ϕ are also rejected. This is the calibration pulser box cut to reject untagged calibration pulser events, and it can be seen in Figure 4.7. As this dissertation was being written, I was reminded that the surface cut was lowered to 17° during the final stage of the diffuse analysis, so I modified the cut so events that are above that angle are rejected. This is not reflected in some of the figures, but the final results have included that modification.

4.2.2 Distribution of backgrounds

After imposing our quality cuts, discarding thermal events, filtering CW events, and reconstructing the source of the remaining events, we have a final set of events that we call background events. We expect these events to be distributed all over the sky (with respect to A2), but to have no events reconstructing to above the ice surface, which corresponds to 37° above horizontal for a source hypothesis of 300 m in the interferometric technique. Figure 4.7 shows the angular distribution of these events along with locations of some landmarks with respect to A2. As it can be see, the distribution of events seems to have a θ-dependence. The stripe at about $-41°$ corresponds to cross-talk between the top and bottom antenna pairs on each string, as explained by my colleagues Brian Clark and Ming-Yuan Lu [28, 79]. We will choose our control sample accordingly, as described in the next subsection.

4.2.3 Control sample and neutrino box

Because further studies with data are needed to assess the true polarization reconstruction capabilities of ARA, we decided to be conservative and assume nothing about the polarization angle resolution. There is room for improvement once we can determine the

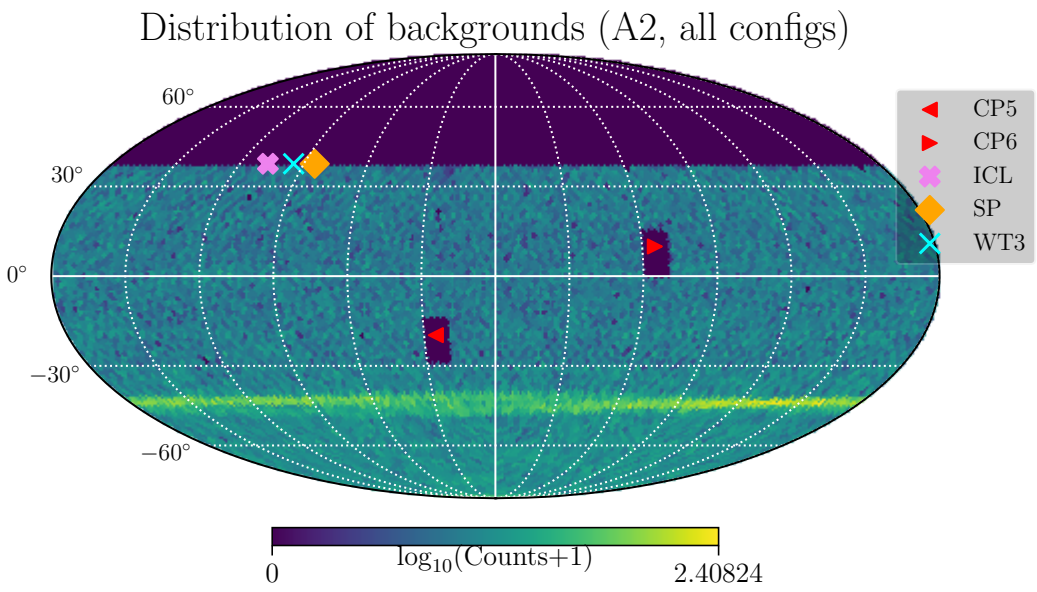

Figure 4.7: Mollweide projection of the reconstructed distribution of radio backgrounds in A2 local coordinates, along with some landmarks such as the calibration pulsers 5 (CP5) and 6 (CP6), the IceCube Laboratory (ICL), the South Pole Station (SP) and the wind turbine # 3 (WT3). The 0° on the y-axis corresponds to the horizon with respect to the center-of-mass of A2 (imagine sitting on an antenna and looking to the horizontal). Events that reconstruct above the ice surface, which in this case corresponds to 37° above the horizontal, are rejected. Similarly, events that reconstruct close to the calibration pulsers are not considered for the analysis.

polarization resolution, and thus better constrain the neutrino source, which will in turn allow us to decrease the number of backgrounds and reduce analysis thresholds.

The neutrino box

The neutrino box cut is applied in the A2 local coordinate system. Our neutrino box was derived from Figure 4.5. We let the sides of the box to be the area enclosing 90% of the events for both ϕ and θ, centered at the mean of the reconstructed RF and width of the sides given by the area enclosing 90% of the area for the individual distributions ($\phi_{RF} = -89^{+33.00}_{-33.00}, \theta_{RF} = -5^{+13.0}_{-10.0}$), as specified in Figure 4.5.

The control sample

As shown in Figure 4.7, the number of backgrounds is θ-dependent. Because of this, we use a control sample defined by a band of width $\Delta\theta_{\mathrm{RF}} = 13°$, at the same range in θ_{RF} as the neutrino box, but extending to all ϕ_{RF} values except those containing the neutrino box.

4.2.4 The final cut: RCut

Once the wavefront-RMS filter has been applied, CW contamination has been removed and events reconstructing above the ice and to known locations of anthropogenic noise have been rejected, the final cut needs to be applied. From the study of the properties of Askaryan signal and from simulations, we expect these signals to reconstruct well and thus have a high C_{sky} parameter. This is one of the parameters that will be used for our final cut. The other parameter will be related to the sensitivity of our experiment at discerning neutrino signals from noise, namely the signal-to-noise ratio (SNR). This will be the second parameter in our final cut. This leaves us with a bivariate cut that will separate neutrino signals over noise. This cut was called the RCut for the diffuse analysis, and we will refer to it as such henceforth.

Graphically, this cut is represented by a line of certain slope m and intercept y_i on a SNR vs C_{sky} space that will separate interesting events over the rest of events. Events of interest will be those those that satisfy the following inequality

$$SNR > mC_{sky} + y_i. \tag{4.11}$$

The determination of the parameters m and intercept y_i have to be done through a process known as optimization, in which a grid scan is performed for different values of m and y_i such that they maximize, or minimize, a certain value. This will be explained in the next subsection.

4.3 RCut optimization

We are analyzing 10% of our total data (unblinded dataset) for four years of a single station. Since we expect to detect $\mathcal{O}(1)$ events every ten years with our current experiment layout in the complete dataset, the probability of finding a neutrino event is small. Because of this, we optimize our RCut such that we minimize the UHE neutrino flux limit that we can constrain. We expect the number of detected UHE neutrinos to follow a Poisson distribution (the observations are independent of each other, and we expect them to occur at certain rate, ~ 1 every 10 years). The likelihood function for detecting n events given that we have

observed s events in the presence of background events b is given by

$$\mathcal{L}(n|s) = \frac{(s+b)^n}{n!} e^{-(s+b)} \tag{4.12}$$

We can use Bayes' theorem to calculate the likelihood of observing s signal events in the presence of b background events given that we have measured n events:

$$\mathcal{L}(s|n) = \frac{\mathcal{L}(n|s)\pi(s)}{\int_0^\infty \mathcal{L}(n|s)\pi(s)ds} \tag{4.13}$$

$$= \frac{\mathcal{L}(n|s)}{\int_0^\infty \mathcal{L}(n|s)ds}, \tag{4.14}$$

where in the last step we assumed a flat prior: $\pi(s) \sim$ constant. We can estimate an upper limit on the number of signal events S_{up}. For this measurement we want the 90% confidence level (CL) upper limit on the number of signal events S_{up} such that:

$$1 - \alpha = 0.9 = \int_0^{S_{up}} \mathcal{L}(s|n) = \frac{\int_0^{S_{up}} \mathcal{L}(n|s)ds}{\int_0^\infty \mathcal{L}(n|s)ds}. \tag{4.15}$$

We expect the number of observed events n to be equal to the number of background events b: $b = n$. Because s is integrated out, the likelihood $\mathcal{L}(n|s)$ only depends on b. We can therefore estimate S_{up} by calculating the number of expected backgrounds b as a function of cut value from a data-driven model.

4.3.1 Background estimation

The estimation of number of backgrounds b will be done by constructing a data-driven model of the data passing all the cuts except the RCut. To do this, we compute the differential distribution of events rejected by the RCut as a function of the y-intercept y_i. This is, for a given slope m and variable intercept y_i, how many events in a the bin i do not satisfy Equation 4.11.

We can fit this differential distribution with an exponential of the form

$$f(SNR) = e^{\beta_1 SNR + \beta_2}, \tag{4.16}$$

where β_1 and β_2 are the fit parameters and they represent in log-space the slope and the intercept of a line. This fit will be the model, and we would like to evaluate how consistent it is with the data. We can do this by estimating the goodness of fit via the computation of the binned log-likelihood (which is directly proportional to the χ^2 for Gaussian distributed variables):

$$-2\ln(\mathcal{L}) = 2\sum_{i=1}^{N} \left[\mu_i - n_i + n_i \ln \frac{n_i}{\mu_i} \right], \tag{4.17}$$

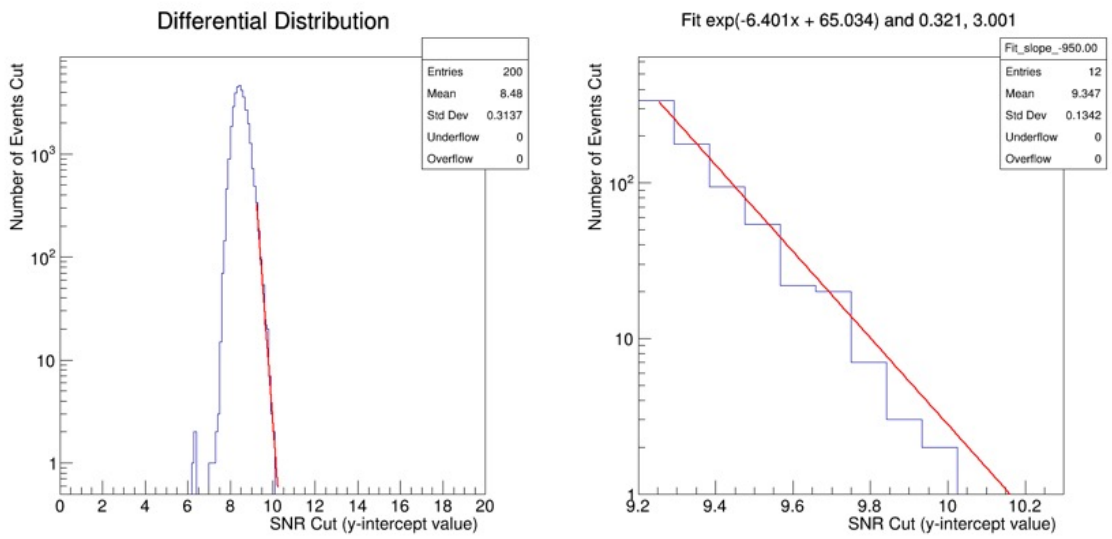

Figure 4.8: Differential distribution of the number of events cut by the RCut as a function of the y-intercept in A2 config. 1.

where N is the total number of SNR bins, μ_i represents the expected number of events in each bin, $\mu_i = e^{\beta_1 SNR_i + \beta_2}$ and n_i is the observed number of events in that particular SNR bin. For bins with $n_i = 0$, the last term in Equation 4.17 is zero. A smaller value of $-2\ln(\mathcal{L})$ corresponds to better agreement between the data and the data-driven model. This can be translated into a p-value as a measure of goodness-of-fit by performing an ensemble of pseudo-experiments. Each pseudo-experiment will follow the exponential distribution given by our data-driven model and with bin content given by a number of events drawn from a Poisson distribution with parameters obtained from the data-driven background model. For each pseudo-experiment we will calculate $-2\ln(\mathcal{L})$, and the p-value will be estimated as the fraction of number of events in the pseudo-experiment ensemble having a likelihood smaller than the value observed from the data-driven model. A p-value greater than 0.05 is usually considered statistically significant, so we say our data-driven model is reasonable if $p > 0.05$.

Once we determine that our model is consistent with data, and establish that it is reasonable, we proceed to determine the number of background events b we expect given our model:

$$b = \int_{y_i}^{\infty} e^{\beta_1 SNR + \beta_2} dSNR = -\frac{1}{\beta_1} e^{\beta_1 y_i + \beta_2}. \tag{4.18}$$

To summarize, for a given slope m and intercept y_i we can calculate the number of expected backgrounds b from a reasonable data-driven model of the differential number of rejected events. This will be a needed piece to connect the number of expected backgrounds

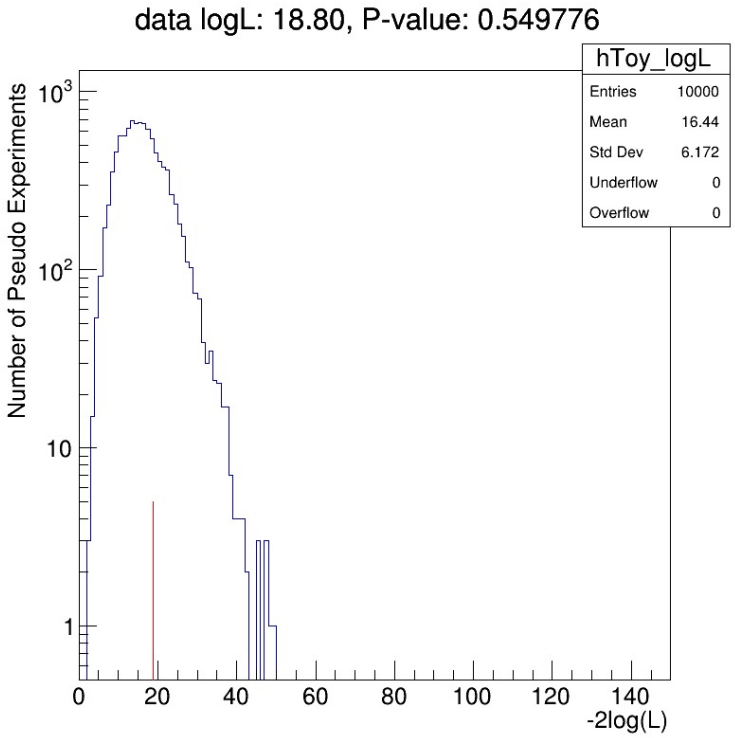

Figure 4.9: Example of a distribution of an ensemble of 10,000 pseudo-experiments, where the x-axis corresponds to $-2\ln(\mathcal{L})$. The p-value is $p > 0.05$, and our data-driven model is reasonable.

with the number of signal events, as will be explained in the next subsection.

4.3.2 Connecting pieces

Once we have an estimate of b, we can use Equation 4.15 to have an expression relating b and S_{up}. Each choice of slope m and y-intercept y_i will yield a different value for b, and consequently a different value for S_{up}. Similarly, each choice of m and y_i will give a different number of simulated neutrino events s passing the RCut. The process of optimization consists of performing a grid scan of different values of m and y-intercept y_i such that we maximize (or minimize) a certain quantity. For our analysis, we want that quantity to be the ratio of passing neutrino events s to the upper limit on the number of signal events S_{up}: S/S_{up}. For this search we expect to obtain the best UHE neutrino limit (best means to get a limit on the smallest flux possible), as we expect to detect no events. Because the UHE neutrino flux limit is inversely proportional to the effective area, and the effective area is proportional to the number of observed neutrinos, we want to maximize S/S_{up}. Hence, our

optimization will consist on looping over different values of m and y_i until we find the ones that return the greatest S/S_{up} ratio. The results of a grid search to optimize the slope for A2 configuration 1 are shown in figure Figure 4.10 for both Vpol and Hpol.

We found an optimized sloped of $m = -780$ and $m = -720$ for Vpol and Hpol, respectively. The optimized y-intercepts are $y_i = 10.40$ and $y_i = 10.50$ for Vpol and Hpol, respectively. These cuts are graphically shown in the bivariate plane (SNR vs. C_{sky}) in Figure 4.11, along with the distribution of events that pass all the cuts. As expected, no events pass the RCut in either Vpol or Hpol channels.

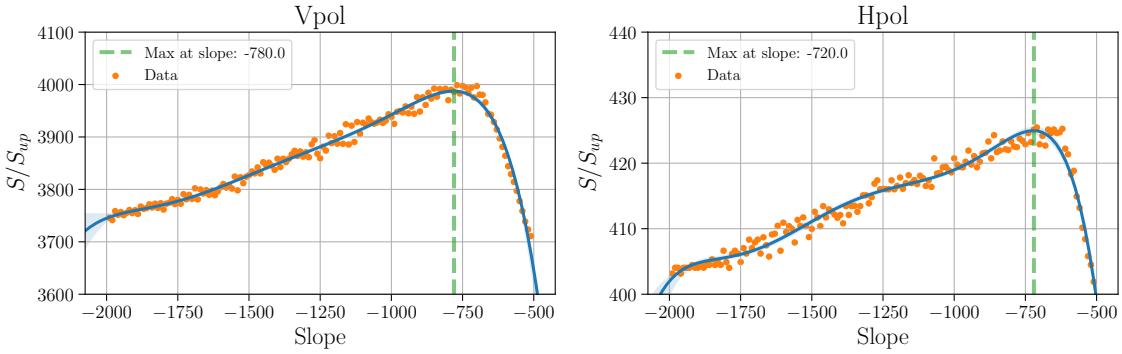

Figure 4.10: Grid search to find the best slope for A2 config 1. To perform this search we loop over different values of the slope m in a coarse set of values, and for each value of m, we loop over different values of the y_i intercept and plot the maximum value of S/S_{up}. We then fit the distribution of values with a polynomial function, and pick the value of m that is located at the maximum value of the fitted function. This values correspond to $m = -780$ and $m = -720$ for Vpol and Hpol, respectively.

4.4 Optimized cut values and background estimation

For the optimized values for the slope and y-intercept we find a background estimate of 0.016 for Vpol and 0.010 for Hpol, which are of the same order of magnitude as the values found for the diffuse search. Similarly, for these optimized cut values we can calculate the neutrino efficiency, which is defined as the sum of weighted events passing all the cuts over the sum of all the weighted events triggering the detector. We do this as a function of two different variables: SNR and energy. Because our directional cut decreased the number of background events for the same RCut, consequently loosening the SNR cut and effectively increasing the number of passing simulated neutrino events s, we expect the efficiency to be greater than the one obtained for the A23 diffuse analysis. Figure 4.13 shows the efficiency

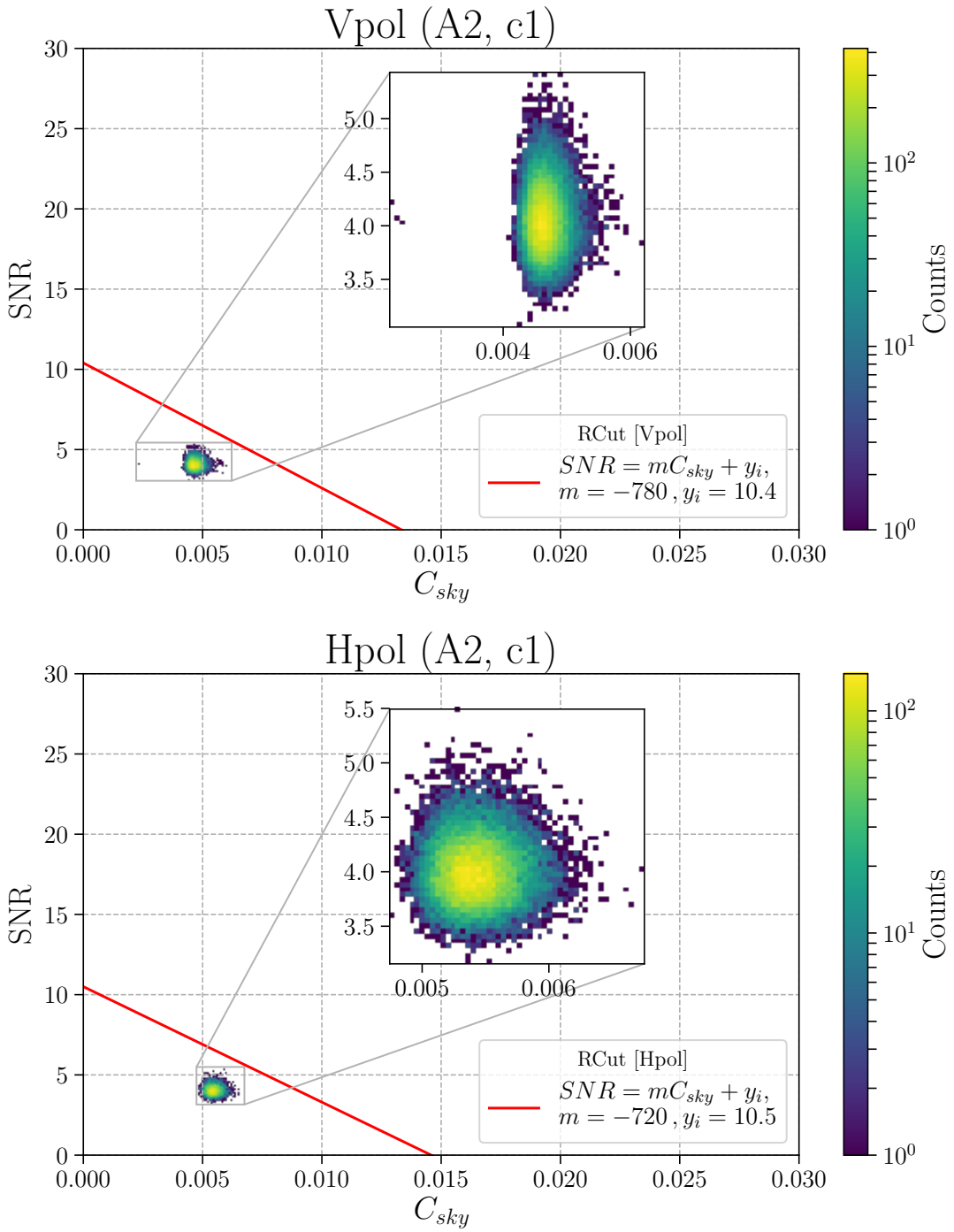

Figure 4.11: Bivariate cut plane for A2, configuration 1.

as a function of the Vpol SNR for both the A23 diffuse analysis and the efficiency set by our preliminary analysis on the 10% of data for A2 config 1. As predicted, the efficiency

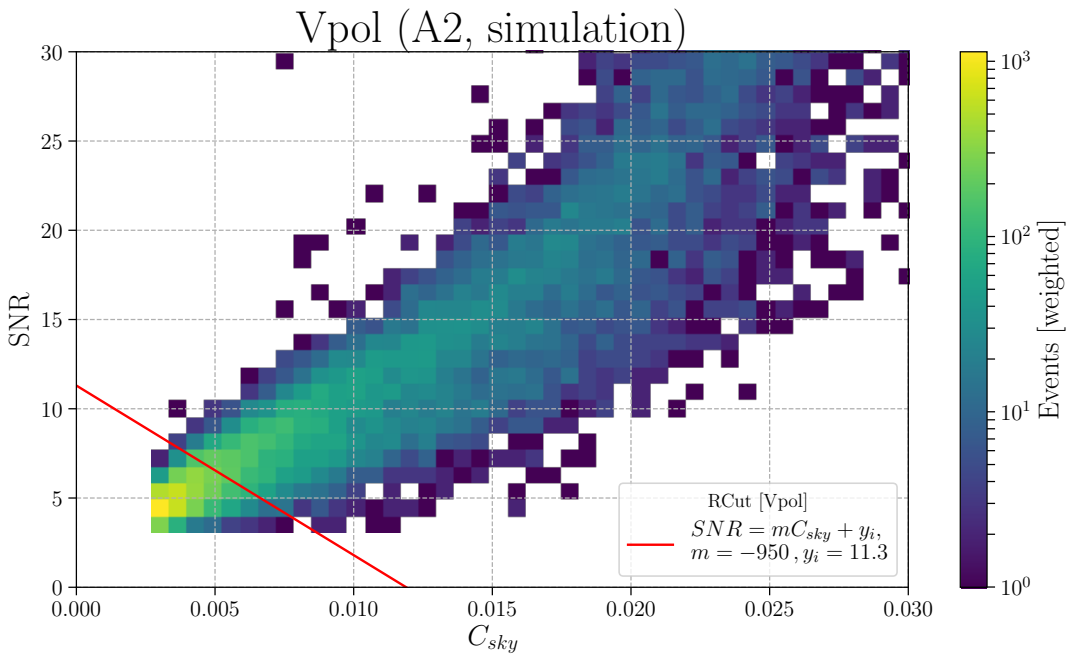

Figure 4.12: Bivariate cut plane for A2, configuration 1. Simulated and Vpol triggered events.

for the source search has an earlier turn-on and it plateaus at around 85% efficiency after an SNR of about 7.5, which is an increase from the diffuse analysis, as show in Figure 4.13.

4.5 Projected UHE neutrino limit

While this thesis was being developed, a bug in the data processing was found. The bug consisted in a set of commented out lines that caused the voltage calibration to not being applied. While this does not change the results of our previous diffuse search, it affected the optimization of configurations c2-c5 because it revealed the presence of new digitizer glitches that were not present in the uncalibrated data. For this reason, I was only able to analyze configuration 1 and thus unable to set a final neutrino limit. However, with the motivated assumption that we will not observe any events in the neutrino box, we can set a projected limit on a point-source search of UHE neutrinos from Centaurus A.

We set a limit on the theoretical model by Kachelriess *et. al.* [104] for UHE neutrinos emitted near the core of Cen A from protons injected with a E^{-2} spectrum. To do this, we follow a similar procedure as the one described in Section 2.5: to calculate the best expected

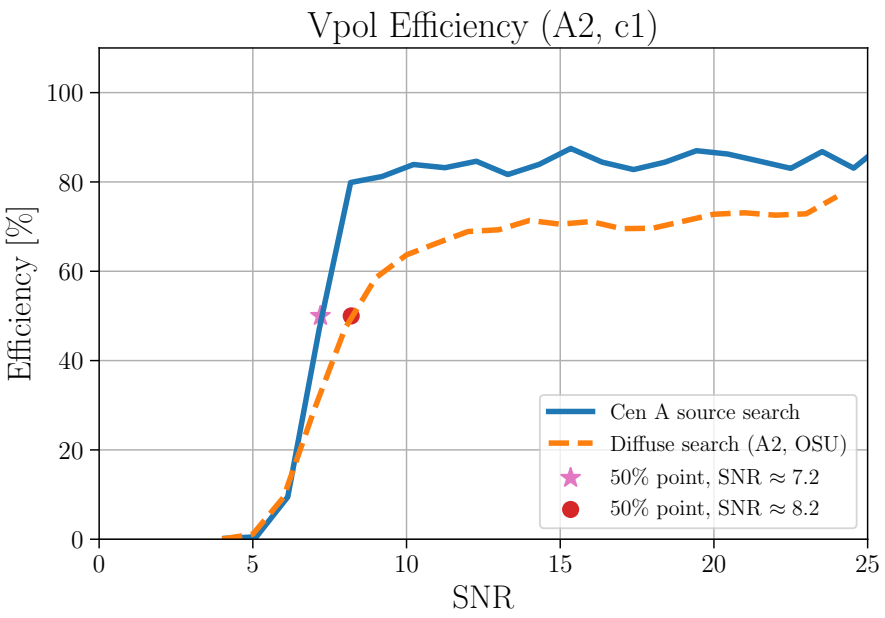

Figure 4.13: Search efficiency as a function of SNR.

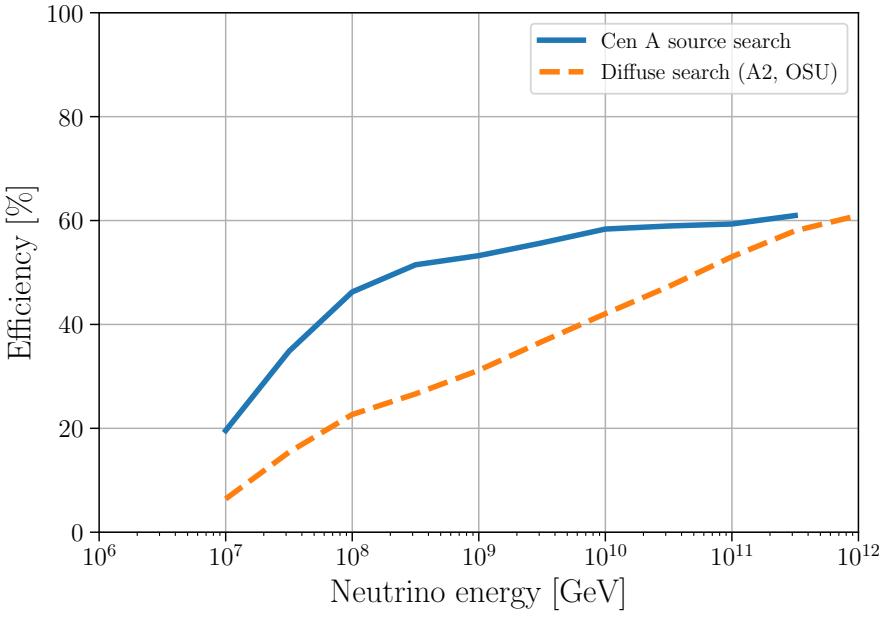

Figure 4.14: Search efficiency as a function of neutrino energy.

90% confidence level (C.L.) upper limit $F_{\mathrm{UL}}(E)$, we compute

$$F_{\mathrm{UL}}(E) = F(E)\frac{N_{\mathrm{UL}}}{N_{\mathrm{exp}}}, \tag{4.19}$$

where $F(E)$ is the theoretical flux model from [104], $N_{\mathrm{UL}} = 2.44$ is the 90% C.L. upper limit on the number of signal events given the number of expected background events (using the Feldman-Cousins approach [86]), and N_{exp} is the number of expected neutrinos that pass the cuts. For each energy bin i , $N_{\mathrm{exp},i}$ is computed as follows:

$$N_{\mathrm{exp},i} = (EdN/dE)_i \Lambda_i d\log_{10} E \log 10, \tag{4.20}$$

where $(EdN/dE)_i$ is the flux at the energy bin i in units of [cm^{-2} s^{-1}], Λ_i is the exposure in units of [cm^2 s] using the effective area shown in Figure 4.15 , and $d\log_{10} E = 0.5$ is the logarithmic energy bin width

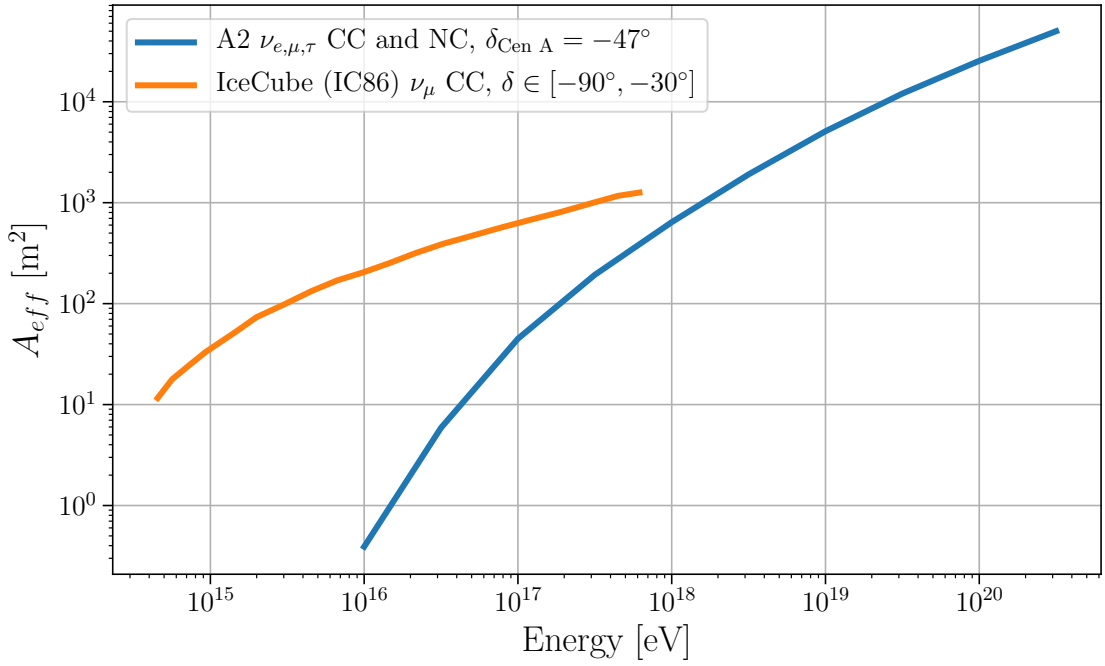

Figure 4.15: Trigger level effective area as a function of energy for A2 for neutrinos emitted from a source at a declination of $\delta = -47°$, which corresponds to Cen A's declination. We also show the IceCube's effective area calculated using simulated neutrinos for the selection of IC86 (seasons 2012-2015) [29] averaged over the solid angle in the declination range $\delta \in [-90°, 30°]$.

From the model and the calculated efficiencies and effective area, we expect 0.0028 neutrinos to pass the cuts. We calculate a projected 90% C.L. limit on the flux of UHE neutrinos from Cen A, and this is shown in Figure 4.16. We also show limits from a point-source search with 14.5 years of data from the Pierre Auger Observatory [31] for the same model by Kachelriess, *et. al*, and we also show limits from ANTARES [30] and IceCube [29]. As it can be seen, we are competitive with the limit imposed by Auger, even though our diffuse limit was not as close. The reason for this is that Auger only sees Cen A $\sim 30\%$ of its total exposure, whereas ARA sees it 100%.

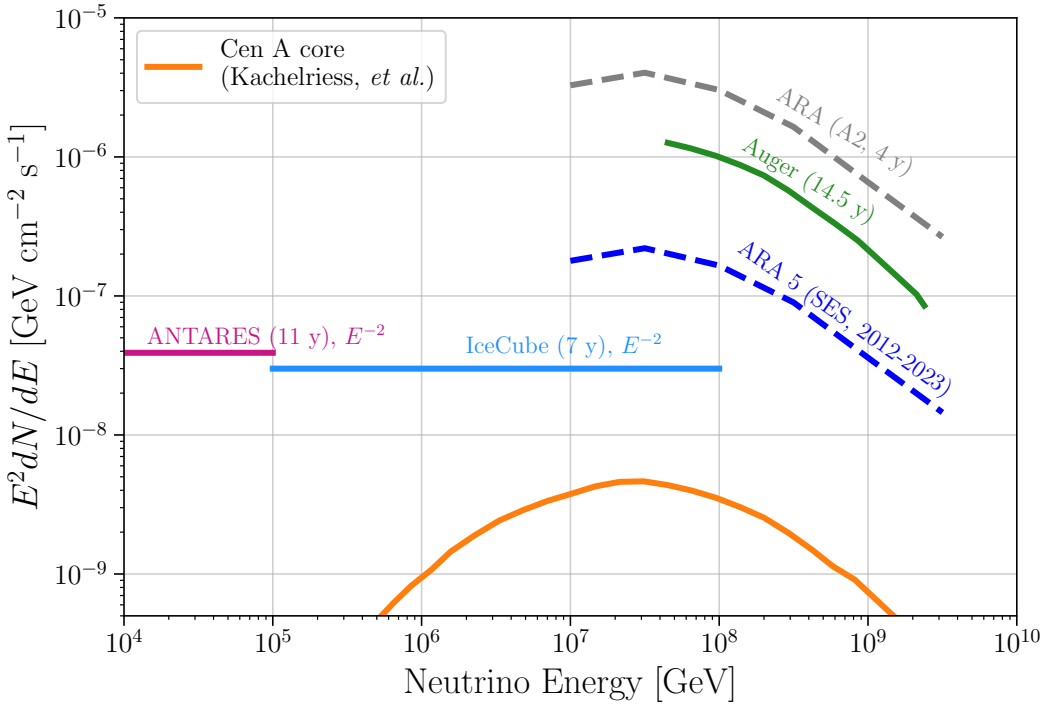

Figure 4.16: Projected limit from our search along with limits from ANTARES [30], The Pierre Auger Observatory [31], and IceCube [29]. All the limits, except our projection, were scaled by a factor of 3 to account for all neutrino flavors.

Chapter 5
Conclusion

In this thesis, I have reported an analysis of four years of data of ARA stations 2 and 3 in Chapter 2, presented both simulation and data studies of polarization reconstruction capabilities of the ARA experiment, as well as their implications on neutrino directional reconstruction in Chapter 3, and finally described an initial approach for a point-source search of UHE neutrinos from Centaurus A with four years of data of A2 in Chapter 4.

The diffuse analysis for four years of data of ARA stations 2 and 3 increased the stations' livetime by a factor of four and resulted in the best limit above 10^8 GeV for in-ice radio experiments. This analysis also showed ARA's capabilities using a continuously growing dataset, which will be important for ARA itself and for the next-generation of in-ice Askaryan experiments. Several lessons were learned that will inform the design of newer experiments so they can be optimized to account for challenges that analysts encounter such as real-time identification of glitches, or making the design uniform across stations so that separate analysis are not needed.

The work on polarization reconstruction and implication for neutrino directional reconstruction presented in Chapter 3 was prompted by the need to have a directional reconstruction framework so that the efficiency of source searches is greatly improved. From my work on simulations, we were able to estimate ARA's polarization resolution and consequently assess the impact on this on the neutrino directional reconstruction capabilities by performing an inverse Monte Carlo approach. Finally, I developed a framework to determine the resolution on the reconstructed polarization vector using the ARA data and tested it with data from the SpiceCore drop performed in December of 2018. An attempt to constrain the polarization resolution was attempted, but further studies are required to make comparisons between simulations and the data.

Lastly, in Chapter 4 I presented the optimization of a point-source search for UHE neutrinos from Cen A for A2 configuration 1. We included a brief explanation of the cuts, with emphasis on a directional requirement in the direction of Cen A by using information on the reconstructed RF location, and with no assumptions on the polarization. For this

study, starting from previous work done for the ARA Solar flares paper, I developed a parallel coordinate system framework that transforms reconstructed RF angular position in station coordinate system to Equatorial coordinates (RA and Dec) using the timestamp of the event. This will be useful for future point-source searches with the ARA experiment, as this works for any celestial body and can be used to impose directional cuts. We use this framework to impose a directional cut on Cen A, and we show that the efficiency of an analysis is significantly improved as this cut reduces the number of background events. This work demonstrates ARA's capabilities for source searches and it will be important for future point-source analyses.

Bibliography

[1] The IceCube Collaboration. Visible universe to photons. https://icecube.wisc.edu/science/research/, 2018. [Online; accessed 15-May-2021].

[2] Markus Ackermann, Markus Ahlers, Luis Anchordoqui, Mauricio Bustamante, Amy Connolly, Cosmin Deaconu, Darren Grant, Peter Gorham, Francis Halzen, Albrecht Karle, Kumiko Kotera, Marek Kowalski, Miguel A. Mostafa, Kohta Murase, Anna Nelles, Angela Olinto, Andres Romero-Wolf, Abigail Vieregg, and Stephanie Wissel. Fundamental physics with high-energy cosmic neutrinos, 2019.

[3] Thomas K. Gaisser, Todor Stanev, and Serap Tilav. Cosmic Ray Energy Spectrum from Measurements of Air Showers. *Front. Phys. (Beijing)*, 8:748–758, 2013.

[4] Mauricio Bustamante and Amy Connolly. Extracting the Energy-Dependent Neutrino-Nucleon Cross Section above 10 TeV Using IceCube Showers. *Phys. Rev. Lett.*, 122(4):041101, 2019.

[5] Joshua P. Ellis. TikZ-Feynman: Feynman diagrams with TikZ. *Computer Physics Communications*, 210:103–123, Jan 2017.

[6] Jaime Alvarez-Muñiz, Andrés Romero-Wolf, and Enrique Zas. Practical and accurate calculations of Askaryan radiation. *Phys. Rev. D,*, 84(10):103003, November 2011.

[7] M. G. Aartsen et al. Observation and Characterization of a Cosmic Muon Neutrino Flux from the Northern Hemisphere using six years of IceCube data. *Astrophys. J.*, 833(1):3, 2016.

[8] M. G. Aartsen et al. Differential limit on the extremely-high-energy cosmic neutrino flux in the presence of astrophysical background from nine years of IceCube data. *Phys. Rev.*, D98(6):062003, 2018.

[9] Alexander Aab et al. Probing the origin of ultra-high-energy cosmic rays with neutrinos in the EeV energy range using the Pierre Auger Observatory. *JCAP*, 10:022, 2019.

[10] P. W. Gorham et al. Constraints on the ultra-high energy cosmic neutrino flux from the fourth flight of ANITA. 2019.

[11] P. Allison et al. Constraints on the diffuse flux of ultrahigh energy neutrinos from four years of Askaryan Radio Array data in two stations. *Phys. Rev. D*, 102(4):043021, 2020.

[12] A. Anker et al. A search for cosmogenic neutrinos with the ARIANNA test bed using 4.5 years of data. *JCAP*, 03:053, 2020.

[13] C. Righi, A. Palladino, F. Tavecchio, and F. Vissani. EeV astrophysical neutrinos from flat spectrum radio quasars. *Astron. Astrophys.*, 642:A92, 2020.

[14] Ke Fang, Kumiko Kotera, Kohta Murase, and Angela V. Olinto. Testing the Newborn Pulsar Origin of Ultrahigh Energy Cosmic Rays with EeV Neutrinos. *Phys. Rev. D*, 90(10):103005, 2014. [Erratum: Phys.Rev.D 92, 129901 (2015)].

[15] Kohta Murase. High energy neutrino early afterglows from gamma-ray bursts revisited. *Physical Review D*, 76(12), Dec 2007.

[16] Markus Ahlers and Francis Halzen. Minimal Cosmogenic Neutrinos. *Phys. Rev.*, D86:083010, 2012.

[17] Arjen van Vliet, Rafael Alves Batista, and Jörg R. Hörandel. Determining the fraction of cosmic-ray protons at ultrahigh energies with cosmogenic neutrinos. *Phys. Rev. D*, 100(2):021302, 2019.

[18] M. G. Aartsen et al. Probing the origin of cosmic rays with extremely high energy neutrinos using the IceCube Observatory. *Phys. Rev.*, D88:112008, 2013.

[19] R. Bard et al. Design and Performance of an Interferometric Trigger Array for Radio Detection of High-Energy Neutrinos. 2018.

[20] Amy Connolly, Robert S. Thorne, and David Waters. Calculation of High Energy Neutrino-Nucleon Cross Sections and Uncertainties Using the MSTW Parton Distribution Functions and Implications for Future Experiments. *Phys. Rev.*, D83:113009, 2011.

[21] P. Allison et al. Design and initial performance of the Askaryan Radio Array prototype EeV neutrino detector at the South Pole. *Astroparticle Physics*, 35:457–477, February 2012.

[22] A. V. Olinto, K. Kotera, and D. Allard. Ultrahigh Energy Cosmic Rays and Neutrinos. *Nucl. Phys. Proc. Suppl.*, 217:231–236, 2011.

[23] K. Kotera, D. Allard, and A. V. Olinto. Cosmogenic Neutrinos: parameter space and detectabilty from PeV to ZeV. *JCAP*, 1010:013, 2010.

[24] Jörg P. Rachen and Björn Eichmann. A parameterized catalog of radio galaxies as ultra-high energy cosmic ray sources, 2019.

[25] Christian Glaser et al. NuRadioMC: Simulating the radio emission of neutrinos from interaction to detector. 2019.

[26] Daniel Foreman-Mackey. corner.py: Scatterplot matrices in python. *Journal of Open Source Software*, 1(2):24, 2016.

[27] A. Albert, R. Alfaro, C. Alvarez, J. R. Angeles Camacho, J. C. Arteaga-Velázquez, K. P. Arunbabu, D. Avila Rojas, H. A. Ayala Solares, V. Baghmanyan, E. Belmont-Moreno, and et al. 3hwc: The third hawc catalog of very-high-energy gamma-ray sources. *The Astrophysical Journal*, 905(1):76, Dec 2020.

[28] Brian Clark. *Optimization of a Search for Ultra-High Energy Neutrinos in Four Years of Data of ARA Station 2*. PhD thesis, The Ohio State University, 2019.

[29] M. G. Aartsen et al. All-sky Search for Time-integrated Neutrino Emission from Astrophysical Sources with 7 yr of IceCube Data. *Astrophys. J.*, 835(2):151, 2017.

[30] A. Albert et al. First all-flavor neutrino pointlike source search with the ANTARES neutrino telescope. *Phys. Rev. D*, 96(8):082001, 2017.

[31] Alexander Aab et al. Limits on point-like sources of ultra-high-energy neutrinos with the Pierre Auger Observatory. *JCAP*, 11:004, 2019.

[32] Konstantin Bikos. Altaz coordinate system. https://www.timeanddate.com/astronomy/horizontal-coordinate-system.html, 2019. [Online; accessed 20-Mar-2021].

[33] P. Allison et al. Observation of Reconstructable Radio Emission Coincident with an X-Class Solar Flare in the Askaryan Radio Array Prototype Station. 2018.

[34] Alberto Franceschini, Giulia Rodighiero, and Mattia Vaccari. The extragalactic optical-infrared background radiations, their time evolution and the cosmic photon-photon opacity. *Astron. Astrophys.*, 487:837, 2008.

[35] M. G. Aartsen et al. Measurement of the multi-TeV neutrino cross section with IceCube using Earth absorption. *Nature*, 551:596–600, 2017.

[36] Jaime Alvarez-Muñiz, Jonathan L. Feng, Francis Halzen, Tao Han, and Dan Hooper. Detecting microscopic black holes with neutrino telescopes. *Phys. Rev. D*, 65:124015, Jun 2002.

[37] Ismael Romero and Oscar A Sampayo. Leptoquarks signals in km3neutrino telescopes. *Journal of High Energy Physics*, 2009(05):111–111, May 2009.

[38] Ian M. Shoemaker and Kohta Murase. Probing BSM Neutrino Physics with Flavor and Spectral Distortions: Prospects for Future High-Energy Neutrino Telescopes. *Phys. Rev. D*, 93(8):085004, 2016.

[39] D. Colladay and V. Alan Kostelecký. Lorentz-violating extension of the standard model. *Physical Review D*, 58(11), Oct 1998.

[40] P. W. Gorham, A. Connolly, P. Allison, J. J. Beatty, K. Belov, D. Z. Besson, W. R. Binns, P. Chen, J. M. Clem, S. Hoover, and et al. Implications of ultrahigh energy neutrino flux constraints for lorentz-invariance violating cosmogenic neutrinos. *Physical Review D*, 86(10), Nov 2012.

[41] Carsten Rott, Kazunori Kohri, and Seong Chan Park. Superheavy dark matter and icecube neutrino signals: Bounds on decaying dark matter. *Physical Review D*, 92(2), Jul 2015.

[42] K. Hirata, T. Kajita, M. Koshiba, M. Nakahata, Y. Oyama, N. Sato, A. Suzuki, M. Takita, Y. Totsuka, T. Kifune, T. Suda, K. Takahashi, T. Tanimori, K. Miyano, M. Yamada, E. W. Beier, L. R. Feldscher, S. B. Kim, A. K. Mann, F. M. Newcomer, R. Van, W. Zhang, and B. G. Cortez. Observation of a neutrino burst from the supernova sn1987a. *Phys. Rev. Lett.*, 58:1490–1493, Apr 1987.

[43] R. M. Bionta, G. Blewitt, C. B. Bratton, D. Casper, A. Ciocio, R. Claus, B. Cortez, M. Crouch, S. T. Dye, S. Errede, G. W. Foster, W. Gajewski, K. S. Ganezer, M. Goldhaber, T. J. Haines, T. W. Jones, D. Kielczewska, W. R. Kropp, J. G. Learned, J. M. LoSecco, J. Matthews, R. Miller, M. S. Mudan, H. S. Park, L. R. Price, F. Reines, J. Schultz, S. Seidel, E. Shumard, D. Sinclair, H. W. Sobel, J. L. Stone, L. R. Sulak, R. Svoboda, G. Thornton, J. C. van der Velde, and C. Wuest. Observation of a neutrino burst in coincidence with supernova 1987a in the large magellanic cloud. *Phys. Rev. Lett.*, 58:1494–1496, Apr 1987.

[44] E. N. Alekseev, L. N. Alekseeva, I. V. Krivosheina, and V. I. Volchenko. Detection of the Neutrino Signal from Supernova 1987A Using the INR Baksan Underground Scintillation Telescope. In *European Southern Observatory Conference and Workshop Proceedings*, volume 26 of *European Southern Observatory Conference and Workshop Proceedings*, page 237, January 1987.

[45] M. G. Aartsen et al. First observation of PeV-energy neutrinos with IceCube. *Phys. Rev. Lett.*, 111:021103, 2013.

[46] M. G. Aartsen et al. Neutrino emission from the direction of the blazar TXS 0506+056 prior to the IceCube-170922A alert. *Science*, 361(6398):147–151, 2018.

[47] M. G. Aartsen et al. Multimessenger observations of a flaring blazar coincident with high-energy neutrino IceCube-170922A. *Science*, 361(6398):eaat1378, 2018.

[48] Veniamin Berezinsky. Supergzk neutrinos. In *11th International Workshop on Neutrino Telescopes*, 9 2005.

[49] John N. Bahcall and Eli Waxman. Ultrahigh-energy cosmic rays may come from clustered sources. *Astrophys. J.*, 542:543–547, 2000.

[50] A. Roberts. The Birth of high-energy neutrino astronomy: A Personal history of the DUMAND project. *Rev. Mod. Phys.*, 64:259–312, 1992.

[51] John David Jackson. *Classical Electrodynamics*. Wiley, New York, NY, 3rd ed. edition, 1999.

[52] M. G. Aartsen et al. The IceCube Neutrino Observatory: Instrumentation and Online Systems. *JINST*, 12(03):P03012, 2017.

[53] S. Adrian-Martinez et al. Letter of intent for KM3NeT 2.0. *J. Phys. G*, 43(8):084001, 2016.

[54] M. Koshiba. KAMIOKA NUCLEON DECAY EXPERIMENT. *Nuovo Cim. C*, 9:141–158, 1986.

[55] G. A. Askar'yan. Excess negative charge of an electron-photon shower and its coherent radio emission. *Sov. Phys. JETP*, 14(2):441–443, 1962. [Zh. Eksp. Teor. Fiz.41,616(1961)].

[56] W. Heitler. *The quantum theory of radiation*, volume 5 of *International Series of Monographs on Physics*. Oxford University Press, Oxford, 1936.

[57] Particle Data Group. Review of Particle Physics. *Progress of Theoretical and Experimental Physics*, 2020(8), 08 2020. 083C01.

[58] E. Zas, F. Halzen, and T. Stanev. Electromagnetic pulses from high-energy showers: Implications for neutrino detection. *Phys. Rev. D*, 45:362–376, 1992.

[59] Soebur Razzaque, Surujhdeo Seunarine, David Z. Besson, Douglas W. McKay, John P. Ralston, and David Seckel. Coherent radio pulses from GEANT generated electromagnetic showers in ice. *Phys. Rev. D*, 65:103002, 2002.

[60] Soebur Razzaque, Surujhdeo Seunarine, Scott W. Chambers, David Z. Besson, Douglas W McKay, John P. Ralston, and David Seckel. Addendum to 'Coherent radio pulses from GEANT generated electromagnetic showers in ice'. *Phys. Rev. D*, 69:047101, 2004.

[61] Tim Huege and Dave Besson. Radio-wave detection of ultra-high-energy neutrinos and cosmic rays. *Progress of Theoretical and Experimental Physics*, 2017(12):12A106, December 2017.

[62] David Saltzberg, Peter Gorham, Dieter Walz, Clive Field, Richard Iverson, Allen Odian, George Re, Paul Schoessow, and Dawn Williams. Observation of the Askaryan effect: Coherent microwave Cherenkov emission from charge asymmetry in high-energy particle cascades. *Phys. Rev. Lett.*, 86:2802–2805, 2001.

[63] Peter W. Gorham, D. Saltzberg, R. C. Field, E. Guillian, R. Milincic, D. Walz, and D. Williams. Accelerator measurements of the Askaryan effect in rock salt: A Roadmap toward teraton underground neutrino detectors. *Phys. Rev. D*, 72:023002, 2005.

[64] P. W. Gorham et al. Observations of the Askaryan effect in ice. *Phys. Rev. Lett.*, 99:171101, 2007.

[65] P. Miocinovic, R. C. Field, P. W. Gorham, E. Guillian, R. Milincic, D. Saltzberg, D. Walz, and D. Williams. Time-domain measurement of broadband coherent Cherenkov radiation. *Phys. Rev. D*, 74:043002, 2006.

[66] J. Alvarez-Muniz, R. A. Vazquez, and E. Zas. Calculation methods for radio pulses from high-energy showers. *Phys. Rev.*, D62:063001, 2000.

[67] S. Barwick, D. Besson, P. Gorham, and D. Saltzberg. South Polar in situ radio-frequency ice attenuation. *J. Glaciol.*, 51:231–238, 2005.

[68] Taylor Barrella, Steven Barwick, and David Saltzberg. Ross ice shelf (antarctica) in situ radio-frequency attenuation. *Journal of Glaciology*, 57(201):61–66, 2011.

[69] J. Avva, J. M. Kovac, C. Miki, D. Saltzberg, and A. G. Vieregg. An in situ measurement of the radio-frequency attenuation in ice at Summit Station, Greenland. *J. Glaciol.*, 61:1005–1011, 2015.

[70] M. Ackermann et al. Optical properties of deep glacial ice at the South Pole. *J. Geophys. Res.*, 111(D13):D13203, 2006.

[71] S. W. Barwick et al. Constraints on cosmic neutrino fluxes from the anita experiment. *Phys. Rev. Lett.*, 96:171101, 2006.

[72] Q. Abarr et al. The Payload for Ultrahigh Energy Observations (PUEO): A White Paper. 10 2020.

[73] P. Allison et al. First Constraints on the Ultra-High Energy Neutrino Flux from a Prototype Station of the Askaryan Radio Array. *Astropart. Phys.*, 70:62–80, 2015.

[74] P. Allison et al. Performance of two Askaryan Radio Array stations and first results in the search for ultrahigh energy neutrinos. *Phys. Rev.*, D93(8):082003, 2016.

[75] Specifications for the iceray sampler (irs) asic. https://www.phys.hawaii.edu/~varner/IRS_spec_v01.pdf, 2009. Accessed: 2020-03-20.

[76] G. S. Varner, L. L. Ruckman, P. W. Gorham, J. W. Nam, R. J. Nichol, J. Cao, and M. Wilcox. The large analog bandwidth recorder and digitizer with ordered readout (LABRADOR) ASIC. *Nucl. Instrum. Meth.*, A583:447–460, 2007.

[77] Jarred M. Roberts, Eric Oberla, Patrick Allison, Gary S. Varner, Stefan Spack, Brendan Fox, and Ben Rotter. LAB4D: A Low Power, Multi-GSa/s, Transient Digitizer with Sampling Timebase Trimming Capabilities. *Nucl. Instrum. Meth.*, A925:92–100, 2019.

[78] Eugene Hong. *Searching for Ultra-high Energy Neutrinos with Data from a Prototype Station of the Askaryan Radio Array.* PhD thesis, The Ohio State University, 2014.

[79] Ming-Yuan Lu. *Search for Ultra-high Energy Neutrinos with the Askaryan Radio Array.* PhD thesis, University of Wisconsin-Madison, 2020.

[80] P. Schellart et al. Detecting cosmic rays with the LOFAR radio telescope. *Astron. Astrophys.*, 560:A98, 2013.

[81] Amanda Cooper-Sarkar, Philipp Mertsch, and Subir Sarkar. The high energy neutrino cross-section in the Standard Model and its uncertainty. *JHEP*, 08:042, 2011.

[82] I. Kravchenko, D. Besson, and J. Meyers. In situ index-of-refraction measurements of the South Polar firn with the RICE detector. *Journal of Glaciology*, 50:522–532, 2004.

[83] P. Allison, S. Archambault, J.J. Beatty, D.Z. Besson, C.C. Chen, C.H. Chen, P. Chen, A. Christenson, B.A. Clark, W. Clay, and et al. Long-baseline horizontal radio-frequency transmission through polar ice. *Journal of Cosmology and Astroparticle Physics*, 2020(12):009–009, Dec 2020.

[84] Jan Conrad, O. Botner, A. Hallgren, and Carlos Perez de los Heros. Including systematic uncertainties in confidence interval construction for Poisson statistics. *Phys. Rev.*, D67:012002, 2003.

[85] Gary C. Hill. Comment on 'Including systematic uncertainties in confidence interval construction for Poisson statistics'. *Phys. Rev.*, D67:118101, 2003.

[86] Gary J. Feldman and Robert D. Cousins. A Unified approach to the classical statistical analysis of small signals. *Phys. Rev.*, D57:3873–3889, 1998.

[87] Measurement of the multi-tev neutrino interaction cross-section with icecube using earth absorption. *Nature*, 551(7682):596–600, Nov 2017.

[88] Ben Hokanson-Fasig. PyREx - (Python package for Radio Experiments). Github, 2021.

[89] P. Allison et al. Constraints on the Ultra-High Energy Neutrino Flux from Gamma-Ray Bursts from a Prototype Station of the Askaryan Radio Array. *Astropart. Phys.*, 88:7–16, 2017.

[90] A. Romero-Wolf et al. An interferometric analysis method for radio impulses from ultra-high energy particle showers. *Astropart. Phys.*, 60:72–85, 2015.

[91] A. Anker, S.W. Barwick, H. Bernhoff, D.Z. Besson, N. Bingefors, D. García-Fernández, G. Gaswint, C. Glaser, A. Hallgren, J.C. Hanson, and et al. Probing the angular and polarization reconstruction of the arianna detector at the south pole. *Journal of Instrumentation*, 15(09):P09039–P09039, Sep 2020.

[92] Pauli Virtanen et al. SciPy 1.0: Fundamental Algorithms for Scientific Computing in Python. *Nature Methods*, 17:261–272, 2020.

[93] S. W. Barwick et al. Observation of classically 'forbidden' electromagnetic wave propagation and implications for neutrino detection. *JCAP*, 07:055, 2018.

[94] Christoph Welling, Philipp Frank, Torsten A. Enßlin, and Anna Nelles. Reconstructing non-repeating radio pulses with information field theory, 2021.

[95] Sara Buson, Ke Fang, Azadeh Keivani, Thomas Maccarone, Kohta Murase, Maria Petropoulou, Marcos Santander, Ignacio Taboada, and Nathan Whitehorn. A Unique Messenger to Probe Active Galactic Nuclei: High-Energy Neutrinos. *Bull. Am. Astron. Soc.*, 51:228, 2019.

[96] N. Gehrels. The swift gamma-ray burst mission. *AIP Conference Proceedings*, 2004.

[97] M. Ackermann, M. Ajello, A. Allafort, W.B. Atwood, M. Axelsson, L. Baldini, G. Barbiellini, D. Bastieri, K. Bechtol, R. Bellazzini, and et al. In-flight measurement of the absolute energy scale of the fermi large area telescope. *Astroparticle Physics*, 35(6):346–353, Jan 2012.

[98] Eli Waxman and John N. Bahcall. Neutrino afterglow from gamma-ray bursts. *The Astrophysical Journal*, 541(2):707–711, Oct 2000.

[99] M. G. Aartsen, M. Ackermann, J. Adams, J. A. Aguilar, M. Ahlers, M. Ahrens, I. Al Samarai, D. Altmann, K. Andeen, T. Anderson, and et al. Extending the search for muon neutrinos coincident with gamma-ray bursts in icecube data. *The Astrophysical Journal*, 843(2):112, Jul 2017.

[100] B. Theodore Zhang, Kohta Murase, Shigeo S. Kimura, Shunsaku Horiuchi, and Peter Mészáros. Low-luminosity gamma-ray bursts as the sources of ultrahigh-energy cosmic ray nuclei. *Physical Review D*, 97(8), Apr 2018.

[101] Glennys R. Farrar and Tsvi Piran. Tidal disruption jets as the source of ultra-high energy cosmic rays, 2014.

[102] Cecilia Lunardini and Walter Winter. High Energy Neutrinos from the Tidal Disruption of Stars. *Phys. Rev. D*, 95(12):123001, 2017.

[103] A. Cuoco and S. Hannestad. Ultrahigh energy neutrinos from centaurus a and the auger hot spot. *Physical Review D*, 78(2), Jul 2008.

[104] M. Kachelriess, S. Ostapchenko, and R. Tomas. High energy radiation from Centaurus A. *New J. Phys.*, 11:065017, 2009.

[105] J. Abraham, P. Abreu, M. Aglietta, C. Aguirre, D. Allard, I. Allekotte, J. Allen, P. Allison, C. Alvarez, and et al. Correlation of the highest-energy cosmic rays with nearby extragalactic objects. *Science*, 318(5852):938–943, Nov 2007.

[106] Adrian M Price-Whelan, BM Sipőcz, HM Günther, PL Lim, SM Crawford, S Conseil, DL Shupe, MW Craig, N Dencheva, A Ginsburg, et al. The astropy project: Building an open-science project and status of the v2. 0 core package. *The Astronomical Journal*, 156(3):123, 2018.

[107] IEEE standard for definitions of terms for antennas. pages 1–50, March 2014.

[108] John D Kraus and Ronald J Marhefka. *Antenna for all applications*. McGraw-Hill, 2002.

Appendix A
Additional Information for the A2 source search

A.1 Coordinate Systems

A.1.1 Celestial object coordinates

To perform a source search, one needs to determine the position of the object as a function of time. For this analysis, we choose Centaurus A (Cen A) to be the celestial object for which we will do the analysis.

The location of Cen A as a function of time is determined with the `SkyCoord` class of the `Astropy` [106] package. For a given time and position on the Earth (latitude and longitude), the program returns the location of Cen A given in azimuth and zenith angles with sub-arcsecond accuracy. The coordinate system that `Astropy` uses is a horizontal coordinate system where the azimuth is oriented East of North, and increases eastward (clockwise), i.e. N = 0°, E = 90°, S = 180°, W = 270°. The zenith angle is defined as the complementary angle of the altitude, which is defined as the angle between the observer and the celestial body. Figure A.1 describes `Astropy` coordinate system. Figure A.2 shows the way the azimuth angle is defined and measured in this system.

One of the advantages of this method is that one can explicitly specify where on Earth the observation location is, taking care of any associated rotations and corrections.

A.1.2 ARA global coordinates

We use the coordinate system set by South Pole surveyors, setting the origin at (15.240 km Easting, 15.250 km Northing). The y-axis (azimuth = 90°) of the South Pole surveyor system is parallel to the Northing unit vector, which is defined to lie along the Prime Meridian. The x-axis is consequently parallel to the local Easting unit vector, producing

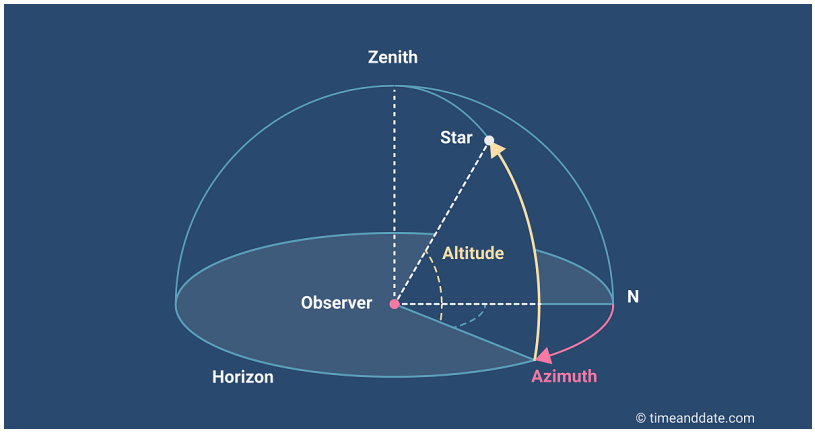

Figure A.1: Horizontal coordinate system, also known as the Altitude-Azimuth system used by `Astropy` to return the location of a celestial body. Figure from [32].

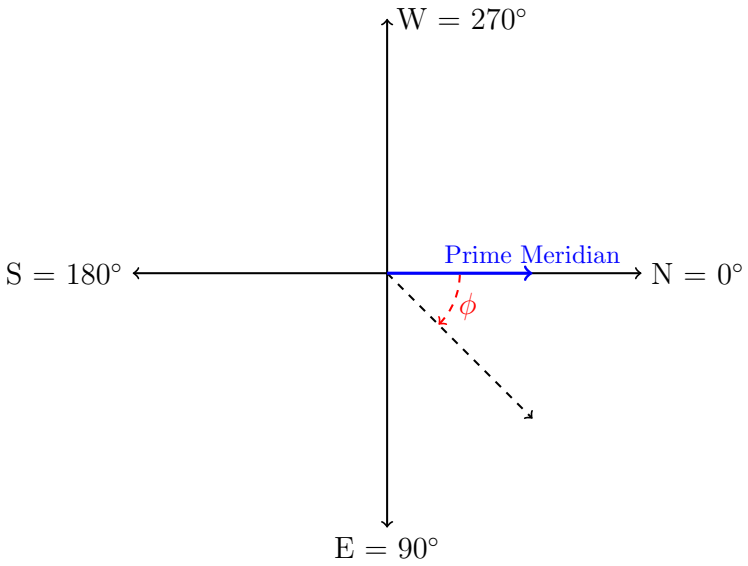

Figure A.2: Coordinate system for the azimuth angle (ϕ) used by `Astropy`. The azimuth angle is measured in a clock-wise fashion, with $\phi = 0$ aligned with the Prime Meridian (North).

the following coordinate system definition: E = 0°, N = 90° = Prime Meridian[1], W = 180°, and S = −90°.

[1]It is important to notice that this is different from the standard definition of longitude, where the Prime Meridian is defined to be at N = 0°. This will have to be taken into account when one does the coordinate transformation between `Astropy` and ARA's local coordinate system.

Station	Latitude	Longitude
Testbed	-89.97	-74.44
A2	-89.96	-109.83
A3	-89.95	-88.17

Table A.1: Table of the latitud and longitude of A2 and A3, in degrees. These can be substituted in Astropy's `EarthLocation` function to obtain the locations of celestial bodies in the global coordinate frame of A2 or A3.

From the station positions, one can determine the latitude and longitude at which they are located. Table A.1 contains the latitude and longitude for ARA Testbed, and ARA stations 2 and 3.

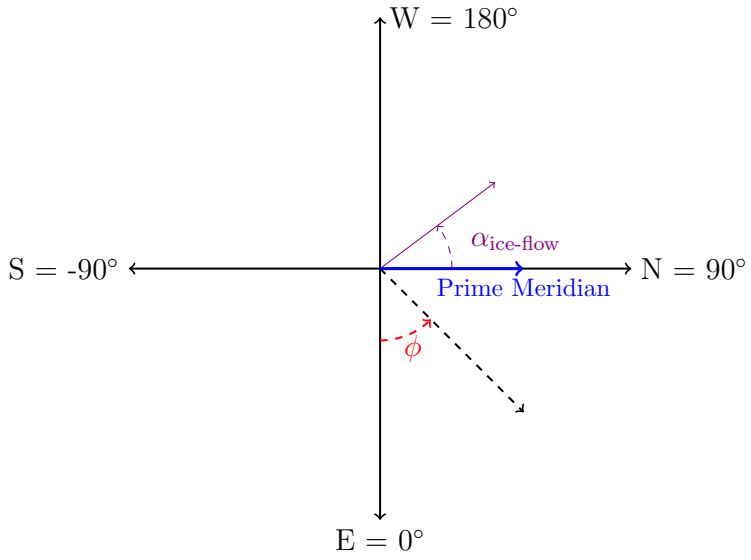

Figure A.3: Azimuth coordinate system for the ARA global coordinates. Unlike the `Astropy` azimuth coordinate system, the azimuth angle (ϕ) is measured in a counter clockwise direction and $\phi \in [-180°, 180°]$, with $\phi = 0$ aligned with the Easting vector. Note that in this convention the Northing vector is parallel to the Prime Meridian, but does not correspond to an azimuth of $\phi = 0$, as it is standard. The purple vector indicates the direction of the ice-flow, which makes an angle of $\alpha_{\text{ice-flow}} = 36.773°$

A.1.3 A2 and A3 Local Coordinates

Since the position of the stations A2 and A3 is not at the global origin, a translation is required to locate their respective DAQ box. Additionally, the orientation of the local coordinate system has to be rotated so it aligns with the ice-flow direction. The ice-flow is 36.773° W (where N is the Prime Meridian), meaning that the y-axis of the local coordinate system is rotated counter-clockwise by an angle of 36.773° + 90° = 126.773° with respect to the surveyor coordinate system. As discussed before, the 90° account for the phase difference between the standard latitude convention and the convention adopted by the South Pole surveyor system.

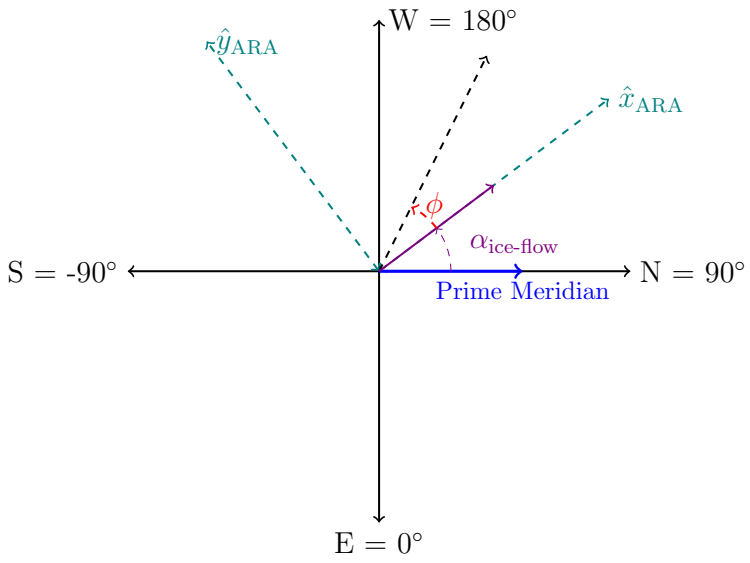

Figure A.4: Azimuth coordinate system for the ARA local coordinates. For the global coordinate system, the x-axis was aligned with the Easting vector, but for the local ARA coordinate system the axes were rotated by 126.773° so the x-axis is parallel to the ice-flow direction. The azimuth angle still is measured in a counterclockwise fashion and $\phi \in [-180°, 180°]$ as in the global coordinate system.

A.1.4 Interferometric map coordinate transformation

The reconstruction maps obtained from reconstructing the signal with the interferometric technique set its origin at $\theta = 0$ corresponding to a horizontal view from the center of the station (one can imagine to be sitting of top of an antenna, and looking horizontally), and $\phi = 0$ corresponding to the direction of the Antarctic continent ice-flow, as the local

coordinate convention. The interferometric map gets rotated by a similar amount so it gets aligned with the global coordinates.

Unlike `Astropy`, the azimuth angle is reported in a counter-clockwise fashion and in a coordinate system where E=0°, N=90°, W=180°, S=-90°. We thus want to convert the `Astropy` coordinates to ARA global coordinates, since our analysis will be done in ARA's framework. To do this, we construct the function `convertToARACoord` which does the desired operation:

```
def convertToARACoord(phi_AstroPy):
    phi_CCW = np.mod(np.pi/2-phi_AstroPy,2*np.pi) # Convert from CW coord. system to CCW
    phi_ARA = np.mod((phi_CCW+np.pi),2*np.pi)-np.pi+np.pi/2 #Convert from [0,360] to [-180,180] + 90 deg out of phase with Prime Meridian
    return phi_ARA
```

The code and utilities to perform these transformations are stored in `returnCenA.py`.

Example and cross-check validation

We want to validate this method by comparing to the location of observed signals by ARA. Since the location of the calibration pulsers is fixed, we would like to use a dynamic source as a reference that has been observed by ARA. We choose the Sun. ARA published results on the observation and reconstruction of radio emission coincident with a solar flare [33], so we can use the same data to validate our tracking algorithm and coordinate system. The radio emission was observed by ARA's prototype station, also known as ARA Testbed. This instrument was located at a longitude of 74.22° W from Primer Meridian

We use `Astropy` to set the observation location at the Testbed, located at the South Pole but at longitude of 74.22° W from Prime Meridian, and at a depth of ~ 30 m:

```
import astropy.units as u #astropy's units module
from astropy.time import Time
from astropy.coordinates import SkyCoord, EarthLocation, AltAz

south_pole = EarthLocation(lat=-90.0*u.deg, lon=-74.22*u.deg, height=-30*u.m) #Location of ARA Testbed
```

We then use Astropy's function `get_sun` to obtain the Sun location at a given time. Since we want to cross-check with the solar flare data, we choose a period of time between 2:00 and 3:00 hours UTC on February 15 2011:

```
from astropy.coordinates import get_sun

utcoffset = -0*u.hour  # No UTC offset, as the South Pole uses UTC
time = Time('2011-2-15 00:30:00') - utcoffset
```

```
delta_endtime = np.linspace(0, 90, 90*2)*u.minute #Times at which we want
    the  location. I'm choosing to get the location of the Sun for 90 min
    after time, twice a minute.
frame_endtime = AltAz(obstime=time+delta_endtime, location=south_pole) #Get
    coordinates of observation point
sunaltazstimeRange = get_sun(timestimeRange).transform_to(frametimeRange)#
    Get Sun coordinates and transform to local coor. system.
```

Because `Astropy` reports results for the azimuth angle $\phi \in [0, 360]$ and there is a discrepancy between the coordinate system in which the results are in and ARA's coordinate system, these need to be converted to the same range and coordinate system used by the interferometric maps to match them with the data points. We do this by applying the function `convertToARACoord` that we previously defined.

We compare the Sun location at those times with the data obtained from the solar flare analysis. The comparison can be seen in Figure A.5

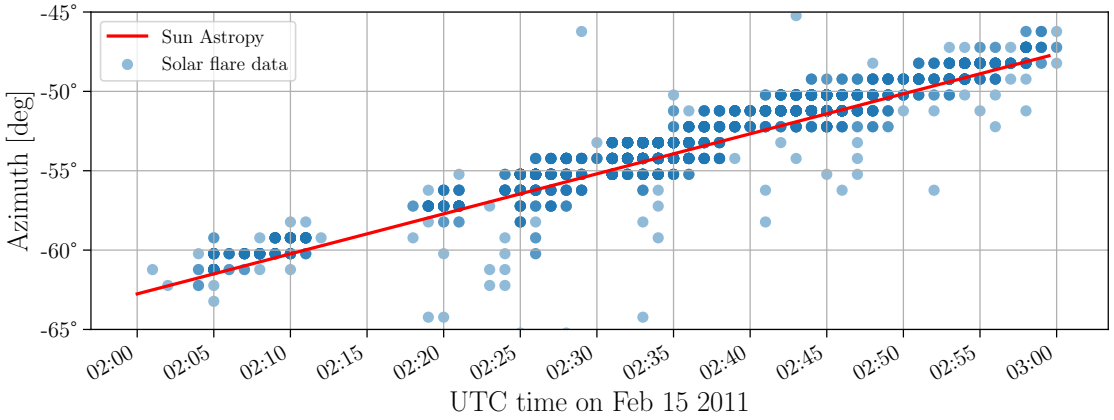

Figure A.5: Position of the Sun as seen from the Testbed instrument as a function of time for the day in which the solar flares were observed by the instrument. The red line corresponds to the expected Sun location obtained with `Astropy`, and the blue dots correspond to the interferometric reconstruction of ARA Testbed triggered events. As it can be seen, the red line matches qualitatively well the data points (for a quantitative treatment, see the solar flare paper [33])

Appendix B

Additional information for the reconstruction chapter

B.1 Polarization angle calculation

Let ϕ and θ the azimuth and zenith angles, respectively, at which the signal arrives at the antennas. Because the Vpol antenna and Hpol antenna in AraSim are relatively close to each other ($\sim$ 2 m), and because we expect the neutrino vertex to be away from the antennas, we can assume that these angles are the same for both adjacent antennas.

We also know R, the ratio of deconvolved amplitudes, in terms of the polarization vector and the spherical unit vectors $\hat{\theta}$ and $\hat{\phi}$, which becomes the first equation of our system of equations

$$R \equiv \frac{A_H}{A_V} = \frac{\hat{p} \cdot \hat{\phi}}{\hat{p} \cdot \hat{\theta}}, \tag{B.1}$$

where $\hat{p} = (p_x, p_y, p_z)$ is the unit polarization vector of the electric field arriving at the antennas. $\hat{p}$ is what we want to determine.

We can write $\hat{\phi}$ and $\hat{\theta}$ in terms of the arrival angles ϕ and θ:

$$\hat{\phi} = (-\sin\phi, \cos\phi, 0) \tag{B.2}$$

$$\hat{\theta} = (\cos\theta\cos\phi, \cos\theta\sin\phi, \sin\theta). \tag{B.3}$$

Therefore

$$\hat{p} \cdot \hat{\phi} = -p_x \sin\phi + p_y \cos\phi \tag{B.4}$$

$$\hat{p} \cdot \hat{\theta} = p_x \cos\theta\cos\phi + p_y \cos\theta\sin\phi - p_z \sin\theta \tag{B.5}$$

Let us also define the arriving vector at the antenna (which technically is the Poynting unit vector) in terms of ϕ and θ

$$\hat{d} = (\sin\theta\cos\phi, \sin\theta\sin\phi, \cos\theta). \tag{B.6}$$

We can use the orthogonality of the polarization unit vector $\hat{p}$ and the propagation unit vector $\hat{d}$ to obtain the second equation of our system of equations:

$$\hat{p} \cdot \hat{d} = p_x \sin\theta \cos\phi + p_y \sin\theta \sin\phi + p_z \cos\theta \tag{B.7}$$

$$= 0 \tag{B.8}$$

The third and final equation comes from the fact that the polarization unit vector is normalized to 1

$$|\hat{p}|^2 = 1 \tag{B.9}$$

The system of equations composed of Equation B.1, Equation B.8, Equation B.9 can be solved, yielding

$$p_x = \pm \frac{\cos\theta \cos\phi - R \sin\phi}{\sqrt{1+R^2}}, \tag{B.10}$$

$$p_y = \pm \frac{\cos\theta \sin\phi + R \cos\phi}{\sqrt{1+R^2}}, \tag{B.11}$$

$$p_z = \mp \frac{\sin\theta}{\sqrt{1+R^2}}. \tag{B.12}$$

B.2 Calculation of pulser SNR at ARIANNA's site

We use A1 to perform this calculation, as data for that station exists in Besson's *et al.* paper [83]. The geodesic between A1 and the SPICEcore pulser has a length of R_{ARA} =1561.82 m, when the pulser was lowered at about 800 m. At that distance, the measured SNR was ≈ 10, from Fig. 10 in the paper (Top 4 VPols). Similarly, from the ARIANNA's polarization paper [91], the ARIANNA station was at a horizontal distance of 953 m and at a vertical distance of 1100 with respect to the SPICEcore pulser. This yields a vector connecting the pulser and ARIANNA whose length is R_{ARIANNA} =1244.27 m.

The attenuation factor of RF in ice is given by

$$F_{\text{att}} = \exp\left(-R/L_{\text{att}}\right), \tag{B.13}$$

where R is the distance traveled by the ray and $L_{\text{att}} = 690$ m is the average attenuation length of RF in ice measured by ARA [78]. From this, we get that the attenuation factors for the A1 and ARIANNA stations are

$$F_{\text{att},ARA} = 0.103 \tag{B.14}$$

$$F_{\text{att},ARIANNA} = 0.165, \tag{B.15}$$

respectively.

A signal emitted by the pulser will be attenuated as follows

$$A_{\mathrm{Rx}} = A_{\mathrm{Tx}} \frac{F_{\mathrm{att}}}{R}, \tag{B.16}$$

where A_{Rx} is the signal measured at the receiver and A_{Tx} is the signal measured at the transmitter, when they are separated by a distance R. From this, we can estimate the signal-to-noise ratio (SNR) that an ARA station located at ARIANNA's site would measure:

$$SNR_{\mathrm{ARIANNA}} = \frac{F_{\mathrm{att},ARIANNA} R_{\mathrm{ARA}}}{F_{\mathrm{att},ARIANNA} R_{\mathrm{ARIANNA}}} = 20.3. \tag{B.17}$$

B.3 Useful antenna definitions

There are many factors that influence the performance of an antenna, and that are of great importance when designing a device for a particular task. In this subsection we will describe the most important ones regarding receiving antennas. Definitions in quotation marks are from the *IEEE Standard for Definitions of Terms for Antennas* [107].

Gain

The gain is "the ratio of the radiation intensity in a given direction to the radiation intensity that would be produced if the power accepted by the antenna were isotropically radiated." Mathematically, the gain factor is

$$G = 4\pi \frac{U(\theta, \phi)}{P_{in}(\text{lossless isotropic source})}, \tag{B.18}$$

where $U(\theta, \phi)$ is the radiated power per solid angle of the antenna, and P_{in} is the total input power.

Gain is usually expressed in dBi, scaled with respect to an ideal, isotropic radiator. The gain of an antenna in dBi can be found from the gain factor as follows:

$$G_{\mathrm{dBi}} = 10 \cdot \log_{10}(G). \tag{B.19}$$

For example, an antenna of gain factor $G = 2$, meaning that the antenna emits/receives twice the power relative to an isotropic antenna, has a gain of $\sim$3 dBi.

Efective area

The effective area is "in a given direction, the ratio of the available power at the terminals of a receiving antenna to the power flux density of a plane wave incident on the antenna from that direction, the wave being polarization matched to the antenna. If the direction is not specified, the direction of maximum radiation intensity is implied." This area is related

to the gain G as follows:

$$A_e = \frac{P}{S} = \frac{G\lambda^2}{4\pi}, \tag{B.20}$$

where $\lambda = c/\nu$ is the wavelength, and S is the Poynting vector. In other words, the output power of an antenna in watts (W) is equal to the power density of the radio waves (W/m^2) multiplied by its aperture (m^2): $P = A_e \cdot S$.

Effective height

A receiving antenna captures electromagnetic waves, which need to physically hit it, and extracts power from them by converting it to a voltage induced on the open-circuit terminals of the antenna. There are antennas which are not defined by a physical area, e.g., monopoles and dipoles, and thus cannot be characterized by an effective area. For them, the effective height $\boldsymbol{h_e}$ plays an analogous role as the effective area for aperture antennas and it helps to characterize the degree of polarization mismatch that may exist between the incident field and the antenna. $\boldsymbol{h_e}$ is a complex vector in the $\theta\phi$-plane:

$$\boldsymbol{h_e}(\theta, \phi) = \hat{\boldsymbol{e}}_{\boldsymbol{\theta}} h_\theta(\theta, \phi) + \hat{\boldsymbol{e}}_{\boldsymbol{\phi}} h_\phi(\theta, \phi), \tag{B.21}$$

and its magnitude is given in meters.

Let $\boldsymbol{E}$ be the incident electric field, and V_{oc} be the open circuit voltage at antenna terminals. The vector effective height $\boldsymbol{h_e}$ is related to the last two quantities in the following way:

$$V_{oc} = \boldsymbol{E} \cdot \boldsymbol{h_e} \tag{B.22}$$

Note that no voltage is induced if the polarizations of the antenna and the electric field are orthogonal to each other.

VSWR

The voltage standing wave ratio (VSWR) relates the reflected power P_R to the transmitted power P_T on an antenna in the following way:

$$\frac{P_R}{P_T} = \left(\frac{\text{VSWR} - 1}{\text{VSWR} + 1}\right)^2. \tag{B.23}$$

VSWR also satisfies the following:

$$\text{VSWR}(\nu) = \frac{|\rho(\nu) + 1|}{|\rho(\nu) - 1|}, \tag{B.24}$$

where $\rho(\nu)$ is the complex voltage coefficient of the antenna (the ratio of the electric field strength of the reflected wave to that of the incident wave) and is related to the effective

power transmission coefficient T as follows

$$T(\nu) = |1 - \rho(\nu)|^2. \tag{B.25}$$

VSWR= 1 denotes full transmission of the wave (no reflections), as can be seen from Eq. B.25, and thus no standing wave along the transmission line[2]. On the other hand, very high values mean high reflection and standing wave behavior along the transmission line.

Antenna temperature

Every object whose temperature is not zero Kelvin emits radiation described by Planck's law. This radiation can be intercepted by an antenna, creating unwanted noise. The quantification of this noise is important, as it could be greater than the expected signal, and we describe it below.

Consider an antenna of narrow beam whose pattern is confined to a solid angle $d\Omega$ and is pointed toward the (θ, ϕ) direction. The received power in $d\Omega$ is

$$\frac{dP_{\text{rec}}}{d\Omega} = \frac{k_B T(\theta,\phi) G(\theta,\phi) \Delta\nu}{4\pi}, \tag{B.26}$$

where $T(\theta, \phi)$ is the temperature of the source at those angles, $G(\theta, \phi)$ is the gain, k_B is the Boltzmann constant, and $\Delta\nu$ is the frequency bandwidth of the receiver. Integrating over all the angles yields the total received power:

$$\begin{aligned} P_{\text{total}} &= \frac{k_B \Delta\nu}{4\pi} \int_{4\pi} G(\theta,\phi) T(\theta,\phi) d\Omega \\ &= k_B \Delta\nu T_{\text{ant}}, \end{aligned} \tag{B.27}$$

where

$$T_{\text{ant}} = \frac{1}{4\pi} \int_{4\pi} G(\theta,\phi) T(\theta,\phi) d\Omega. \tag{B.28}$$

This parameter describes how much noise an antenna produces in a given environment, and does not represent the physical temperature of the antenna. Significant contributions to the antenna temperature can come from small GT products over large areas (low-gain antennas looking all over the sky), or large GT products over small areas (high-gain antennas looking over a small area).

Signal-to-noise ratio (SNR)

The signal-to-noise ratio is defined as the ratio of the signal voltage to the thermal noise voltage. Here we derive the SNR in terms of other antenna parameters.

[2]A transmission line is the device (usually a coaxial cable) used to transmit radio frequency energy between the antenna and the radio receiver/transmitter.

The expected signal strength E_0 induces a voltage at the antenna receiver given by[3]

$$V_s = h_e E_0 \Delta\nu. \tag{B.29}$$

Kraus [108] derives the following expression for the antenna effective height h_e

$$h_e = 2\sqrt{\frac{Z_a \eta A_e}{Z_0}} \cos\theta_p, \tag{B.30}$$

where Z_a is the antenna radiation resistance, η is the antenna efficiency, A_e is the effective area, $Z_0 = 377\,\Omega$ is the impedance of free space, and θ_p is the polarization angle of the antenna with respect to the plane of polarization of the radiation. Thus,

$$V_s = 2\sqrt{\frac{Z_a \eta A_e}{Z_0}} \cos\theta_p E_0 \Delta\nu. \tag{B.31}$$

Similarly, from the fact that $P = \frac{E^2 A_e}{Z_0}$ (cf. Eq. B.20) and Eq. B.27, one can get the average thermal noise voltage in the system

$$V_n = \sqrt{4 k_B T_{\text{ant}} Z_a \Delta\nu}. \tag{B.32}$$

Thus, the SNR is

$$SNR \equiv \frac{V_s}{V_n} = E_0 \cos\theta_p \sqrt{\frac{\eta A_e \Delta\nu}{k_B T_{\text{ant}} Z_0}}. \tag{B.33}$$

One can find the minimum detectable field strength by setting SNR=1 in the last equation and solving for E_0.

B.4 Neutrino directional resolution plots

The following figures correspond to the values shown in Table 3.1. We can notice how the shape of the blob where most of the events are contained changes as we scan over different uncertainties for the polarization angles, the launch angles, and the viewing angles.

[3]The units of E_0 are given in the Fourier domain [V/m/Hz].

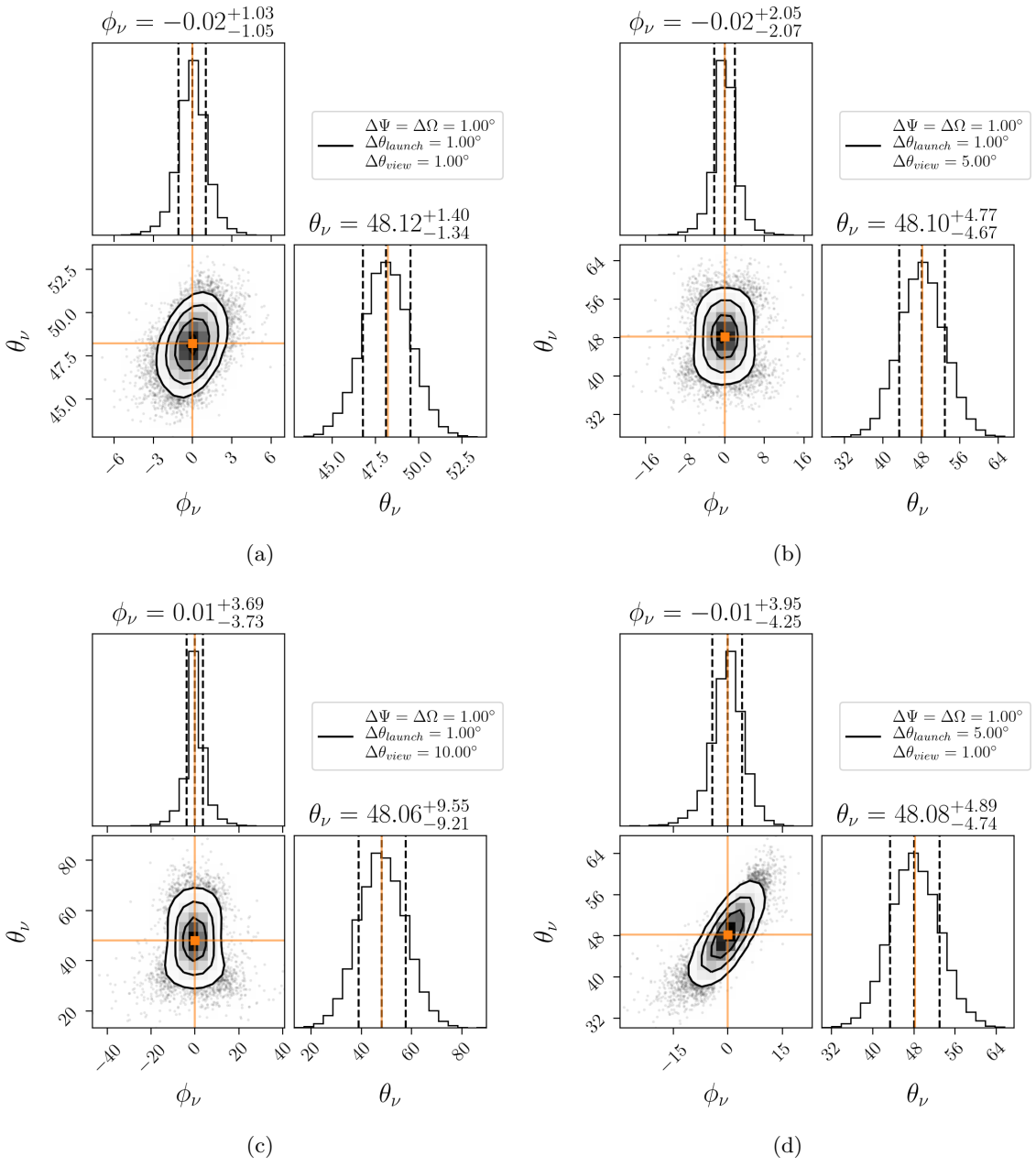

Figure B.1: Corner plots for the different uncertainties in Table 3.1.

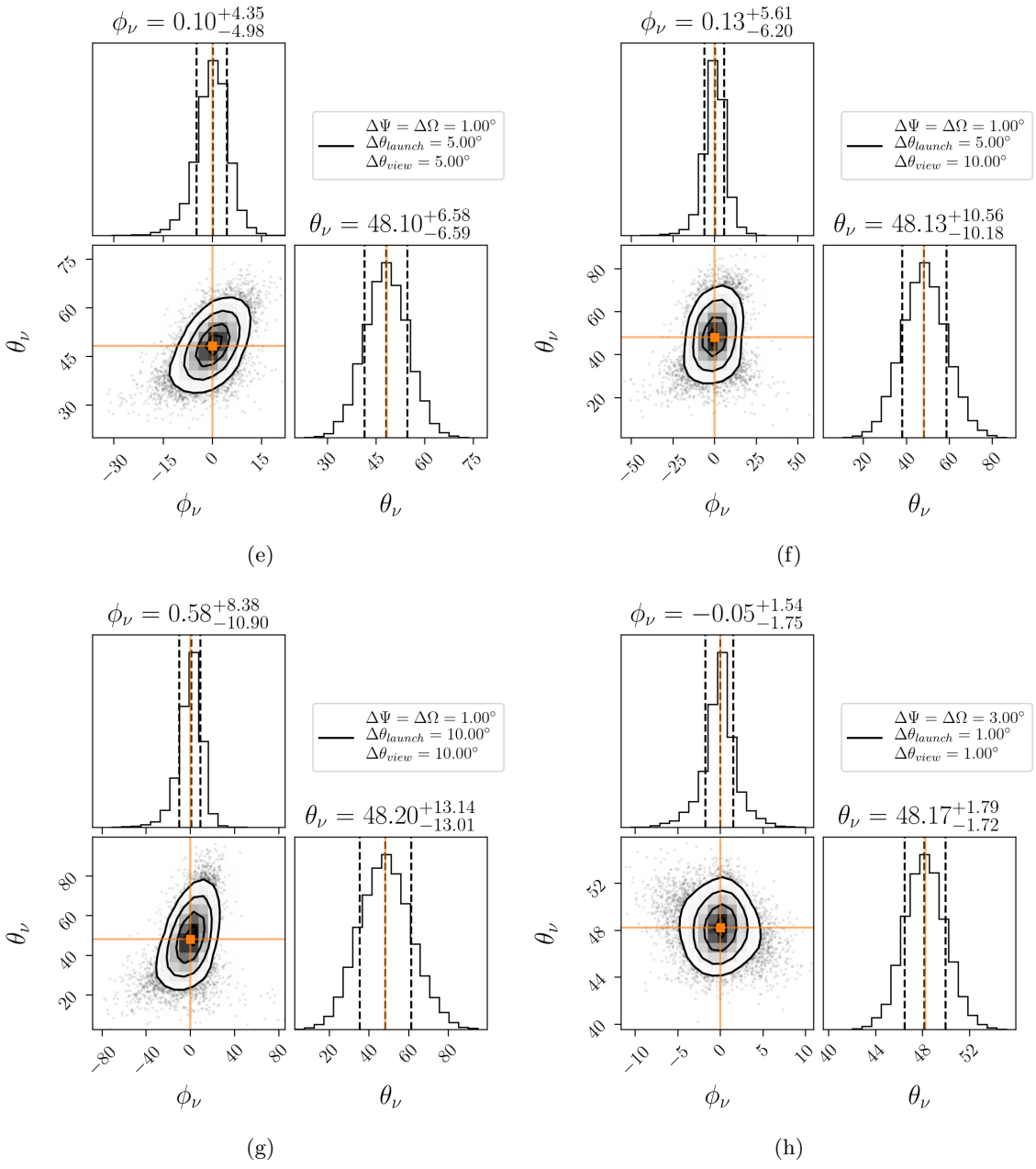
$\phi_\nu = 0.10^{+4.35}_{-4.98}$
$\theta_\nu = 48.10^{+6.58}_{-6.59}$
$\Delta\Psi = \Delta\Omega = 1.00°$
$\Delta\theta_{launch} = 5.00°$
$\Delta\theta_{view} = 5.00°$
(e)
$\phi_\nu = 0.13^{+5.61}_{-6.20}$
$\theta_\nu = 48.13^{+10.56}_{-10.18}$
$\Delta\Psi = \Delta\Omega = 1.00°$
$\Delta\theta_{launch} = 5.00°$
$\Delta\theta_{view} = 10.00°$
(f)
$\phi_\nu = 0.58^{+8.38}_{-10.90}$
$\theta_\nu = 48.20^{+13.14}_{-13.01}$
$\Delta\Psi = \Delta\Omega = 1.00°$
$\Delta\theta_{launch} = 10.00°$
$\Delta\theta_{view} = 10.00°$
(g)
$\phi_\nu = -0.05^{+1.54}_{-1.75}$
$\theta_\nu = 48.17^{+1.79}_{-1.72}$
$\Delta\Psi = \Delta\Omega = 3.00°$
$\Delta\theta_{launch} = 1.00°$
$\Delta\theta_{view} = 1.00°$
(h)

Figure B.1

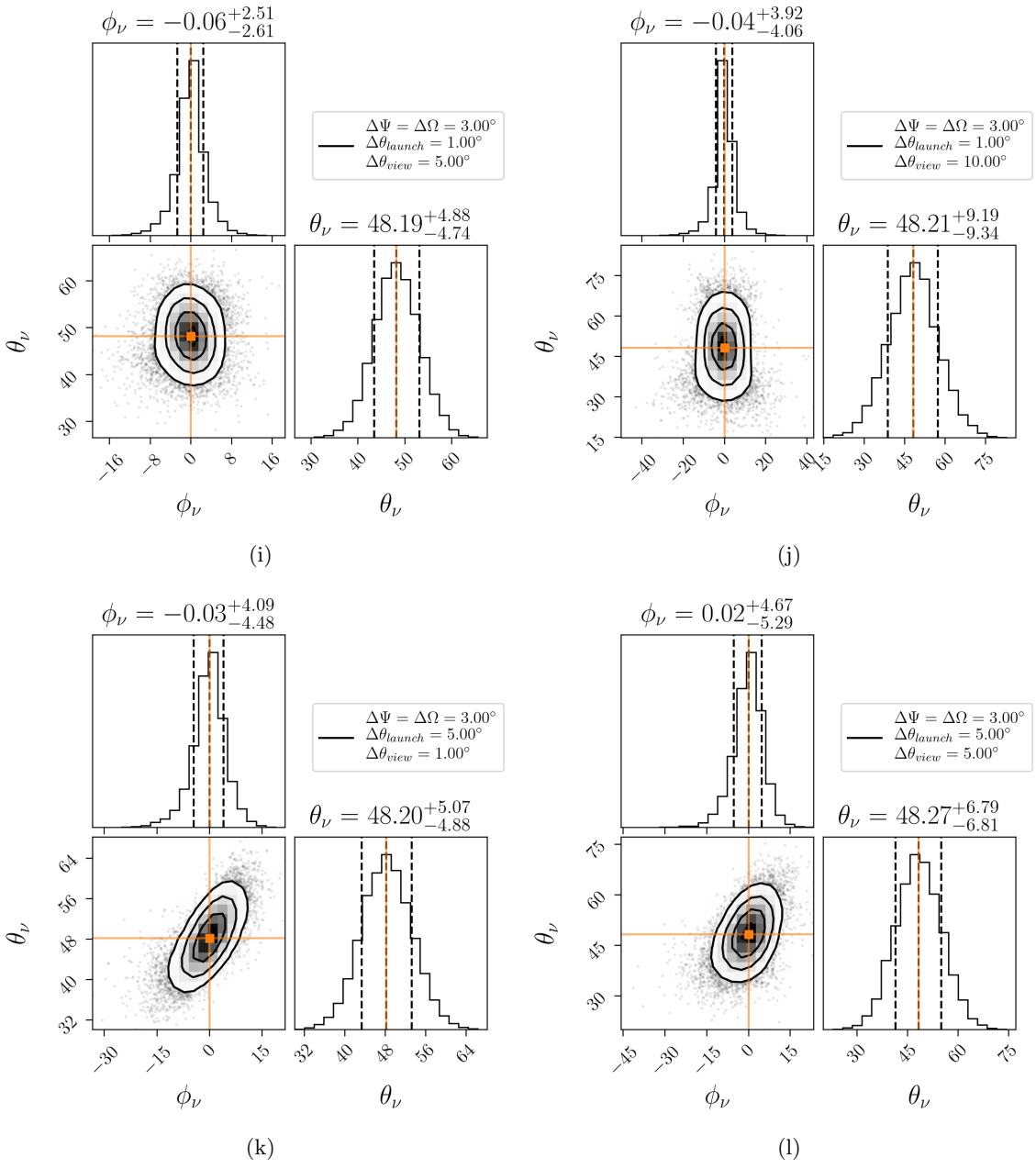
$\phi_\nu = -0.06^{+2.51}_{-2.61}$
$\theta_\nu = 48.19^{+4.88}_{-4.74}$
$\Delta\Psi = \Delta\Omega = 3.00°$
$\Delta\theta_{launch} = 1.00°$
$\Delta\theta_{view} = 5.00°$
(i)
$\phi_\nu = -0.04^{+3.92}_{-4.06}$
$\theta_\nu = 48.21^{+9.19}_{-9.34}$
$\Delta\Psi = \Delta\Omega = 3.00°$
$\Delta\theta_{launch} = 1.00°$
$\Delta\theta_{view} = 10.00°$
(j)
$\phi_\nu = -0.03^{+4.09}_{-4.48}$
$\theta_\nu = 48.20^{+5.07}_{-4.88}$
$\Delta\Psi = \Delta\Omega = 3.00°$
$\Delta\theta_{launch} = 5.00°$
$\Delta\theta_{view} = 1.00°$
(k)
$\phi_\nu = 0.02^{+4.67}_{-5.29}$
$\theta_\nu = 48.27^{+6.79}_{-6.81}$
$\Delta\Psi = \Delta\Omega = 3.00°$
$\Delta\theta_{launch} = 5.00°$
$\Delta\theta_{view} = 5.00°$
(l)

Figure B.1

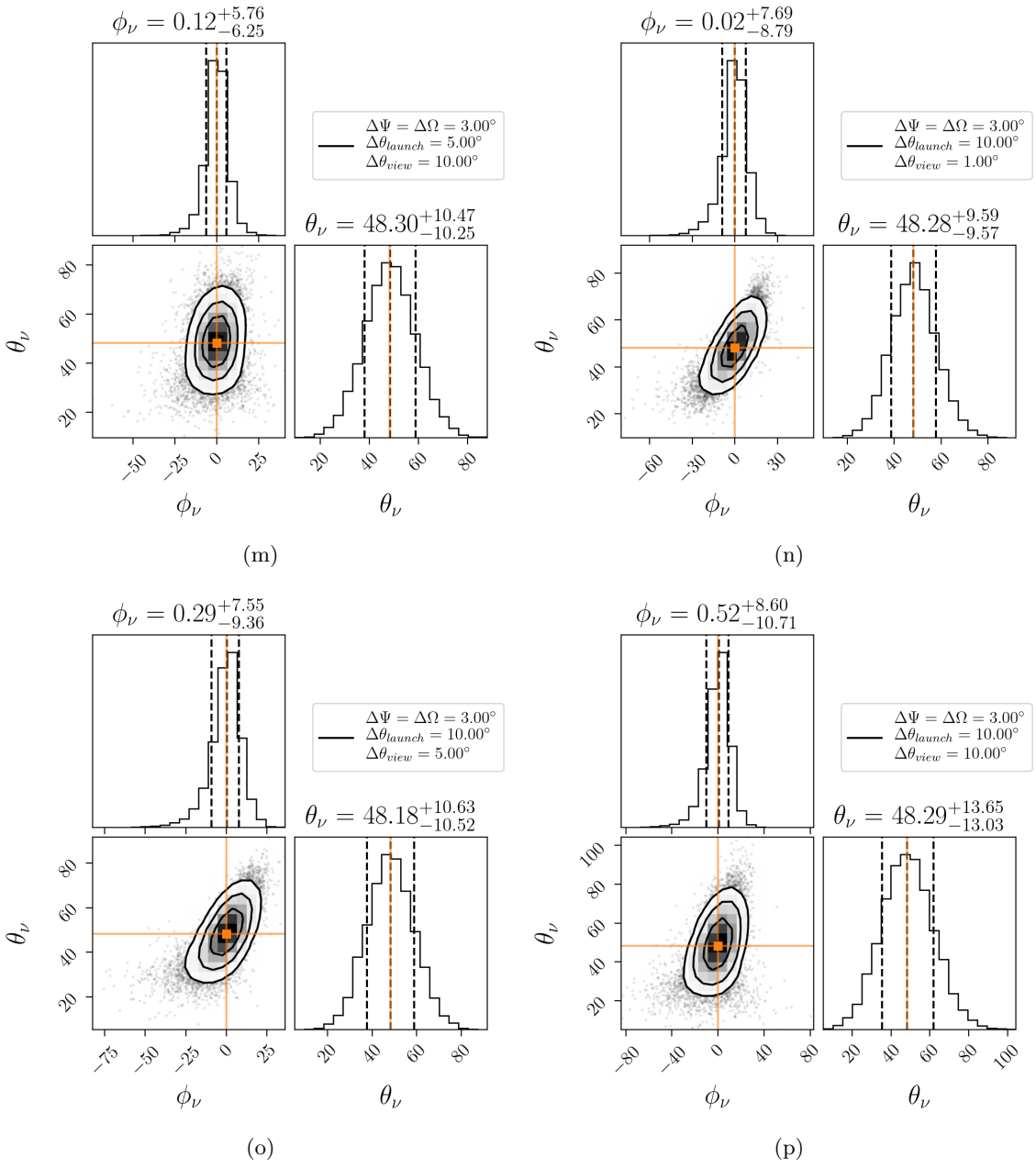
$\phi_\nu = 0.12^{+5.76}_{-6.25}$
$\theta_\nu = 48.30^{+10.47}_{-10.25}$
$\Delta\Psi = \Delta\Omega = 3.00°$
$\Delta\theta_{launch} = 5.00°$
$\Delta\theta_{view} = 10.00°$
(m)
$\phi_\nu = 0.02^{+7.69}_{-8.79}$
$\theta_\nu = 48.28^{+9.59}_{-9.57}$
$\Delta\Psi = \Delta\Omega = 3.00°$
$\Delta\theta_{launch} = 10.00°$
$\Delta\theta_{view} = 1.00°$
(n)
$\phi_\nu = 0.29^{+7.55}_{-9.36}$
$\theta_\nu = 48.18^{+10.63}_{-10.52}$
$\Delta\Psi = \Delta\Omega = 3.00°$
$\Delta\theta_{launch} = 10.00°$
$\Delta\theta_{view} = 5.00°$
(o)
$\phi_\nu = 0.52^{+8.60}_{-10.71}$
$\theta_\nu = 48.29^{+13.65}_{-13.03}$
$\Delta\Psi = \Delta\Omega = 3.00°$
$\Delta\theta_{launch} = 10.00°$
$\Delta\theta_{view} = 10.00°$
(p)

Figure B.1

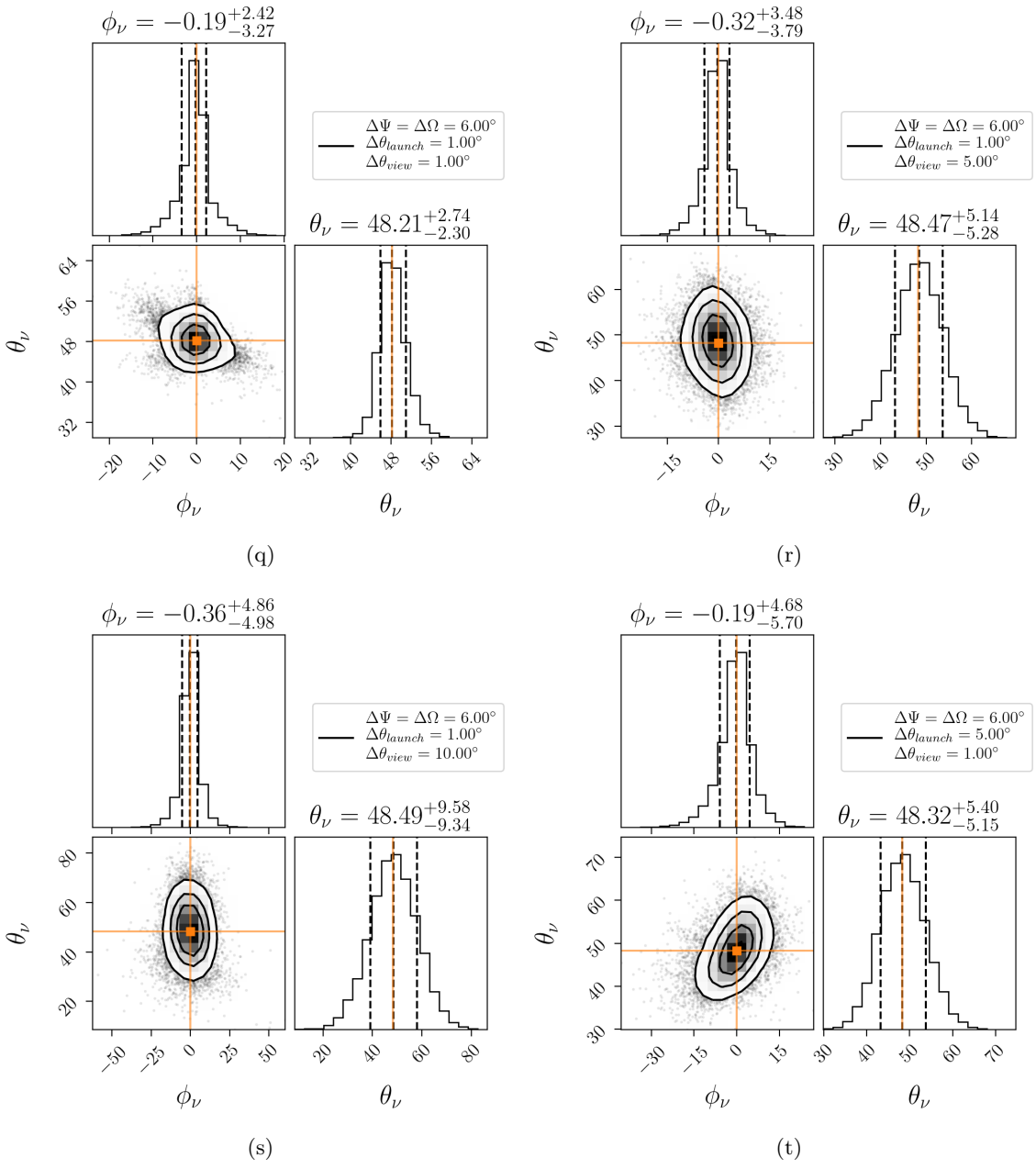
$\phi_\nu = -0.19^{+2.42}_{-3.27}$
$\theta_\nu = 48.21^{+2.74}_{-2.30}$
$\Delta\Psi = \Delta\Omega = 6.00°$
$\Delta\theta_{launch} = 1.00°$
$\Delta\theta_{view} = 1.00°$
(q)
$\phi_\nu = -0.32^{+3.48}_{-3.79}$
$\theta_\nu = 48.47^{+5.14}_{-5.28}$
$\Delta\Psi = \Delta\Omega = 6.00°$
$\Delta\theta_{launch} = 1.00°$
$\Delta\theta_{view} = 5.00°$
(r)
$\phi_\nu = -0.36^{+4.86}_{-4.98}$
$\theta_\nu = 48.49^{+9.58}_{-9.34}$
$\Delta\Psi = \Delta\Omega = 6.00°$
$\Delta\theta_{launch} = 1.00°$
$\Delta\theta_{view} = 10.00°$
(s)
$\phi_\nu = -0.19^{+4.68}_{-5.70}$
$\theta_\nu = 48.32^{+5.40}_{-5.15}$
$\Delta\Psi = \Delta\Omega = 6.00°$
$\Delta\theta_{launch} = 5.00°$
$\Delta\theta_{view} = 1.00°$
(t)

Figure B.1

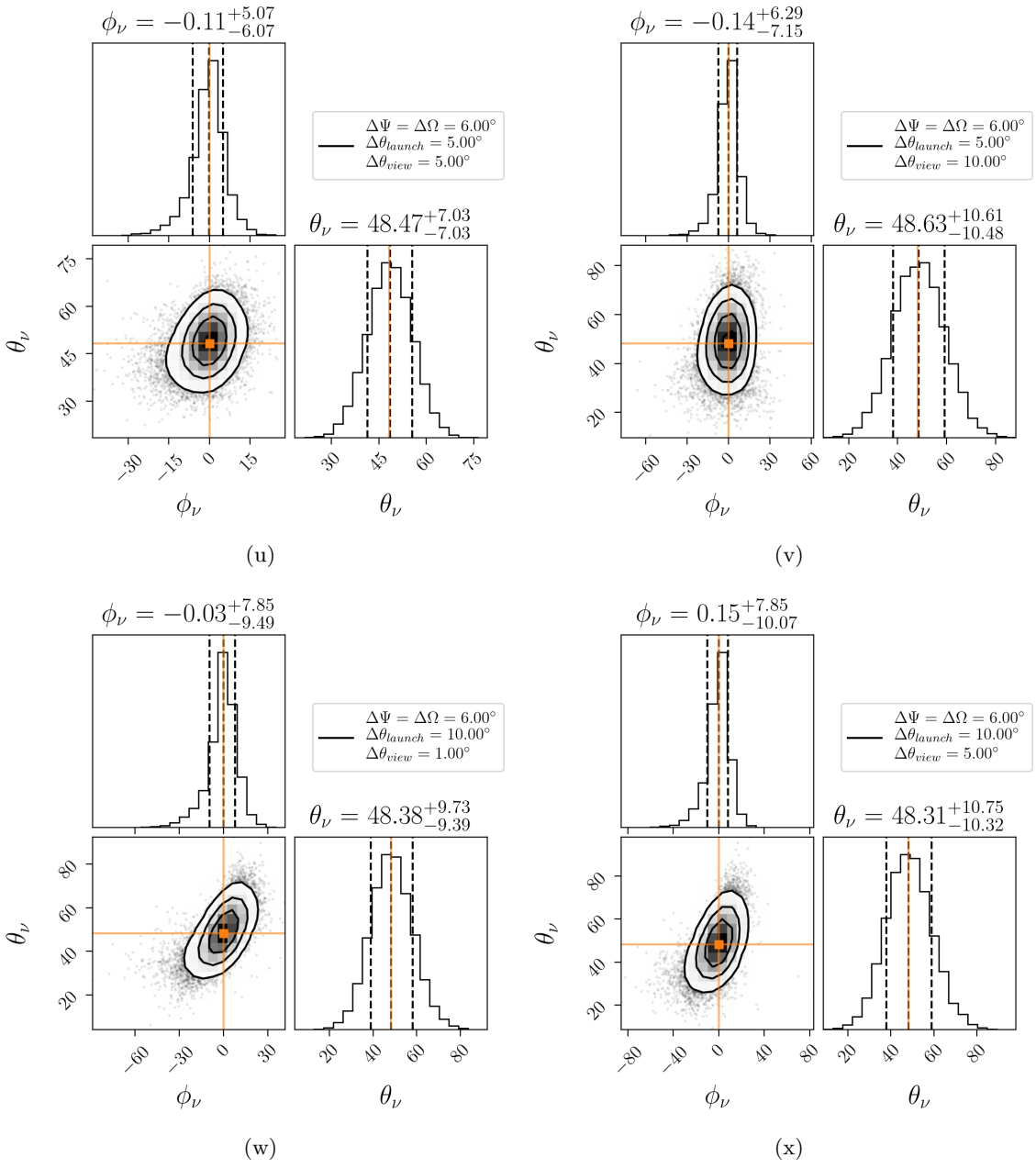
$\phi_\nu = -0.11^{+5.07}_{-6.07}$
$\theta_\nu = 48.47^{+7.03}_{-7.03}$
$\Delta\Psi = \Delta\Omega = 6.00°$
$\Delta\theta_{launch} = 5.00°$
$\Delta\theta_{view} = 5.00°$
(u)
$\phi_\nu = -0.14^{+6.29}_{-7.15}$
$\theta_\nu = 48.63^{+10.61}_{-10.48}$
$\Delta\Psi = \Delta\Omega = 6.00°$
$\Delta\theta_{launch} = 5.00°$
$\Delta\theta_{view} = 10.00°$
(v)
$\phi_\nu = -0.03^{+7.85}_{-9.49}$
$\theta_\nu = 48.38^{+9.73}_{-9.39}$
$\Delta\Psi = \Delta\Omega = 6.00°$
$\Delta\theta_{launch} = 10.00°$
$\Delta\theta_{view} = 1.00°$
(w)
$\phi_\nu = 0.15^{+7.85}_{-10.07}$
$\theta_\nu = 48.31^{+10.75}_{-10.32}$
$\Delta\Psi = \Delta\Omega = 6.00°$
$\Delta\theta_{launch} = 10.00°$
$\Delta\theta_{view} = 5.00°$
(x)

Figure B.1

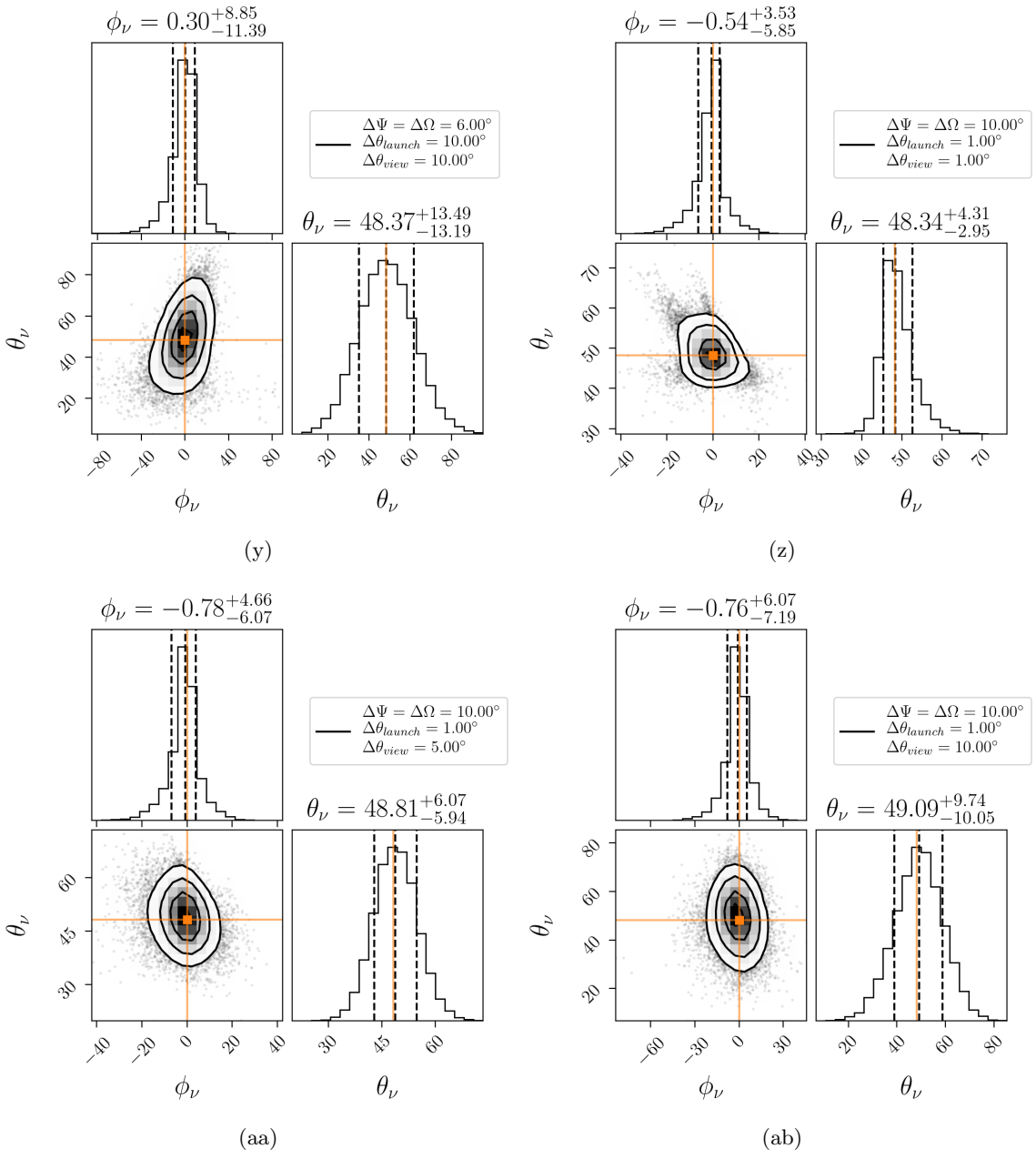
$\phi_\nu = 0.30^{+8.85}_{-11.39}$
$\theta_\nu = 48.37^{+13.49}_{-13.19}$
$\Delta\Psi = \Delta\Omega = 6.00°$
$\Delta\theta_{launch} = 10.00°$
$\Delta\theta_{view} = 10.00°$
(y)
$\phi_\nu = -0.54^{+3.53}_{-5.85}$
$\theta_\nu = 48.34^{+4.31}_{-2.95}$
$\Delta\Psi = \Delta\Omega = 10.00°$
$\Delta\theta_{launch} = 1.00°$
$\Delta\theta_{view} = 1.00°$
(z)
$\phi_\nu = -0.78^{+4.66}_{-6.07}$
$\theta_\nu = 48.81^{+6.07}_{-5.94}$
$\Delta\Psi = \Delta\Omega = 10.00°$
$\Delta\theta_{launch} = 1.00°$
$\Delta\theta_{view} = 5.00°$
(aa)
$\phi_\nu = -0.76^{+6.07}_{-7.19}$
$\theta_\nu = 49.09^{+9.74}_{-10.05}$
$\Delta\Psi = \Delta\Omega = 10.00°$
$\Delta\theta_{launch} = 1.00°$
$\Delta\theta_{view} = 10.00°$
(ab)

Figure B.1

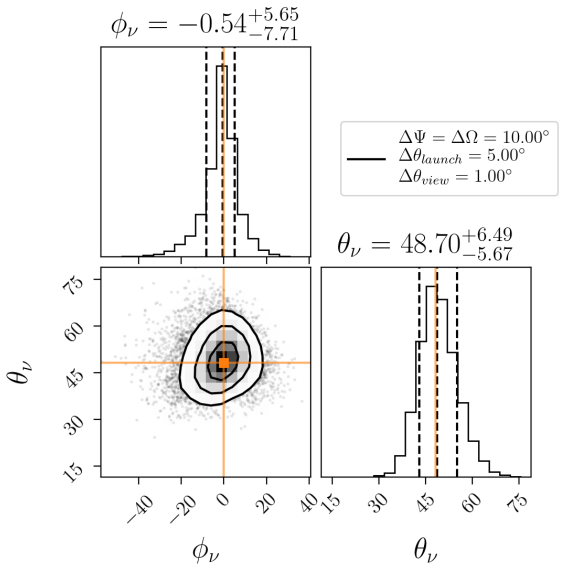

(ac)

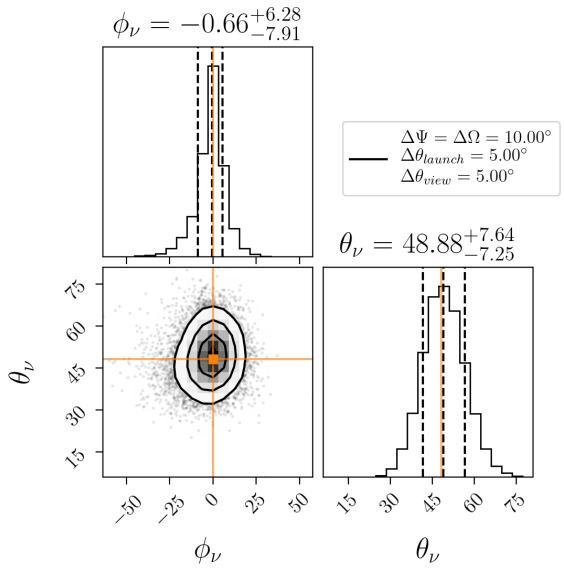

(ad)

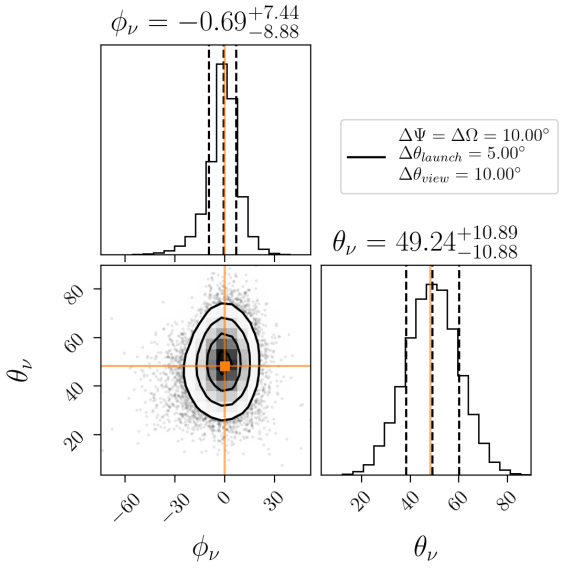

(ae)

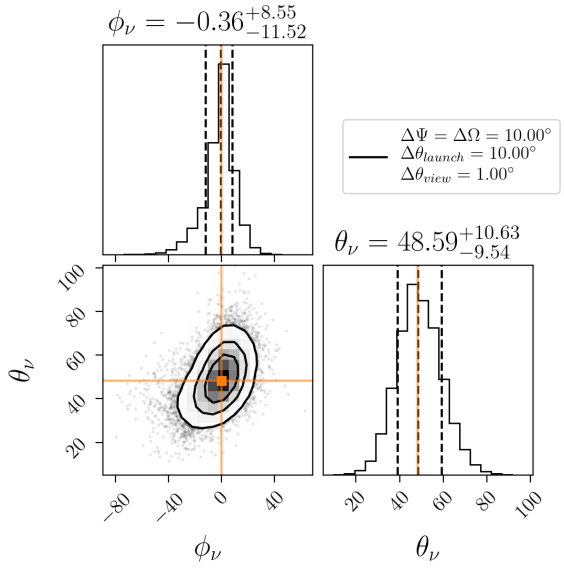

(af)

Figure B.1

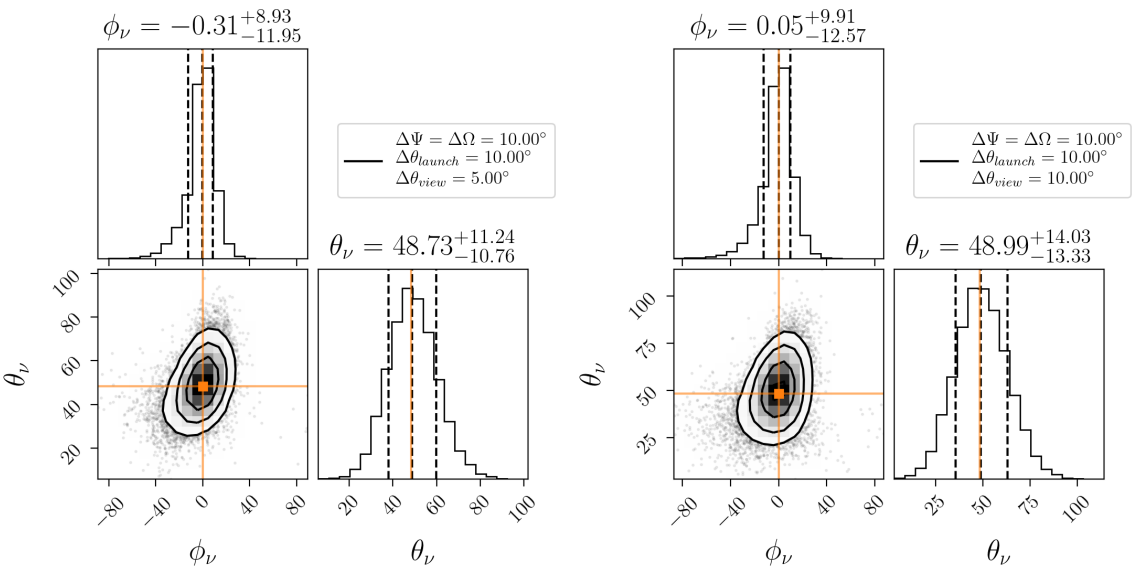

(ag) (ah)

Figure B.1

Appendix C

Additional information for the diffuse analysis chapter

C.1 Periods of time where the CW identification and the peak over baseline rates where high

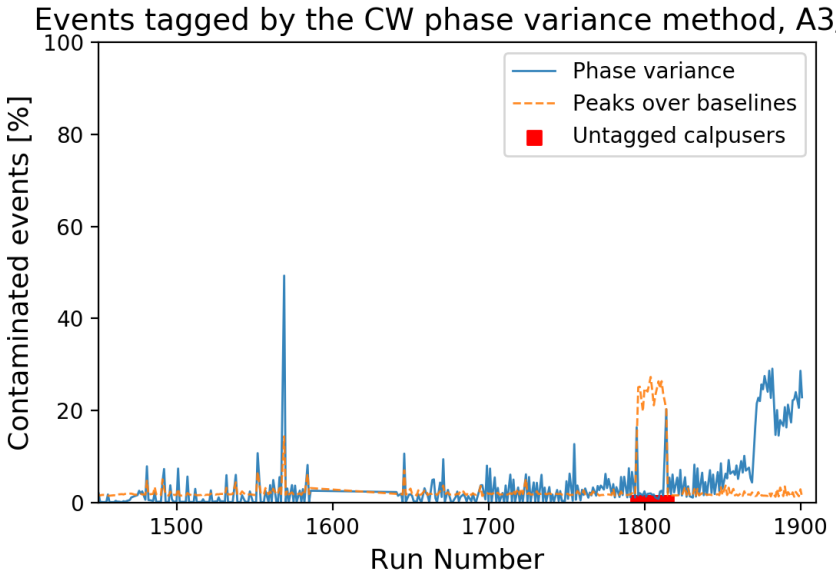

Figure C.1: High CW and peak over baseline rates:A3, configuration 1.

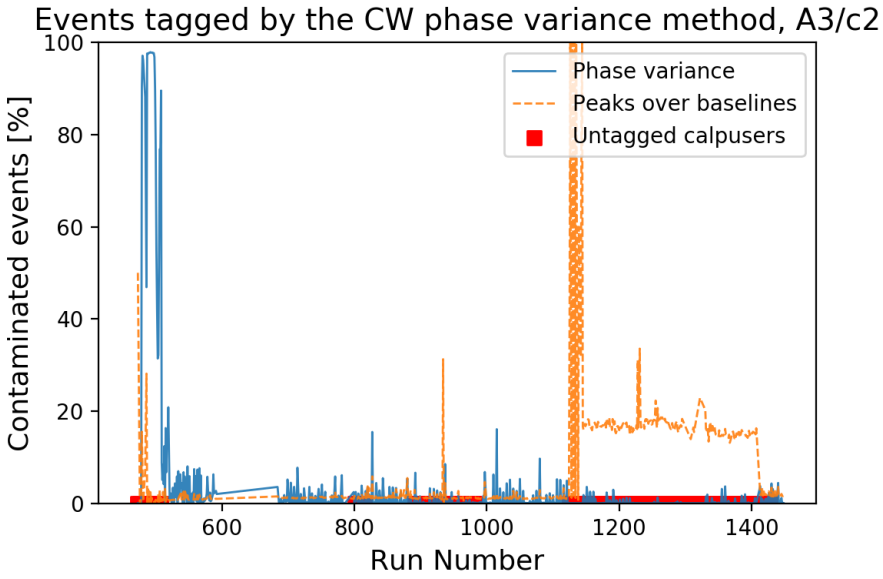

Figure C.2: High CW and peak over baseline rates:A3, configuration 2.

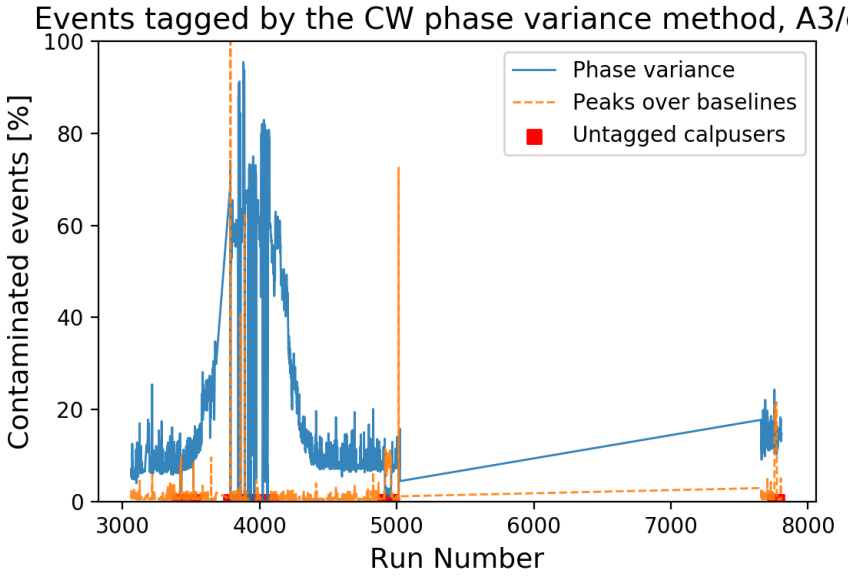

Figure C.3: High CW and peak over baseline rates:A3, configuration 3.

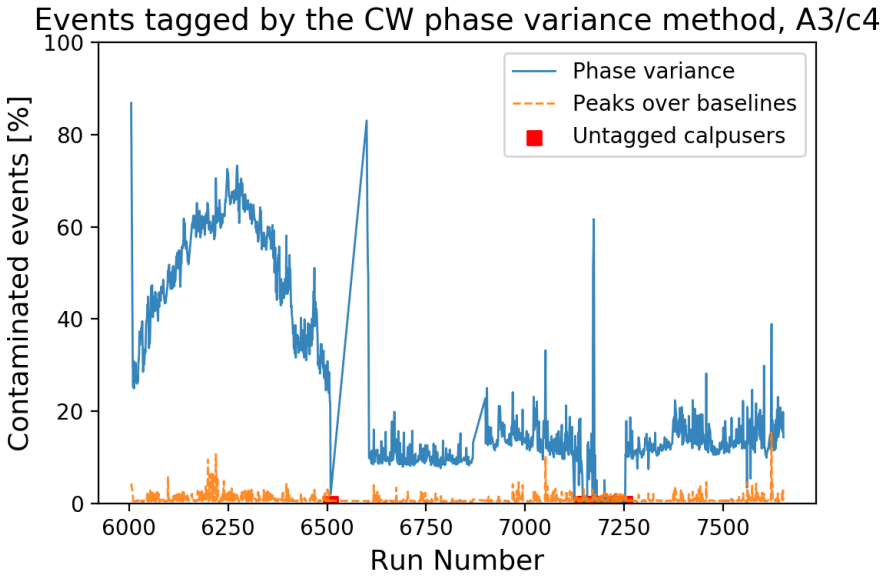

Figure C.4: High CW and peak over baseline rates:A3, configuration 4.

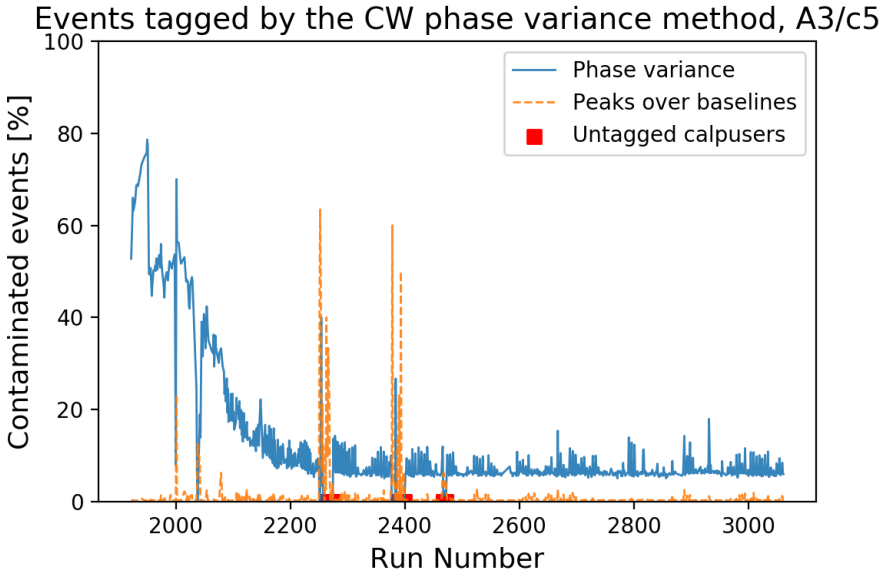

Figure C.5: High CW and peak over baseline rates:A3, configuration 5.

C.2 Calibration pulser events reconstruction for anomalous periods of time

We wanted to know if the features that we see in the phase variance method for some calibration pulser events in A3 affect their interferometric reconstruction. We reconstructed all calpulser events in a run and plotted a 2d histogram of their reconstructed coordinates as a function of run number. There is no evidence of anomalous reconstruction for periods of time where we observe unexpected behavior in the phase variance technique.

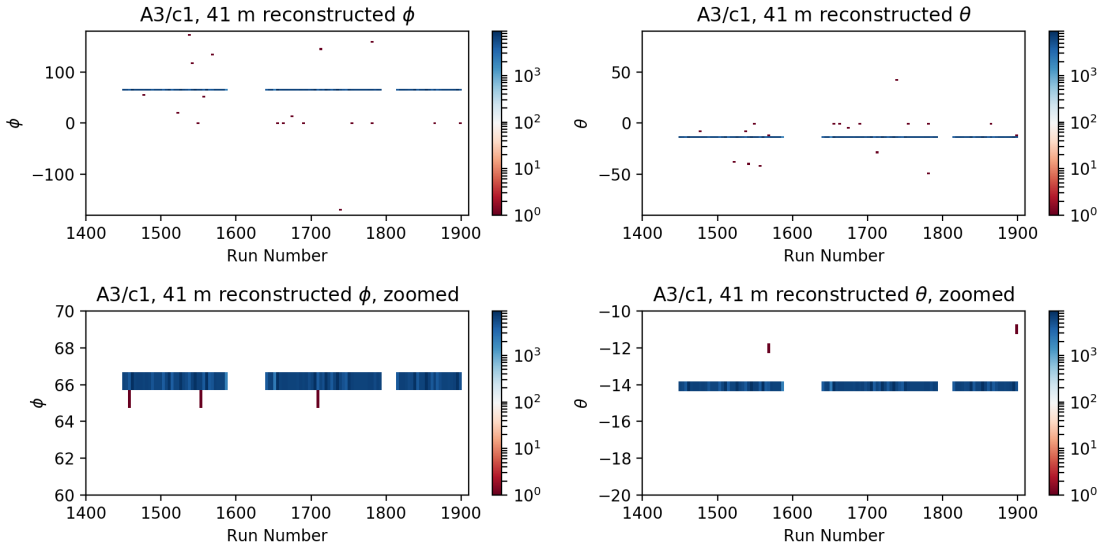

Figure C.6: Interferometric reconstruction of calibration pulser events as a function of run number for A3, configuration 1 (c1).

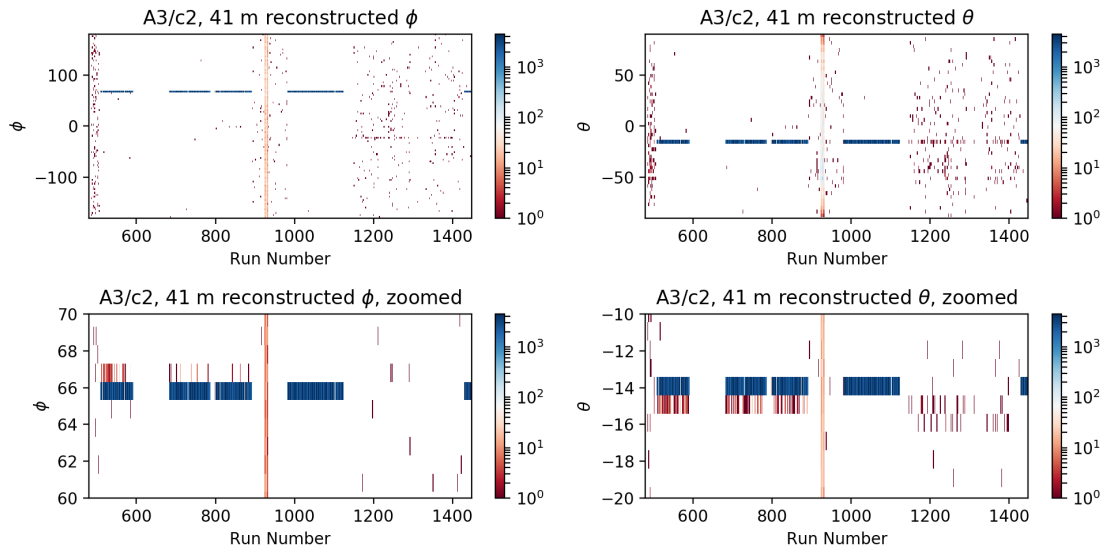

Figure C.7: Interferometric reconstruction of calibration pulser events as a function of run number for A3, configuration 2 (c2). Events around run 600, and events around run 1200-1400 correspond to periods of time where calibration pulser events where untagged.

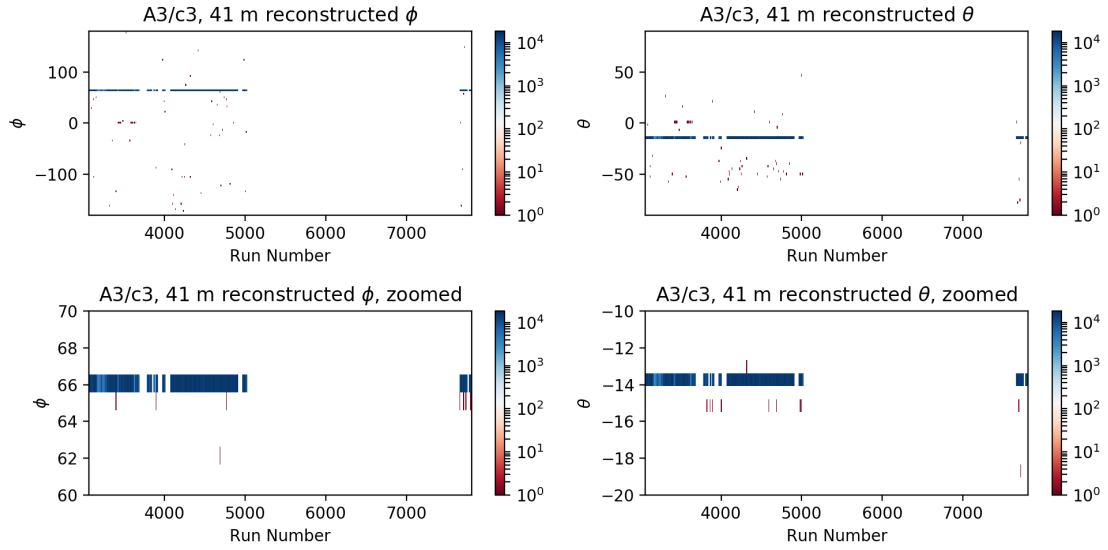

Figure C.8: Interferometric reconstruction of calibration pulser events as a function of run number for A3, configuration 3 (c3). Events around run 600, and events around run 1200-1400 correspond to periods of time where calibration pulser events where untagged.

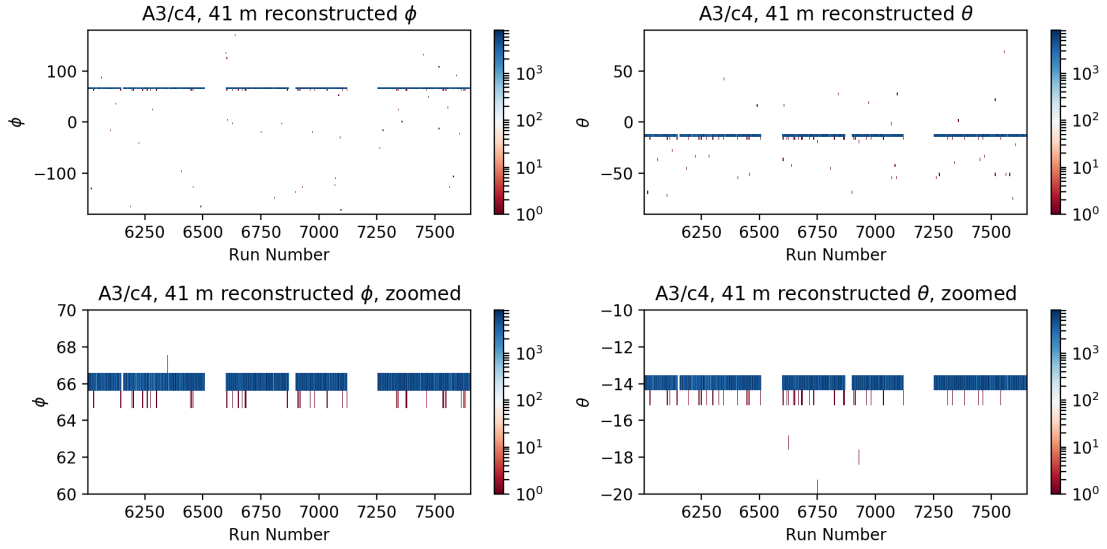

Figure C.9: Interferometric reconstruction of calibration pulser events as a function of run number for A3, configuration 4 (c4).

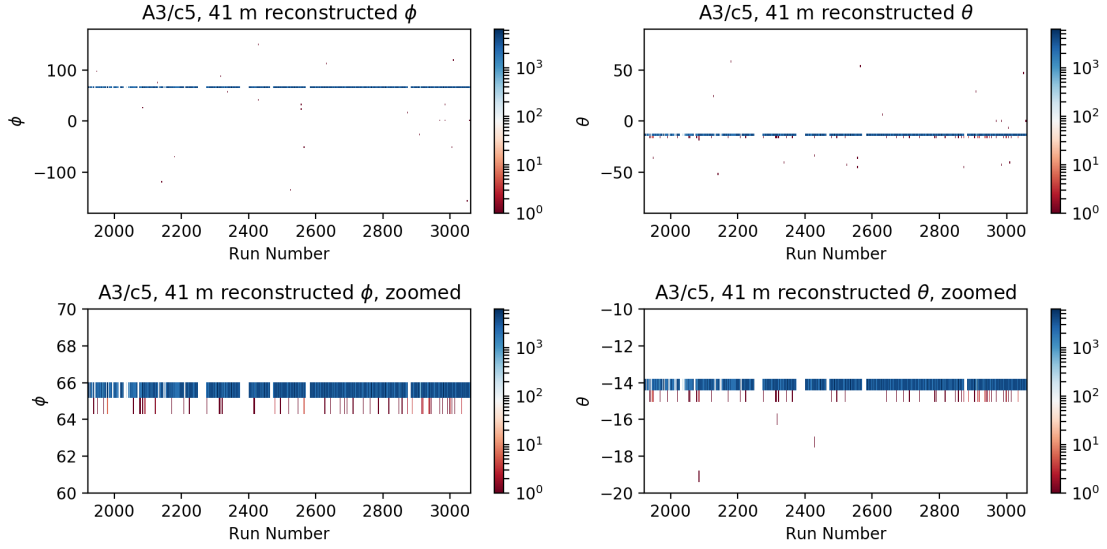

Figure C.10: Interferometric reconstruction of calibration pulser events as a function of run number for A3, configuration 5 (c5).

C.3 Untagged calibration pulser events

It was found that some A3 runs had untagged calibration pulser events. For normal runs about 15% of the total events are calibration pulsers, so we plotted this rate as a function of run to identify runs that contain untagged calibration pulser events. The following plots show the rate of calpulsers for each configuration of A3.

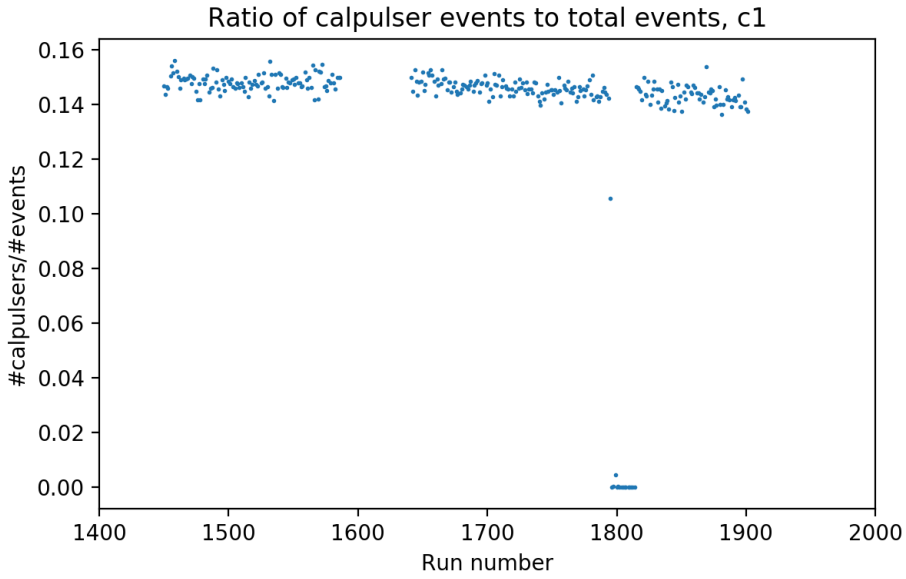

Figure C.11: Rate of calibration pulser events: A3, configuration 1.

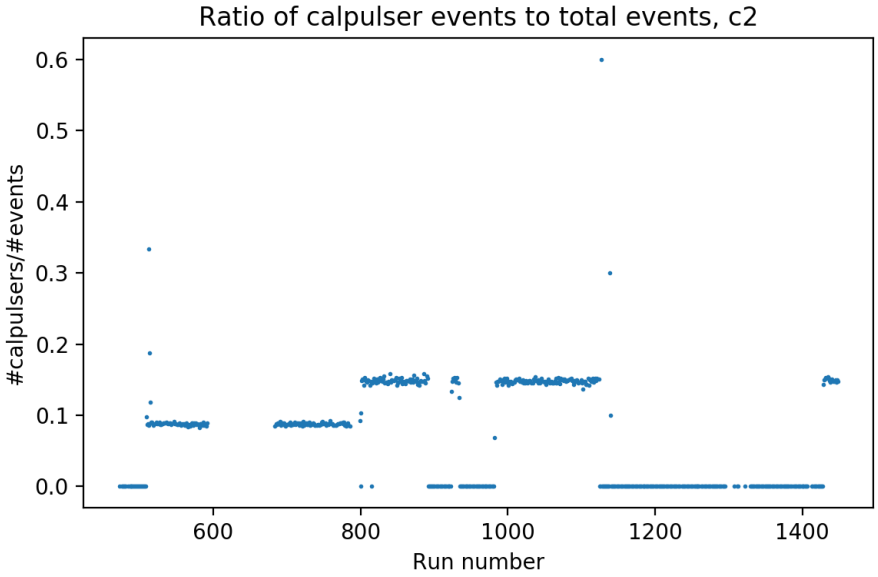

Figure C.12: Rate of calibration pulser events: A3, configuration 2.

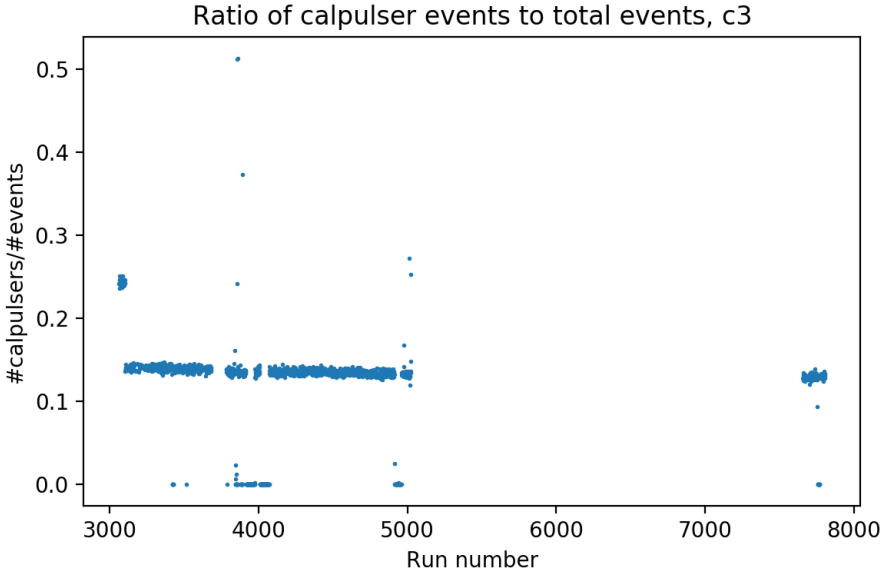

Figure C.13: Rate of calibration pulser events: A3, configuration 3.

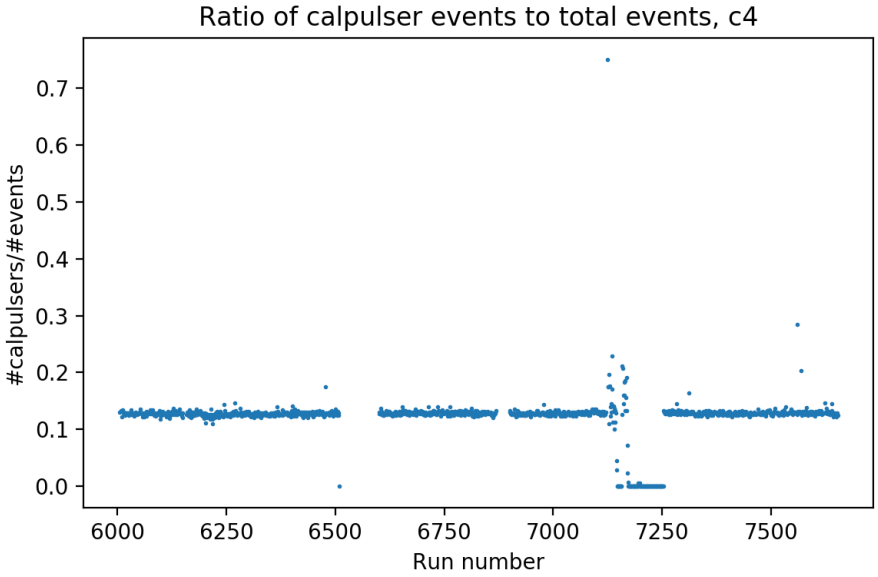

Figure C.14: Rate of calibration pulser events: A3, configuration 4.

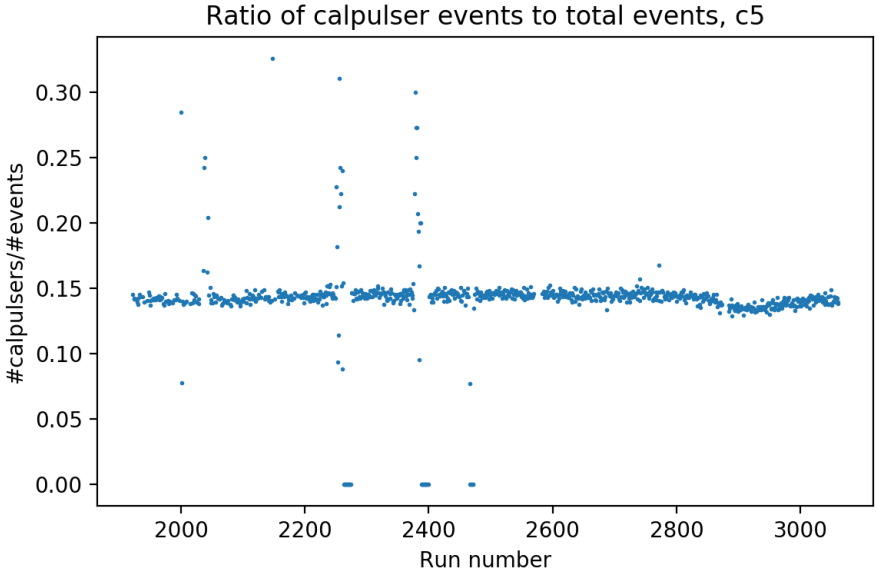

Figure C.15: Rate of calibration pulser events: A3, configuration 5.